SCALE DEPENDENT FORCING ON ICE ALGAE DYNAMICS: OBSERVATIONS AND MODELLING

by

Christopher-John Mundy

A Thesis submitted to the Faculty of Graduate Studies of
The University of Manitoba
in partial fulfillment of the requirements of the degree of

DOCTOR OF PHILOSOPHY

Centre for Earth Observation Science
Department of Environment and Geography
University of Manitoba
Winnipeg

THE UNIVERSITY OF MANITOBA

FACULTY OF GRADUATE STUDIES

*****

COPYRIGHT PERMISSION

SCALE DEPENDENT FORCING ON ICE ALGAE DYNAMICS:

OBSERVATIONS AND MODELLING

BY

Christopher-John Mundy

A Thesis/Practicum submitted to the Faculty of Graduate Studies of The University of

Manitoba in partial fulfillment of the requirement of the degree

DOCTOR OF PHILOSOPHY

Abstract

Sea ice algae play a critical role as the first available food source in ice-covered polar oceans. Changes in the thermal, physical and optical properties of the snow-sea ice system and feedbacks between various temporal and spatial scales affect accumulation of algae at the sea ice bottom and are the focus of this dissertation. The principle objective is to determine the importance of various characteristics and scales of physical processes on the accumulation and loss of bottom ice algae during the spring season. Field data used in the dissertation come from two spring field seasons undertaken in 2002 and 2003 near Resolute Bay, Nunavut, on landfast first-year sea ice. Results show that transmitted light, ice temperature and bottom ice structure are largely dependent on the spatial distribution and highly variable depth history of the overlying snow cover, which induces variability on ice algae biomass. Furthermore, the physical processes controlling the magnitude of biomass can differ based on snow depth from a thermal melt-off effect under thin snow to light limitation and thermal insulation under thick. It is also noted that destructive point sampling of the sea ice for algal biomass estimation limits a direct analysis of the principle objective. Therefore, algae optical absorption properties are used to develop methods for remote estimation of ice algal biomass. A coupled ice algae growth model is also employed to further examine the principle objective. Improvements were made to the model using detailed measurements of snow, sea ice and ice algae thermal and optical properties. The results supported the conclusions drawn from observations; however, simulations also demonstrated that the thermal and optical factors are not exclusive in their effects on algal accumulation and loss based on snow depth. The model was also

found to be very sensitive to variability in light attenuation and the ice warming rate. This dissertation highlights the importance of snow cover history and distribution on the sea ice system operating below. Furthermore, results emphasize the sensitivity of the bottom ice algae ecosystem to Arctic climate change through potential shifts in snow depth distribution and thermophysical changes induced by atmospheric or oceanic changes in temperature.

Acknowledgements

One learns a lot when undertaking a Ph.D. I not only refer here to the scholarly aspects a Ph.D. dissertation, but also friendship, collaboration and family. It is safe to say that such an undertaking is a life changing experience. The dissertation you hold is the result of friendship, collaboration and family as without these, the scientific research accomplished within could not have been accomplished. Therefore, I wish to extend my appreciation to the following people and organizations.

I start first with my advisor, David Barber, whom I thank for guidance, support and friendship. I extend my gratitude to my co-advisor, Christine Michel, who was always available for long conversations regarding my Ph.D. dissertation and had numerous suggestions for its improvement. Special thanks are also extended to my committee members, Michel Gosselin, Tim Papakyriakou and Rick Riewe and to my external examiner, Don Perovich.

I thank all my friends and collaborators who contributed to this thesis in one form or another (too many to mention individually). Of particular note, I thank Jens Ehn for both friendship and collaboration from which I believe we have both learnt a lot. In a similar fashion, I also extend my gratitude to Bob Hodgson and Alex Langlois. Special thanks are given to Jennifer Lukovich and Mats Granskog for helpful suggestions with respect to Chapter 5. I also thank Diane Lavoie and John Hanesiak for their help towards my modelling efforts in Chapter 7. Help in the field has also been greatly appreciated with contributions from Owen Owens, Martin Fortier, Kim Morris, Susan Zabenskie, John Iacozza, Bernard Leblanc, Rick Marsden and Michel Poulin. I thank the staff of the

Centre for Earth Observation Science including David Mosscrop, Denise Whynot and Wayne Chan, as well as the staff of the Department of Environment and Geography.

Funding for my Ph.D. came from a University of Manitoba Graduate Fellowship and the Northern Studies Training Program (NSTP). Additional support was provided through NSERC, CRC and CRYSYS grants to D. Barber, a DFO Strategic Science Fund to C. Michel and a Canadian Space Agency (CSA) grant to D. Barber and C. Michel. Logistical support in the field was provided by the Polar Continental Shelf Project.

Finally, I would like to thank my wife, Kate, my parents, Dan and Marie-Anne and the rest of my family and close friends who have helped make this long journey come to a close. I look forward for the years to come.

I dedicate this dissertation to my incredible wife, Katherine Mundy, who helped me stay strapped in during this rollercoaster ride called a Ph.D.

Table of Contents

List of Tables

List of Figures

CHAPTER 1: Introduction

1.1 Scientific Rationale

The Earth's climate, which results from a complex interaction between incoming solar radiation, emitted Earth radiation and the characteristics of the planet's surface and atmosphere, has been dynamic throughout its history. However, increased atmospheric CO_2 levels and a climate warming over the past century have raised public concern. A question of whether this change has an anthropogenic origin or is simply the natural variability of the Earth's climate has been posed (World Climate Research Program (WCRP), McBean, 1992). It is noted that there is increasingly more evidence to support the anthropogenic influence on climate change (ACIA, 2004). Throughout the last four decades, climate change research has had a strong focus on polar regions where important feedback mechanisms associated with ocean–sea ice–atmosphere interactions will likely cause change to be amplified relative to temperate and tropical regions of the planet (e.g., Barry et al., 1993; Boer et al., 2000).

Due to its vast extent and seasonal variation, snow-covered sea ice influences the earth climate system by increasing the global albedo and dictating the exchange of gas, mass and energy between the ocean and atmosphere. Spatial and temporal variations in ice extent are largely accounted for by first-year (seasonal) sea ice. Close to half the Arctic Ocean is currently covered by multi-year (perennial) sea ice. However, some global climate models under an anthropogenic forcing scenario predict a seasonally ice free Arctic within this century (e.g., Boer et al., 2000). It is noted that various climate models exist and that they show significant variation in the rate of sea ice retreat in the Arctic due

largely to the way they deal with processes affecting the snow and sea ice cover (Flato et al., 2004). Although many uncertainties surround these predictions, it is apparent that the Arctic ice cover is currently changing in extent and thickness (e.g., Parkinson et al., 1999; Rothrock and Zhang, 2005) and at an increasing rate (e.g., Comiso, 2002) and that the majority of ice in the near future will be first-year. It is important to note however, that these observations were derived from datasets that span 40 years at most whereas century long time series of temperature suggest that the changes may be part of a longer 65-70 year oscillation (Comiso, 2003).

Snow cover in the Arctic is also slated to change; however, observations and models do not appear to currently agree. Long term observations of snow over central Arctic pack ice have shown a decreasing trend in snow depth which led to a conclusion that snowfall had likely decreased over the Arctic Ocean (Warren et al., 1999). In contrast, with an exposed and warming ocean there is a projected increase in precipitation (ACIA, 2004) that would, given the expected climatology, fall as snow. It is noted that spatial and temporal coverage of the observations used in Warren et al. (1999) may have resulted in a bias. Furthermore, no method currently exists to make large scale (i.e., Arctic Ocean) observations of snow depth. On the other hand, climate models used in Arctic simulations have been developed using land-based forcing where meteorological records are readily available. However, it has been shown that land-based observations vary greatly from on-ice observations and that the differences between the two are not systematic (Hanesiak et al., 1999). A further ambiguity in observations of the snow cover revolves around its spatial distribution and redistribution. Models that deal with mass balance changes of the snow cover associated with wind events over sea ice (i.e., blowing snow) are still in their

infancy with small scale processes and interactions of snow with leads and cracks just beginning to be acknowledged (e.g., Déry and Tremblay, 2004). The result of all this uncertainty warrants the need to further study and understand the physical processes surrounding snow-covered sea ice.

Sea ice also provides a unique and important polar habitat for a thriving biological community of viruses and bacteria (e.g., Maranger et al., 1994, Junge et al., 2004) through to metazoans (Horner et al., 1992). In particular, most attention in the published literature has been directed to ice algae. Sea ice primary production precedes (Fortier et al., 2002) and can exceed (Gosselin et al., 1997) annual phytoplankton production in the Arctic, encapsulating the critical role of ice algae in the Arctic ecosystem. It is expected that the Arctic ecosystem will be very sensitive to climate change (Sakshaug, 2004). Perhaps the most apparent change will be a decrease in the spatial extent of ice algae associated with the change in sea ice extent observed from satellite data (Parkinson et al., 1999; Comiso, 2002).

However, ice algae may be more impacted by changes that are less easily discerned. One example of a potential impact involves observations that the distribution of heat in the Arctic Ocean appears to be changing towards a new warmer state (Polyakov et al., 2005), sea ice thickness has been decreasing at an alarming rate (Wadhams and Davis, 2000; Rothrock and Zhang, 2005) and Inuit are noticing more dangerous springtime ice conditions associated with bottom ice erosion (ACIA, 2004). These observations suggest a trend towards an enhanced ocean–ice heat flux which may continue into the future. It has also been suggested that the timing of bottom ice algal biomass loss has a strong sensitivity to the ocean–ice heat flux through interior ice melt and erosion of the

bottom ice habitat (Lavoie et al., 2005). Therefore, it can be hypothesized that warming of the Arctic Ocean will result in a decrease in the bottom ice algae growth season through an enhanced ocean–ice heat flux and therefore an earlier spring season erosion of the bottom ice algae habitat. However, the process of bottom ice melt is still being investigated by the scientific community. For example, field based research is just starting to uncover new interactions of oceanic heat and turbulence on bottom ice desalination (Widell et al,. 2006) and modelers are still deciding how to best physically represent the structure of sea ice (e.g., Feltham et al., 2006; Golden et al., 2006).

Another and perhaps more complex example involves the predicted change in the hydrological cycle with a potential for increased snowfall precipitation. Enhanced snow accumulation may decrease the amount of algal growth through attenuation of light, but increase the algal growth season by insulating the cold ice from the warming spring atmosphere. More snow may also cause surface flooding of the ice which would influence the location of the ice algal habitat. Furthermore, these impacts are complicated by blowing snow processes which will influence temporal and spatial variability in the system. The preceding examples help to illustrate our need to better understand what physically controls ice algae accumulation and loss for improved predictions of how the Arctic ecosystem may respond to climate change. In order to identify these potential impacts we need to take a 'system' science approach to comprehend the interconnections and interrelationships that ice algae experience in their physical environment.

System theory takes an interdisciplinary approach to science, considering processes which act to integrate the actual properties of the system. Furthermore, the need to look at different scales is prompted by a need to understand the various interdependent and

cross-scale processes of the system. For example, remote sensing from satellites, airplanes, or even meteorological stations can give estimates of bulk properties of snow-covered ice such as albedo, ice thickness, etc.; however, the physical processes resulting in these bulk observations are only revealed at the microscale (Eicken, 2003).

Processes may be defined as a series of actions or steps that bring about an end point or result. Within an earth system such as the marine cryosphere, processes are interdependent and the boundaries separating each process and their respective temporal and spatial scales are normally considered as a continuum or cascade of scales (Steffen et al., 2004). In the dissertation, spatial and temporal variability in bottom ice algal biomass is examined by relating to physical processes which affect the accumulation and loss of algal biomass at various scales. It is believed that this approach will lead to a better understanding of how bottom ice algae will respond to its physical environment and therefore improve our understanding on the sensitivity of ice algae to our future climate.

A system level diagram of the various physical processes relevant to bottom ice algae in the marine cryosphere is presented in Figure 1.1. The physical processes considered in this dissertation are numbered in the diagram and include (1) radiative transfer, (2) thermodynamics and (3) blowing snow, as well as processes related to (4) snow structure and (5) ice structure. It is noted that processes encompassed within (4) and (5) include a collection of processes such as snow metamorphism, snow and ice desalination, interior and bottom ice melt and ice-ocean interactions.

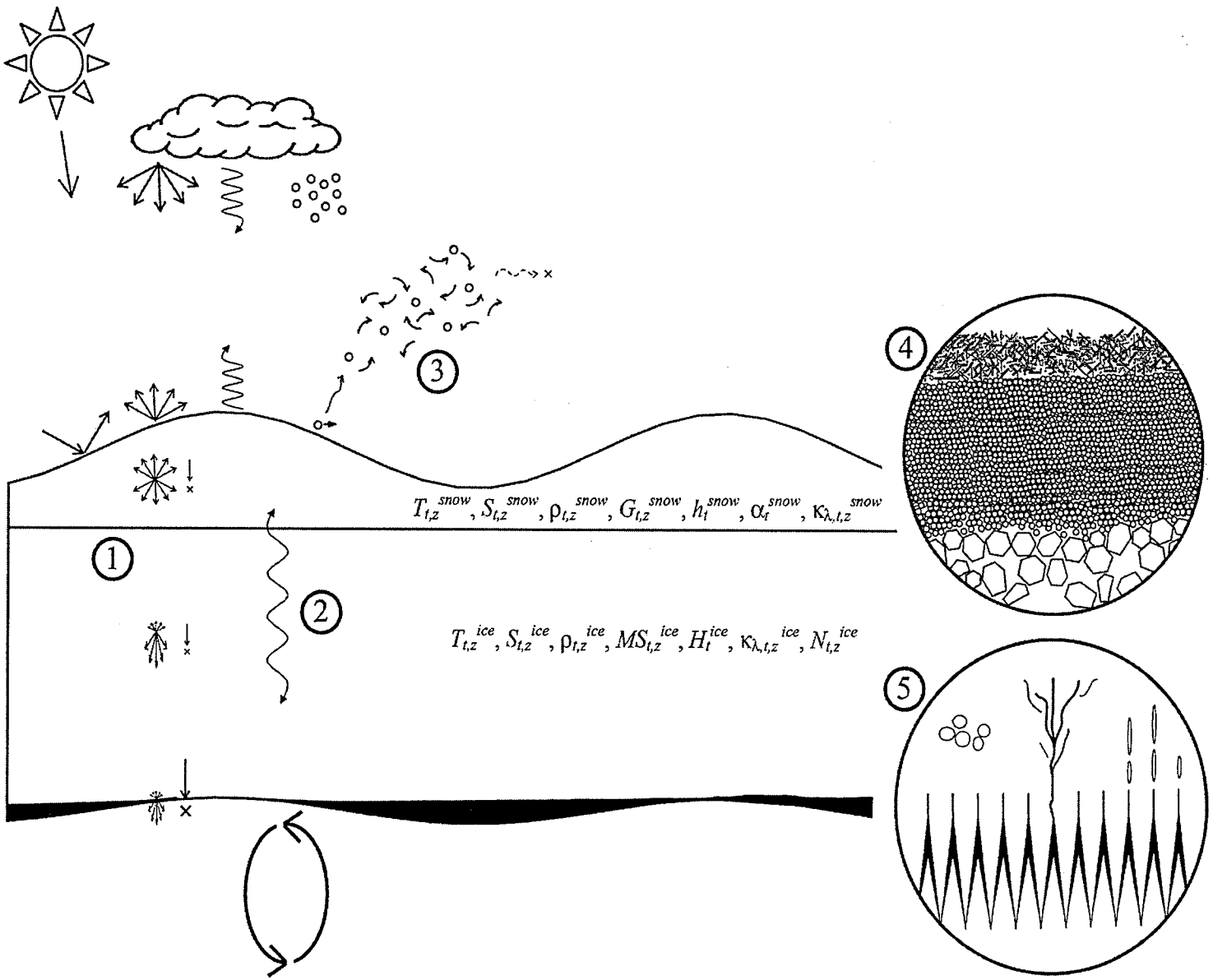

Figure 1.1. A schematic of physical processes of the marine cryosphere system which are pertinent to bottom ice algae in first-year sea ice. Please refer to the text for explanation of numbers and variable symbols.

In order to examine physical processes using field observations, thermophysical state variables and optical properties need to be defined. It is noted that state variables describe the momentary condition of a system, often referred to as thermodynamic variables (e.g., Cutnell and Johnson, 2005). Figure 1.1 lists variables of interest in the snow and ice, denoted by corresponding superscripts, which include: temperature (T), salinity (S), density (ρ), snow grain size (G), snow depth (h), surface albedo (α), spectral attenuation coefficient (κ_λ), ice thickness (H), ice microstructure (MS, including crystal size, brine layer spacing, brine channel density and size and inclusion density and size) and nutrients (N). Subscripts t and z denote time and depth, respectively.

1.2 Thesis Outline

Through numerous field studies, bottom ice algal accumulation and growth have been found to be controlled by light (Gosselin et al., 1986; Smith et al., 1988; Welch and Bergmann, 1989; Gradinger et al., 1991), nutrients (Gosselin et al., 1985; Cota and Horne, 1989; Michel et al., 1988; Gosselin et al., 1990) and habitat space and stability (Legendre et al., 1991; Krembs et al., 2001); and influenced by temperature and salinity (Legendre et al., 1991; Arrigo and Sulivan, 1992). My dissertation examines many of these environmental factors by investigating what gives rise to their variability.

The principle objective of my dissertation is to determine the importance of various characteristics and scales of physical processes on the accumulation and loss of sea ice algae during the spring season. This objective is investigated through both observations and modeling and is addressed as a series of sub-objectives within the chapters of this dissertation. An emphasis is placed on snow as its physical, thermal and subsequent

optical properties are an order of magnitude more important than the atmosphere and sea ice. Given the importance of snow, it is hypothesized that the history and distribution of snow over sea ice control the magnitude of ice algae biomass through both thermophysical and radiative processes.

In Chapter 2, I provide a discussion of the key physical processes which control the temporal and spatial distribution of ice algae biomass and production as a backdrop for the results, discussion and conclusions presented in Chapters 4 to 8. Chapter 2 reviews ice algae habitats and physical controls, then provides an in depth review of the physical processes that influence the distribution of ice algae through access to light, nutrients, and substrata as well as exposure to temperature and salinity variability. In Chapter 3, I describe the dataset and models used in the dissertation.

In Chapter 4, I document and summarize some of the key processes outlined in Figure 1.1 using a case study. Acknowledging the principle objective, I examine the following sub-objectives:

(1) To document variability of thermal, physical and optical properties of snow-covered landfast first-year sea ice pertinent to sea ice algae biomass in spring;

(2) To examine how these physically-based variables affect ice algae biomass.

A focus is made in this analysis on surface forcing factors which affect the accumulation and loss of algal biomass in the bottom ice.

In Chapter 5, I change my focus to physical factors operating near the ice bottom which affect the distribution of algal biomass. I provide an examination of the microscale

distribution of algal biomass in relation to variability of the ice microstructure, brine drainage features and tidal currents in an effort to meet the following sub-objectives:

(1) To describe the spatial elements of algae and ice structure/brine drainage features;

(2) To investigate the linkages between ice structure and brine drainage and the microscale distribution of ice algal biomass.

It is noted that extensive spatial sampling of ice algal biomass remains limited due in part to limitation in field methods and non-invasive time-series measurements are currently non-existent. This fact is emphasized in Chapter 4 where destructive point sampling of the sea ice limit a direct analysis of the principle objective. Therefore in Chapter 6, I investigate the following sub-objectives in an effort to develop a means to study the effects of changing environmental variables on ice algal biomass:

(1) To provide a comprehensive examination of the spectral dependence of transmitted irradiance on snow cover and algal biomass;

(2) To improve spectral parameterizations of a radiative transfer model using field observations;

(3) To develop a method to remotely estimate ice algal biomass using spectral transmitted irradiance.

The improved radiative transfer model employed in Chapter 6 is further coupled with a thermodynamic and ice algae growth model in Chapter 7. Using results and conclusions drawn in the preceding chapters, the model is used to examine the sensitivity of bottom

ice algae accumulation and loss to thermal and optical factors. In Chapter 7, I investigate the following sub-objectives:

(1) To couple one-dimensional thermodynamic, radiative transfer and ice algae growth models and match to field observations;

(2) To examine the response of the model to a series of sensitivity analyses examining the response of algal biomass to important thermal and optical factors.

In Chapter 8, I restate the principle objective and review the pertinent results of each sub-objective by integrating the important conclusions within the framework of the system schematic depicted in Figure 1.1. I conclude my dissertation with a summary of its caveats and limitations and potential directions for future research.

CHAPTER 2: Background

2.1 Introduction

In this chapter, I describe briefly the habitat and physical factors which influence ice algal biomass accumulation and loss, then discuss in more detail the physical processes that drive these factors. The chapter is sub-sectioned accordingly. This discussion is provided as a backdrop for the results presented in Chapters 4 to 7 of my dissertation.

2.2 Sea Ice Algae

2.2.1 Habitat

The various sea ice algae habitats have been summarized in response for a need to standardize terminology among the research community (Horner et al., 1988, 1992; Cota et al., 1991; Arrigo, 2003). A schematic representation of the habitats is depicted in Figure 2.1. Generally, there are three different habitats based on vertical location in the ice: surface, interior or internal and bottom. These habitats are associated with specific ice structure as will be discussed in Section 2.3.

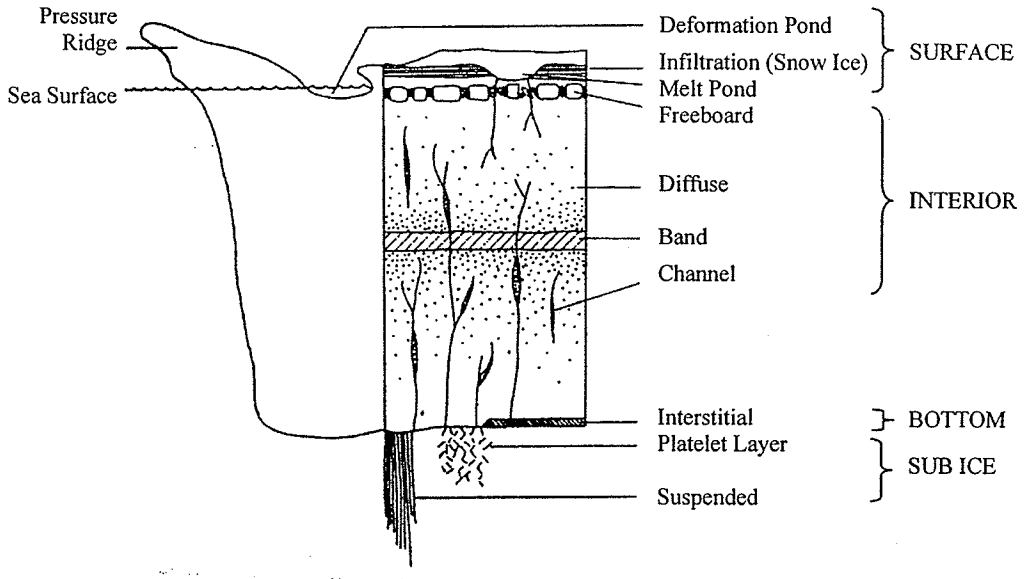

Figure 2.1. Diagrammatic representation of ice algae habitats. Adapted from Horner et al. (1992).

Surface and internal habitats are mostly constrained to periods of melt and warmer ice temperatures, while access to nutrients is the main limit on algal growth. These habitats include surface meltponds (low salinity meltwater), surface deformation ponds (infiltrated seawater pond), internal brine inclusions and channels, and internal layers of consolidated frazil or previous years' sea ice growth. One exception to the restriction of warmer temperatures is a surface infiltration habitat. This habitat occurs when sufficient snow loading forces the sea ice below the sea surface resulting in surface flooding. Algal growth in these habitats can take place throughout the growth season (i.e., sufficient light and presence of sea ice) and significantly contribute to annual primary production (Arrigo et al., 1997); however, the occurrence of surface flooding is largely restricted to the Antarctic (Wadhams et al., 1987). The seeding of the surface communities and other internal frazil layers is thought to occur during sea ice formation as algae are scavenged from the water column by frazil crystals floating to the surface (Garrison et al., 1989).

The seeding of other internal habitats may be due to algae being overgrown by a rapid ice growth rate or through the introduction of cells by convective mechanisms within the sea ice.

The majority of biomass accumulation resides within bottom ice habitats, particularly within the bottom few centimeters of an ice cover. This layer is characterized by protruding lamellar crystals (see Section 2.3.1) and brine channels (see Chapter 5), which provide a large colonization surface. The advantage of this habitat is that access to light and space are maximized while direct contact with seawater provides relatively stable temperature and salinity as well as access to nutrients via turbulent mixing, molecular diffusion (Cota and Horne, 1989) or convective exchange (Reeburgh, 1984). The upper limit of algal growth into the ice cover appears to be limited by temperature and salinity (Arrigo and Sulivan, 1992), however, nutrient availability (Cota et al., 1991) and space (Krembs et al., 2001) may also be limiting factors. Ice algae growing in this habitat are usually governed by light in early spring and by nutrients in late spring (Smith et al., 1988; Gosselin et al., 1990). Further, accumulation may be affected by: the process of ice melt causing their habitat to degrade, ice melt through their own heat absorption (Zeebe et al., 1996; Lavoie et al., 2005) or bottom ice topography that may cause preferential erosion and accumulation of algae due to under ice turbulent currents (e.g., Krembs et al., 2002).

Other habitats include the sub ice environment where algae can suspend themselves off the sea ice bottom and the platelet layer where frazil accumulates at the ice bottom as it forms through contact with cold ice shelf waters. Although the former habitat is most commonly observed during periods of melt due to light shading by the bottom ice algae,

it may contain some of the most productive ice algal blooms in the Arctic (Gosselin et al., 1997). These algal communities were thought to be restricted to multiyear pack ice where they had been sporadically, yet exclusively observed (Syvertsen, 1991). More recently, the highest production and biomass observations of these communities have been shown to be associated with first-year ice covers in the central Arctic pack (Gosselin et al., 1997). The latter habitat, platelet layer, is largely restricted to the Antarctic and supports some of the highest known concentrations of algal biomass in the World's oceans (Arrigo, 2003). The low salinity melt layer formed under the sea ice late in the season may also form a habitat for algae sloughed off from the ice bottom, however, only a few observations of this phenomenon appear to exist (Cota and Horne, 1989; Gradinger, 1996).

2.2.2 Physical Controls

Noted in Chapter 1, ice algal accumulation and growth have been found to be controlled by light, nutrients and habitat space and stability; and influenced by temperature and salinity. The effect of these physical factors on ice algal growth is demonstrated by the calculation used for the specific algal growth rate, μ (d^{-1}) (Arrigo and Sulivan, 1994):

$$\mu = \mu_{max}\, LR\, S_f \qquad [2.1]$$

where: μ_{max} (d^{-1}) is the temperature dependent maximum specific growth rate, LR is the dimensionless resource limitation coefficient and S_f is the fractional growth rate allowed by salinity. The specific calculations for each component in equation 2.1 are presented in Chapter 3. Within upper and lower temperature limits μ_{max} generally increases exponentially with temperature according to a sensitivity rate coefficient (Eppley, 1972). S_f denotes a polynomial relationship with salinity (Fig. 2.2). It should be noted that these data have been derived from a single study in the Antarctic (Arrigo and Sullivan, 1992). LR is determined through the fractional growth rate induced by the single most limiting resource, for which a recent study has considered light, nutrients or ice growth rate to be the three limiting factors (Lavoie et al., 2005). In this work, ice growth rate limitation was used as a proxy for habitat space and stability. Light as a resource to algal growth is important in both its intensity and spectral quality. Therefore, Arrigo et al. (1991) used the value of photosynthetically usable radiation (PUR) in their model calculations, which is dependent on the absorption properties of the algal community as well as the spectral distribution of downwelling photosynthetically available radiation (PAR; 400 to 700 nm). It is noted that the effect of available substrate space and habitat stability on ice algae is just beginning to be studied (e.g., Krembs et al., 2001) and that incorporation of the ice growth rate coefficient as a limiting factor on algal growth in ice algae growth models may be more complex than previously considered. For example, habitat space may have a greater influence on algal accumulation and not growth. This point is discussed in more detail in Chapter 7.

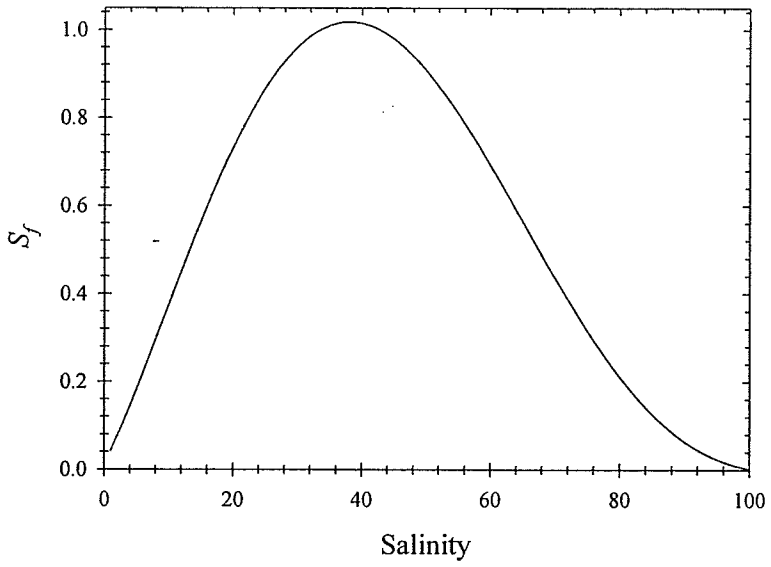

Figure 2.2. The salinity-dependent growth coefficient as a function of salinity and calculated from the polynomial given in Arrigo (2003).

The previous point has also brought to attention the need to distinguish between biomass and primary production. Biomass is a measure of the amount of algae accumulated at one point in time and for ice algae is usually expressed in units of mg chl *a* m^{-2} or mg C m^{-2} (Horner et al., 1992). Whereas primary production is the total carbon fixed by an algal community over time and is usually expressed in units of mg C m^{-2} d^{-1} or Tg C y^{-1} for a region (e.g., Legendre et al., 1992). Calculating changes in biomass over time could be used as a conservative estimate of primary production; however, the value would represent net and not gross production. This is because losses of material due to respiration, exudation and grazing would not be accounted for (Arrigo, 2003). Further, algal biomass losses and gains due to sloughing off and accumulation onto the ice, respectively, would not be accounted for.

The above-mentioned physical controls on ice algal biomass and growth have overlapping scales of temporal and spatial variability, which operate to determine the distribution of ice algal biomass and production. I focus the next section on the physical processes driving the physical controls mentioned above.

2.3 Physical Processes

In this section of the Chapter, I review and evaluate physical processes that influence the distribution of ice algae through access to light, nutrients, and substrata as well as exposure to temperature and salinity variability. My arbitrary separation of scales will be to first examine the temporal dimension through the processes behind sea ice formation and melt and the result of these processes on radiative transfer through the snow-covered sea ice. I then examine the spatial dimension through the processes behind snow accumulation. I end this section with a short remark on processes and scales.

2.3.1 Sea Ice Growth and Decay

Sea ice is defined as any form of ice found within the ocean that has originated from the freezing of seawater (WMO, 1970). Seawater is a combination of pure water and various dissolved solids (salts) and gases with an approximate salinity of 32 to 35 in oceanic environments (salinity units are defined as a dimensionless ratio of g of salt to 1000 g of water). It is noted that ocean salinity varies beyond this, particularly at polar latitudes due to sea ice accretion and ablation and substantial terrestrial based water run-off (Carmack, 1990). The formation of ice from seawater is a complex process where the salt and gas components are squeezed out and trapped within as the pure water

component creates hydrogen bonds forming crystals of ice. The result is a mixture of ice, brine (a concentrated salt-water mixture), solid salts (if temperatures are cold enough) and gas (Weeks and Ackley, 1982). The interdependence of this system is such that the thermal properties of the forming sea ice influence the relative volume and physical structure of each component within the sea ice, which in turn determines its thermal properties.

2.3.1.1 Sea Ice Formation and Structure

Ice crystals begin to form when seawater is supercooled (i.e., cooled below its freezing point of approximately –1.8°C). Unlike freshwater, the freezing point of seawater is higher than its temperature of maximum density (Fig. 2.3). However, like freshwater, the solid state of seawater is less dense than its liquid. Therefore, surface cooling of seawater induces thermohaline convection, creating a surface mixed layer up to several meters thick. This mixed layer may also deepen by wave and wind stress on the ocean surface. Disc shaped, highly saline ice crystals, termed frazil, rapidly form around nuclei in this supercooled mixed layer and rise. Congealed frazil forms the surface layer of all first-year sea ice (Weeks and Ackley, 1982). As described in Section 2.2.1, formation of frazil ice may also be an important mechanism for scavenging of algae from the water column into the newly forming sea ice cover (Garrison et al., 1989).

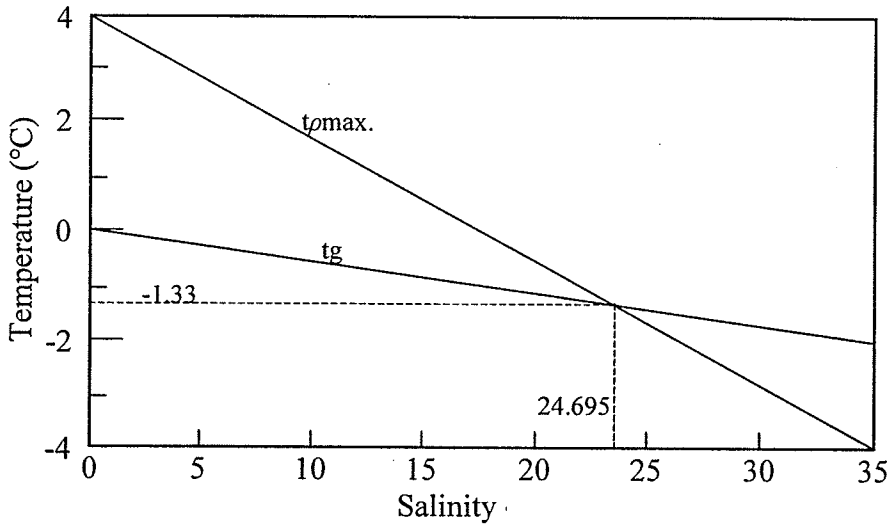

Figure 2.3. Temperature of the density maximum (tρmax) and of the freezing point (tg) for seawater of different salinities. Adapted from Weeks and Ackley (1982).

In calm, cold conditions, frazil ice accumulates at the surface and quickly congeals into a thin highly plastic surface known as grease ice. These conditions can occur anywhere where oceanic and atmospheric forcing are sufficiently low to allow for quiescent growth (e.g., bays, wind-protected coastal areas, etc.). In areas of higher wind and wave turbulence, the frazil layer can be up to a meter thick and much less uniform, however, these conditions are usually restricted to the Antarctic (Weeks and Ackley, 1982). Wave action on accumulating surface frazil favors production of circular ice formations with upturned edges, termed pancake ice (up to 3 m in diameter and typically < 10 cm thick; Wadhams et al., 1987). The repeated contacts due to convergence and divergence between neighboring pieces of ice create the circular form and push frazil onto the edge of the pancakes (Weeks and Ackley, 1982). Eventually, pancakes consolidate into continuous ice sheets.

Once an ice surface has been produced, ice will begin to form as a result of heat conduction upward along a temperature gradient through the ice volume. Consequently, ice crystals grow on the lower surface of the ice sheet and are therefore limited in their growth direction (Weeks and Ackle,y 1982). Over a thin layer (approximately 5-10 cm) the process of geometric selection causes vertical alignment of crystal growth. This type of growth results in a characteristic and fairly uniform ice structure termed columnar or congelation ice, which constitutes the dominant structure of sea ice in the Arctic. Geometric selection is caused by the fact that crystals grow faster perpendicular to their *c* axis. Therefore, crystals with a horizontal *c* axis orientation will grow ahead of neighboring crystals with different orientations (Weeks and Gow, 1978). Eventually, the vertically oriented growth crystals isolate the other crystals from access to the seawater resulting in a highly anisotropic crystal orientation with *c* axes in a horizontal plane. Another important mechanism is the formation of the bottom ice lamellar surface. During congelation ice growth, salt segregation occurs where salt ions are rejected out of the sea ice forming a dense layer at the ice-water interface. The difference in diffusion rates of salt (flux of ions) and heat (transfer of momentum) creates an unstable constitutionally supercooled layer at the ice-water interface, which essentially provides a heat sink (Fig. 2.4). Crystal protrusions into this layer are at a growth advantage as they can access the heat sink in addition to heat conduction through the ice, thus forming a lamellar surface of vertical crystal protrusions. These crystal protrusions form the skeletal or interstitial layer that can be 1 to 5 cm thick and is where ice algae are typically found in the Arctic (Fig. 2.1). Further, it is between these protrusions, or ice platelets, where brine and gas are trapped as the ice bottom grows downward. Congelation ice crystals consist of many

vertical ice platelets. The platelets are typically > 5 cm in length and 0.4 to > 1.0 mm in width (Weeks and Ackley, 1982; Nakawo and Sinha, 1984). The width of these crystal platelets also determines the spacing of vertical brine and gas inclusions, which are trapped between adjacent platelets due to formation of small ice bridges. Spacing also increases with ice thickness as growth rates slow (Nakawo and Sinha, 1984).

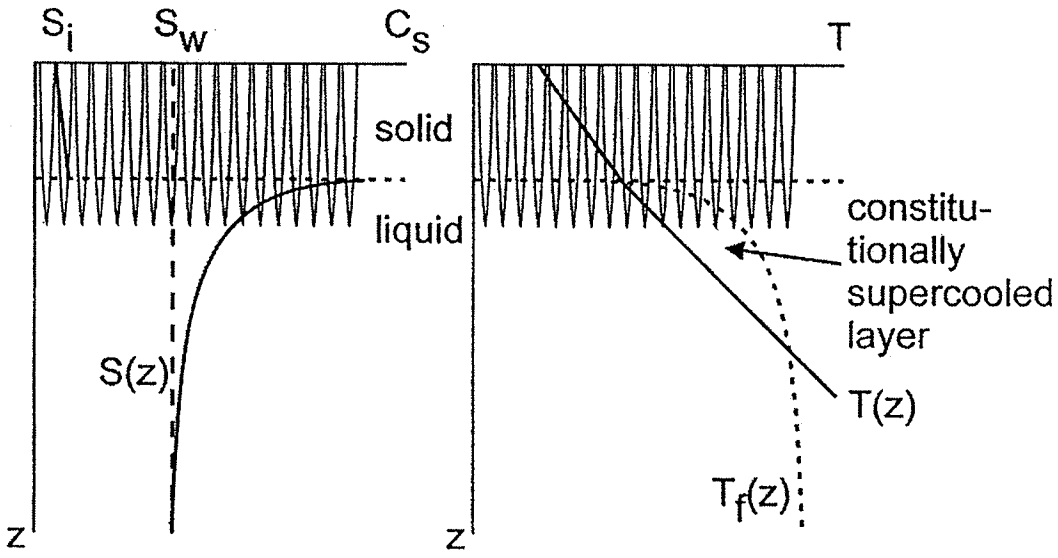

Figure 2.4. Diagrammatic representation of the lamellar bottom ice surface (skeletal layer) with corresponding salinity (Cs) and temperature (T) scaled gradients demarked as S(z) and T(z), respectively. The salinity-dependent freezing temperature profile is shown as a dashed line (T_f), with the constitutionally supercooled layer bounded by T(z) and T_f (z). Si and Sw represent salinity of the ice and the seawater at depth, respectively. Adapted from Eicken (2003).

During initial growth of the ice sheet, wave and wind stress may cause rafting of floes onto one another. With further ice growth, the vertical crystal structure and formation processes lend themselves to desalination processes (see 2.3.1.3), decreasing bulk ice salinity with age (Fig. 2.5; Weeks and Ackley, 1982). The decreased salinity reduces the ice sheet's elasticity. As a consequence, rafting becomes much less common with ice

deformation processes (rubbling) dominating. Rubbling occurs due to compressive failures within an ice sheet as wind and current action cause converging horizontal pressures (Mellor, 1986). This results in the forcing of one portion of the ice sheet upward and the other downward, forming a sail and keel, respectively. Common results of rubbling are the formation of extensive linear features termed pressure ridges (Mellor, 1986) or extensive rubble fields, which both act to thicken the average ice sheet thickness (Thorndike et al., 1975). Further, it may form additional habitats for ice algae (see Section 2.2).

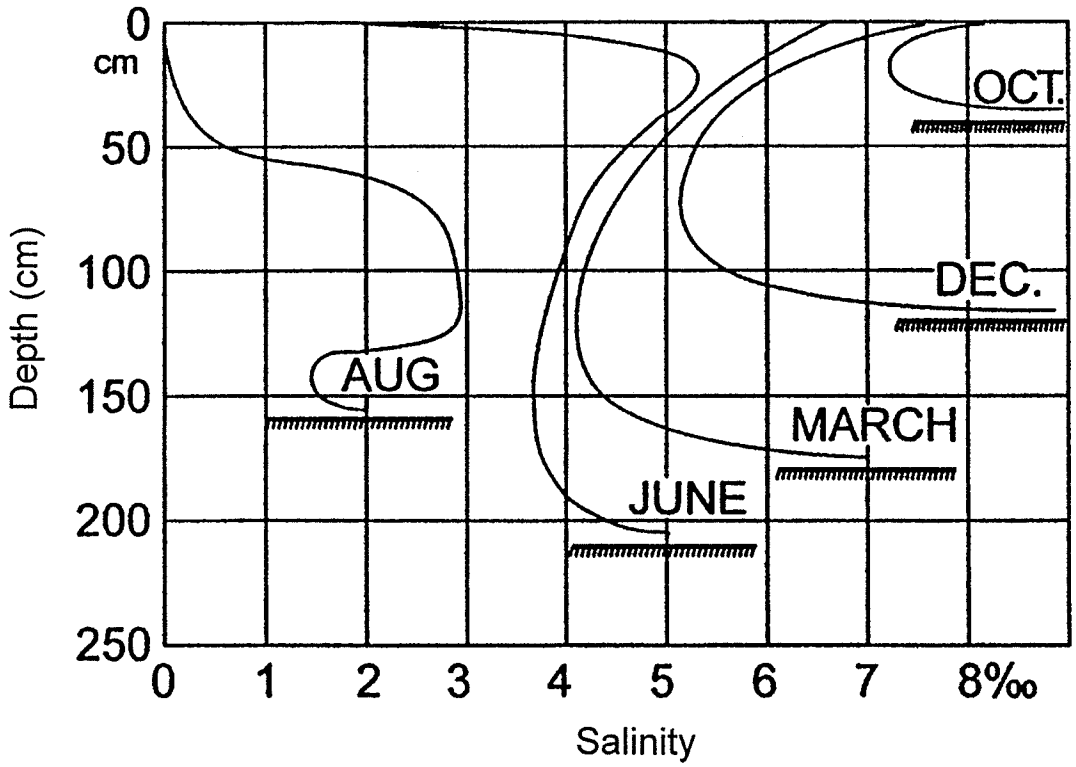

Figure 2.5. Evolution of Arctic first-year ice salinity profiles from formation (December) through to advanced melt (August). Adapted from Eicken (2003).

When first-year sea ice remains intact after one melt season (accumulation > ablation), the ice is then termed old or multiyear ice. Approximately half the Arctic Ocean is

currently covered by multiyear ice. This ice type is much less saline than first year ice due to preferential melt of brine pockets and subsequent brine drainage that occurs during ablation. Thickness of a multiyear ice sheet increases through successive winters. This is due to annual growth layer additions to the bottom of the sheet, which can be used (in a similar fashion to tree rings) to tell the minimum age of an ice sheet (Weeks and Ackley, 1982). Similar to first-year ice, multiyear ice can form pressure ridges and rubble ice due to wind and current stresses. This deformation can also act to increase the average thickness of an ice sheet. For example, the hummocks of very old ice can be well over 5 m, whereas the equilibrium ice thickness due to annual heat budgets of the Arctic is limited to approximately 3 m (Maykut, 1986).

2.3.1.2 Heat Budget and Ice Growth

Sea ice growth occurs as heat is extracted from the warm ocean into the cold atmosphere. The energy flux at the atmosphere-ice and ice-ocean interfaces as well as the thermal properties of the snow and sea ice govern the rate of this heat extraction and therefore sea ice growth. At thermal equilibrium with the atmosphere, sea ice thermodynamic processes adhere to the law of energy conservation in that fluxes entering or leaving the sea ice surface must be balanced. This is demonstrated with the following vertical flow surface heat balance equation for the atmosphere-ice interface:

$$(1-\alpha)SW_S - SW_T + LW_D - LW_U + Q_H + Q_E + Q_C + Q_M = 0 \qquad [2.2]$$

where $(1-\alpha)SW_S - SW_T$ represents the shortwave flux with albedo (α; ratio of upwelling to downwelling shortwave energy), incoming shortwave energy at the surface (SW_S) and

transmitted shortwave flux through the sea ice (SW_T), $LW_D - LW_U$ represents the incoming minus outgoing longwave flux, the turbulent sensible and latent heat fluxes are Q_H and Q_E, respectively, Q_C is the conductive heat flux and Q_M is the flux associated with any phase transition at the ice surface (Maykut, 1986).

In the Arctic, the net radiation balance (shortwave and longwave fluxes) drives the surface heat budget with other fluxes up to a factor of magnitude less on average (Maykut, 1986). In winter, when shortwave fluxes are negligible or nonexistent, outgoing longwave fluxes dominate, however, turbulent heat fluxes can play an important role in initial sea ice formation (Steffen and DeMaria, 1996), particularly in polynya environments (Roberts et al., 2001). At the sea ice surface, the majority of these fluxes are balanced by Q_C (Steffen and DeMaria, 1996).

The conductive heat flux indicates the vertical heat transfer rate and is governed by the temperature gradient and the physical/thermal properties of the transfer medium, as demonstrated in Fourier's law (Oke, 1987):

$$Q_C = -\gamma_{si}\left(\frac{\partial T}{\partial z}\right) \qquad [2.3]$$

where $(\partial T/\partial z)$ is the linear temperature gradient with depth and γ_{si} (W m^{-1} K^{-1}) is the effective thermal conductivity of the ice. γ_{si} is a function of salinity and temperature in the ice (Schwerdtfeger, 1963; Yen et al., 1991). Generally, sea ice is less conductive than freshwater ice as the thermal conductivity of brine is lower than that of pure ice by at least a factor of 4 with the discrepancy increasing at lower temperatures (Yen et al., 1991). It is further noted that sea ice is a complex material where the vertical transport of

heat may occur due to a number of processes, including conductive, convective and advective processes. As the relative magnitude of each process is difficult to isolate, they have been incorporated into γ_{si} (Yen et al., 1991).

A useful term directly proportional to the thermal conductivity, but inversely proportional to the amount of heat required to induce a temperature change is the thermal diffusivity, ν_{si} ($m^2\ s^{-1}$). The thermal diffusivity of ice is its ability to diffuse thermal influences (Oke, 1987). The relationship of thermal conductivity and diffusivity is such that a medium can have a higher thermal conductivity, but lower diffusivity than another. This is clearly demonstrated in the comparison of these two thermal properties between air and ice. For example, the thermal conductivity of air is two orders of magnitude less than that of ice, however its thermal diffusivity is an order of magnitude larger due mainly to its very low density as demonstrated in the following equation (Oke, 1987):

$$\nu_{si} = \frac{\gamma_{si}}{\rho_{si} Cp_{si}} \qquad [2.4]$$

where ρ_{si} is the ice density ($kg\ m^{-3}$) and Cp_{si} is the specific heat of the ice volume ($J\ kg^{-1}\ K^{-1}$; where $W = J\ s^{-1}$). Opposite to the thermal conductivity of sea ice versus freshwater ice, the specific heat of sea ice is much larger. This is due to phase changes that occur with any change in temperature of the sea ice (see section 2.3.1.3), resulting in a latent heat requirement in addition to changing the solid and brine temperatures (Schwerdtfeger, 1963). The end result of the quotient in equation 2.4 is a much smaller thermal diffusivity for sea ice relative to freshwater ice. Therefore, sea ice is essentially able to thermally insulate the ocean to a greater degree than would freshwater ice.

Mentioned previously, ice growth is dependent on the heat balance at both the upper and lower interfaces. Given equation 2.2, for a homogeneous volume of ice with a linear temperature gradient from a cold atmosphere to warm ocean, the conductive flux, Q_C, would be equal throughout. Therefore, at the ice-ocean interface, the conductive heat flux is balanced with the oceanic heat flux, Q_W, by the latent heat of fusion, L (J kg^{-1}), for an ice thickness change ($\partial H/\partial t$) and an ice density, ρ_i:

$$Q_C + Q_W + \rho_i L\left(\frac{\partial H}{\partial t}\right) = 0 \qquad [2.5]$$

Therefore, incorporating equations 2.3 and 2.5, one can formulate a very simplistic equation for ice growth (melt) rate:

$$\frac{\partial H}{\partial t} = \frac{\left(\frac{-\gamma_{si}(T_0 - T_f)}{H}\right) + Q_W}{\rho_{si} L} \qquad [2.6]$$

where $(T_0 - T_f)$ is the linear temperature gradient from the surface, T_0, to the bottom, T_f, over an initial ice thickness, H. Though in many ways an oversimplification, equation 2.6 provides a good framework for the process of ice growth. The equation demonstrates the key role thermodynamic processes play in the process of sea ice formation. Further, the importance of the oceanic flux is made clear. It is worth noting that in the central Arctic Ocean, the oceanic flux is only 2 W m^{-2} (Wadhams, 2000) as compared to 5 to 30 W m^{-2} in the Antarctic (Lytle et al., 2000). The oceanic heat flux is due to a residue of heat stored from solar warming of the mixed layer during summer and/or the transfer of heat from warmer water masses residing in deeper or lateral waters. The difference between

the two polar regions is the latter heat source. In the Arctic, the advection of heat is negligible due to strong stratification and a surrounding landmass providing protection from the open ocean (Maykut and McPhee, 1995), whereas the opposite applies to the Antarctic. The result of the differing heat flux is a mean annual growth of first-year ice to be 1.7-2.4 m and 0.5-0.7 m in the Arctic and Antarctic, respectively (Maykut, 1986; Flato and Brown, 1996; Wadhams, 2000). However, it is noted that in shelf regions with shallow and narrow waterways, such as is found within the Canadian Arctic Archipelago, tidal mixing of cold surface Arctic waters with warmer bottom waters can occur (Melling et al., 1984). Consequently, winter estimates of up to 10 W m^{-2} have been made for the ocean-ice heat flux in the northern Canadian Arctic (Melling, 2002; Lavoie et al., 2005). Another significant aspect of equation 2.6 is that as the ice thickens, its growth rate slows. The growth rate of sea ice and its seasonal thickness has important consequences on its salinity profile, which is examined in the next section. Snow also plays an important role here in that the thermal diffusivity and conductivity of snow dominates the overall temperature gradient through the snow/sea ice system and as such the timing and magnitude of snow deposition, relative to the young growing ice sheet, is very important (see section 2.3.2).

2.3.1.3 Sea Ice Salinity and Phase Relationships

Mentioned previously, sea ice is a mixture of ice, brine, solid salts (if temperatures are cold enough) and gas (Weeks and Ackley, 1982). Salt ions are unable to be incorporated within the ice crystal lattice, thus the mixture of each component is initially determined by the growth rate of sea ice as impurities are squeezed out and trapped between ice

crystals through a process called segregation (Nakawo and Sinha, 1981). Generally, slower ice growth rates allow more time for the diffusive and convective removal of salt ions from the growing ice edge prior to entrapment between ice crystals. Given that the growth rate of ice decreases with thickness, the application of salt segregation alone would result in a decrease in salinity with depth, however typical ice salinity profiles have a characteristic C-shape (Fig. 2.5). The C-shape results through the processes of gravity drainage and brine expulsion (Weeks and Ackley, 1982). Gravity drainage occurs due to the temperature gradient in sea ice. The temperature gradient creates an unstable brine density gradient resulting in convective exchange with underlying brine or seawater that is warmer and less saline. This process can contribute greatly to the transfer of heat within the ice (Lytle and Ackley, 1996) and may be an important biological factor in the convective transport of nutrients (Arrigo et al., 1993). However, Cota et al. (1991) suggested that this mechanism alone would not equal the demand by a rapidly growing bottom ice algal community such as is found near Resolute Bay, Canada. Instead, turbulent exchange at the ice water interface due to ocean currents is thought to be a much more important mechanism supplying nutrients to the bottom ice community (Cota et al., 1991). Brine expulsion, the final factor contributing to desalination of a growing ice sheet, occurs when pressure is built up within a brine pocket due to a decrease in the pocket's volume from surrounding ice growth, resulting in an ejection of brine. This process is not as important to desalination of the ice sheet as are segregation and gravity drainage (Weeks and Ackley, 1982), however it may play an important role in the formation of surface frost flowers (Martin et al., 1995; see section 2.3.2).

Once the sea ice cover has formed with internal brine inclusions, changes in the fractional volumes of ice, brine and solid salts become a function of temperature. Figure 2.6 depicts the temperature-phase relationships between ice, water, and dissolved and solid salts for a closed system with an initial seawater salinity of 34. It shows that as ice forms past the freezing point of –1.86°C, the dissolved salt fraction in brine (water and dissolved salts) increases, which acts to suppress the freezing point, slowing the formation of ice with decreasing temperature. At –8.2 °C, salt concentrations in the brine are supersaturated with respect to sodium sulphate, and begin to precipitate out. Past –22.9 °C salt precipitation greatly increases until approximately –60 °C. Although this temperature may be reached in the snowpack, it is rarely reached in the sea ice due to the insulating effects of snow (Maykut, 1986).

Useful equations derived from these phase relationships have been used to estimate the fractional volumes of brine, gas and solid salts as a function of ice temperature and salinity (Cox and Weeks, 1983), however their specific formulations are beyond the scope of this discussion. Models also exist that incorporate fractional volumes of pure end points of ice, brine and gas to calculate the thermal properties of sea ice (Schwerdtfeger, 1963; Yen et al., 1991). Generally, as discussed in the previous section, brine acts to depress the conductive heat flux in sea ice. It is interesting to note that for large grained columnar sea ice as fractional brine volumes rise above 5%, a point that is reached around -5°C for an ice salinity of 5, brine on average becomes freely motile throughout the ice (Golden et al., 1998). This piece of evidence may be very important for the transfer of heat, as well as nutrients within the ice. It also breaks down the application of phase relationships through 'opening' of the system.

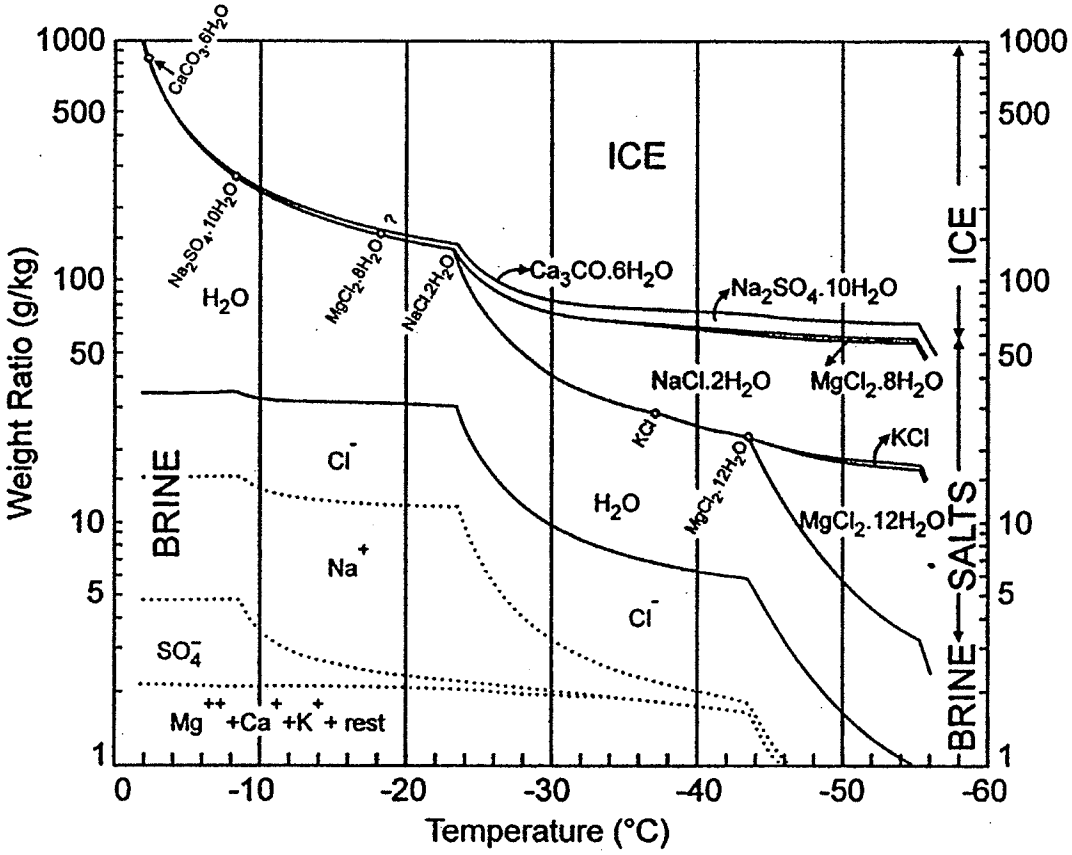

Figure 2.6. Phase diagram of sea ice demonstrating the mass fractions of solid ice, solid salts and brine (water and dissolved salts). Adapted from Assur (1958).

2.3.2 Snow Physical and Thermal Properties

Snow can be defined as a meteoric deposition of freshwater ice crystals. Its average depth over Arctic sea ice is at least a factor of magnitude less than the thickness of sea ice. However, its importance to the system is perhaps a factor of magnitude greater owing to its unique physical, thermal and optical properties. Snow over sea ice is a mixture of ice, brine, solid salts (if cold enough), water vapour and air. One of the main contributing factors to the differences between snow and sea ice is its density, which is attributable to the amount of air trapped within a snow volume. Typically, snow density can range from 100 to 450 kg m^{-3} (Mellor, 1977), whereas sea ice densities range between 850 to

900 kg m^{-3} with the exception of the active layer of multiyear ice that can be much less dense (Weeks and Ackley, 1982).

Snow over sea ice is unique compared with snow over land or freshwater ice in that high concentrations of salinity are typically observed. As the sea ice cover initially freezes, brine and salts are expelled both below and onto the surface of the forming ice cover (Weeks and Ackley, 1982). Under very cold temperatures and high relative humidity, hoar frost can form with upward brine expulsions, resulting in highly saline crystal formations called frost flowers (Martin et al., 1995). Capillary suction can also act to draw additional quantities of brine from the surface and into the salt flowers (Drinkwater and Crocker, 1988). These authors also state that over a short period of time, frost flowers can grow in size and numbers creating a continuous snow cover prior to any atmospheric snowfall or blowing snow event.

After the first major snowfall or blowing snow event, surface brine is wicked up into the new snow cover through capillary suction (Drinkwater and Crocker, 1988). Barber et al. (1995) also found salinity to move up through a stable snowpack with time suggesting a complex interaction of capillary suction and vapor gradient mass transfer. More recently, this phenomenon has been shown to respond to diurnal changes in the snowpack temperature and subsequently, vapor gradients (Langlois et al., 2006). It is logical that wind redistribution of frost flowers and saline snow may also act to mechanically incorporate the salinity deeper into the snow cover and preferentially deposit the saline snow in newly forming drifts. However, it is apparent from literature that the relative contribution of each mechanism on the incorporation of brine into the snowpack is not well understood and requires further study.

Once deposited, the snowpack undergoes substantial metamorphism and wind densification creating a distinct vertical structure in its physical properties, particularly over first-year sea ice. Fig. 2.7 demonstrates typical vertical profiles of density, salinity and grain size for a cold first-year sea ice snowpack. Snowpacks have been found to conform to 2-3 statistically distinct layers based on density (Papakyriakou, 1999) or snow grain morphology (Barber et al., 1995). Generally, density is low and highly variable at surface and bottom layers due to new snow deposition events and highly faceted crystal development (see below), respectively. Salinity decreases dramatically with distance from the ice surface due to mechanisms described in the previous two paragraphs. Snow grain morphology typically shows large grains with high variability in bottom layers and relatively homogeneous small grain sizes in upper layers. One exception is that surface layers may experience faceted crystal growth (see below).

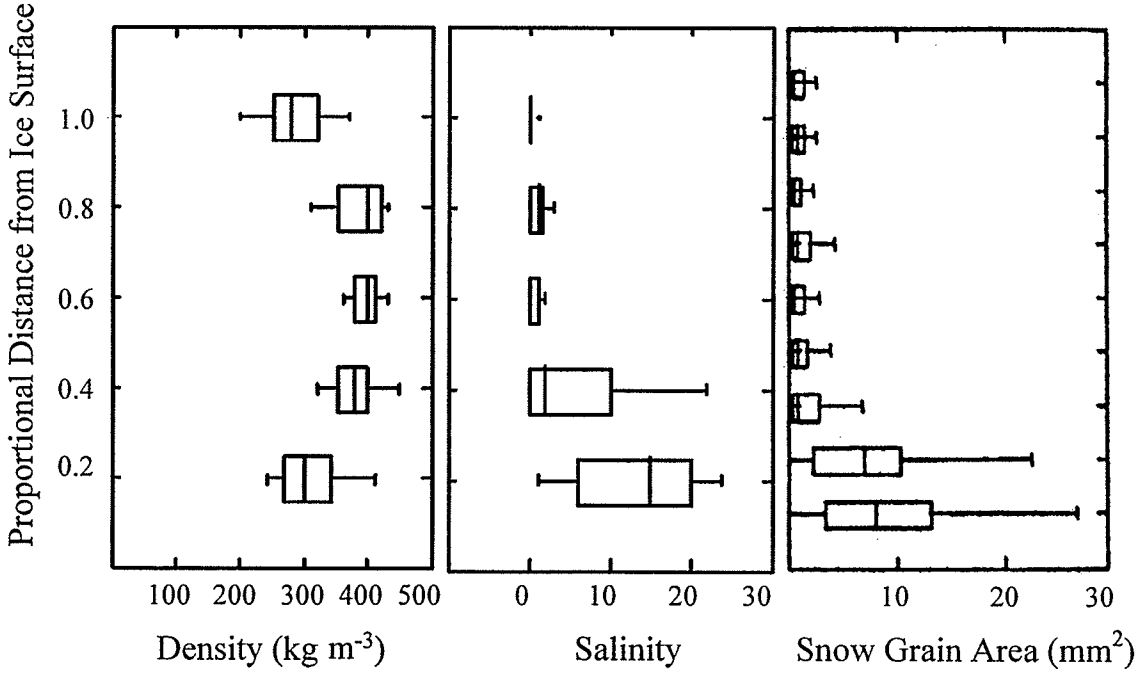

Figure 2.7. Typical vertical profiles of snow density (a), salinity (b) and grain area (c) (a and b are after Papakyriakou, 1999; c is after Barber et al., 1995).

Cold or dry metamorphism of snow grains is the main process leading to the distinct groupings described above. Metamorphism of dry snow has been categorized based on crystal shape into an equilibrium form and a kinetic growth form (Colbeck, 1982). The tendency for equilibrium forms (spherical or rounded) occur at very slow metamorphic rates, typically associated with small temperature gradients and warmer temperatures. Mass flow vapor diffusion among particles occurs because of larger vapor pressures over smaller particles. Therefore, preferential vapor diffusion results in the sublimation of dendritic branches of snowflakes, termed destructive metamorphism, or the growth of large grains at the expense of small grains, termed constructive metamorphism (Colbeck, 1982). The overall effect is for snow grains to tend toward a roughly spherical shape and gradually increase in size with time. Temperature gradients speed this process until gradients of 10 to 20 °C m^{-1} are experienced, at which point kinetic growth occurs. Kinetic growth involves the growth of faceted (flat surface) crystals at the expense of rounded crystals. It is associated with large growth rates due to the temperature gradient, which induces a strong vapor pressure gradient. Mass flow occurs in the direction of heat conduction as rounded grains are sublimated, causing supersaturation of the air and subsequent recrystallization further along the gradient forming large, highly faceted crystals. Kinetic growth occurs predominantly at the ice-snow interface where higher temperatures are experienced. This process leads to the formation of the snowpack hoar layer (approximately the bottom 20 - 40% of a snowpack; Papakyriakou, 1999; Sturm et al., 2002), where it acts to decrease the density and dramatically increase grain size more than an order of magnitude larger than grains in the upper snowpack (Colbeck, 1982).

The thermal properties of the snow cover are a function of salinity, temperature and air. As with sea ice, salinity reduces the effective thermal conductivity of snow due to the phase relationships with temperature and the subsequent presence of brine at temperatures above approximately – 60°C (Fig. 2.6). However, it is the large volume of air trapped within the snow that acts to decrease the thermal conductivity of the snowpack by an order of magnitude relative to that of sea ice. Therefore, snow acts as a powerful insulator between the atmosphere and sea ice, limiting ice growth as can be demonstrated through its incorporation in equation 2.6. Its insulating effects may also play an important role in keeping the ice volume relatively warmer, which may result in: a greater sensitivity to the oceanic heat flux on the ice bottom and an influence on biological production as the 5% percolation threshold could be met at higher levels in the ice volume in colder atmospheric conditions (Golden et al., 1998). Alternatively, snow will insulate the sea ice from a warming atmosphere, causing a decrease in the warming rate of sea ice during melt.

A competing effect caused by the volume of trapped air in the snow is a low specific heat and density. These properties greatly lower the snow's heat capacity (the product of specific heat and density), causing it to cool, warm and melt more easily than sea ice (Ledley, 1991). However, salinity at the base of the snow can dramatically increase the snow's heat capacity, thus complicating this process (Papakyriakou, 1999).

Snow loading can also have a strong effect on the thermal properties of snow and sea ice through the formation of snow ice. If sufficient snowfall occurs, the weight of the snow cover can act to push an ice cover below its freeboard (floating height), eventually causing flooding of the sea ice surface. Seawater at the surface changes thermal gradients

within the snow-sea ice volume, essentially displacing ice growth to the ice surface/snow bottom. A subsequent result is an increase in ice growth rate as the insulating effects of the ice cover and the snow bottom where seawater has penetrated are nil (Flato and Brown, 1996). However, snow ice formation is usually associated with a relatively thin ice cover where sufficient snow loading can actually occur. Therefore, snow ice is only widespread in the Antarctic due to the influence of the oceanic heat flux on annual sea ice growth (Wadhams et al., 1987). Snow ice is also an important biological habitat (see Section 2.2.1) and, due to its extensive formation in the Antarctic, can result in a significant proportion of annual Antarctic primary production (Arrigo et al., 1997).

2.3.3 Melt of Snow-Covered Sea Ice

Much of the above discussion has been dedicated to a description of the physical and thermal development of snow and sea ice from fall freeze-up through winter. This was largely accomplished as a prerequisite to better evaluate the process of melt. Melt in snow-covered sea ice is a complex process involving an initial warming of the snow and ice volumes resulting in snow metamorphism, sea ice desalination and microstructural changes and finally actual thinning of the snow and ice. Melt initially occurs through warming and subsequent metamorphism of the snowpack and a release of cooling on the ice volume as temperatures increase and the net radiation becomes slightly positive (heat flux into the surface).

As solar radiation increases in early spring, the high albedo of the snow cover (approx. 85%) dominates shortwave radiative exchange. During this period, dry snow metamorphism continues within the middle layers of the snowpack (Barber et al., 1995). Diurnal cycling of solar radiation induces temporal variations in temperature at the sub-

surface of the snowpack where slight amounts of radiation are absorbed. Some of this absorbed energy is conducted down in the form of a temperature wave, however most of the energy is transferred back to the colder, convective atmosphere at night, which acts to cool the surface (Papakyriakou, 1999). The temperature wave is propagated through the snow cover loosing amplitude exponentially with depth according to the snow's thermal diffusivity. The wave is also time-lagged within the diurnal cycle, not reaching depth until night. Penetration depth is also limited by the saline basal layer of the snow where the wave is essentially cancelled out by phase changes of the brine (Papakyriakou, 1999). As the surface cools at night and the temperature wave reaches depth, the result is a potentially strong temperature gradient in the middle to surface layers, which can result in overnight kinetic grain growth at these layers (Birkeland, 1998). Alternatively, when surface snow temperatures warm during the day, a positive temperature gradient is created causing a flip in the direction of faceted crystal growth (Birkeland, 1998). Although not extensively documented, diurnal recrystallization of snow layers appears to be widespread over Arctic sea ice (Sturm et al., 2002; Barber, personal communication, 2004). Its occurrence warrants further investigation as to its impact on snowpack grain growth and the initial stages of snowmelt.

It is not until atmospheric temperatures rise that significant snow metamorphism occurs. As the season progresses, the lower atmosphere and snow surface absorb radiation resulting in temperature increases in the snow volume. The majority of the subsequent heat is conducted down into the snow and ice volume where temperatures increase more gradually and linearly with depth according to the respective material's thermal diffusivity. The result is for the snowpack to warm first, creating a C-shape in the

snow-ice temperature profile. The C-shape is augmented by the very low thermal diffusivity of the saline basal layer that acts to decouple atmospheric influence on sea ice thermodynamics (Papakyriakou, 1999).

The warming snowpack results in a mixture of dry and wet snow metamorphism. Distinction between these two processes is based on liquid water content in the snow. Further, wet snow has been separated into pendular and funicular regimes. The pendular regime occurs as liquid water contents range between approximately 2 to 7%, where capillary forces act to limit water to a thin film around grains and contacts between grains (Colbeck, 1982). In this instance air occupies a continuous path between pore spaces. During the pendular regime, a large increase in grain growth is experienced relative to dry snow under a small temperature gradient. This is due to liquid contacts between grains that act to increase mass flow between growing and shrinking particles. Further, particles tend to cluster into two to four crystal aggregates thereby increasing the effective size of the grain (Colbeck, 1982). The funicular regime occurs when liquid water occupies a continuous path between pore spaces and can therefore freely drain. This regime is experienced at a liquid content range of 7 to 14% (Colbeck, 1982). Under the funicular regime, grain growth is even more pronounced compared to the pendular regime, as mass flow is not limited by air spaces. However, once the funicular regime is met, water begins to drain out of the snowpack. The effect of draining has been the suggested reason for the nonlinear decrease of melt rates observed over thicker snow covers (Iacozza and Barber, 2001). Above liquid water contents of about 15%, the snow becomes slush where the water-snow mixture is completely flooded and contains relatively small volumes of air (Papakyriakou, 1999).

As with early melt, snowpack temperature fluctuations are experienced as diurnal temperature waves propagate downward. These fluctuations induce melt-freeze cycles in the snowpack. The effect is to further increase grain size through the formation of very large polycrystalline aggregates (Colbeck, 1982; Barber et al., 1995). For example, as temperatures warm and the pendular and funicular regimes are experienced, relatively small crystal clusters form and then re-freeze as temperatures drop. When temperatures rise again, the already present clusters form further clusters, thus increasing in size. Prolonged exposure to solar radiation can break down bonds between crystals (Colbeck, 1982), perhaps limiting this process to depth within a snowpack.

The saline basal layer can experience high liquid water contents at temperatures well below 0 °C. Therefore, melt is experienced much earlier than higher in the snowpack. Again, it is worth noting that metamorphic processes in the basal layer are limited by phase changes in the brine. However, the funicular regime eventually occurs resulting in gravity drainage of brine from the snowpack (Barber et al., 1995). Ablation continues as the funicular regime is experienced throughout the snowpack, draining water onto the surface of the ice until the snowpack disappears and melt ponds form (Holt and Digby, 1985).

Concurrent with snowmelt are melt-induced structural changes of the ice cover as ice temperatures increase, inducing an increase in brine volume. Increases in brine volume are associated with changes in the morphology, size and connectivity of brine inclusions (Eicken et al., 2000). At approximately –6 °C (depending on salinity) brine inclusions have been observed to start linking up (Eicken et al., 2000), until a potential 5% brine fraction percolation threshold is met and brine is free to move throughout the ice cover

(Golden et al., 1998). Although the potential percolation threshold has been relatively accepted in literature (e.g., Light, 2000), its value was determined through indirect evidence and a simple microstructural model. This fact lead Eicken (2003) to note that field observations of ice permeability provided evidence of a more complex microstructural evolution that requires further investigation.

When brine inclusions do fully connect, they form continuous brine channel networks that open to the surface. Snow meltwater begins to percolate into the ice cover, displacing brine and essentially draining the surface (Untersteiner, 1968). At the same time, melt can occur at the bottom of the ice cover if sufficient oceanic heat is supplied, which may result in convective mixing as lower salinity melt water displaces cooler high salinity brine. Similar to freezing processes, brine displacement and convective mixing result in a rapid warming of the ice cover (Papakyriakou, 1999). It is noted that bottom melt is typically limited in the Arctic due to a relatively small oceanic heat reservoir (Maykut and McPhee, 1995).

Meltwater flushing and warming eventually result in a low salinity ice cover (Weeks and Ackley, 1982) with a nearly isothermal ice volume where temperatures are within a degree of freezing (Perovich and Elder, 2001). With time, brine channels form and grow in diameter as meltwater preferentially drains; however, processes involved in ice deterioration are not well understood or studied due to logistical difficulties of late season data collection. One important mechanism recognized in advanced stages of melt is the formation of melt ponds at the ice surface, which act to significantly decrease the surface albedo and increase light transmission (e.g., Perovich et al., 1998; Hanesiak et al., 2001).

Melt ponds form as long as surface meltwater contributions do not fully drain (Holt and Digby, 1985). Their surface coverage is dependent on the nonlinear rates of snowmelt with snow thickness (Iacozza and Barber, 2001) and can be as high as 80% with strong spatial variability depending on their interconnectivity (Yackel et al., 2000). Drainage into the ice can cause a reduction and variability in the areal coverage, however melt ponds appear to persist late into the summer and even into the next freeze-up (Perovich et al., 2002). As the sea ice surface continues to melt and drain, a new formation termed white ice results (Grenfell and Maykut, 1977). White ice formations are remnant ice crystals left after draining that act to substantially increase surface albedo at a time when rain is the dominant precipitation. It is noted that there does not appear to be much in the literature on the mechanisms causing melt pond variability once brine channels are connected from the surface to ocean. Perovich et al. (2002) documented a relationship between melt pond coverage and synoptic systems. One can speculate that complex interactions of atmospheric forcing, surface melt, drainage, ice buoyancy and tides influence melt pond coverage. I note that the formation of a meltwater lens at the bottom of first-year ice has seemed to be largely overlooked in the literature, with the exception of observations within a multiyear ice pack (e.g., Gradinger, 1996). The lens has been studied in terms of its contribution to stratification of the water column at ice edges and after ice break-up (e.g., Niebauer and Smith, 1989), whereas further research to examine its importance to physical and biological processes at the ice bottom is warranted.

2.3.4 Effects of Clouds

Clouds play a critical role in the surface energy balance influencing both freeze-up and melt processes and therefore justifying the following short discussion in this chapter. Clouds induce a cloud-radiative feedback mechanism with opposite effects on the shortwave and longwave portions of the surface energy balance (Papakyriakou, 1999). The cloud-albedo feedback mechanism acts to reflect solar wavelengths causing a cooling effect (negative feedback). Further, attenuation of light by clouds may have an effect on ice algal growth if light limited. However, clouds also absorb and emit longwave radiation. The net effect is to warm the snow/sea ice surface (positive feedback). This feedback appears to be important in early spring where a cloud cover can limit refreezing within the snow, and therefore induce earlier melt (Papakyriakou, 1999). In late spring, the importance of clouds is limited to the evening where they may further act to reduce freezing. As further noted in Papakyriakou (1999), clouds may cause precipitation in late spring in which case it would either delay melt in the form of snow or accelerate melt in the form of rain.

2.3.5 Radiative Transfer

2.3.5.1 Theory

Due to the speed of light, the transfer of light through the atmosphere, snow and sea ice is essentially instantaneous. In the following discussion, radiative transfer is considered an instantaneous process dependent on the physical and subsequent optical properties of the materials it is transferring through and between (Thomas and Stamnes, 1999). My

discussion will be limited to a functional review of the theory. I will also focus the discussion on optical wavelengths.

Radiation interacts with materials through reflection (I_R; or scattering), absorption (I_A) and transmission (I_T) as demonstrated through the radiative balance equation:

$$I_0{}^{\lambda} = I_R{}^{\lambda} + I_A{}^{\lambda} + I_T{}^{\lambda} \qquad [2.7]$$

where λ represents the wavelength dependence of this interaction. In radiative transfer, we are concerned with calculating the amount of light penetrating to depth (i.e., transmission). Given a homogeneous or pure material that is optically thick (i.e., albedo (α) is independent of the underlying surface), transmission can be estimated with the Beer-Lambert-Bouguer law (Thomas and Stamnes, 1999):

$$I_T{}^{z,\lambda} = I^{0,\lambda} \exp(-z\,\kappa^{\lambda}) \qquad [2.8]$$

where $I_T{}^{z,\lambda}$ (W m^{-2} nm^{-1}) is the spectral transmitted irradiative flux, $I^{0,\lambda}$ is the spectral incident irradiative flux entering the material (i.e., $(1-\alpha)\,I_0$), z is depth of transmission (m) and κ^{λ} is the spectral attenuation coefficient (m^{-1}). κ^{λ} can be further broken down into the sum of the absorption and scattering coefficients. Through the use of these coefficients, a mixture material can be broken down into the optical properties of its components and their relative contribution to bulk optical properties of the material.

The absorption coefficient is directly proportional to the imaginary part of the complex index of refraction for a pure medium (Wiscombe and Warren, 1980). In a mixture medium such as snow-covered sea ice, the absorption coefficient can be calculated by summing the products of each pure end component coefficient with its respective

fractional volume (e.g., Grenfell, 1991). Scattering on the other hand is generally determined through discontinuity between two mediums of the real part of the refractive index. In optical wavelengths, scattering in snow and sea ice is generally assumed independent of wavelength as inclusions are significantly larger than the wavelength. Based on Mie theory, scattering within a host medium is dependent on the scattering efficiency (approx. 2 for radius >> wavelength; Grenfell, 1991), radius and number density of inclusions demonstrating discontinuity in its refractive index with that of the host medium. Further, according to Mie theory scattering has a directional component in the form of a phase function that describes the angular redistribution of light during a single scattering event. Generally, as the refractive index contrast between host medium and inclusion decreases and inclusion size increases, a stronger forward-peaked phase function results (e.g., Light, 2000), essentially decreasing scattering into the medium. In contrast, as inclusion sizes decrease, more diffuse scattering results. The incorporation of directional scattering into radiative transfer highlights the importance of direct *versus* diffuse radiation and specular reflection at the boundaries between mediums (Wiscombe and Warren, 1980; Grenfell, 1991).

2.3.5.2 Radiative Transfer in Snow-covered Sea Ice

The complexity of radiative transfer in snow-covered sea ice is depicted in the system diagram as process (1) (Fig. 1.1). As with thermal properties, bulk optical properties for snow and sea ice are a function of the fractional volume and structural arrangement of each component. It is significant to note that thermal properties largely determine the fractional and structural components of snow-covered sea ice, therefore allowing the

potential to link snow and sea ice thermodynamic processes with radiative transfer processes.

Peak spectral transmission through snow-covered sea ice ranges between 450 to 550 nm. Past approximately 600 nm, the attenuation coefficient rapidly increases (Fig. 2.8; Grenfell and Maykut, 1977). This trend in spectral attenuation is largely the result of the spectral absorption coefficients for pure ice and seawater (Fig. 2.8). The contribution of air and water vapour to the bulk absorption coefficient are usually assumed zero (e.g., Light, 2000). Therefore, given an incident radiative flux spectrum, absorption properties of ice and water and their volume fractions control the spectral distribution of transmitted radiation. The result is a slight shift in the peak spectral transmission toward approximately 450 to 500 nm. However, significant amounts of particulate matter may act to further shift the spectral distribution toward a red peak at 600 nm (Fig. 2.9; Warren and Wiscombe, 1980; Perovich et al., 1998; Light et al., 1998). These spectral shifts have resulted in specific acclimation mechanisms and adaptation of ice algae photosystems (Barlow et al., 1988; Robinson et al., 1995; Aguilera et al., 2002). Further, ice algae can significantly alter the spectral distribution of penetrating light (e.g., Maykut and Grenfell, 1975; Legendre and Gosselin, 1991; Perovich et al., 1993; see Chapter 6), such that they may shade algae growing lower in the ice (Smith et al., 1988; Arrigo et al., 1991).

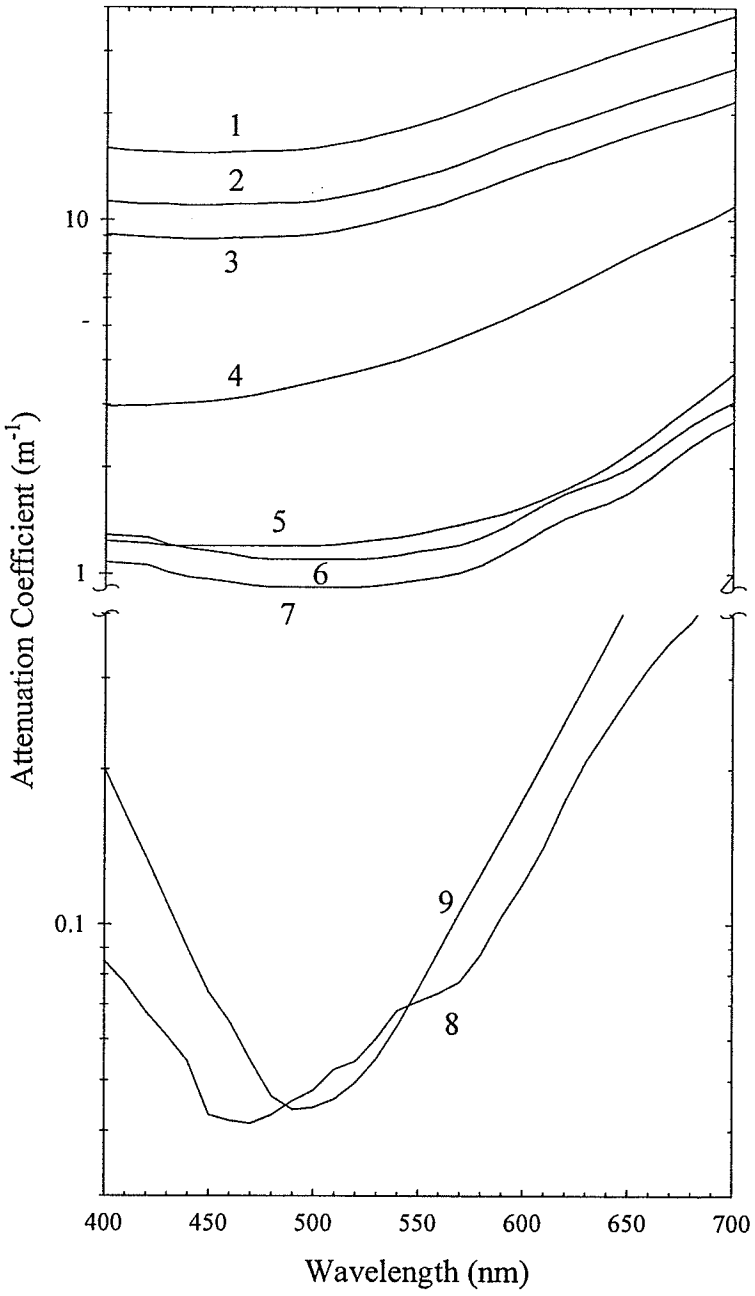

Figure 2.8. PAR spectral attenuation coefficients for nine medium types: 1) dry snow, 2) melting snow, 3) ice colder than –23 °C, 4) surface scattering layer of white ice, 5) interior portion of white ice, 6) cold blue ice, 7) melting blue ice, 8) bubble-free fresh ice and 9) clear arctic water. Adapted from Perovich (1990).

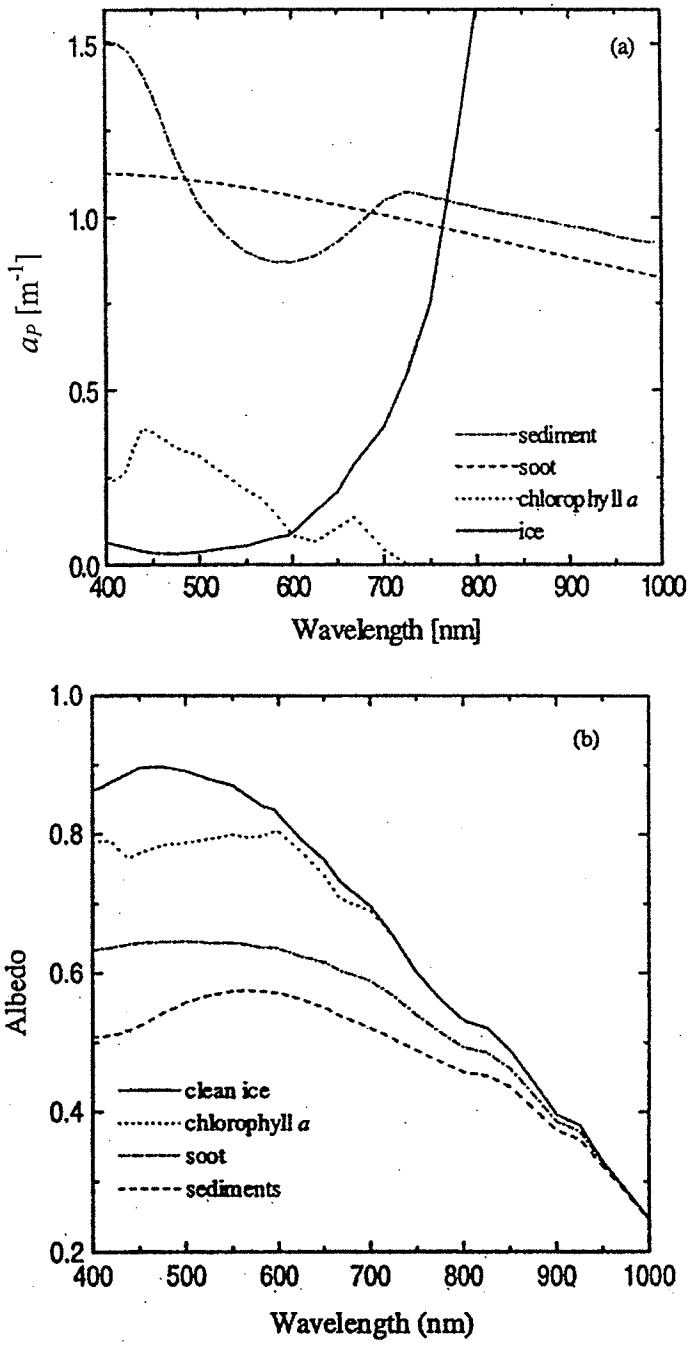

Figure 2.9. Effects of sediment, carbon soot and chlorophyll *a* on (a) the spectral particulate absorption coefficient (a_p) and (b) the spectral albedo of particle laden sea ice. The absorption coefficient and albedo for pure ice are also shown. Adapted from Light et al. (2003).

Although absorption properties are important to the spectral distribution of transmitted radiation, it is scattering that dominates the attenuation of light with depth (Warren, 1982), with the exception of particulate laden ice (Light et al., 1998) and pure end components (e.g., bubble free ice in Fig. 2.8). Scattering is largely dependent on the radius and number density of inclusions within a host medium. For example, in optical models for snow, the host medium is air and the inclusions are snow grains, snow clusters and particulates (Wiscombe and Warren, 1980; Warren and Wiscombe, 1980; Zhou and Li, 2002). Whereas in sea ice optical models, ice generally acts as the host medium and the inclusions are brine, gas, precipitated salts and particulates (e.g., Grenfell, 1991; Light, 2000; Light et al., 2003). However, white ice and the active layer in multiyear ice would act more like a snow cover with respect to its scattering. An apparently overlooked portion of the snowpack in many, if not all investigations on radiative transfer is the basal layer, although observations show basal layers to vary interannually and spatially (Papakyriakou, 1999). Clearly more investigation of snowpack optical properties and modeling is warranted.

The following discussion of the evolution of optical properties during sea ice melt pulls from both observation and modeling studies. During winter, low density, dry snow results in a high surface albedo due to highly diffuse scattering caused by small grains. Under low snow depths, the surface albedo is influenced by the albedo of the underlying ice surface (Wiscombe and Warren, 1980). It is not until a depth of 2 to 10 cm – with snow grain radii of 50 to 200 μm, respectively – that the effect of the ice surface on the surface albedo becomes nil. A snowpack of these depths is referred to as optically deep or semi-infinite (Wiscombe and Warren, 1980). As dry grains grow with age, the tendency is for

decreased albedo and increased absorption, particularly at infrared wavelengths, with less change at visible wavelengths. The increase in infrared absorption plays an important role in snowmelt (Wiscombe and Warren, 1980) and the ice-albedo feedback mechanism (Curry et al., 1995). Snowmelt and the rapid growth of grain clusters can significantly increase transmission over a short period of time (Grenfell and Maykut, 1977; Papakyriakou, 1999; Zhou and Li, 2002). However, few details on the temporal evolution of this process are currently available in the literature.

Demonstrated in Figure 2.8, the attenuation coefficient of sea ice jumps from a high integrated value when below –23 °C (type 3) to a relatively constant lower value with increasing temperature from cold blue ice to melting blue ice to saturated white ice (types 6 to 7 to 5). Further, drained white ice formation results in a scattering increase and therefore a jump in the attenuation coefficient (type 4, Fig. 2.8). Therefore, sea ice melt results in a much different transition in transmission with respect to snowmelt due to the difference in host media and scattering inclusions.

Knowledge on radiative transfer and structural-optical relationships in sea ice has increased greatly over the last few years (e.g., Light, 2000; Light et al., 2003). Light (2000) developed an innovative technique to measure optical properties of ice cores concurrent with microstructural observations in a temperature-controlled laboratory. Her experiments provided insight into structural-optical processes that take place in sea ice as it cools and warms. The following is a summary of her results, which were tested against a structural-optical model that she developed (Light, 2000).

At temperatures below –23 °C, solid salts governed scattering with ice bulk attenuation coefficients much higher than at warmer temperatures. As temperatures warmed between

–23 and –8 °C, no significant changes were observed in scattering coefficients. This was due to a competing effect where enlarging brine inclusions, connecting brine tubes (increasing structural anisotropy) and dissolving salts increased forward scattering, but the dilution and warming of brine increased the refractive index contrast between brine and solid crystals in the brine, causing an increase in backscatter. At temperatures greater than –8 °C, scattering was again fairly constant with brine channel forward scattering balanced against structural changes that caused an increase in backscatter (Light, 2000). Therefore, bulk sea ice optical properties lacked temperature dependence above –23 °C due to structural changes which appear to have competing effects on the optical properties of sea ice. It was concluded that more work needs to be accomplished in order to understand the specific mechanisms responsible for the observed and modeled changes, particularly at warmer temperatures (Light, 2000; Light et al., 2003).

As melt ponds form on the surface, their effect is to significantly decrease aerially averaged albedo with regional estimates of 0.4 to 0.55 (Hanesiak et al., 2001; Perovich et al., 2002). Depth of melt ponds and their variable coverage can result in significant variation of cover type albedos. Hanesiak et al. (2001) found albedo to range from 0.21 for deep melt ponds, 0.32 to 0.36 for shallow ponds, 0.52 to 0.65 for shallow wet and saturated snow to 0.75 for deep moist snow. Perovich et al. (2002) further showed that melt ponds persist as long as an ice cover is present. More important to biology, transmission of visible wavelengths into the ice volume also increase under ponds (Perovich et al., 1998).

2.3.6 Snow as a Spatial Variable

The effects of snow depth on the various processes discussed thus far in the chapter have been highly nonlinear. This has led some researchers to observe that the importance of snow depth distribution outweighs the importance of its areal average on light transmission (Perovich, 1990; Iacozza and Barber, 1999) and heat transfer (Sturm et al., 2002). Surprisingly, the study of snow distribution and redistribution has not been extensively examined over sea ice (Iacozza and Barber, 1999). Most studies on this subject have been limited to terrestrial environments where mass balance inquiries for flood and drought predictions, avalanche predictions or glacier contributions drive the research.

2.3.6.1 Accumulation Processes

Snow accumulation occurs as a result of precipitation and blowing snow processes that act to redistribute snow. Blowing snow is ubiquitous in regions where fetch distances are large. Further, low surface roughness results in the occurrence of blowing snow at slower wind speeds. Therefore, snow-covered sea ice encounters widespread blowing snow events with occurrences of up to 100 days per year over the Arctic Ocean (Déry and Yau, 1999).

Blowing snow is a dynamic mechanism during which snow particles undergo creep, saltation, suspension and sublimation due largely to interacting forces of wind and gravity (Fig. 2.10). Creep occurs when wind pushes particles causing them to roll along the snow cover. The process of creep is very slow and accounts for very little transport of snow (Schmidt, 1986). Saltation takes place when strong threshold winds eject particles

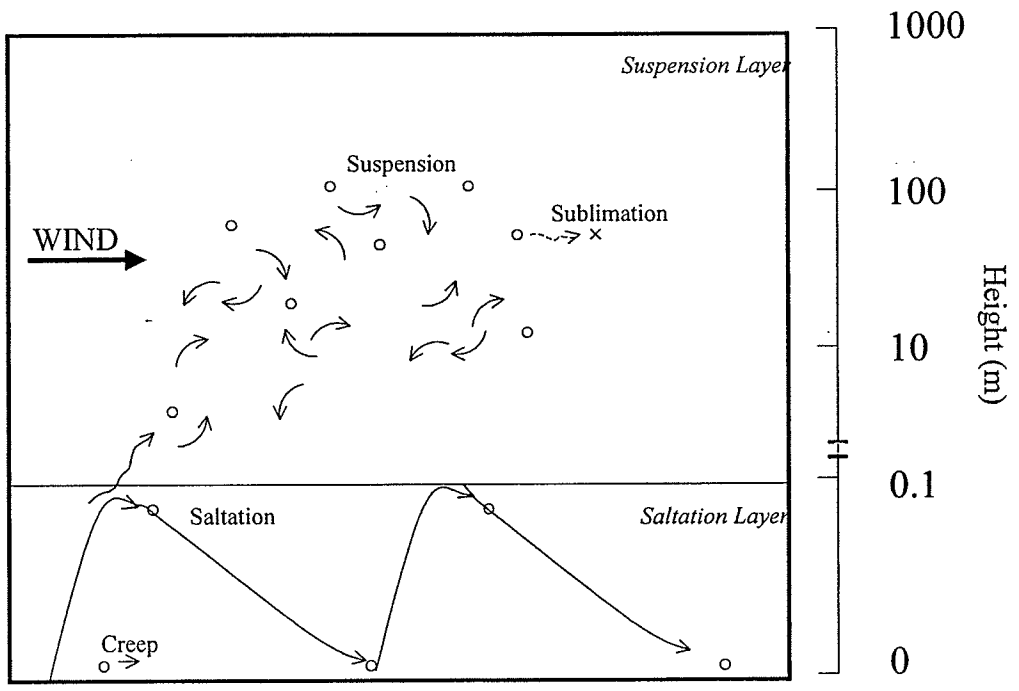

Figure 2.10. A schematic representation of blowing snow processes occurring in the saltation and suspension layers.

from the surface, which then either bounce along the snow surface or collide with other particles on the surface, forcing them into the air. This mechanism occurs within a shallow layer above the snow surface termed the saltation layer (typically < 10 cm; Schmidt, 1986). Saltation also results in a slow rate of snow transport; however, it controls snow erosion and is therefore needed for suspension and sublimation of snow to occur (e.g., Pomeroy and Li, 2000). An interesting observation is that electrostatic charges, built up by friction between moving snow and the surface, may significantly contribute to the trajectory of particles within the saltation layer (Schmidt and Dent, 1993). Suspension occurs when sufficient turbulent airflow acts to lift particles above the layer of saltation. A balance between downward gravitational forces and upward turbulent diffusion is met (e.g., Déry and Tremblay, 2004). The final mechanism

mentioned above for blowing snow processes is sublimation, which is the loss of snow back to the atmosphere. Sublimation of snow grains occurs at a much higher rate during a blowing snow event in comparison to surface sublimation of a snowpack (Schmidt, 1982) and can therefore have a significant effect on cooling the atmospheric boundary layer (Déry and Yau, 2002). Within a sea ice environment, leads and cracks may also have a significant effect on decreasing snow accumulation (Eicken et al., 1994; Déry and Tremblay, 2004).

Field investigations and models used to estimate snow transport and accumulation usually involve the calculation of a snow cover mass balance. Snow mass balance equations calculate a snow accumulation rate ($\partial S/\partial t$) over a point or grid location as the following:

$$\frac{\partial S}{\partial t} = P - \nabla F - E_B - E - M \qquad [2.9]$$

where P is precipitation, ∇F is the downwind transport rate of blowing snow, E_B is blowing snow sublimation, E is snow surface sublimation and M is melt (Pomeroy and Li, 2000). ∇F is a balance of an outflow minus inflow of mass through contributions by saltation and suspension. A further flux parameter has been added in a recent modeling study to equation 2.9 in order to represent loss of blowing snow to leads and cracks within a sea ice environment (Déry and Tremblay, 2004). Through field observation and model sensitivity studies, snow mass balance has been found to be dependent on wind speed, surface roughness/topography and fetch, relative humidity and snow temperature and age/density (e.g., Pomeroy and Li, 2000).

The redistribution of blowing snow results in the formation of characteristic snow drifts over the sea ice. Their initial formation occurs as a result of some irregularity over the surface that causes a disruption in the boundary layer flow of blowing snow and therefore results in preferential erosion and deposition (Déry and Tremblay, 2004). After initial drifts form, aeolian processes result in particles eroded from the windward side of a drift and deposited on the leeward side forming long gradual and short steep slopes, respectively. Over relatively smooth surfaces, snowdrifts take aeolian transport shapes of barchan (crescent-shaped), sastrugi (wind sculpted), or longitudinal dunes (Sturm et al., 2002), dependent on the amount of snow available for transport. Similarly, over rough surfaces such as multiyear hummocks and pressure ridges, snow accumulates on the leeward side of surface roughness elements. However, the process of snowdrift formation via aeolian processes is complicated by sublimation and inter-particle cohesion forces (e.g., sintering; Schmidt, 1986). Further, small-scale surface variations in snow cover properties and boundary layer flow result in spatial intermittency of blowing snow events (Pomeroy and Li, 2000; Sturm et al., 2002). It is noted that most blowing snow models have been developed for medium (100 m to 1 km) to large-scale (1 km to 100 km) applications of snow transport and accumulation (e.g., Pomeroy et al., 1993; Liston and Sturm, 1998). Only one model (Déry and Tremblay, 2004) appears to exist that attempts to model small-scale (1 m) formation of drifts. Further, this model has been developed for Arctic sea ice and therefore may provide interesting contributions to future knowledge of blowing snow processes over sea ice.

The limited knowledge existing on drift formation and snow catchment over sea ice has led to studies investigating the statistical distribution over different sea ice types. Iacozza

and Barber (1999) found that geostatistical techniques could be used to model the spatial distribution of snow within various sea ice catchment types (e.g., first-year, rubble and multiyear sea ice). They found typical cross drift sizes of 10 to 20 meters. Similar results were observed by Sturm et al. (2002). Generally, the greater the surface variability, the greater the depth and variability in snow depth. Sturm et al. (2002) also found 10 separate storm events to result in 10 distinct layers within the various snowpacks, therefore, noting the importance of these events on shaping the snowpack vertical structure. However, these events occurred over 240 days, suggesting the low frequency of such events in the Arctic.

It is noted that small-scale temporal variability of snowdrifts associated with blowing snow processes remains largely unknown. The spatially variable nature of blowing snow over a surface can theoretically lead to a temporally dynamic snow cover over any particular location. This would result in unique temporally integrated light and thermal regimes under an ice cover and therefore affect algal growth on spatial scales larger than simply the snowdrift size. This was perhaps indirectly observed by Gosselin et al. (1986) who found algae patchiness at a scale of approximately 100 m during early spring. There is therefore an apparent and important relationship, however it requires further investigation.

2.3.7 Bottom Ice – Ocean Interactions

To this point in the chapter, I have focused my review on processes related to snow-covered sea ice and atmosphere-ice interactions. Subsequently little emphasis has been placed on oceanic influences on the bottom ice. However, the ocean plays an important role in the bottom ice algal ecosystem. In the Arctic, the ocean's main influence on this

system appears to revolve around fluxes of heat (Maykut, 1986) and nutrients (Cota et al., 1991), which are largely governed by tidal influences. Lavoie et al. (2005) provided theoretical evidence that both of these fluxes are very important to the accumulation and loss of bottom ice algae.

Stated earlier in section 2.3.1.2, the oceanic heat flux has a direct influence on ice growth and ablation. As the dissertation is focused on study sites located within the Canadian Arctic Archipelago, it is important to make some distinctions of this region relative to the central Arctic Basin with respect to heat fluxes. Melling (2002) has noted that little is known on the actual oceanic heat flux supplied to the sea ice bottom during the period of ice cover in the Archipelago. It has been argued that the shallow and narrow waterways within the Canadian Arctic Archipelago cause strong mixing of cold surface Arctic waters with warmer bottom waters driven by tidal currents (Melling et al., 1984). Melling (2002) provided an estimate of at least 15 W m^{-2} needed to account for warmer surface temperatures and decreased stratification in the northern Archipelago in comparison to Arctic Ocean hydrographic profiles. It was further estimated that an oceanic heat flux of approximately 10 W m^{-2} influences the ice cover in the northern Archipelago. From a recent study near Resolute Bay, Nunavut, oceanic heat fluxes to the sea ice of greater than 20 W m^{-2} were estimated from temperature data and a mixed layer model during the period of ice melt (Lavoie et al., 2005). Therefore, the Canadian Arctic Archipelago appears to have an enhanced oceanic heat flux to the sea ice in comparison to the central Arctic Ocean due to turbulence generated by tidal stress on the sloping walls of the channels (Melling, 2002).

The Canadian Arctic Archipelago is predominantly covered by landfast ice during winter and spring due to the narrow network of channels between the islands. Therefore, the ice cover is generally smoother than pack ice in the Arctic Ocean, particularly under areas of landfast first-year sea ice (Melling, 2002). The relatively smooth undersurface of the ice results in the oceanic flux of heat and nutrients to the sea ice to be limited by molecular exchange across the molecular sublayer (McPhee, 1990; Crawford et al., 1999). Molecular exchange is a direct function of the scalar gradient and eddy diffusion/viscosity coefficient and indirect function of the sublayer thickness. The thickness of the molecular sublayer can be further estimated as the quotient of the kinematic viscosity of seawater divided by the tidal varying friction velocity (Lavoie et al., 2005, and references therein). Therefore, the fortnightly tidal cycle causes a decrease of the molecular sublayer thickness during spring tides resulting in a greater potential for transfer of heat and nutrients from the ocean to the sea ice in comparison to neap tides. The thicker molecular sublayer experienced during neap tide is believed to result in the periodic limitation of nutrients on ice algal growth even though nutrients in the mixed layer are in ample supply (see Cota et al., 1991 for a review) and can influence bottom ice growth and melt which may affect the accumulation and loss of algal biomass (Lavoie et al., 2005). A more recent finding suggests that oceanic heat flux into the bottom of first-year sea ice may control the permeability of the ice cover (Widell et al., 2006). Widell et al. suggested that a brine drainage event from the ice cover, usually associated with an inflow of sea water that freezes within the ice resulting in a decrease in permeability, can be sustained (i.e., increased ice permeability) if there is an enhanced oceanic heat supply available.

Another physical factor of the ocean on the ice is its momentum flux which would supply a more mechanical influence on bottom and sub-ice algae communities. I speculate that this flux may be important for the clearing of algal mats and cells hanging into the water column from the ice bottom. However, to my knowledge this process has not yet been investigated in the literature.

3.0 Summary

Understanding processes driving a system is a key requirement to undertake a study of that system. In this chapter I have provided a review of the current knowledge relating to physical processes controlling bottom ice algal biomass accumulation and loss in the Arctic. More specifically, physical processes governing the influences of light, nutrients, space, temperature and salinity on bottom ice algae were reviewed. Throughout the discussion, although not explicitly stated, various scales of variability exist when considering these physical processes. For example, light as a physical control on algae can temporally vary with the annual solar cycle and sea ice formation and melt processes (months), synoptic activity (days to weeks), and snow depth (hours to days). Spatially, light can vary horizontally over regional scales associated with ice concentration and synoptic activity (hundreds to thousands of kilometers), ice type and thickness (kilometers to hundreds of kilometers) and snow distribution (tens to hundreds of meters) and vertically with ice and snow microstructure and bulk properties (micrometers to meters). The recognition of these scales is a critical component in understanding a system.

My purpose of this chapter was not to supply an exhaustive review of the processes influencing ice algal biomass and production, but rather to provide the background needed to better understand the studies to meet the stated sub-objectives of this dissertation. In the next chapter, I present the methods, data analysis and models used to examine these sub-objectives.

CHAPTER 3: Data Collection and Models

3.1 Introduction

In this chapter, I describe the dataset and models used in my dissertation. The chapter has been separated in sections accordingly. In the first section, the methods used to collect physical and biological data during two separate field campaigns are described. In the second section, the optical, thermodynamic and ice algae growth models applied in Chapters 6 and 7 are described. Statistical and analytical methods and changes to model input parameters including adjustments to model parameterizations are described in conjunction with the presentation of data in separate chapters.

3.2 Data Collection

3.2.2 Study Site

All field data were collected during two spring field programs conducted on smooth landfast first-year sea ice in the central Canadian Arctic near Resolute Bay, NU: (1) the 2002 Collaborative – Interdisciplinary Cryospheric Experiment (C-ICE'02; Mundy and Barber, 2003) and (2) the 2003 Fisheries and Oceans Canada Resolute Passage ecosystem monitoring project (Carcajou'03). The study site for C-ICE'02 was located to the west of Truro Island in McDougall Sound, approximately 80 km northwest of Resolute Bay, NU (Fig. 3.1). Sampling during C-ICE'02 was conducted over a five week period from May 4 (Day 124) to June 9 (Day 160). The study site for Carcajou'03 was located in Resolute Passage, NU (Fig. 3.1). Sampling during Carcajou'03 occurred over a three week period

from May 3 (day 123) to May 21 (day 141). Data collected over both field programs are delineated as either time series measurements (single location) or point samples collected periodically within a localized area over time.

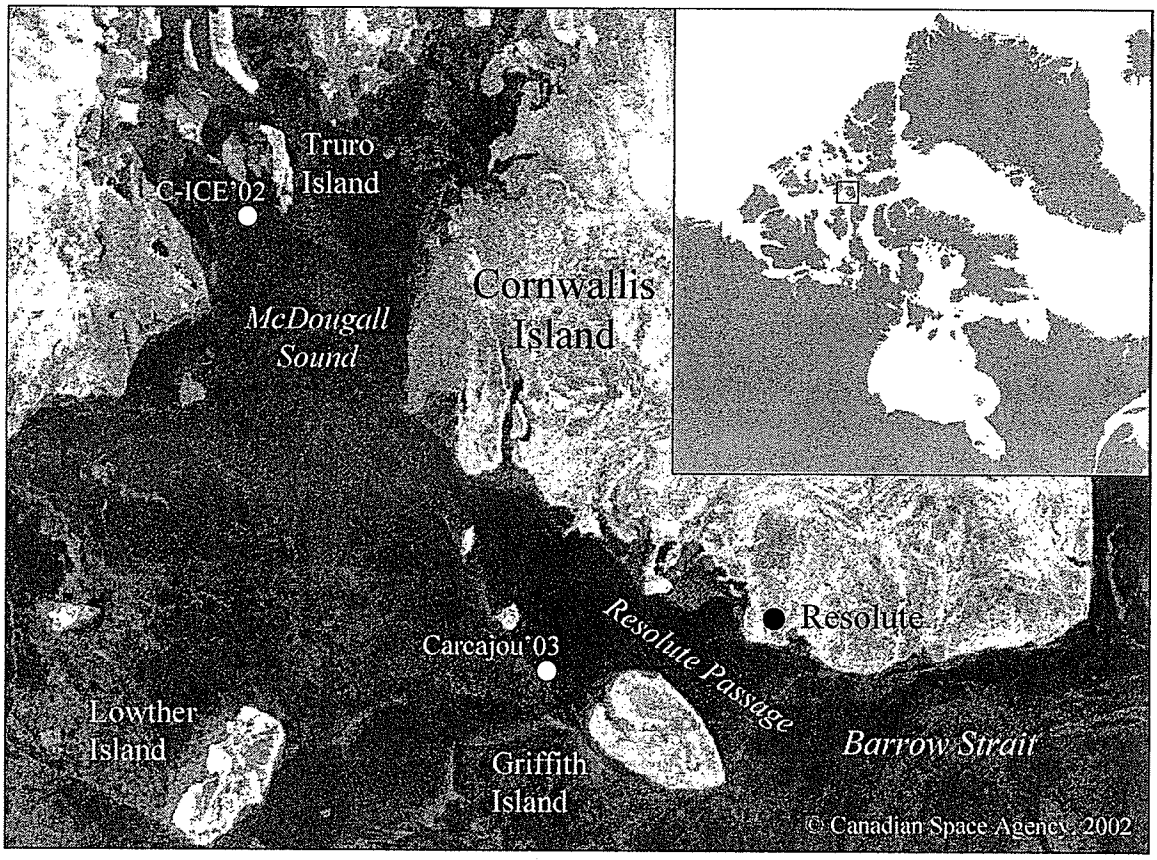

Figure 3.1. Map of the C-ICE'02 and Carcajou'03 study sites located in McDougall Sound (75° 14.1′ N, 97° 19.0′ W) and near Resolute Passage (74° 42.5′ N, 95° 49.5′ W) Nunavut, Canada, respectively.

3.2.2 Time Series Measurements

Radiative and thermophysical observations of the atmosphere, snow and sea ice were made via on-ice automated micrometeorological (micromet) sites set up during the two field programs (75° 14.83′ N, 97° 14.19′ W). Further, additional measurements of the snow and ocean were made separate from the micromet sites. Table 3.1 outlines all the

time series variables collected and Table 3.2 is a Gantt chart specifying the dates and field programs during which the variables were collected.

3.2.2.1 C-ICE'02

Meteorological measurements made during C-ICE'02 include air temperature (Ta), relative humidity (RH), wind speed (U) and wind direction (Ω). Radiative measurements included shortwave downwelling (SW_D) and upwelling (SW_U; albedo, $\alpha = SW_D / SW_U$), longwave downwelling (LW_D) and upwelling (LW_U), PAR downwelling (PAR_D) and PAR transmitted to the ice-snow interface (PAR_{IS}). Thermal measurements of the snow and ice included profiles of snow (T_S) and ice (T_I) temperature. Snow depth was monitored via a sonic ranging sensor (h_{snow}^{SR}, snow depth site A) mounted to the tower. As the sonic ranging sensor was sensitive to airborne snow, its daily standard deviation was used as a blowing snow index (BSI).

Wooden dowels were installed at the PAR_{IS} and snow and ice temperature profile site, 5 m south-southwest of the meteorological tower. The two wooden dowels were positioned directly north-south of each other with a spacing of 1 m. Snow depth was recorded from the dowels in the morning, during daily visits to the study site (h_{snow}^{Dow}). These time series were labeled snow depth sites B (north) and C (south), whereas site A was monitored via the ranging sensor mounted on the micromet tower. Throughout the study period, snowfall, recorded in millimeters snow water equivalent (SWE) was monitored at 6 h intervals using a Nipher-shielded cylinder gauge on land near the C-ICE'02 base camp (approximately 3 km from the study site; 75° 25′ N, 97° 16′ W). The

measurements were corrected for wind speed as suggested by Goodison et al. (1998) by dividing the measured SWE by an under-catchment ratio (R),

$$R = 0.01\ (100 - 0.387\ U^2 - 2.022\ U) \qquad [3.1]$$

where U is wind speed, $m \cdot s^{-1}$, averaged over a 6 h period.

Time series measurements of SW_D, SW_U, PAR_D, PAR_{IS}, U and Ω, and BSI during C-ICE'02 were intermittent following day 149 due to technical problems. Daily averages of wind speed and BSI data are presented since their dependence on time of day is not as direct as shortwave measurements, which are not presented.

Table 3.1. Time series variables monitored during C-ICE'02 and Carcajou'03.

Variable	Units	Description	Sensor
SW_D and $_U$	$W\ m^{-2}$	Downwelling and upwelling shortwave radiation (0.3 to 3 μm)	pyranometer (Eppley)
LW_D and $_U$	$W\ m^{-2}$	Downwelling and upwelling longwave radiation (> 3 μm)	pyrgeometer (Eppley)
$PAR_{D, U}$ and $_{IS}$	$\mu E\ m^{-2}\ s^{-1}$	Photosynthetically Available Radiation (400 to 700 nm) downwelling, upwelling and transmitted to the ice surface	quantum sensor (LI-COR models LI-190 and -192)
Ta and RH	°C and %	Air temperature and relative humidity	CS500 (CSI)
U and Ω	$m\ s^{-1}$ and °	Wind speed and direction	RM Young Wind Monitor (Model 5103-10A)
h_{snow}^{SR}	cm	Snow depth at site A	Sonic Ranging Sensor (SR50; CSI)
BSI	cm	Blowing Snow Index (daily standard deviation of H_S^{SR})	Sonic Ranging Sensor (SR50; CSI)
Snowfall	mm	Cummulative snow water equivalent (SWE)	Nipher gauge corrected for wind speed
$V^{3.37}$	$cm\ s^{-1}$	Current velocity centered at a 3.37 m water depth	Workhorse Sentinel – Self Contained ADCP (RDI)
T_S and T_I	°C	Snow and ice temperatures	Thermocouple (Type T)
h_{snow}^{Dow}	cm	Snow depth	Marked dowel

Table 3.2. Gantt chart of time series variables monitored during C-ICE'02 (black bars) and Carcajou'03 (white bars).

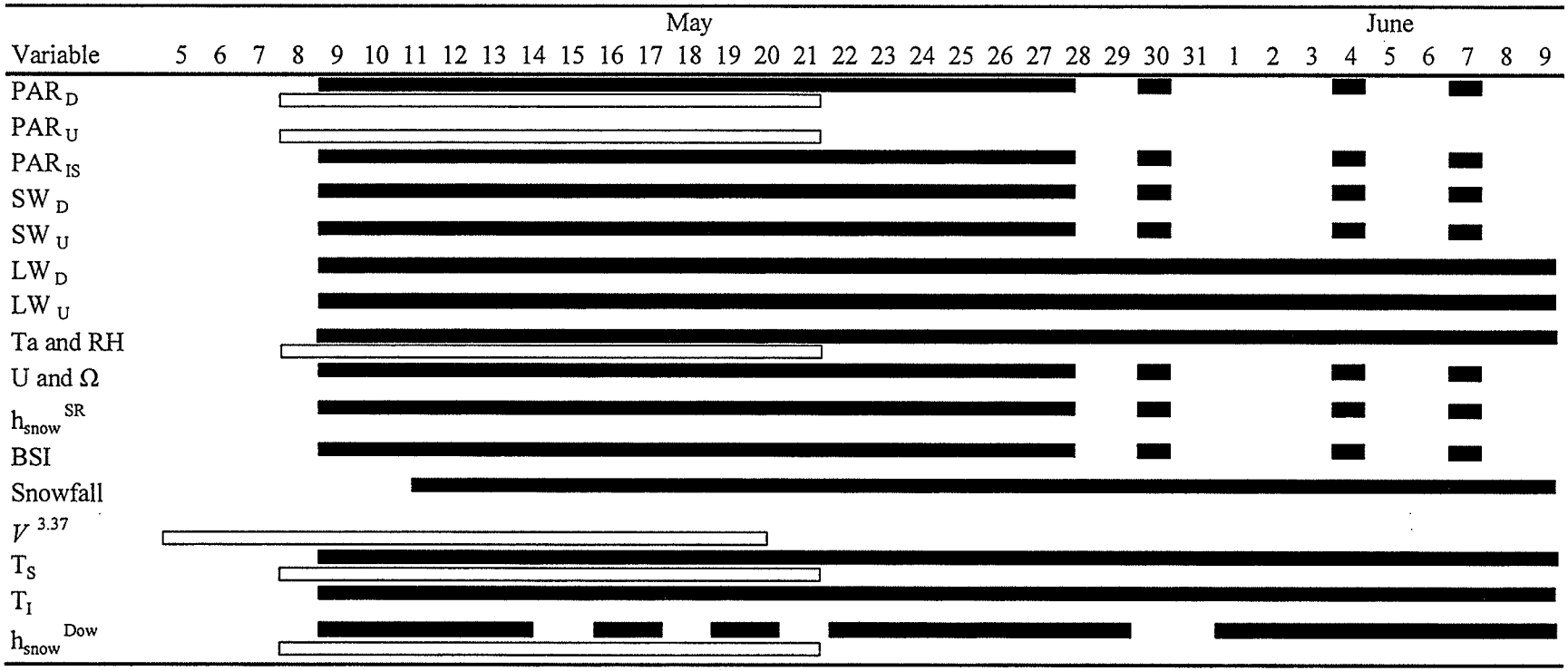

3.2.2.2 Carcajou'03

The on-ice micromet site used in Carcajou'03 monitored Ta, PAR_D, PAR_U (upwelling) and a profile of T_S spaced at 3 cm vertical intervals from the ice-snow interface. Snow depth (h_{snow}^{Dow}) was recorded daily adjacent to the T_S profile location. Water current velocities ($V^{3.37}$) were monitored using an acoustic Doppler current profiler (ADCP) mounted at the ice bottom looking downwards. The ADCP was operational from May 5 (day 125) through to May 20 (day 140). Hourly averaged data from the ADCP, sampled at 3.35 m from the ice-water interface, are presented here.

3.2.3 Point Sampling

3.2.3.1 C-ICE'02

An extensive snow distribution survey was carried out on day 131. At that time, snow depth was sampled every meter over a 100 m by 100 m area using a radial transect pattern at 45 degree increments in order to compute a variogram model of the spatial distribution following Iacozza and Barber (1999). A Gaussian variogram model with anisotropy was fit to the data and kriging was used to interpolate the snow surface.

Sampling for C-ICE'02 was carried out over a '3-4 days on', '1 day off' interval, in an area adjacent to the snow survey site. On each sampling day, a 5 m by 5 m area was selected. Five different snow depths were chosen within the selected area. At three of the snow depths, a snow pit was excavated to obtain attenuation of PAR in the snowpack and profiles of snow density, salinity and grain size. All measurements were made near solar

noon (approximately 13:30 CDT). Coincident measurements of incident (PAR_0) and transmitted (PAR_Z) PAR were made at 2 cm intervals within the diffusely lit wall of a covered snow pit using two LI-COR LI-190 quantum sensors (mounted on a tripod for PAR_0 measurements). These measurements were used to determine the relative attenuation of PAR ($\ln(PAR_0/PAR_Z)$) for each depth interval within the snow cover. Following the assumptions of Beer's law,

$$PAR_Z \approx PAR_0 \exp(-\kappa_{PAR}\, z) \qquad [3.2]$$

where κ_{PAR} is the PAR bulk attenuation coefficient (m^{-1}) and z is depth (m) into the snow cover at which PAR_Z was measured, κ_{PAR} was estimated from the slope of the relationship between the relative attenuation of PAR and z. Slope calculations used measurements from the homogeneous middle layer of the snowpack. Near surface measurements (top 4 to 6 cm) were not used as energy was lost from the snowpack (i.e., albedo). Measurements within the basal layer (bottom 2 to 4 cm) were associated with different salinities, densities and snow grain sizes and therefore different slopes.

Snow samples were collected at a 2 cm interval using a 66.36 cm^3 density cutter. Samples were immediately put in Whirl-pack bags in a cooler and brought back to camp for analysis. Density samples were weighed to the nearest hundredth of a gram using a digital scale. A minimal number (15 to 30) of individual snow grains were removed from the sample and digitally photographed on a black aluminum plate inscribed with a 2 mm scale. Post-field image analysis involved the extraction of grain size (mm^2) using the public domain NIH Image program (developed at the U.S. National Institutes of Health

and available on the Internet at http://rsb.info.nih.gov/nih-image/). An example procedure is outlined in Mundy (2000). Due to melt of snow grains between sampling and photographing, snow grain size was only collected between days 132 and 148. Snow samples were then melted and salinity was measured using a WTW 330si conductivity meter, which has an accuracy of ±0.5% of reading. A dimensionless description of salinity is used in the dissertation (e.g., g salt/1000 g sea water).

At all five sites, snow depth was measured and two 9 cm diameter ice cores were collected for biological analysis using a Mark II ice corer (Kovacs Enterprise). The bulk of algae biomass in the study area is found in the bottom 5 cm of first-year columnar sea ice (Smith et al., 1990). Therefore, the bottom 5 cm of the two cores were pooled in a 1.5 L isothermal container. During collection, care was taken to not touch the bottom 5 cm cores and minimize their exposure to direct sunlight. Ice thickness was measured at each site.

Pooled cores were slowly melted in Whatman GF/F filtered surface seawater collected at the time of sampling. Duplicate subsamples were filtered onto GF/F filters, which were then placed in 10 ml of 90% acetone for 24 h at approximately 5 °C in the dark to extract chlorophyll *a* (chl *a*) from the algal cells (Parsons et al., 1984). Following subsample collection, salinity of the melted cores and surface seawater was measured using a WTW 330si conductivity meter. The chl *a* – acetone solution was then measured for fluorescence with a Sequoia-Turner fluorometer Model 450. Chl *a* concentration ([*chl a*]) was calculated using the following equation from Holm-Hansen et al. (1965) adjusted using a multiplication ratio (*MR*) – calculated by multiplying the volume of the melted

cores with a dilution factor, to account for the added filtered sea water, then dividing by the area of the two original cores – to provide mg chl *a* m^{-2}.

$$[chla] = Fd\frac{\tau}{\tau - 1}(Rb - Ra)\frac{v}{V}MR \qquad [3.3]$$

where *Rb* and *Ra* are the fluorescence measurements before and after acidification of the chl *a* – acetone solution with 3 drops of 10 % HCl, *Fd* is the response factor of the fluorometer calibrated to a pure chl *a* standard (i.e., $[chl\ a]^{std}/Rb^{std}$), τ is the acidification ratio of the chl *a* standard measured by the fluorometer (Rb^{std}/Ra^{std}), *v* is the volume of acetone used and *V* is the volume of the subsample filtered (Parsons et al., 1984).

Approximately every 5 days, subsamples of the surface sea water and melted pooled cores from the medium snow depth site of the particular day's samples were taken prior to any other subsampling. The nutrient subsamples were obtained using a clean syringe, rinsed 3 times with the sample, then slowly pushed through a combusted GF/F syringe filter into 5 sterile 2 ml cryovials. The cryovials were immediately placed into a –20 °C freezer and stored for analysis down south. Nutrient concentration of silicic acid, nitrite, nitrate and phosphate were determined via a Technicon II Autoanalyzer.

3.2.3.2 Carcajou'03

Each day during the Carcajou'03 program, three varying snow depths were chosen for sample collection. A total of 47 sites were visited during the sampling period. Every second day a snow pit was dug at the middle snow depth to collect a profile of snow

physical properties at 2 cm intervals using the methods outlined above for density, salinity and grain size. Snow wetness (% water volume) was also measured using a PSI 944 capacitance plate. This sensor has a 12.5 cm x 14 cm surface area with an operating temperature range from –20 °C to +40 °C.

The main sampling device deployed during Carcajou'03 was an underice arm which held an underwater camera, a spectral radiometer sensor head and an underwater PAR sensor (Fig. 3.2). To deploy the radiometer sensors underneath the ice, an 8-inch hole was drilled 1.5 m north of the sample collection site. The underwater arm was used to position the sensors below the sample location at a 60 cm distance (camera focus distance) from the ice bottom. The hole effect on the light field was assumed negligible due to the positioning of the sample site 1.5 m south of the hole. At each sample collection site, snow depth was measured and two 9 cm diameter ice cores were collected for biological analysis as outlined above.

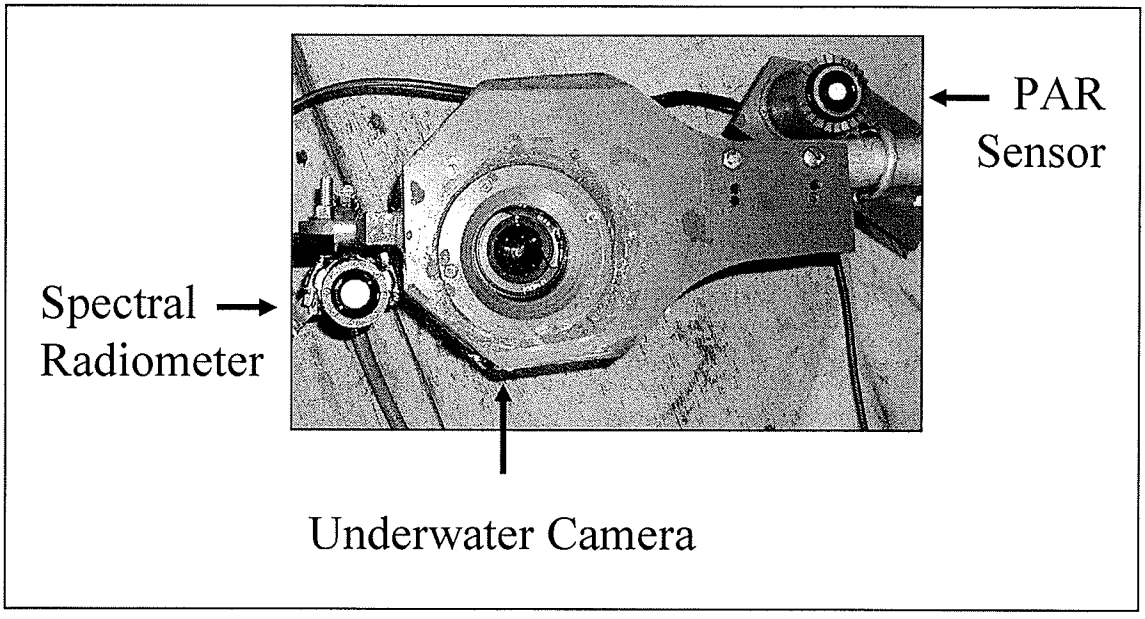

Figure 3.2. Picture of the three sensors mounted on the underice arm.

The camera set-up consisted of an Electroimage Tripix© digital USB camera with a 1280 x 1024 Motorola high performance monochrome micro lens CMOS (complimentary metal-oxide semiconductor) sensor (MCM20027) and housed in a custom built underwater enclosure. The CMOS sensor's linear response to light was tested by exposing the sensor to a constant light source and varying the exposure time. Regression analysis confirmed a linear response ($R^2 > 0.99$) across the entire range of the sensor. A Nikon AF Nikkor 24 mm wide-angle lens (1:2.8 D) was used to focus and increase the viewing area of the camera. The micro lens CMOS sensor provided a microscopic view of the ice-water interface with a pixel resolution of 220.75 μm. Therefore, the ice bottom surface was imaged with sufficient resolution to distinguish individual ice lamellae, which are generally > 1 mm wide under thick ice (Weeks and Ackley 1982). The USB interface provided manual control where the gain was held constant at 1 (i.e., linear) and exposure time was adjusted to maximize the dynamic range of the image. Due to logistical difficulties, the distance between the camera and ice was sometimes less than 60 cm. A distance difference of 10 cm resulted in a loss of focus which corresponded to an 11 % change in pixel size. Only those pictures in focus (i.e., crystal plates were visible) were analyzed, and 11 % represents a maximum pixel resolution error. At each site, 4 gray-scale (8-bit) images were captured which included ones taken under a red, green and blue interference filter and one with no interference filter. Due to the spectral absorption properties of snow, ice and algae (Mundy et al. 2007), the green filter provided the largest dynamic range out of the 4 images and therefore only those images taken with the green interference filter were used in this investigation. Although 47 sites

were visited throughout Carcajou'03, only 10 images were in sufficient focus to use in the analysis presented in Chapter 5.

Underice, high-resolution (1.4 nm band width) spectral measurements of irradiance were made over the wavelength range of 400 to 700 nm using an Analytical Spectral Device© (ASD) Fieldpro spectral radiometer with an underwater calibrated reverse cosine receptor (180° field of view). Each measurement represents averages of at least 5 irradiance scans. All data were transformed to absolute units of irradiance ($W\ m^{-2}\ nm^{-1}$) based on laboratory calibrations of the radiometer. Simultaneous measurements of incident and transmitted PAR were recorded using the LI-COR quantum sensors, LI-190 (mounted on a tripod) and LI-192, respectively.

3.3 The Models

Due to the complexity needed for simulating bottom ice algae accumulation and loss, three separate models were used. The first is a one-dimensional thermodynamic model (Flato and Brown, 1996) used to simulate changes in ice temperature and thickness over time under a varying snow cover. The second is a two-stream radiative transfer model based on attenuation parameterizations described by Perovich (1990). The third is an ice algae growth model which has been based on models produced by Arrigo and Sullivan (1994) and Lavoie et al. (2005). All notations for the models are provided in Table 3.3.

Table 3.3. Values and units for all variables used in the models.

Notation	Description	Value	Units
	Thermodynamic Model		
ρ	Density		kg m^{-3}
C_P	Specific heat capacity		J kg^{-1} K^{-1}
T	Temperature		K or °C
t	Time		d
k	Thermal conductivity		W m^{-1} K^{-1}
z	Depth from the surface of the snow to the undersurface of the ice		m
SW_D	Downwelling shortwave irradiance		W m^{-2}
I_0	Fraction of shortwave flux which penetrates the surface	0.17 if snow $\leq$ 0.1 m, otherwise is equal to 0.0	dimensionless
α	Surface albedo	0.85	dimensionless
κ^{ice}	Bulk attenuation coefficient for ice	1.5	m^{-1}
F_0	Net downward surface heat flux		W m^{-2}
	Radiative Transfer Model		
$E_D{}^{(z,\lambda)}$	Spectral downwelling irradiance at depth z		W m^{-2} nm^{-1}
$E_U{}^{(z,\lambda)}$	Spectral upwelling irradiance at depth z		W m^{-2} nm^{-1}
E_0	Incident solar irradiance	Set to 1 for transmittance output	W m^{-2}
R_0	Specular reflection	0.05 for air/ice, 0 for air/snow	dimensionless
b	Scattering coefficient, superscripts snow, ice and chl denote snow, ice and algae		m^{-1}
κ_λ	Spectral attenuation coefficient, superscripts snow, ice and chl denote snow, ice and algae		m^{-1}
a_λ	Absorption coefficient, superscripts snow, ice and chl denote snow, ice and algae		m^{-1}
$a_\lambda{}^{*,chl}$	Chlorophyll *a* specific absorption coefficient		m^2 mg chl a^{-1}
$E_{1,\lambda}$, $E_{2,\lambda}$	Under ice spectral transmitted irradiance, subscripts 1 and 2 represent a thick snow, low chl *a* concentration and thin snow, high chl *a* concentration, respectively		W m^{-2} nm^{-1}
$E_\lambda{}^W$, $E_\lambda{}^{\mu E}$	Spectral irradiance		W m^{-2} μE m^{-2} s^{-1}
B, B_1, B_2	Biomass concentration, subscripts 1 and 2 represent a thick snow, low chl *a* concentration and thin snow, high chl *a* concentration, respectively		mg chl *a* m^{-2}
h_a	Ice algal layer thickness	0.05	m
N_A	Avagadro's number	6.022×10^{23}	mol^{-1}
h	Plank's constant	6.626×10^{-34}	J
c	speed of light	2.998×10^8	m s^{-1}
λ	wavelength		nm
	Ice Algae Growth Model		
μ	Specific algal growth rate		d^{-1}
μ_{max}	Maximum temperature dependent growth rate		d^{-1}
μ_0	Specific algal growth rate at 0 °C	0.8511	d^{-1}
r_μ	Log-linear sensitivity of μ_{max} to temperature	0.0633	$°C^{-1}$
N_{lr}	Nutrient limitation coefficient		dimensionless
N	Nutrient concentration, chl subscript denotes ice algal layer		mmol m^{-3}
N_{up}	Nutrient uptake by algal growth		mmol m^{-2} s^{-1}
K_S	Half-saturation constant for silicic acid uptake	3.9	mmol m^{-3}

Table 3.3. Continued.

Notation	Description	Value	Units
F_N	Flux of nutrients to the top of the mixed layer		mmol m^{-2} s^{-1}
F_{Nchl}	Flux of nutrients to the ice algal layer		mmol m^{-2} s^{-1}
u_τ	Tidal varying friction velocity		m s^{-1}
k_v	Kinematic viscosity of seawater	1.85×10^{-6}	m^2 s^{-1}
K	Turbulent mixing coefficient		m^2 s^{-1}
Si	Molar mass of silicon	28.09	mg $mmol^{-1}$
W_{Si}/W_{Chla}	Ratio Si(OH)4 in mmol required to produce 1 mg chl *a*		mmol mg^{-1}
D	Molecular diffusion coefficient of silicic acid	1×10^{-9}	m^2 s^{-1}
h_v	Molecular sublayer thickness		m
L_{lr}	Light limitation coefficient		dimensionless
PAR_{chl}	PAR irradiance reaching the top of the ice algal layer		µE m^{-2} s^{-1}
I_k	Photoacclimation parameter		µE m^{-2} s^{-1}
IGR_{lr}	Ice growth rate limitation coefficient		dimensionless
S_f	Salinity dependent algal growth coefficient		dimensionless
S_b	Brine salinity		dimensionless
L_{RES}	Fractional loss of algae due to respiration		dimensionless
RES_0	Specific respiration rate at 0 °C	0.05	d^{-1}
L_{GRA}	Fractional loss of algae due to grazing pressure		dimensionless
L_{IGR}	Fractional loss of algae due to ice ablation		dimensionless
$T_{2.5}$	Ice temperature in the middle of the ice algae layer		°C
H	Ice thickness		m
h_{snow}	Snow depth		m

3.2.1 Thermodynamic Model

Models for ice growth which can provide analytical solutions (e.g., equation 2.6) are based on the simple premise that heat released by freezing at the ice bottom is conducted away through the ice and snow by a constant temperature gradient (e.g., Leppäranta, 1993). Therefore, such a model is only applicable to the period of ice growth. As the

application of the model in my dissertation is for the spring transition when surface temperatures climb above freezing, a numerical model is needed to model ice growth and melt. I chose to use the one-dimensional thermodynamic model described in detail by Flato and Brown (1996) and Hanesiak (2001).

The model is based on the following heat conduction equation including absorption of solar radiation as presented by Maykut and Untersteiner (1971),

$$\rho C_P \frac{\partial T}{\partial t} = \frac{\partial}{\partial z} k \frac{\partial T}{\partial z} + SW_D I_0 (1-\alpha) \kappa^{ice} \exp(-\kappa^{ice} z) \qquad [3.4]$$

where T is temperature within the snow or ice, t is time and z is depth from the snow surface to the undersurface of the ice. All variables and parameters used in the models are defined in Table 3.3. Equation 3.4 is set to the following boundary conditions: (1) at the ice-water interface, T is equal to the freezing temperature of sea ice (–1.8 °C); (2) at the upper surface, T is equal to the melting temperature of the snow (0 °C) or sea ice (–0.1 °C) if the net heat flux (F_0) is into the surface, otherwise the surface temperature gradient is a direct function of the net heat flux away from the surface.

Ice growth and melt are computed at the bottom boundary according to the balance of the conductive heat flux into the ice with the heat flux from the surface mixed layer of the ocean and the shortwave energy which penetrates through the ice bottom and assumed as input into the ocean mixed layer. At the upper surface boundary, melt of the snow cover occurs prior to any surface ice melt. Therefore, as a snow cover is present during all model runs in the dissertation, changes in ice thickness are the result of changes at the ice bottom.

The net heat flux at the surface is equal to the surface energy budget (equation 2.2), where the upwelling longwave flux is determined through Stefan-Bolztmann law using the surface radiative temperature. The model in its original form is forced with daily averages of air temperature, relative humidity, cloud amount and wind speed with parameterizations to calculate the terms of the surface energy budget (Flato and Brown, 1996). However, to more realistically model ice growth and ablation in the study area, I used field data from the C-ICE'02 micromet site for LW_D and SW_D as daily input into the model. The model was also forced with a daily snow depth file. The model was set to 51 layers, 1 variable depth snow layer and 50 equal ice thickness layers. Outputs from the thermodynamic model used in the ice algae model described below include the daily ice temperature profile and thickness change. Note that z within the radiative transfer model and ice algae growth model is used as a depth from the snow surface to ice surface and depth from the ice surface to ice bottom, separately.

3.2.2 Radiative Transfer Model

The two-stream radiative transfer model and its parameterizations presented in Perovich (1990) have evolved from previous papers by Dunkle and Bevans (1956), Grenfell and Maykut (1977), Grenfell (1979; 1983) and Grenfell and Perovich (1984). The two-stream label of the model refers to its calculations of a downwelling (E_D) and an upwelling (E_U) irradiance in the transfer medium (in this case, snow, sea ice and algae). The model has n-layers which are plane parallel (i.e., homogeneous in x, y and z) and provides continuity at boundaries between layers by assuming no reflection or absorption at interfaces (Fig. 3.3; Perovich, 1990). The optical properties of a layer are defined by

the scattering (b) and spectral attenuation (κ_λ) coefficients. Presented in Perovich (1990), the change in downwelling ($\partial E_D{}^{(z,\lambda)}$) and upwelling ($\partial E_U{}^{(z,\lambda)}$) irradiances at depth within the medium is controlled by equations (3.5) and (3.6), respectively:

$$\partial E_D{}^{(z,\lambda)} = -(a_\lambda E_D{}^{(z,\lambda)}\partial z) - (b E_D{}^{(z,\lambda)}\partial z) + (b E_U{}^{(z,\lambda)}\partial z) \qquad [3.5]$$

where a_λ is the spectral absorption coefficient and the terms on right side of the equation represent loss to absorption, scattering loss from downwelling and scattering gain from upwelling, and

$$\partial E_U{}^{(z,\lambda)} = (a_\lambda E_U{}^{(z,\lambda)}\partial z) - (b E_D{}^{(z,\lambda)}\partial z) + (b E_U{}^{(z,\lambda)}\partial z) \qquad [3.6]$$

where the terms on right side of the equation represent loss to absorption, scattering gain from downwelling and scattering loss from upwelling. Together, the scattering and absorption coefficients define κ_λ where $\kappa_\lambda = (a_\lambda{}^2 + 2a_\lambda b)^{0.5}$. As noted by Perovich (1990), if no scattering inhomogeneities are present, equation 3.5 can be reduced and integrated to yield Beer's law. The surface boundary condition is defined by:

$$E_D{}^{(0,\lambda)} = (1 - R_0)E_0 + R_0 E_U{}^{(0,\lambda)} \qquad [3.7]$$

where E_0 is the incident solar irradiance and R_0 is the specular reflection at the surface. At the bottom boundary, all downwelling irradiance is assumed to escape into the ocean (i.e., no specular reflection nor upwelling).

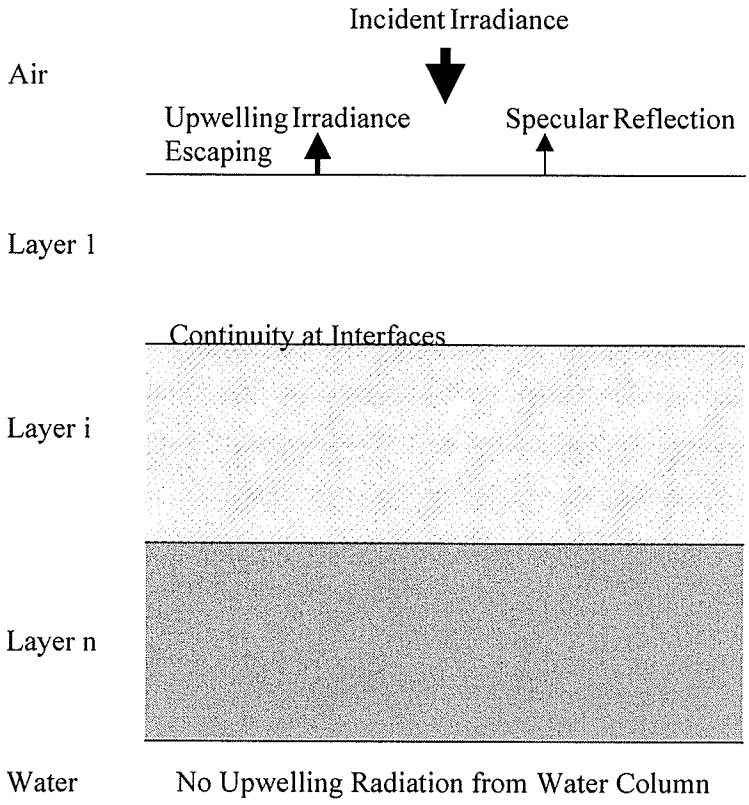

Figure 3.3. Schematic of the two-stream, n-layer model. Adapted from Perovich (1990).

The model assumes wavelength independent scattering coefficients over the PAR range. Using spectral attenuation coefficients for different snow and ice types from the literature, scattering coefficients were determined by matching model output to spectral albedos measured in the field (Perovich, 1990). In this dissertation, three separate layers are used in the model: snow, sea ice and a 5 cm bottom ice algal layer.

For snow, Perovich (1990) provides two different medium types, cold dry snow and melting wet snow. The cold dry snow parameterization was obtained from Grenfell and Maykut (1977), whereas the melting wet snow was approximated by adjusting the scattering coefficient for cold dry snow to match a measured spectral albedo over melting snow (Grenfell and Perovich, 1984), respectively. It is noted that specular reflection can

be accounted for in the model between two media with differing refractive indices (e.g., air and ice). However, due to the granular surface of a snowpack, specular reflection could not be distinguished from scattering and was therefore assumed to be zero at the interface of air and snow (Perovich, 1990). For reasons discussed in Chapters 6 and 7, the snow attenuation parameter was replaced with a spectral diffuse attenuation coefficient obtained using the model of Warren and Wiscombe (1980) and snow grain sizes measured in the field. The model of Warren and Wiscombe (1980) is based on the pure snow Mie theory scattering model presented in Wiscombe and Warren (1980) with the additional capability to account for soot particulates in the snow cover. The model was coded by T.N. Papakyriakou (Papakyriakou, 1999). Soot was added in the model to increase the attenuation coefficient to match field observations in the PAR range. Similarly, the scattering coefficient for snow in the two-stream model, b^{snow}, was obtained from comparisons with PAR transmittance data. The above input data are discussed later within Chapter 6.

For ice, many parameterizations were provided by Perovich (1990), however only the cold blue ice parameterization, which represents first-year columnar ice – approximated from melting blue ice and measurements of albedo over cold blue ice (Grenfell and Perovich, 1984) in the same fashion as the melting wet snow parameterization – was used in this dissertation.

Algal biomass was added to the bottom 5 cm ice layer, where the bulk of ice algae biomass is observed within first-year columnar sea ice in the region studied (Smith et al., 1990). κ_λ for this layer was modified using the following equation:

$$\kappa_\lambda = [(a_\lambda^{ice} + a_\lambda^{chl})^2 + 2(a_\lambda^{ice} + a_\lambda^{chl})\,(b^{ice} + b^{chl})]^{0.5} \qquad [3.8]$$

where the superscripts ice and chl denote sea ice and algae, respectively. For reasons discussed later in Chapter 6, I assume that the spectral dependence of attenuation does not appreciably change with varying snow depth and ice thickness. Therefore, the chl *a* specific absorption coefficient $a_\lambda^{*,chl}$ was estimated from field data by using two under ice irradiance spectra, one for thick snow and low chl *a* concentration, $E_{1,\lambda}$, and one for thin snow and high chl *a* concentration, $E_{2,\lambda}$:

$$a_\lambda^{*,chl} = \frac{\ln\left(\frac{E_{1,\lambda}}{E_{2,\lambda}}\right) - \ln\left(\frac{E_{1,700}}{E_{2,700}}\right)}{B_2 - B_1} \qquad [3.9]$$

where B is the biomass (mg chl *a* m^{-2}) and E_{700} is the irradiance at 700 nm. The absorption coefficient for algae was thus given by:

$$a_\lambda^{chl} = \frac{a_\lambda^{*,chl} B}{h_a} \qquad [3.10]$$

where h_a is the thickness of the algal layer (0.05 m). Furthermore, it is assumed that the presence of algal cells and the porous ice structure in the bottom algae layer did not significantly increase scattering above the value used for the interior ice (i.e., $b^{chl} = 0$ m^{-1} in equation (3.8)).

The actual model used in the dissertation was coded by Jens K. Ehn (Ehn, 2001), based on Perovich (1990). The code provides for selection of the number, type and thickness of layers and provides spectral transmittance at each layer for output. Transmitted irradiance

is calculated by multiplying the surface downwelling spectral irradiance with the spectral transmittance.

Irradiance units in the model are in W m^{-2}, whereas the biological equations employed below use units of μE m^{-2} s^{-1}. Therefore, the following equation is used to convert between units with PAR representing the integration from 400 to 700 nm:

$$E_\lambda{}^W = E_\lambda{}^{\mu E} 10^{-6} \left(\frac{N_A hc}{\lambda} \right) \qquad [3.11]$$

where $E_\lambda{}^W$ and $E_\lambda{}^{\mu E}$ are spectral irradiance in W m^{-2} and μE m^{-2} s^{-1}, respectively, N_A is Avagadro's number, h is Plank's constant, c is the speed of light, λ is wavelength in m and 10^{-6} is a scaling factor to change μE to E.

3.2.3 Ice Algae Growth Model

The ice algae growth model presented here represents a combination of two published models (Arrigo and Sullivan, 1994; Lavoie et al., 2005). The model takes into consideration three limiting and two influencing factors on ice algal growth. The limiting factors include nutrients, light and the ice growth/melt rate whereas the influencing factors include temperature and brine salinity of the sea ice. It is noted that the limiting factor for accretion and ablation of sea ice, first employed by Lavoie et al. (2005), indirectly accounts for issues of habitat availability and stability. To keep consistent with

data collection methods for algal biomass, the ice algal growth model presented here is applied to a single 5 cm layer at the bottom of the sea ice.

Ice algal growth is assumed to be limited by one resource factor at any given time, but affected by both influencing factors making the specific daily algal growth rate (μ) equal to:

$$\mu = \mu_{max} \min(N_{lr}, L_{lr}, IGR_{lr})\, S_f \qquad [3.12]$$

where μ_{max} is the maximum temperature dependent daily growth rate, $\min(N_{lr}, L_{lr}, IGR_{lr})$ is an expression which uses the coefficient value of the most limiting resource, and S_f is the salinity dependent growth coefficient. It is again noted that all variables and their units are provided in Table 3.3.

Abiding by the model of Arrigo and Sullivan (1994), the temperature dependent growth rate for algae follows the description by Eppley (1972):

$$\mu_{max} = \mu_0 \exp(r_\mu T_{2.5}) \qquad [3.13]$$

where μ_0 is the specific growth rate at 0 °C, r_μ is a rate constant that determines the sensitivity of μ_{max} to changes in temperature and $T_{2.5}$ is the temperature of the sea ice at 2.5 cm from the bottom (i.e., middle of the algal layer). Based on the growth of various phytoplankton species acclimated to temperatures >2 °C, Eppley (1972) determined μ_0 and r_μ to be 0.8511 d^{-1} and 0.0633 $°C^{-1}$, respectively.

The nutrient limitation coefficient (N_{lr}) is calculated using Michaelis-Menton kinetics:

$$N_{lr} = \frac{N_{chl}}{K_S + N_{chl}} \qquad [3.14]$$

where N_{chl} is the concentration of the limiting nutrient in the algal layer and K_S is the half-saturation constant for uptake of the limiting nutrient. In the case of nutrient limitation, I followed the model of Lavoie et al. (2005) who assumed silicic acid was the sole limiting nutrient due to the findings of previous studies and the fact that dissolution of biogenic silica is too slow for sufficient recycling of nutrients in the ice algal layer compared to the more effective regeneration of nitrogen and phosphorus. Therefore, K_S represents the half-saturation constant for $Si(OH)_4$ uptake and has the value of 3.9 mmol m^{-3} taken from an average for a variety of diatom species (Sarthou et al., 2005).

Algal physiological factors and growth rates measured for ice algae growing under landfast ice in the Arctic have shown nutrient limitation to occur during low tidal ranges associated with the fortnightly tidal cycle (Cota et al., 1987; Gosselin et al., 1985). These findings support that the main supply of nutrients to the ice algae in this environment is from the mixed layer. Therefore, the governing factors for nutrient re-supply to the ice algal layer in the model are assumed to be controlled by turbulent mixing processes between the lower and upper mixed layer and across the molecular sublayer at the ice-water interface. Following Lavoie et al. (2005), the flux of nutrients to the surface of the mixed layer (F_N) is equal to:

$$F_N = K\frac{\partial N}{\partial z} \qquad [3.15]$$

where K is the tidal varying mean eddy diffusion coefficient and ($\partial N/\partial z$) is the vertical nutrient concentration gradient between the molecular sublayer at the ice-water interface and the concentration at 2.5 m. Over a single time step, F_N is added to the previous time

step nutrient concentration at the bottom of the molecular sublayer. The flux of nutrients through the sublayer and into the algal layer (F_{Nchl}) is equal to:

$$F_{Nchl} = D\frac{\partial N_{chl}}{h_v} \qquad [3.16]$$

where D is the molecular diffusion coefficient for silicic acid (1×10^{-9} m^2 s^{-1}; Lavoie et al., 2005), ($\partial N_{chl}/h_v$) is the nutrient gradient across the molecular sublayer and h_v is the tidal varying molecular sublayer thickness. h_v is estimated by:

$$h_v = \frac{k_v}{u_\tau} \qquad [3.17]$$

where k_v is the kinematic viscosity of seawater (1.85×10^{-6} m^2 s^{-1}) and u_τ is the tidal varying friction velocity (m s^{-1}). The timing of the fortnightly tidal cycle was obtained by fitting a sine curve to the maximum daily tidal height from tidal predictions made for Resolute Bay, NU, by the Canadian Hydrographic Service. The sine curve was used to scale the neap and spring tide averages for K and u_τ as given by Lavoie et al. (2005). Figure 3.4 shows a plot of the tidal varying values for K and h_v used in the ice algae model over the duration of the C-ICE'02 field program.

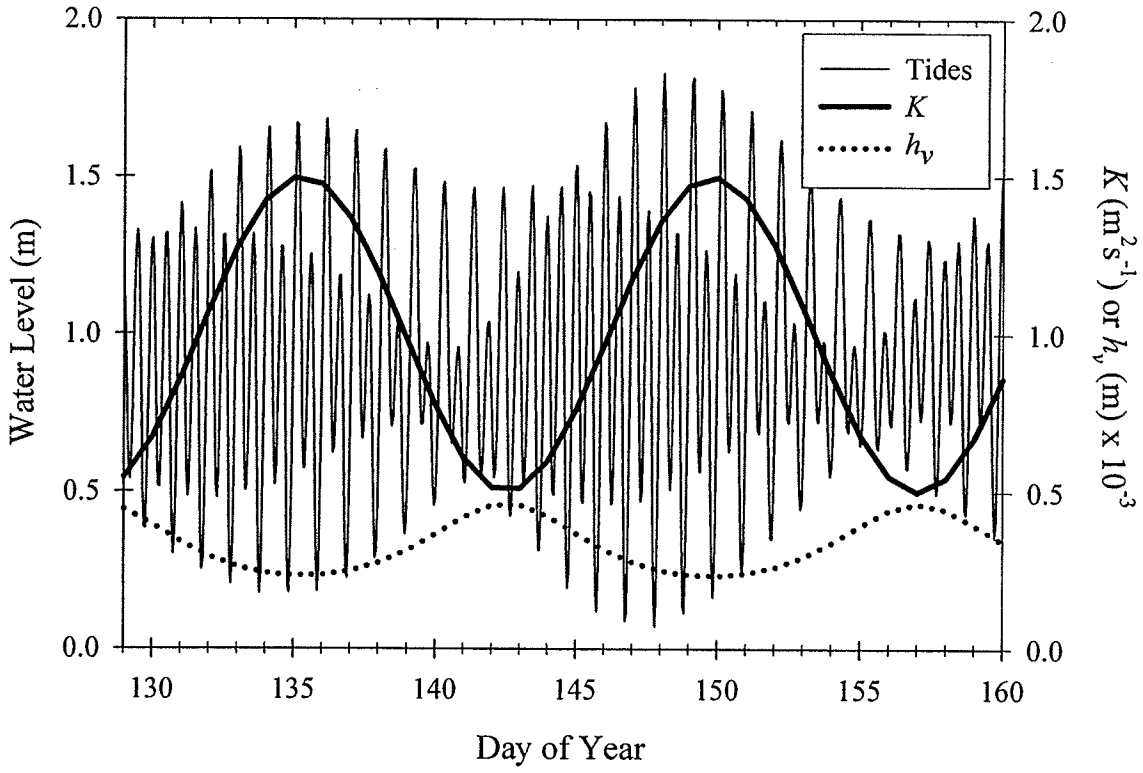

Figure 3.4. Tidal predictions for Resolute Bay, NU, during C-ICE'02 and the calculated eddy diffusion coefficient (K) and molecular sublayer thickness (h_v) used in the ice algae model. Data were plotted in a similar fashion as Lavoie et al. (2005).

The biological uptake of silicic acid in the algal layer (N_{up}) is calculated as a function of B and μ:

$$N_{up} = \mu B \frac{W_{Si} / W_{Chla}}{Si} \qquad [3.18]$$

where Si is the molar mass of silicon (28.09 mg mmol^{-1}), (W_{Si}/W_{Chla}) is the ratio of the amount of $Si(OH)_4$ required to produce 1 mg of chl a, given as 17 mg $Si(OH)_4$ mg chl a^{-1} by Lavoie et al. (2005) based on measurements from a study site located in Resolute

Passage during 2002. At the end of a daily run, the change in silicic acid in the algal layer is calculated as:

$$\frac{\partial N_{chl}}{\partial t} = \frac{F_{Nchl} - N_{up}}{h_a} \qquad [3.19]$$

Light limitation in the model is calculated following the Photosynthesis-Irradiance (PI) model by Platt et al. (1980) while neglecting photoinhibition as in Arrigo and Sullivan (1994):

$$L_{lr} = 1 - \exp\left(\frac{PAR_{chl}}{I_k}\right) \qquad [3.20]$$

where PAR_{chl} is the irradiance integrated across PAR wavelengths reaching the top of the algal layer and I_k is the photoacclimation parameter. I_k is dependent on the short-term history of light levels experienced by the ice algae and is derived by dividing the maximum chl *a* specific photosynthetic rate by the chl *a* specific photosynthetic efficiency. Values of I_k taken from spring ice algal studies near Resolute Bay, NU (Smith et al., 1988; Cota and Horne, 1989), show an exponential relationship with snow depth ($R^2 = 0.85$) of the form:

$$I_k = A_1 \exp(-A_2 h_{snow}) + A_3 \qquad [3.21]$$

where the regression coefficients, A_1, A_2 and A_3 are 15.88, 36.63 and 3.999, respectively, and h_{snow} is snow depth in meters. Similar to Arrigo and Sullivan (1994), I chose an exponential relationship to reach an asymptotic value of I_k at higher snow depths which

in essence represents lower irradiance levels. Unlike Arrigo and Sullivan (1994), an asymptotic value was not met at low snow depths (i.e., high irradiance levels), which may be a factor of thicker ice in the northern Canadian Arctic relative to the Antarctic and more southerly Arctic. In a similar fashion as Arrigo and Sullivan (1994), I_k is calculated from a three day snow depth average.

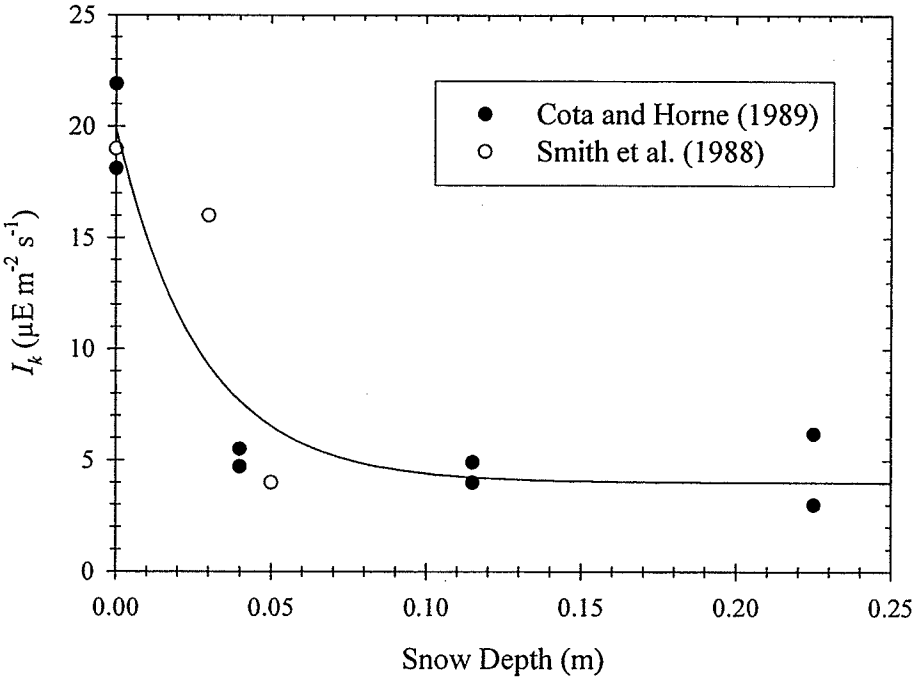

Figure 3.5. Ice bottom algae photoadaptation parameters (I_k) over varying snow depths (h_{snow}) from two separate spring time studies near Resolute Bay, NU. The exponential equation plotted is $I_k = 15.88 \exp(-36.63\ h_{snow}) + 3.999$.

According to Lavoie et al. (2005), IGR_{lr} is a function of the rate of ice accretion and ablation with an absolute change in ice thickness when ($\partial H/\partial t$) threshold of 0.0085 m d^{-1}, above which the ice growth rate limitation coefficient is zero, i.e.,

$$IGR_{lr} = \begin{cases} 0 & \text{when} \quad \left|\frac{\partial H}{\partial t}\right| \geq 0.0085 \text{ m d}^{-1} \\ 1 - \frac{\left|\frac{\partial H}{\partial t}\right|}{0.0085} & \text{when} \quad 0 < \left|\frac{\partial H}{\partial t}\right| < 0.0085 \text{ m d}^{-1} \end{cases} \qquad [3.22]$$

This was the case for matching their model to field data where ice melt occurred over most of the study period (Lavoie et al., 2005). Although high ice growth rates have been found to limit the availability of habitat space and density dependent stability (Legendre et al., 1991; Krembs et al., 2001), slower ice growth rates should not affect ice algal growth. Reeburgh (1984) suggests that gravity drainage associated with ice growth may assist in convection of nutrients into the skeletal layer and therefore could benefit ice algal growth. Further, some authors have suggested ice algae to move with the growing ice bottom (e.g., Welch and Bergmann, 1989; Arrigo et al., 1993). Therefore, only ice melt is assumed to affect the ice algae growth rate at absolute changes in ice thickness of less than 0.0085 m d^{-1} in the model causing a slight adjustment to equation 3.22, i.e.,

$$IGR_{lr} = \begin{cases} 0 & \text{when} \quad \left|\frac{\partial H}{\partial t}\right| \geq 0.0085 \text{ m d}^{-1} \\ 1 - \frac{\left|\frac{\partial H}{\partial t}\right|}{0.0085} & \text{when} \quad -0.0085 < \frac{\partial H}{\partial t} < 0 \text{ m d}^{-1} \\ 1 & \text{when} \quad 0 \leq \frac{\partial H}{\partial t} < 0.0085 \text{ m d}^{-1} \end{cases} \qquad [3.23]$$

The influence of brine salinity on ice algal growth was first presented by Arrigo and Sullivan (1992; see Fig. 2.2). The salinity dependent growth coefficient (S_f) used in this model is calculated following the equation presented in Arrigo (2003):

$$S_f = \alpha_0 + \alpha_1 S_b + \alpha_2 S_b^2 + \alpha_3 S_b^3 \quad [3.24]$$

where S_b is the brine salinity in the middle of the algal layer, $\alpha_0 = -0.12073$, $\alpha_1 = 0.07097$, $\alpha_2 = -1.33 \times 10^{-3}$ and $\alpha_3 = 6.342 \times 10^{-6}$. S_b is calculated as a direct function of ice temperature as presented in Assur (1958):

$$S_b = \beta_0 + \beta_1 T_{2.5} + \beta_2 T_{2.5}^2 + \beta_3 T_{2.5}^3 \quad [3.25]$$

where S_b is the brine salinity in the middle of the algal layer, $\beta_0 = -3.9921$, $\beta_1 = -22.7$, $\beta_2 = -1.0015$ and $\beta_3 = -0.019956$.

The change in algal biomass overtime is a balance of ice algal growth and loss, of which the loss term has not yet been considered. Loss of algae in the model is a function of algal respiration, grazing and ice melt. The loss of potential algal growth due to algal respiration (L_{RES}) is a function of temperature and is calculated the same as temperature dependent growth (equation 3.13) by replacing the specific growth rate (μ_0) with a specific respiration rate (RES_0) at 0 °C which is equal to 0.05 (Arrigo and Sullivan, 1994). Not much is know of grazing rates on ice algae, so following both Arrigo and Sullivan (1994) and Lavoie et al. (2005), the loss of algae due to grazing (L_{GRA}) is assumed a constant fraction of 0.10 of the net algal growth rate ($\mu - L_{RES}$). Finally, the loss of algae due to ice ablation (L_{IGR}) represents a sloughing of algal biomass and therefore is given as a fraction of the total ice algal layer thickness that is melted over the time step, i.e.,

$$L_{IGR} = \begin{cases} 0 & \text{when} \quad \dfrac{\partial H}{\partial t} \geq 0 \text{ m d}^{-1} \\ \dfrac{\left|\dfrac{\partial H}{\partial t}\right|}{h_a} & \text{when} \quad \dfrac{\partial H}{\partial t} < 0 \text{ m d}^{-1} \end{cases} \qquad [3.26]$$

The total change in algal biomass overtime ($\partial B/\partial t$) is therefore equal to:

$$\frac{\partial B}{\partial t} = B\left(\mu - L_{RES} - L_{GRA} - L_{IGR}\right) \qquad [3.27]$$

3.4 Summary

In this chapter, I have described the methods of data collection and the dataset used in my dissertation. The dataset includes both physical and biological measurements made during spring over two separate field programs, C-ICE'02 and Carcajou'03. The data are distinguished as either time series measurements (single location) or point samples collected periodically within a localized area over time. I have also described the models which are ultimately used in Chapter 7 for a sensitivity analysis examining factors affecting ice algal growth. It is noted that statistical and analytical methods and alterations made to the models and their parameterizations are presented with the presentation of data in the succeeding chapters. In the next chapter, I examine the variability of key thermal, physical and optical properties of the snow and ice which are pertinent to algal accumulation and loss at the ice bottom using the dataset collected during C-ICE'02.

CHAPTER 4: Variability of snow and ice thermal, physical and optical properties pertinent to sea ice algae biomass during spring

4.1 Introduction

Variability in the thermal, physical and optical characteristics of snow-covered sea ice has a substantial influence on physical-biological coupling at the base of the ice. Previous studies and reviews examining spatial and temporal variability of snow-covered sea ice have typically focused on sea ice (e.g., Tucker et al., 1984; Eicken et al., 1991; Perovich et al., 1998; Eicken, 2003). However, physical, thermal and subsequent radiative properties are an order of magnitude more important for snow than ice (e.g., Oke, 1987; Perovich, 1990; Papakyriakou, 1999).

Low irradiance has often been found to limit ice algal growth in spring. This has been documented from physiological studies (e.g., Michel et al., 1988; Smith et al., 1988; Cota and Horne, 1989) or through inverse relationships between ice algae and snow depth (Gosselin et al., 1986; Welch and Bergmann, 1989) as snow controls light transmission through the snow-ice matrix (e.g., Perovich, 1990). The optical properties of snow largely depend on its geophysical properties, including density, salinity and snow grain size (Warren, 1982). Furthermore, studies on snow geophysical properties over sea ice have demonstrated substantial variability in these properties over scales ranging from millimeters to hundreds of meters (e.g., Garrity, 1992; Barber et al., 1995; Papakyriakou, 1999; Sturm et al., 2002).

Due to the control snow has on light transmission through the snow-ice matrix, the spatial distribution and wind re-distribution of a snow cover has been linked to patchiness of ice algae (Gosselin et al., 1986). Horizontal distribution of snow is controlled by snowfall and aeolian mechanisms and is affected both by storm events (e.g., Sturm et al. 2002) and by the type of catchment. Work by Iacozza and Barber (1999) shows that a statistical model can be used to simulate the distribution of snow relative to the type of sea ice catchment (i.e., rubble, flat first-year, multiyear). These models provide a predictive measure of the spatial distribution over a range of scales from the meter to hundreds of meters. Other blowing snow models have been developed for medium (100 m to 1 km) to large-scale (1 km to 100 km) applications of snow transport and accumulation (e.g., Pomeroy et al., 1993; Liston and Sturm, 1998). Modeling efforts at small spatial scales (e.g., 1 m) remain in their infancy (Déry and Tremblay, 2004).

Later in spring, observed relationships between bottom ice salinity and chlorophyll drive speculation that algal variability may also be governed by the thermal properties of the snow-ice cover (Gosselin et al., 1986). The thermal evolution of the snow-sea ice matrix both affects and is affected by its physical and optical properties. Spatial variations in the heat flux through the snow-sea ice system are controlled by the distribution and history of the snow cover (Sturm et al., 2001).

The history and distribution of the snow cover and its thermal, physical and optical state are therefore important variables in the highly coupled sea ice biophysical system. Thus it was hypothesized in Chapter 1 that the history and distribution of snow over sea ice control the magnitude of ice algae biomass through both thermophysical and radiative processes. In this chapter, I document and summarize key processes operating in this

system using a case study. More specifically, a focus on the spring transition period is made to: (1) document variability of thermal, physical and optical properties of snow-covered landfast first-year sea ice pertinent to sea ice algae biomass in spring and (2) examine how these physically-based variables affect ice algae biomass. I note that the results in this chapter have been published in the peer-reviewed literature (Mundy et al., 2005).

4.2 Results and Discussion

4.2.1 Physical Variability

The dataset used in this chapter comes from the C-ICE'02 field program (see section 3.2). This field program occurred during the spring transition from a cold dry snowpack through to the beginning of early melt; a period where snow begins melt metamorphism and liquid water appears in the snowpack (Livingstone et al., 1987). Top of the atmosphere solar flux (SW_{TOA}) and photosynthetically active radiation (PAR_{TOA}; daily averages calculated for latitude) increased from 386 to 501 W m^{-2} and 695 to 903 μE m^{-2} s^{-1}, respectively, over the study period. The fraction of SW_{TOA} and PAR_{TOA} reaching the snow surface for mostly clear skies was approximately 80% and 90%, respectively. Only 25 % of PAR (0.4-0.7 μm) compared to 35 % of integrated shortwave radiation (0.3-3 μm) was blocked by cloud cover due to the spectral selection effect of clouds. Shortwave albedo averaged 85% and did not show any seasonal change during our study (Fig. 4.1). Albedo did show some variability, however it was impossible with the current dataset to separate effects of a new snowfall, snow metamorphism, or clouds on albedo.

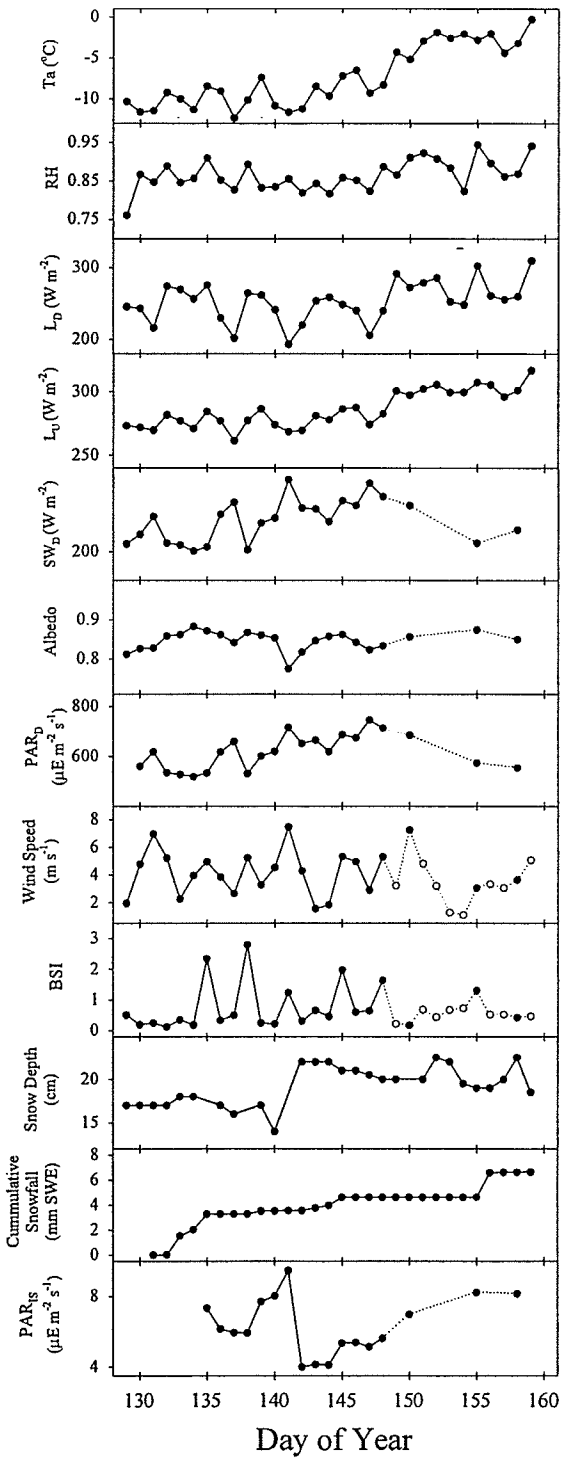

Figure 4.1. Daily averaged time series of selected meteorological variables monitored at the C-ICE'02 on-ice micrometeorological station. Dashed lines and open circles represent sporadic time series. Snow depth measurements came from site C. See Table 3.1 for abbreviations.

Due to the high albedo, most of the shortwave energy was reflected from the surface leaving conductive fluxes associated with increases in air temperature to dominate warming of the snow and sea ice cover (Papakyriakou, 1999).

Air temperature increased nonlinearly during the study period from –12 °C to 0 °C (Fig. 4.1). The strongest increase occurred after day 142 concurrent with increases in longwave energy and relative humidity. Prior to day 142, air temperature did demonstrate large fluctuations between daily averages of –12 °C to –7 °C over a couple days with even greater diurnal fluctuations.

Snow and ice temperature profiles on day 128 demonstrated a typical winter state with a steep negative gradient in the snowpack and moderate gradient within the ice (Fig. 4.2a). The snowpack surpassed a daily average temperature of –8.2 °C after day 132. This temperature has been noted as a critical temperature, above which the volume of precipitated salts relative to brine volume is negligible (Weeks and Ackley, 1982) and where brine volume begins to increase exponentially with increasing temperature at the snow-ice interface (Barber and Nghiem, 1999). However, diurnal fluctuations in snowpack temperature reached above –8.2 °C from the beginning of our study period (results not shown). As the season progressed, snow surface temperatures warmed more rapidly than lower in the snow and ice matrix, causing an inversion in the snowpack temperature gradient (Fig. 4.2a).

Unlike the strong rise in air temperature after day 142 (Fig. 4.1), the seasonal increase in temperature of the snow and sea ice became more linear with depth (Fig. 4.2b). This was an inverse function of the snow and sea ice thermal diffusivities (Oke, 1987; Papakyriakou, 1999). The low thermal diffusivity of snow and sea ice causes any

temperature fluctuations to rapidly loose amplitude as they are propagated through the medium, particularly at the highly saline basal snow layer (Papakyriakou, 1999). By a depth of 100 cm into the sea ice (extent of the measurements), the temperature increase was nearly linear with time (Fig. 4.2b) and theoretically would be more linear at greater ice thickness. A deeper snow cover would further slow this process, thermally insulating the sea ice from the atmosphere.

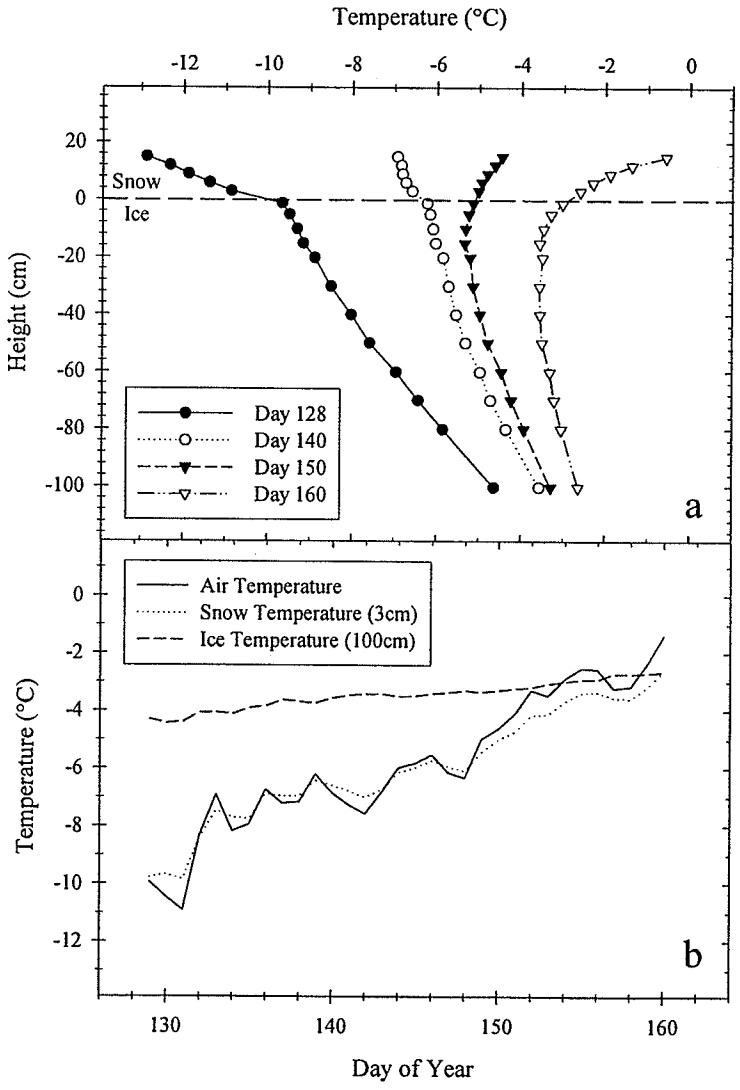

Figure 4.2. Vertical profiles of selected daily averaged snow and ice temperatures (a) and time series of daily averaged air temperature, snow temperature at 3 cm height and ice temperature at 100 cm depth (b).

Snowpacks over sea ice have been found to conform to 2 to 3 statistically distinct layers based on density (Papakyriakou, 1999) or snow grain morphology (Barber et al., 1995). Therefore, to simplify interpretation of the snow physical properties, results are presented over three vertically grouped layers: the upper 30% (surface), the middle 60% (middle) and the lower 10% (bottom) of the snowpack. Snow density, salinity and grain size averaged over the entire time period demonstrated typical vertical profiles for spring season snow (Fig. 4.3 and Table 4.1). The surface and middle layers of the snowpack were wind packed with high densities (342-372 kg m^{-2}) compared to significantly lower densities (203 kg m^{-2}) within the bottom layer ($p < 0.001$ for both cases using Tamhane's T2 Post Hoc Test; Table 4.1). Salinities were near zero in the surface and middle layers of the snowpack and increased to an averaged 7.6 within the bottom layer. Snow grain size, represented by average area, increased from 0.66 mm^2 in the surface layer to 1.22 mm^2 in the middle layer and 15.96 mm^2, at the bottom of the snowpack.

Geophysical properties of the snowpack are inherently variable due to the multitude of processes causing change in the snowpack. During our study, snowpack density did not show any significant seasonal trends, corresponding to observations by Barber et al. (1995; Fig. 4.3a). Surface density rapidly decreased from average densities to minima of 148-284 kg m^{-3} following new snow depositions on days 132, 143, 155 and 159 (Fig. 4.3a). In all cases, wind redistribution of snow acted to increase densities back to averages within a day or two, a phenomenon that has been previously observed (Barber et al., 1995). This densification of snow has important consequences on both the thermophysical properties of the snowpack and on its formation of a fairly uniform

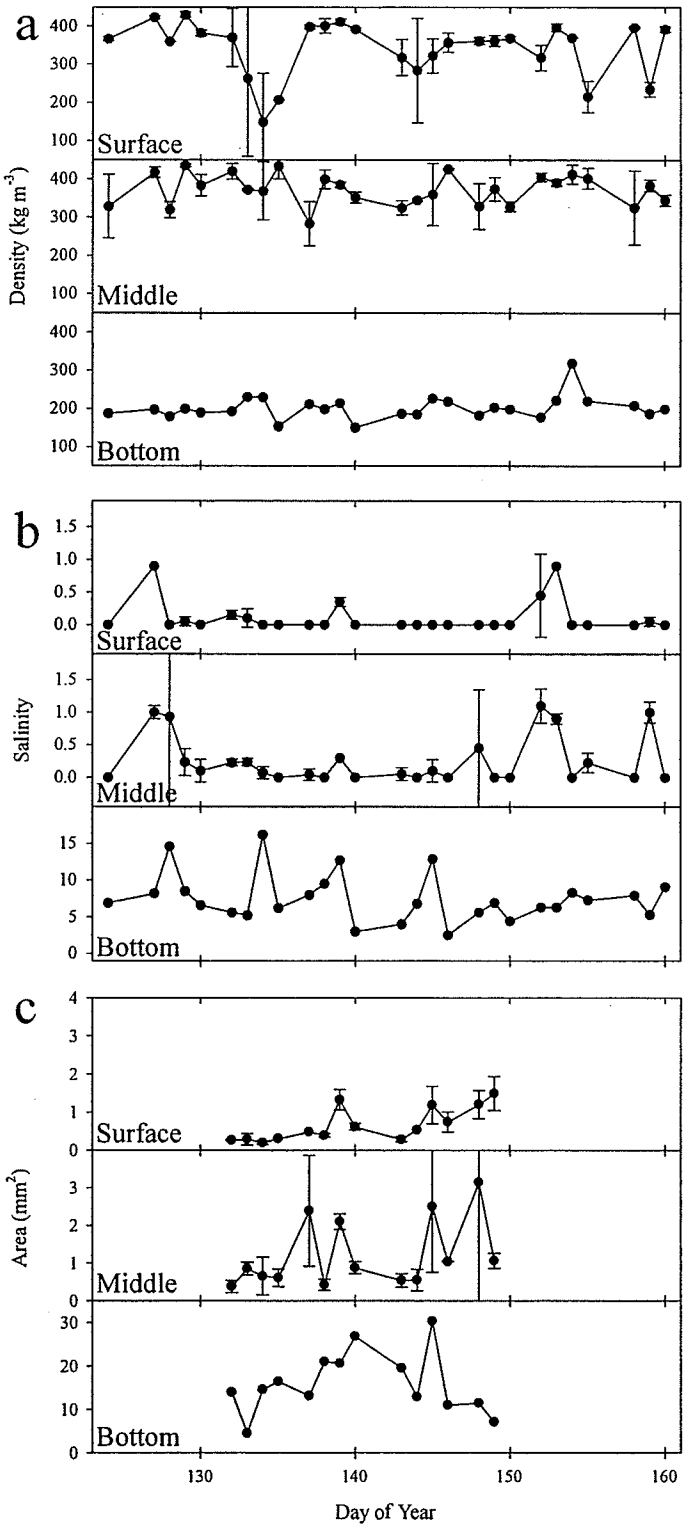

Figure 4.3. Average (± standard deviation error bars) snowpack layer density (a), salinity (b) and grain size (c) over the study period. Note the salinity and grain size axis scales for the surface and middle layers are different from the bottom layers.

surface, impeding an observer's ability to differentiate between new and old snowpacks without careful examination.

Table 4.1. Study period averages (± standard deviation) of snow density, salinity and grain size for the surface, middle and bottom snowpack layers.

	Density ($kg\ m^{-3}$)	Salinity	Grain Size (mm^2)
Surface	342.4 (72.6)	0.11 (0.25)	0.66 (0.45)
Middle	372.1 (40.5)	0.26 (0.37)	1.22 (0.91)
Bottom	202.8 (30.8)	7.59 (3.30)	15.96 (7.14)

Snowpack salinity showed an almost regular pattern of variability, which was attributed to spatially stratified sampling (Fig. 4.3b). Toward the end of the study period, salinity of the bottom layer demonstrated a decrease in variability. High salinities in the bottom layer depress the melting point of snow, thus allowing earlier snowmelt relative to higher layers in the snowpack. The increased meltwater will leach soluble salts and settle laterally along the bottom layer causing the observed decrease in salinity variability.

Peaks in salinity at the bottom, middle and, to a lesser extent, top layers tended to coincide, particularly prior to day 150 (Fig. 4.3b). These peaks are attributed to differences in the snowpack age. During fall/winter freeze-up, brine is expelled both below and onto the surface of the forming ice cover (Weeks and Ackley, 1982). The formation of frost flowers and the deposition of new snow can quickly draw surface brine into the snow due to capillary suction (Drinkwater and Crocker, 1988). Wind redistribution of frost flowers and saline snow could also mix brine deeper into the snow cover through deposition onto forming drifts. Barber et al. (1995) also found salinity to move up through a stable snowpack with time. These mechanisms would result in greater

salinities within older and more stable drifts. Therefore, the salinity peaks in this study most likely represent older snow covers. Corresponding peaks in snow grain size on days 139, 145 and 148, particularly in the middle snowpack layer, support this conclusion (Fig. 4.3c).

Transmission of light through the snowpack is dependent on both absorption and scattering, which are incorporated into the attenuation coefficient (e.g., κ_{PAR}). In a snowpack, scattering is inversely related to snow grain size. Seasonally, snow grain size in the surface layer showed a significant log-linear increase in grain size (Fig. 4.3c; $p < 0.01$; $R^2 = 0.60$). Although not significant due to higher variability compared with the surface layer, an increase in middle layer grain size was observed. Therefore, as the snowpack experienced the initial stages of warming, the most prominent response was a growth of grain size, similar to observations made by Barber et al. (1995).

In the bottom layer, the increase in snow grain size was more pronounced, but decreased towards the end of the period (Fig. 4.3c). The high brine content in the hoar layer would have resulted in elevated water content relative to the other snow layers causing an increase in liquid contacts between grains that act to increase mass flow from smaller to larger particles (Colbeck, 1982). Therefore, the strong increase in hoar grain size was attributed to elevated water in vapor phase in the bottom layer. I speculate that the decrease in grain size following day 140 was due to equilibrium growth, changing highly faceted kinetic growth grains into more rounded equilibrium shape forms (Colbeck, 1982) in the presence of water in liquid phase. Therefore, although the measured surface area would decrease, the volume could stay stable or even increase.

However, more detailed data on the volume and shape of the snow grains would be required to support this speculation.

The increase in snow grain size at all levels in the snowpack resulted in an increase in PAR transmission over time. The PAR bulk attenuation coefficient (κ_{PAR}) derived at mid snowpack ranged between 7.6 and 21.8 m^{-1} over the sample period (Fig. 4.4). Standard errors from the slope estimates of κ_{PAR} are used to show precision of each individual value on Figure 4.4. κ_{PAR} demonstrated a significant decreasing rate of –0.23 m^{-1} d^{-1} (R^2 = 0.34; $p < 0.01$).

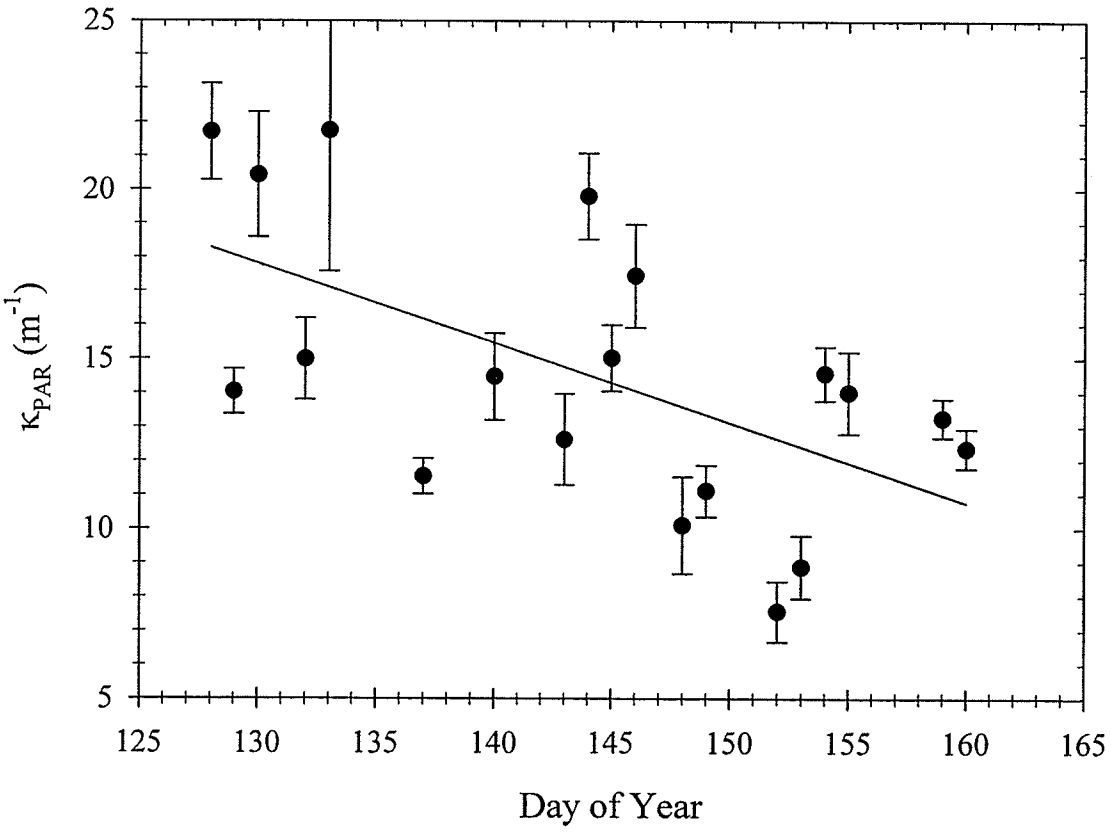

Figure 4.4. Ordinary least squares regression of the PAR bulk attenuation coefficient (κ_{PAR}) against day of year (YD; $\kappa_{PAR} = -0.235$ YD + 48.35). Standard error bars from the slope estimates for κ_{PAR} are plotted.

Generally, absorption properties of a snowpack are important to the spectral distribution of transmitted radiation, whereas scattering dominates attenuation of light with depth (Warren, 1982). Noted in Chapter 2, scattering is dependent on the radius and number density of inclusions within a host medium where in snow the host medium is air and the inclusions are snow grains, snow clusters and particulates. Therefore, as the snowpack warmed, snow grain size increased, causing a decrease in the PAR attenuation coefficient (Fig. 4.4).

Light transmission was also affected by changes in snow depth, both spatially and temporally. Average snow depth measured at the variogram site on day 131 was 12.7 cm (±7.8 SD) with a range of 2 to 45 cm. These values corresponded with those at the daily sampling site, which averaged 17.0 cm (±10.1 SD) and ranged from 1.7 to 42.4 cm. Snow distribution exhibited geometric anisotropy with the long axis of anisotropy oriented at a 30° direction with drift sizes encompassing major and minor distances of 31.2 m by 10.6 m as determined by the anisotropic ellipse ranges (Fig. 4.5a). This average drift size compared closely with other studies that average approximately 20 m (e.g., Gosselin et al., 1986; Iacozza and Barber, 1999; Sturm et al., 2002). Aeolian processes result in particles eroded from the windward side of a drift and deposited on the leeward side forming long gradual and short steep slopes, respectively. This formation was apparent in the interpolated image with long gradual slopes facing N-NE, corresponding to the predominant strong wind direction (Fig. 4.5a, b).

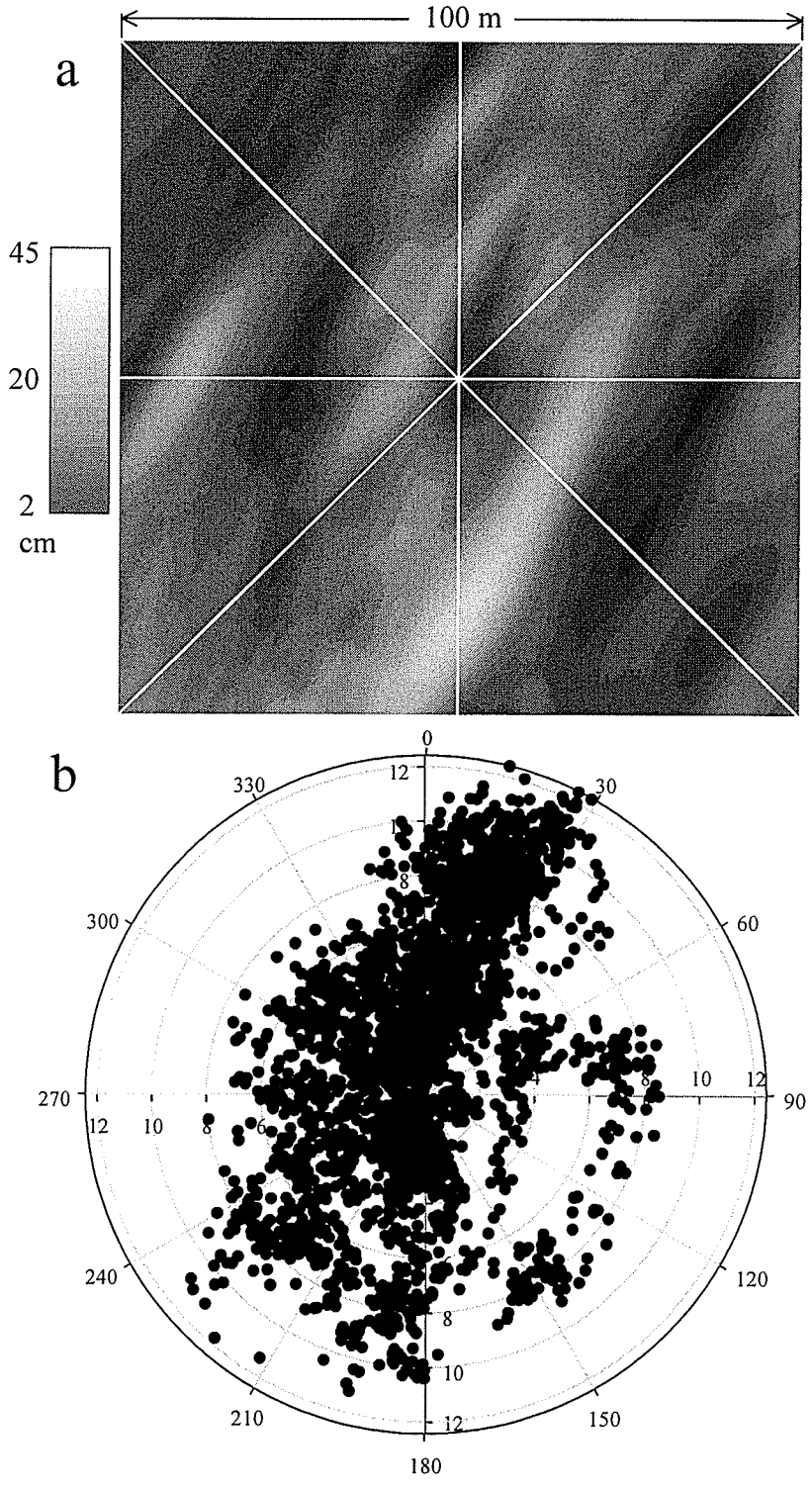

Figure 4.5. Interpolated snow depth over a 100 m x 100 m grid (a) and 15 minute averages of wind speed (radii; $m \cdot s^{-1}$) and direction (radials; °) monitored at the on-ice meteorological station over the entire study period (b).

Applying Beer's law to the decreasing rate of κ_{PAR} (Fig. 4.4), making note that PAR attenuation estimated in this study only applies to the homogeneous middle layer of the snowpack, the daily percent change of PAR transmission (∂PAR_T) under a variable snow cover can be quantified by:

$$\partial PAR_T = 100[\exp(0.23\ h_{snow}) - 1] \qquad [4.1]$$

where h_{snow} is snow depth in meters. Therefore, the percent change in PAR transmission will be greatest under a thicker snow cover; however, the change in magnitude of PAR transmission is a function of both κ_{PAR} and snow depth (see equation 3.2; Fig. 4.6). Figure 4.6 shows the effect of a $-0.23\ m^{-1}\ d^{-1}$ change in κ_{PAR} on the daily increase of transmitted PAR over the range of snow depths and PAR attenuation coefficients observed in this study. Under very thin snow covers, little light is attenuated over the natural range of observed κ_{PAR} and therefore, only a small increase occurs. Under a thick snow cover, the increase in transmitted light is relative to the strong attenuation. That is, little light is transmitted and therefore only a small change in transmitted PAR is observed. At mid snow depths, the increase is much more pronounced over the attenuation coefficients observed in this study. This relationship could be important to the biophysical system operating at the bottom of the sea ice, however further investigation is required.

Abrupt changes in transmitted PAR (PAR_{IS}) temporally corresponded to changes in snow depth, particularly between days 141 and 142 (Fig. 4.1). Time series of snow depth showed substantial variability over a very localized area (Fig. 4.7). During the study period, snow depth at sites A, B and C (see section 3.2.2) showed similar ranges of

variation of 7.4, 6.5 and 8.5 cm, respectively, with changes of 30 to 38% over a time span of a couple days. In accordance with aeolian processes, snow depths in close proximity (sites B and C) followed similar trends of erosion after day 142 (Fig. 4.7). Whereas, only 5 m away at Site A, snow tended to accumulate over the time series.

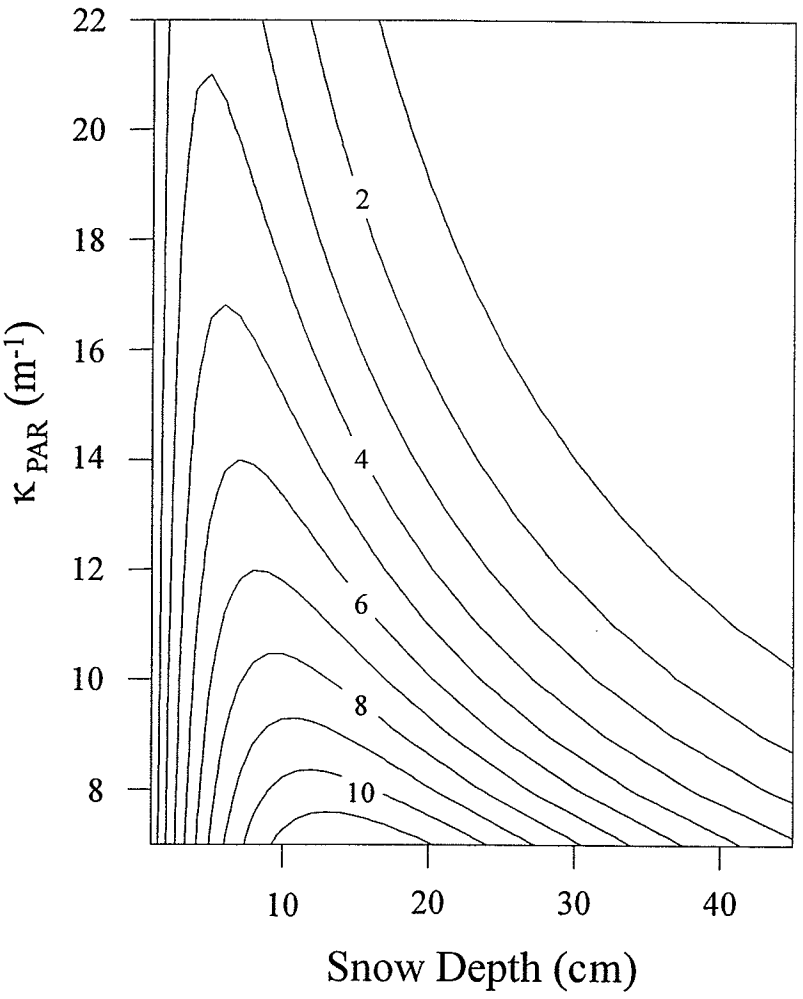

Figure 4.6. Theoretical effects of snow depth and the PAR bulk attenuation coefficient (κ_{PAR}) on the daily transmission increase (isolines) for a surface irradiance (PAR_0) of 1000 $\mu E\ m^{-2}\ s^{-1}$ and κ_{PAR} decreasing rate of $-0.23\ m^{-1}\ d^{-1}$.

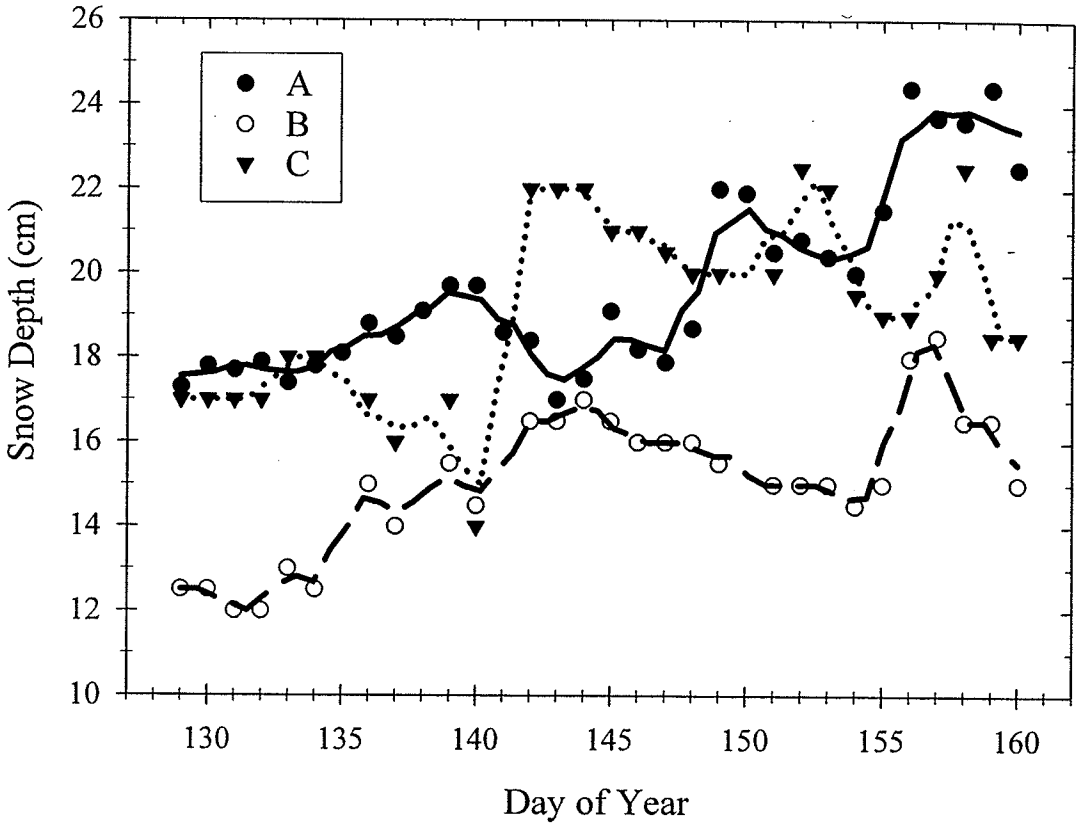

Figure 4.7. Time series of snow depth monitored at sites A (solid line), B (dashed line) and C (dotted line). The trend lines were constructed using inverse distance weighted interpolation.

Aeolian processes behind snowdrift formation are complicated by sublimation and inter-particle cohesion forces (e.g., sintering; Schmidt, 1986). Small-scale surface variations in snowpack physical properties and boundary layer flow result in spatial intermittency of snow redistribution events (Pomeroy and Li, 2000; Sturm et al., 2002). In this study, large changes in snow depth tended to correspond to peaks in the blowing snow index (BSI; e.g., days 135, 141, 148 and 155) and to a lesser extent, snowfall (day 155; Fig. 4.1). However, snow depth changes were not synchronous at all sites due to migration of snowdrifts across the study area. Further, BSI showed peaks coinciding with

strong wind events, however, not all wind events corresponded to BSI peaks (Fig. 4.1). Therefore, strong wind events were not necessarily associated with snow redistribution and similarly snow redistribution did not result in all snow depth changes, demonstrating the intermittency of this process.

The spatially variable nature of blowing snow can therefore result in a spatially heterogeneous snow surface in terms of age. This statement is supported by the large variation observed in κ_{PAR} (root mean square error of 3.4 m^{-1} around the time series trend) and the geophysical properties of snow, all of which depend on the small-scale temporal variability of the overlying snow cover. Further, the residuals around the temporal trend in κ_{PAR} showed a bimodal distribution, indicating there may have been two distinct snowpacks over the sampling sites. I suggest that these snowpacks resulted from two distinct depositional events at very different points in time. The older snowpack would have the lower κ_{PAR} due simply to aging and resultant metamorphic changes. This was supported through the occurrence of coincident snowpack salinity and grain size peaks. Furthermore, 4 of 5 salinity peaks reaching beyond 0.4 in the middle snowpack layer corresponded to the lower PAR attenuation values. Interestingly, although it appeared that the snowpacks were distinct in terms of age or at least their attenuation properties, their melt rates associated with increasing temperatures were similar.

Therefore, when examining point locations of sea ice, the history of the overlying snow cover should be considered. This is particularly relevant when considering not only thermophysical processes, but also biological processes at the bottom of the ice.

4.2.2 Biophysical Processes

When plotting all data points together, bottom ice chl *a* concentrations varied considerably over all snow depths during C-ICE'02 (Fig. 4.8). However, when chl *a* groups were separated based on snow thickness, interesting patterns emerged. Three groups of snow thickness were used: low (< 6 cm), mid (6 – 20 cm) and high (> 20 cm) snow depths. Chl *a* concentrations in the low and high snow classes were skewed (Shapiro-Wilk's W test, $p < 0.05$), while in the mid class, chl *a* concentrations followed a near normal distribution (Shapiro-Wilk's W test, $p = 0.55$). Due to the non-normal distributions of datasets from the low and high snow classes, a square root transformation of both datasets was performed prior to the correlation analysis (Table 4.2).

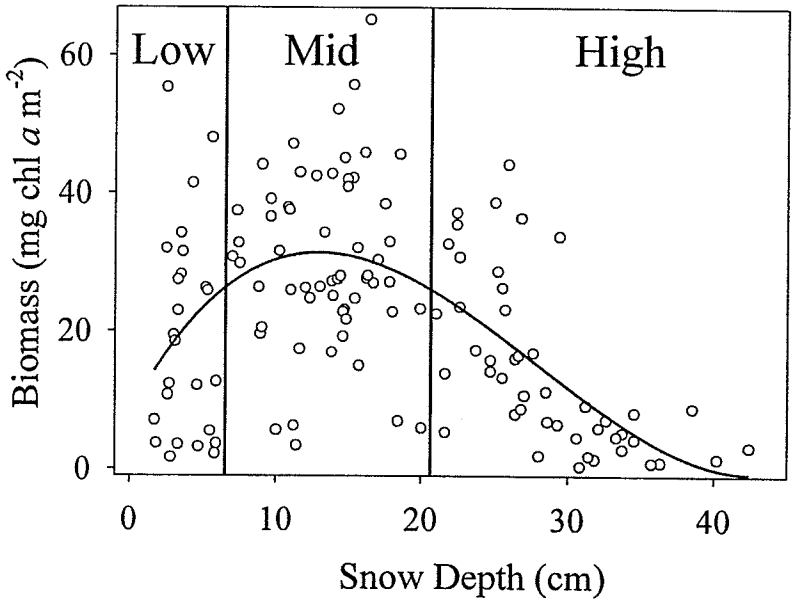

Figure 4.8. Ice algae biomass versus snow depth over the C-ICE'02 sampling period. A 3rd order polynomial was fit to the data.

Table 4.2. Correlation matrices of day of year, ice algae biomass, snow depth, ice thickness and ice bottom salinity for different snow classes.

		Time	Snow	Ice	Salinity
Low $n = 25$	Snow depth	.064			
	Ice thickness	.113	–.245		
	Salinity	–.753*	.233	–.141	
	Biomass	–.899*	.029	–.147	.698*
Mid $n = 58$	Snow depth	.094			
	Ice thickness	.163	–.291*		
	Salinity	–.704*	–.050	.107	
	Biomass	–.378*	–.009	–.094	.489*
High $n = 46$	Snow depth	.050			
	Ice thickness	.299*	–.361*		
	Salinity	–.399*	–.351*	.266	
	Biomass	.035	–.688*	.486*	.497*

Note that chl *a* concentrations for the low and high snow classes were square root transformed.
* $p < 0.05$

Given that algal growth is largely determined by the amount of PAR reaching the ice bottom in early spring, the highly transient nature of a particular snow cover would theoretically result in a highly variable ice algae distribution. However, due to the sampling methods employed I was unable to determine the direct effect of the snow cover history on ice algae. Therefore, this problem is investigated theoretically in Chapter 7.

Temporally, chl *a* concentrations decreased throughout the study period in the low and mid snow classes (Fig. 4.9a, b). However, the decrease in the mid snow class was more moderate at the start of the sampling period. In the high snow class, chl *a* concentrations remained low with high variability (Fig. 4.9c). A portion of this variability was a factor of varying average snow depth and the significant log-linear relationship between chl *a* concentrations and snow depth in the high snow class ($[\text{Chl } a] = 637 \exp(-0.149\ h_{snow}$; $R^2 = 0.465$; $p < 0.001$). However, toward the end of the period chl *a* concentrations in the high snow class followed a slight increasing trend (Fig. 4.9c).

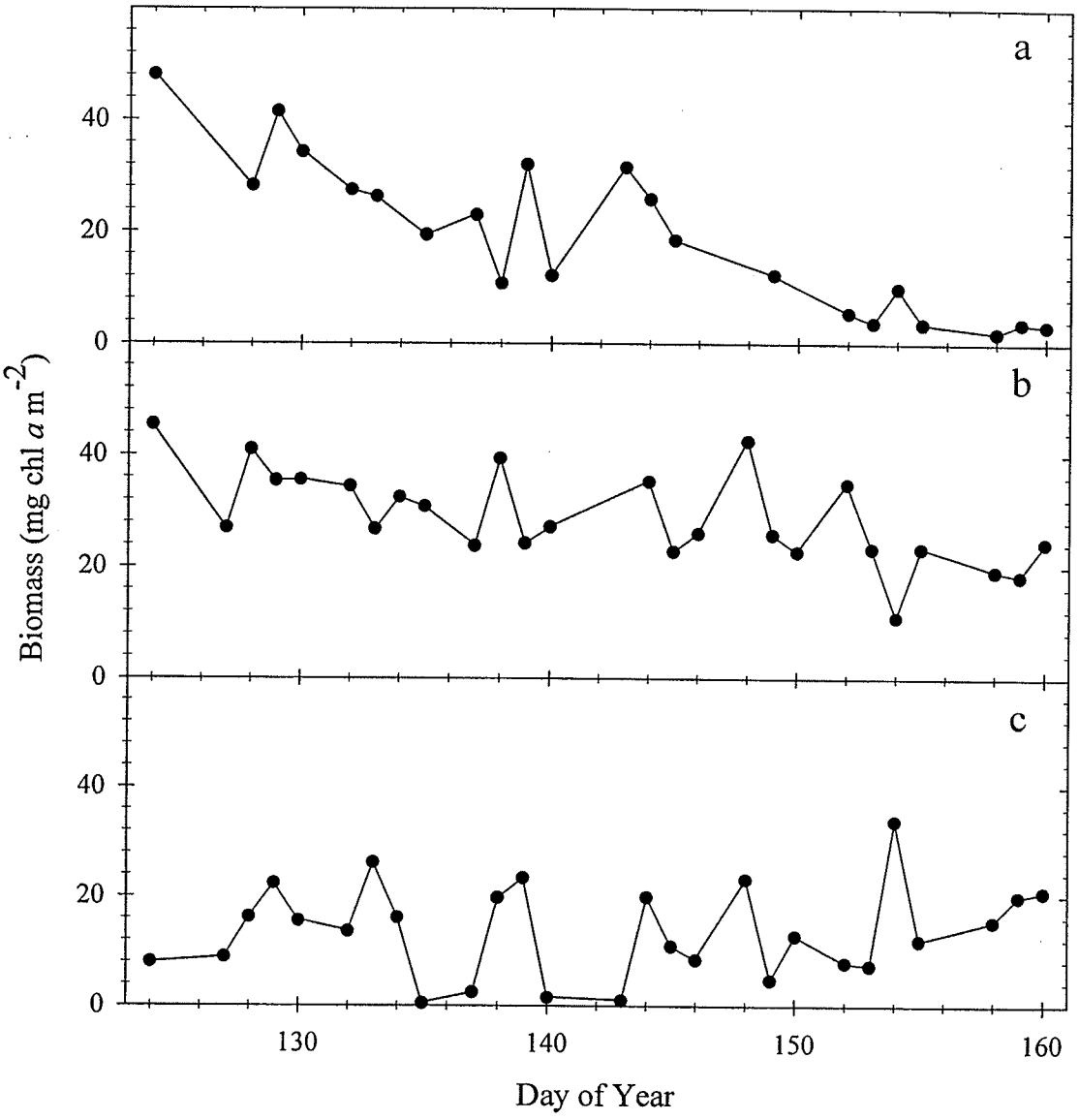

Figure 4.9. Daily averaged ice algae biomass over the study period in low (a), mid (b) and high (c) snow classes.

Table 4.2 shows a correlation matrix for day of year (time), snow depth, ice thickness, ice bottom salinity and algae biomass for each snow class. Snow depth demonstrated no correlation with time and ice thickness was only significantly correlated with time in the high snow class. Ice bottom salinity demonstrated significantly negative correlations with time however, correlation coefficients decreased with increasing snow class (Table 4.2).

Linear regressions were fit to bottom ice salinity versus day of year grouped by snow class (Fig. 4.10). Similar to the strength of correlation, the slope of the linear regressions decreased with increasing snow class from 0.12 d^{-1} ($p < 0.0001$) in the low snow class to 0.10 d^{-1} ($p < 0.0001$) in the mid and 0.06 d^{-1} ($p < 0.01$) in the high. I note that the maximum rate of ice bottom desalination during the C-ICE'02 program is half that observed in Holt and Digby (1985), however, their study occurred later in the seasonal progression. Correlation coefficients between biomass and time decreased with increasing snow class until there was no correlation within the high snow class (Table 4.2). In contrast, snow depth and ice thickness showed weak negative correlations with the strength of the correlation increasing from low to high snow classes. A significant negative correlation existed between snow depth and ice bottom salinity in the high snow class, however, this was thought a factor of the stronger correlations of biomass with snow depth and salinity (Table 4.2).

Given the results presented above, it becomes apparent that snow classes demonstrated variable responses of ice algae biomass with respect to physical processes operating at the site specific scale. The most prominent response was observed in the strong decline of ice algae biomass under the low snow class (Fig. 4.9a). This decline corresponded to the warming ice cover and subsequent decline in ice bottom salinity. Warming of the ice would be quickest at low snow depths due to lower thermal insulation resulting in stronger desalination (Fig. 4.10). Therefore, the biomass decline is expected to be due to gravity drainage of brine from the ice bottom causing ice algae to slough off the ice without a noticeable change in ice thickness, a process that has been proposed in previous studies (e.g., Gosselin et al., 1986; Welch and Bergmann, 1989).

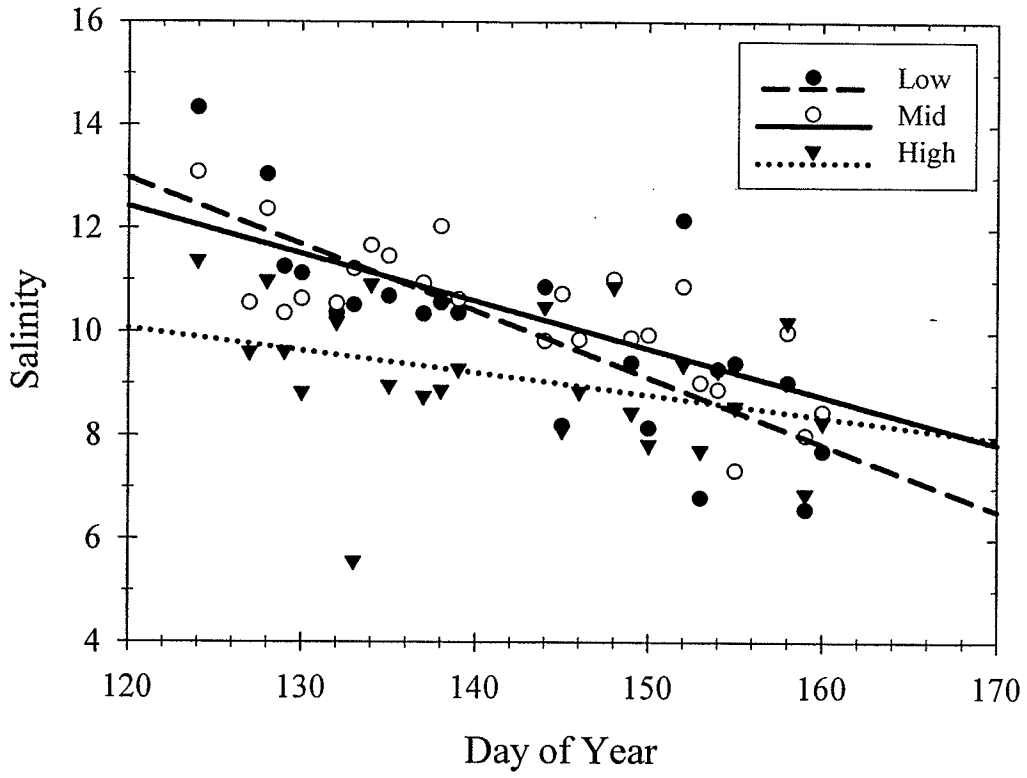

Figure 4.10. Ordinary least squares regression of ice bottom salinity over time measured under low, mid and high snow classes.

I speculate that initially elevated ice bottom salinities, associated with a faster winter ice growth rate under a thinner snow cover (Nakawo and Sinha, 1981), would augment earlier melt in the bottom layers of the sea ice. Another mechanism to consider is the retention of salts at the ice bottom by exopolymeric substances (EPS) produced by the ice algae to possibly increase habitat space (Krembs et al., 2000; 2002). This mechanism is supported through the significant correlations between algal biomass and bottom ice salinity, which was independent of snow class (Table 4.2). Supplemental to atmospheric forcing on ice temperature could have been warming due to absorption and emission of energy by ice algae (e.g., Zeebe et al., 1996; Lavoie et al., 2005).

Similar to the low snow class, a lack of correlation between algal biomass and snow depth in the mid snow class implied a possible absence of light limitation on algal accumulation at the ice bottom (Table 4.2). The slower decrease of biomass and lesser rate of desalination in the mid snow class, relative to the low snow class, implied the thicker snow cover insulated the ice bottom, slowing the sloughing of algae and in essence extending the ice algae season. Furthermore, the fact that the high snow class did not show a significant change in algal biomass with time, but did demonstrate a significant desalination rate, suggests a threshold may exist between the rate of sea ice desalination and the sloughing of ice bottom algae.

In the high snow class, ice algae were light-limited, demonstrated by the strong log-linear relationship between algal biomass and snow depth. The exponential slope of the equation (0.149) compared closely with observations made by Welch and Bergmann (1989) near Resolute Bay. In the high snow class, the deep snow cover limited thermal exchange between the atmosphere and sea ice, further decreasing the desalination rate of the ice cover (Fig. 4.10) and resulting in a strong relationship between snow depth and ice thickness (Table 4.2). Therefore, ice may still have been growing underneath the thicker snow covers, as long as the ice bottom temperature was below the freezing point. Algae biomass in the high snow class also began to follow a slight increasing trend toward the end of the period. This was most likely due to the decrease in κ_{PAR} causing an increase in transmitted PAR through the thicker snow cover. It is plausible that this increase in transmitted PAR surpassed a critical value (e.g., 4 – 7 $\mu E\ m^{-2}\ s^{-1}$; Gosselin et al., 1985) where light no longer limited algae growth under the high snow cover. However, due to the different layers of the snow cover and the fact that κ_{PAR} was

calculated for the middle layer only, it was impossible to calculate the actual amount of radiation reaching the algae layer in this study. This fact is examined more closely during the model sensitivity analysis in Chapter 7.

4.3 Conclusion

The objectives of this chapter were to examine physical and thermal processes affecting PAR transmission and how these variables affect ice algae biomass. An emphasis was placed on snow, as its physical, thermal and subsequent optical properties are an order of magnitude more important than the atmosphere and/or sea ice. In this study, snow depth varied greatly over space with drift orientation conforming to aeolian processes and sizes of 31.2 by 10.6 m on average. The snowpack also varied spatially in age, which resulted in large variability of snowpack physical and optical properties. Peaks in snowpack salinity, larger snow grains and lower PAR extinction coefficients (κ_{PAR}) supported the distinction of snowpack age within the study area.

Temporal variability was associated with atmospheric warming and wind redistribution of snow. Snowmelt, induced by the warming atmosphere, resulted in an increase in snow grain size causing a linear decrease in κ_{PAR} at a rate of -0.23 m^{-1} d^{-1}, independent of snowpack age. Wind redistribution caused snow depths in very close proximity to demonstrate nearly opposite changes of up to 38% over very small temporal scales associated with strong wind and blowing snow events. However, changes were not always predictable by strong wind events due to the intermittent and spatially variable nature of snow accumulation and erosion (Pomeroy and Li, 2000).

Given that algal growth is largely determined by the amount of PAR reaching the ice bottom in early spring, the highly transient nature of a particular snow cover would theoretically result in a highly variable algal distribution. Thin snow covers resulted in a thermal effect causing the reduction of algae due to earlier ice melt. Whereas under deep snow, algae were still light limited and thermally insulated from the warming atmosphere. Therefore, although the thicker snow cover originally limited algal growth, the thermal effect allows algae to increase the length of their growth season.

The results presented in this chapter highlight the importance of knowing the snow depth history, complete with better estimates of climate state variables for both physical and thermal properties of the snow. The problem is that this type of sampling is cost prohibitive; it is not feasible to set-up meteorological stations over the entire year at every single location of interest and current biological sampling techniques do not allow us to observe point location time series of biomass. Therefore, we have to look toward the development of new sampling techniques and the use of models and remote sensing to improve our understanding of this ecosystem and its potential response to Arctic climate variability and change. This chapter represents steps made toward meeting the principle objective of the dissertation; to determine the importance of various characteristics and scales of physical processes on the accumulation and loss of sea ice algae during the spring season. However, to meet this objective more comprehensively, one must also examine the physical habitat of the ice algae and the influence of the ocean. In the next chapter, I take a closer look at the bottom ice algae habitat. I examine the microscale distribution of algal biomass in relation to variability of the ice microstructure, brine

drainage features and tidal currents as a means of assessing the bottom ice habitat and the control which physical processes have on this habitat.

CHAPTER 5: Linkages between ice structure and microscale variability of algal biomass at the ice bottom

5.1 Introduction

In the previous chapter, I examined and discussed surface forcing factors, including thermal, physical and optical factors, which affect the accumulation and loss of algal biomass in the bottom ice. An emphasis was made on the snow cover as its physical, thermal and optical properties are nearly a factor of magnitude more important to the system. In this chapter, I examine physical factors operating near the ice bottom which affect the distribution of algal biomass.

Ice algae are intimately linked to the structure of sea ice and microscale processes operating within. Sea ice is a complex material, consisting of pure ice, brine, air and occasionally solid salts which are highly variable in their spatial and temporal distribution (e.g., Eicken et al., 1991; Cottier et al., 1999; Light et al., 2003). Apart from a thin surface layer of granular ice, underformed first-year sea ice consists of columnar ice, characterized by long crystals and networks of brine channels and inclusions with a preferentially vertical orientation (Weeks and Ackley, 1982; Eicken, 2003). Geometric selection on crystal growth results in the crystal vertical orientation (Weeks and Gow, 1978). Whereas the size and distribution of crystals and inclusions are initially determined by processes occurring over the bottommost centimeters of the ice cover. At the advancing ice-water interface, a constitutionally supercooled layer forms as salts segregated from the freezing seawater are transported away from the interface at a much slower rate than the transport of heat into the ice (Eicken, 2003). Crystal protrusions into

this layer are at a growth advantage, resulting in a lamellar surface of the bottom ice. This lamellar bottom ice layer, called the skeletal layer, is where ice algae reside during spring in Arctic first-year sea ice (Smith et al., 1990; Cota et al., 1991; Michel et al., 1996). Furthermore, it is between these lamellae where brine becomes trapped in the sea ice forming inclusions. The distance between the midpoints of these inclusions is called the brine layer spacing, which typically ranges between 0.4 to > 1.0 mm in first-year sea ice and is inversely proportional to the ice growth rate (Weeks and Ackley 1982; Nakawo and Sinha, 1984).

During spring in the high Arctic, brine salinity and volume vary constantly in ice through phase changes (Assur, 1958) and convection of brine along its channels and smaller inclusions/cracks (Untersteiner, 1968; Lake and Lewis, 1970; Niedrauer and Martin, 1979). Both of these mechanisms are dependent on the thermodynamic state and salinity of the ice cover. Observations and percolation theory for large grained columnar sea ice (i.e., typical first-year sea ice) show that below a critical brine volume of 5% – which corresponds to a temperature and salinity of –5 °C and 5, respectively – sea ice becomes impermeable to liquid (Cox and Weeks, 1975; Weeks and Ackley, 1982; Golden et al., 1998), thus limiting the convection of brine. In bottom ice, brine content is high and thermal equilibrium dictates that the ice bottom is at the freezing temperature of the immediately underlying brine, making it consistently permeable to liquid. This phenomenon is of prime importance to bottom ice algal growth which can become nutrient limited (e.g., Smith et al., 1988; Gosselin et al., 1990; Cota et al., 1991). Other factors that may affect algal growth in the ice bottom are light (Smith et al., 1988; Gosselin et al., 1990), extreme brine salinities (Arrigo and Sullivan, 1992) and available

habitat space and brine channel stability (Krembs et al., 2001). Studies have shown spatial patchiness of ice algae to be associated with mesoscale (m to km) features such as snow distribution and ice salinity (Gosselin et al., 1986; Rysgaard et al., 2001; Mundy et al., 2005; see Chapter 4). Furthermore, small scale (cm to m) variability has been observed in ice algal biomass (e.g., Cota and Smith, 1991; Eicken et al., 1991; Werner and Lindemann, 1997; Rysgaard et al., 2001). To my knowledge, no spatial analysis of the microscale (μm to mm) distribution of bottom ice algae has yet been published. However, it is at this scale where we can gain information on how bottom ice algae interact with microscale processes operating near the ice bottom and in turn how changes in the thermodynamic processes operating across the ocean-sea ice-atmosphere interface may impact ice algae habitats.

Bottom ice has been particularly difficult to sample for a number of reasons. The skeletal layer is very fragile due to the high porosity of the lamellar structure (see Eicken, 2003). This fact, along with brine loss and exposure to the cold atmosphere during extraction of an ice sample, has limited the accuracy of bottom ice microstructure (Lake and Lewis, 1970) and algal biomass measurements, particularly during ice melt (Welch and Bergmann, 1989). These difficulties have required innovative and alternative sampling techniques to examine bottom ice and its biological community.

Following extraction of sea ice samples for physical analysis, storage and laboratory analysis of the samples has traditionally occurred at temperatures much lower than *in situ* temperatures to avoid movement of brine (e.g., Sinha, 1977; Schwarz et al., 1981; Eicken et al., 1991; Cottier et al., 1999; Light et al., 2003). The most common method of ice microstructure examination is to use plane transmitted and cross-polarized light through

thin sections to highlight brine inclusions and ice crystals, respectively (Sinha, 1977; Perovich and Gow, 1996). Replication of thin section surfaces was an innovative approach to examine the three dimensional structure of brine inclusions (Sinha, 1977). This author further suggested the use of this method to examine bottom ice structure; however, to my knowledge such an analysis does not exist in published literature. More recently, new insights into the three dimensional structure and availability of brine spaces in sea ice have been accomplished through techniques which do not require cold temperature storage. These include casting (Weissenberger et al., 1992), magnetic resonance imaging (Eicken et al., 2000) and rhodamine chloride adsorption (Krembs et al., 2000) techniques. However, the use of centrifugation in these techniques does not realistically permit their application for examination of the fragile skeletal layer. In contrast to physical sampling of sea ice, ice growth experiments have provided insights on interactions at the ice-water interface and brine channel evolution during ice growth and melt. In particular the thin ice tank experiments of Eide and Martin (1975) and Niedrauer and Martin (1979) provided information on the lamellar structure of the skeletal layer and how seawater exchanges with sea ice brine at the ice bottom.

Innovative techniques for *in situ* observations of ice algae are numerous. Welch and Bergmann (1989) developed an ice scraping technique which estimated algal biomass in the bottommost 2.5 cm ice layer using measurements of light attenuation through the layer. However, the technique was destructive making it applicable to only spatial measurements of algal biomass. An underwater pulse-amplitude-modulated fluorometer (Diving-PAM) was also used to estimate algal biomass at the ice bottom providing the potential for both spatial and time-series studies, however, these measurements were

limited to the bottom ~1 cm of the sea ice (Rysgaard et al., 2001). More recently, Mundy et al. (2007a; see Chapter 6) followed up on previous research (Legendre and Gosselin, 1991; Perovich et al., 1993) to employ the use of transmitted irradiance and algal absorption properties to estimate algal biomass within the entire ice matrix.

An alternative *in situ* and non-destructive method to investigate ice bottom features and associated biological communities is the use of underwater video and photographs. Video observations have documented a diverse structure of the sea ice bottom from ice bulges and holes to algal and sediment patches in the sea ice at scales of centimeters to meters (Werner and Lindemann, 1997). Photographic techniques have been applied to numerous studies of surface benthic invertebrates including the bottom of sea ice (e.g., Lønne and Gulliksen, 1991; Hop et al., 2000). In this paper, we develop an *in situ* microscale photographic technique to examine linkages of ice algae with bottom ice physical properties of thick landfast first-year sea ice. More specifically we investigate the following objectives: (1) describe spatial elements of algae and the bottom ice and (2) investigate the linkages of brine layer spacing and brine channels with the microscale distribution of ice algae chl *a* biomass. I note that the results from this chapter have been published in the peer-review literature (Mundy et al., 2007b).

5.2 Analytical Methods

5.2.1 Dataset

In this chapter, I use a portion of the dataset collected during the Carcajou'03 field program. In particular, I employ the use of the under-ice images, algal biomass, snow and air temperatures, and current velocity data.

5.2.2 Image Calibration

Images of the ice bottom were obtained using only naturally transmitted light through the snow and ice. Figures 5.1 and 5.2 show low and high chl *a* biomass images (see section 3.2) presented in their raw digital number (RDN) format, respectively. In order to carry out an intercomparison of the bottom ice images, images were calibrated to field measurements of bottom ice chl *a* concentration. It is noted that bottom ice algae absorption coefficients have been estimated from *in situ* measurements of transmitted irradiance through the use of Beer's law,

$$E_z = E_0 \exp(-Kz) \qquad [5.1]$$

where E_z and E_0 are surface and transmitted irradiance to depth z (m) within an attenuating material and K is the attenuation coefficient (m^{-1}; e.g., Perovich et al. 1993; Haines et al. 1997; Mundy et al. 2007a; see Chapter 6). Assuming the image area of the ice bottom of 28.3 x 22.6 cm was taken under a homogenous light field (see Section 5.2.3 for discussion of assumptions), K can be related to the vertically-integrated algal biomass for each pixel. For example, darker colors on the RDN images are considered as higher concentrations of algal biomass (Fig. 5.1 and 5.2). Therefore, algal biomass will be directly proportional to the natural log of the reversed raw digital number (RRDN). The following equation outlines the image calibration calculations to obtain a pixel chl *a* biomass estimation ($B_{i,j}$; mg chl *a* m^{-2}),

$$B_{i,j} = \frac{A_I}{A_P} \frac{\ln(RRDN_{i,j} - RRDN_{\min} + 1)}{\sum_{i,j} \ln(RRDN_{i,j} - RRDN_{\min} + 1)} B_{Field} \qquad [5.2]$$

where A_I is the total unmasked image area (m^2), A_P is the area of an individual pixel (m^2), i and j represent row and column locations of unmasked pixels, respectively, $RRDN_{\min}$ is

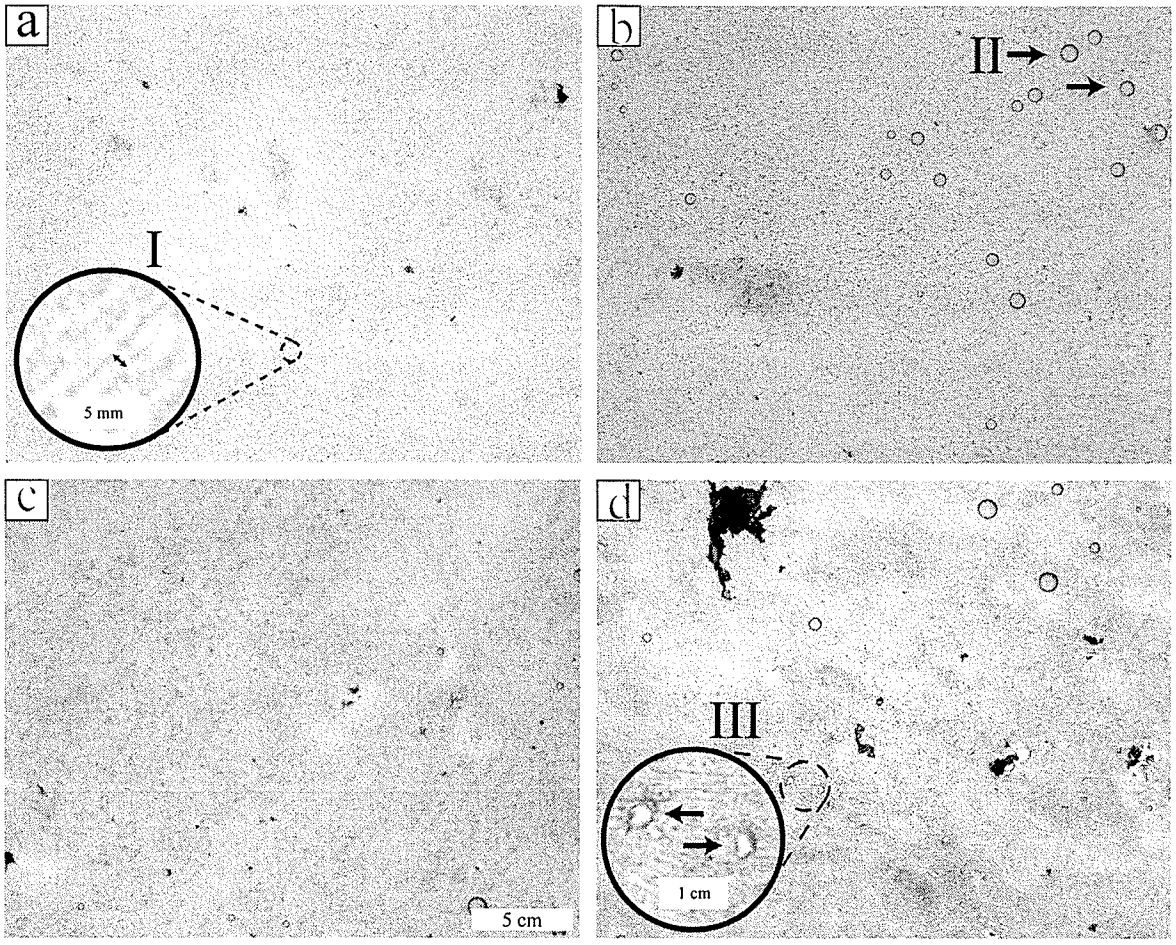

Figure 5.1. Raw gray scale images of the ice bottom with mean algal chl a biomasses on image capture days of 9.2 mg chl a m-2 on day 137 (a), 15.9 mg chl a m-2 on day 141 (b), 16.4 mg chl a m-2 on day 135 (c) and 20.7 mg chl a m-2 on day 140 (d). Roman numerals highlight specific features mentioned in the text including brine layer spacing (I), bubbles at the under surface of the ice (II) and brine drainage features (III).

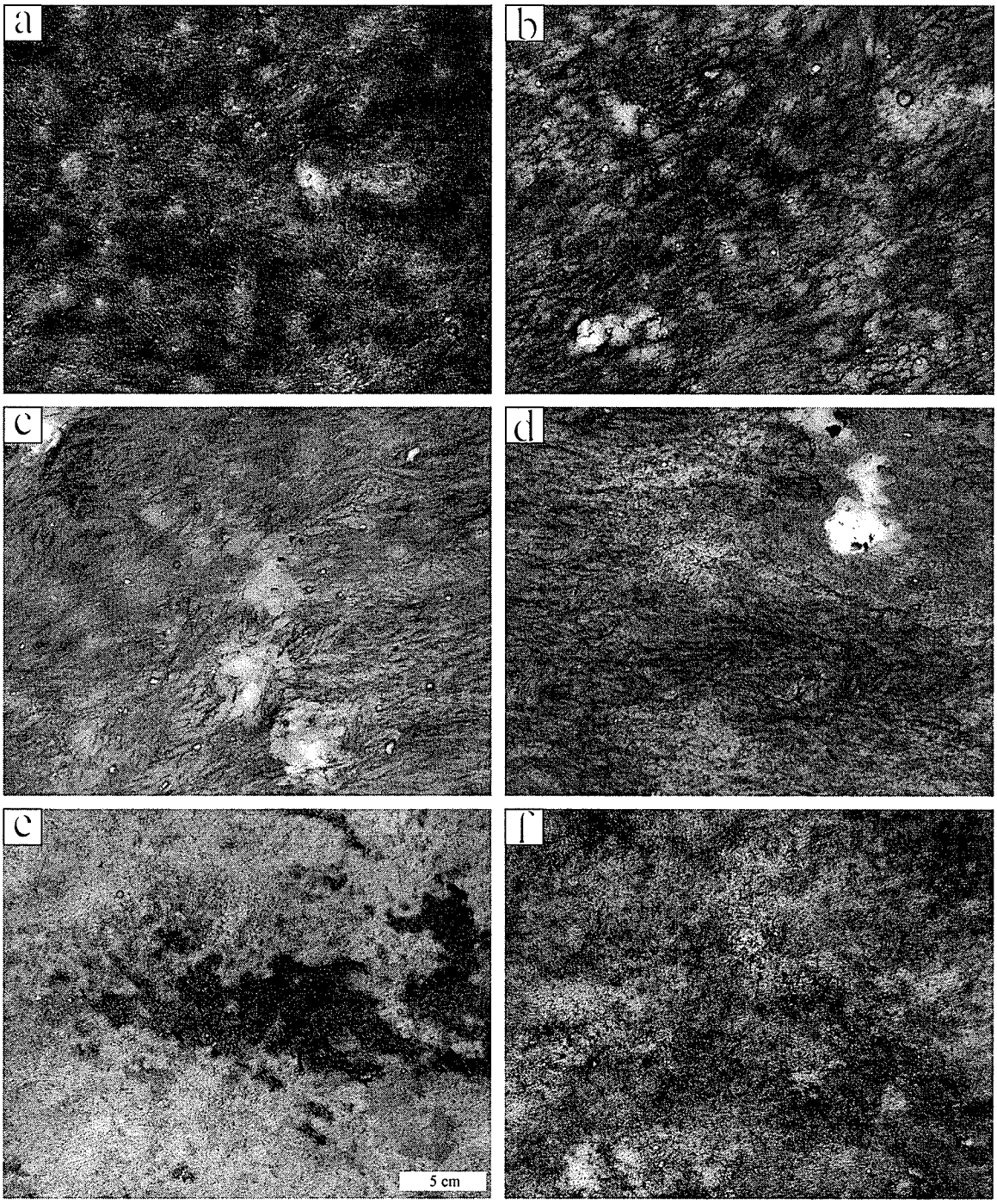

Figure 5.2. Raw digital number images of the ice bottom with mean algal biomasses on image capture days of 108.9 mg chl *a* m^{-2} on day 125 (a), 63.8 mg chl *a* m^{-2} on day 130 (b), 99.0 mg chl *a* m^{-2} on day 132 (c), 47.8 mg chl *a* m^{-2} on day 134 (d), 34.6 mg chl *a* m^{-2} on day 135 (e) and 41.5 mg chl *a* m^{-2} on day 137.

the minimum RRDN in the image and B_{Field} is the field estimate of algal chl *a* biomass (mg chl *a* m^{-2}). The subtraction of $RRDN_{min}$ represents an additional assumption that at least one pixel on each image contained zero algal biomass. This assumption is needed to zero image histograms for standardization of images, following Lillesand and Kiefer (2004).

It is noted that bubbles were present at the ice bottom in most images (e.g., Fig. 5.1b). Horizontal bands of gas inclusions in the bottom ice have been suggested to come from bubbles on the underside of the ice that become entrapped by the growing ice sheet (Cole and Shapiro 1998). Tsurikov (1979) speculated that these bands of gas inclusions may have originated through biological activity. I surmise that the bubbles could have also been created during the camera deployment. As these bubbles existed between the camera and ice bottom, they affected the light field and therefore were visually identified and masked out of the images prior to image calibration.

5.2.3 Assumptions and Limitations of the Camera Technique

Three assumptions had to be made to calibrate the under-ice images to biomass: (1) site measurements of chl *a* biomass from extracted cores represented the mean algal biomass of the image; (2) only chl *a* biomass affected the per pixel distribution of transmitted irradiance at the image scale; and (3) at least one pixel in an image represented zero biomass. The first assumption is reasonable in that bottom ice algal biomass is not expected to significantly vary over the spatial area of a single image in undeformed first-year sea ice. This statement is supported by the *in situ* observations of Rysgaard et al.

(2001) where variation in algal biomass and activity was small over scales of 0.025 to 5 m in radius.

The second assumption can be contested in that irradiance transmitted through columnar sea ice appears to have a preferential downward direction associated with the vertically oriented structure of crystals and brine inclusions (e.g., Buckley and Trodahl, 1987) and the presence of absorbing particulates higher in the ice cover will affect the bottom ice light field. In reference to the first argument, scattering occurs along brine, air and salt inclusions due to a contrast in their index of refraction with ice, making the edges of these features visible (e.g., application of using plane transmitted light for ice microstructure investigations; Sinha, 1977; Perovich and Gow, 1996; Light et al., 2003). It is noted that the diameter of brine inclusions (tubes/pockets) between ice lamellae have been observed to range from 10 to 270 μm (Cole and Shapiro, 1998; Light et al., 2003), which makes them either equal to or less than the pixel resolution of the camera. Therefore, the camera system used here was not sufficiently sensitive in pixel resolution to discern brine inclusions and, as verified by a homogeneous image taken under very low biomass (0.4 mg chl *a* m^{-2}; data not presented), the bit depth resolution was unable to discern bottom ice features without the presence of algal biomass. The second argument is likely to be a substantial problem with application of the technique to areas where sediments and algal growth higher up in the ice is common (e.g., pack-ice, deformed ice, sea ice near estuaries with high sediment loads, melting summer ice, etc.), which leads to a question of the image optical depth. That is, to what depth into the sea ice are the images detecting at the pixel resolution? Dependent on the size and location of the absorbing particulates within the sea ice, the effect will be to dilute the per pixel

estimation of algal chl *a* biomass, particularly in relation to the third assumption discussed below. Therefore, fine focused details of the algal distribution are expected to be derived from the bottommost centimeters of the ice from which field measurements were made. Furthermore, the sea ice investigated in our study would have minimal absorbing particulates higher into the ice cover as it formed in place under quiescent conditions (i.e., undeformed landfast sea ice) and ice algal growth is largely confined to the bottom few centimeters of first-year sea ice in the region during spring (e.g., Smith et al., 1990; Cota et al., 1991).

The final assumption of at least one pixel containing zero algal biomass cannot be discussed in the context of previous investigations as *in situ* observations at this scale simply do not exist. However, it is a realistic assumption that a lamellar plate or brine drainage hole should have very little or no algae. This statement is revisited within the discussion section. It is noted that the assumptions and camera sensitivity discussed above will limit precision and accuracy of the per pixel chl *a* biomass estimation, however there are no other studies with which to compare our results. Therefore, hereinafter, a distinction is made between field estimates and per pixel estimates of chl *a* biomass by referring to the latter as pixel biomass.

Another limitation worth mentioning concerns the 2-dimensional view of the images in that I was unable to distinguish between a bulge and a hole at the bottom of the sea ice. Therefore, the camera technique will need to be altered if it is to be applied to ice where both of these features are common (e.g., pack-ice, deformed ice and melting ice). However, the application to undeformed first-year sea ice in this paper is appropriate as a recognizable uniform ice bottom surface is expected. For example, lamellar protrusions

are known to be elongated perpendicular to the c-axis and approximately 1 mm in width at the bottom of thick first-year sea ice (e.g., Weeks and Ackley, 1982) and due to their draining nature, brine channel holes are expected to be roughly circular.

5.2.4 Spatial Analysis

In this section I describe a new approach to examine results from numerous variograms of a single image in one plot. A variogram is a quantitative measure of the spatial continuity of a variable (Cressie, 1993). The application of this method to the under-ice imagery will therefore statistically characterize the spatial patchiness of algal biomass within the limits of the image spatial resolution. The variogram characterizes spatial continuity using semivariances calculated for a set of lag distances (h) over the dataset. An omnidirectional variogram is estimated from every possible lag pair in every look direction over a variable such that it will result in the most clearly defined spatial continuity of the dataset (Isaaks and Srivastava, 1989). Therefore, omnidirectional variograms were used in our investigation. The semivariance ($\hat{\gamma}(h)$) is estimated as follows:

$$\hat{\gamma}(h) = \frac{1}{2N(h)} \sum_{(i,j)|h_{ij}=h} (s_i - s_j)^2 \qquad [3]$$

where the spatial observations are s_i and s_j and h_{ij} is the lag which represents the distance from point i to j resulting in $N(h)$ pairs of data. At $h = 0$, the semivariance will equal zero. As h increases, the semivariance increases until a plateau is reached asymptotically, past which the semivariance is considered independent of h. The value of h at which the plateau is reached is called the range and the semivariance of the plateau is called the sill.

At the minimum h of a particular variogram, defined here as the start lag, the semivariance can jump dramatically due to unexplained variation caused by a structural component smaller than the start lag or by sampling error (Cressie, 1993). This apparent discontinuity at the origin is referred to as the nugget and can be expressed as a percentage of the sill. These parameters are determined by fitting a model to the experimental variogram. The model is a mathematical function fit to the variogram for which a variety of common models exist (Cressie, 1993). In general the model which best fits the dataset is to be used. For this investigation, an exponential model with a nugget effect (i.e., the model is not confined to pass through the origin) was found to provide the best fit over all length scales.

The new approach applied in this study was the use of what is termed here a start lag plot. Using the ArcGIS software package (© 1999-2004 ESRI Inc.), a series of variograms were constructed for each image by incrementally increasing the start lag by 1 pixel, while holding the total number of lags to 15, until a start lag of 34, at which point the 15^{th} lag equates to just less than half the vertical axis of the image. The range and percent nugget (as a percent of the sill) were extracted from each variogram. These parameters were then plotted against the start lag, for each image, to determine the dominant spatial continuity of the images.

In order to illustrate how the above start lag plot will be interpreted, a hypothetical series of variograms for different start lags were developed (Fig. 5.3). Figure 5.3a shows a variogram with a start lag of 1 that does not reach a sill, causing the range to be determined as the maximum lag of 15. At a start lag of 2 and 5, a range is observed at 15 with a 0% nugget (Fig. 5.3b, c). This range represents the dominant spatial continuity

characterized by the variogram. In my investigation, this spatial continuity is interpreted as the dominant scale of algal biomass patchiness. Finally, at a start lag of 10, the nugget is nearly 100% and the variogram no longer reaches a sill, resulting in a maximum lag range of 150 (Fig. 5.3d). Therefore, key interpretation features of the start lag plot are that: a) if a dominant spatial continuity is encountered, the range will deviate from the maximum lag range, immediately followed by an increase in the percent nugget; b) if no spatial continuity is encountered, the range will continue to increase along the maximum lag range with little change in the percent nugget.

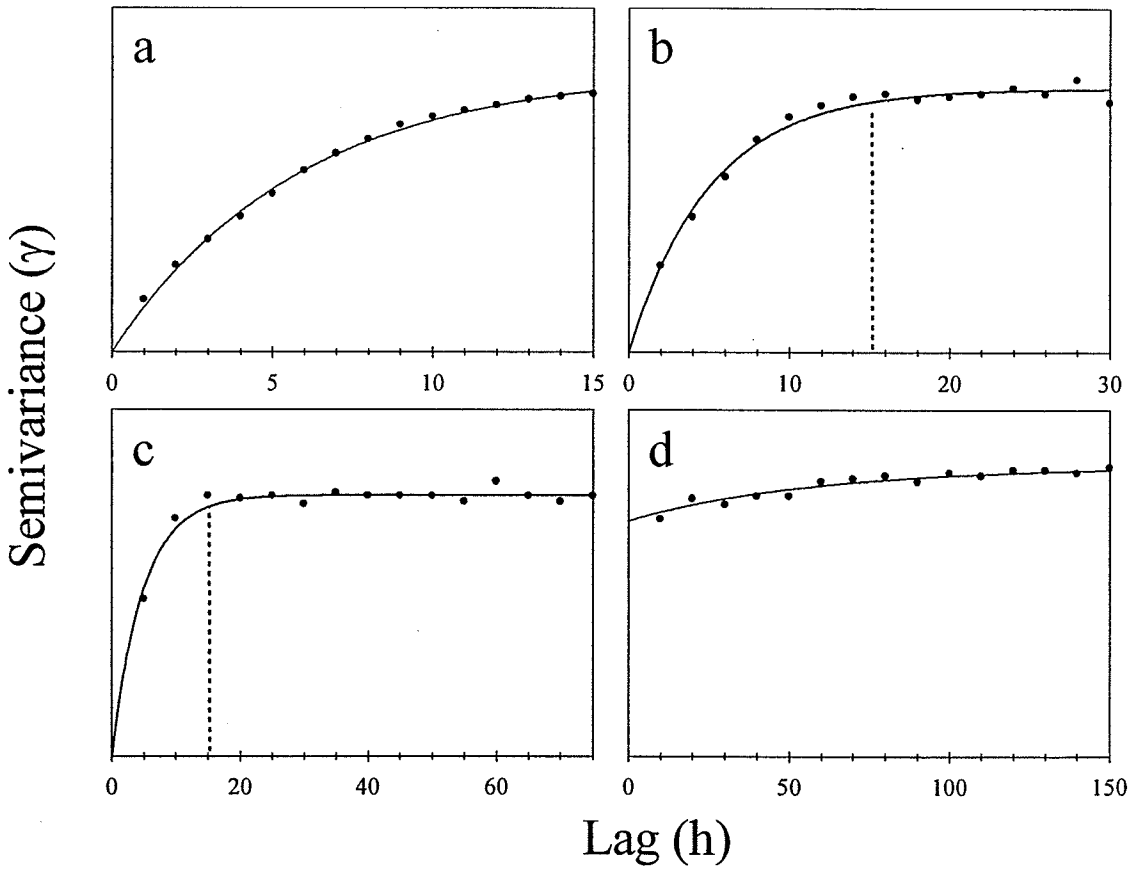

Figure 5.3. A set of variograms constructed using an exponential model, 15 total lags and an increasing start lag of 1 (a), 2 (b), 5 (c) and 10 (d). The variograms were constructed from a hypothetical spatial dataset with a dominant spatial structure of 15 (vertical dashed lines). Note that the x-axes have different scales.

5.2.5 Ice Morphology

Ice algae are known to reside between the crystal plate lamellae and up into the permeable brine spaces of the ice (Cota et al., 1991; Horner et al., 1992; Krembs et al., 2001). This growth pattern of algae between crystal plates is apparent in most images where algae grew within the ice cover (Fig. 5.1 and 5.2). Similarly, the growth pattern highlights features of the bottom ice such as the brine layer spacing (e.g., Fig. 5.1a) and brine drainage channels (e.g., Fig. 5.1d). The crystal plate structure of the ice bottom was apparent on 8 of the 10 images (Fig. 5.1a-d and Fig. 5.2a, d-f). On each of the 8 images, brine layer spacing across lamellar plates was measured over areas where the crystal substructure was clearly defined by peaks of algal biomass between plates. On 6 of the 10 images (Fig. 5.1a, c-d and Fig. 5.2b, c, f), circular features of low pixel biomass values highlighted by a ring of high pixel biomass were observed throughout the images. Werner and Lindemann (1997) observed similar circular features through video of the under ice surface concluding these to be holes at the ice bottom. Therefore the circular features observed on our images were also interpreted as holes representing the bottom of brine drainage channels. The low pixel biomass center of the brine channels were traced on each of the 6 images, highlighting brine channels as distinct polygons in the images, to accomplish an image particle analysis of the channels using the public domain NIH Image program (developed at the U.S. National Institutes of Health and available on the Internet at http://rsb.info.nih.gov/nih-image/).

5.3 Results

5.3.1 Physical Environment

Downwelling PAR showed daily averages ranging from a minimum of 508 μE m^{-2} s^{-1} to a maximum of 619 μE m^{-2} s^{-1} (data not shown). PAR albedo was constant throughout the study at 0.85 and air temperatures remained well below 0 °C (Fig. 5.4a). After May 13 (day 133), daily averaged temperatures that were below –10 °C rose to > –5 °C on May 16, 20 and 21 (days 136, 140 and 141). Ice surface temperatures were relatively constant prior to May 14 (day 134; –9.6 ± 0.3 °C), after which a slight increase occurred until May 17 (day 137) when temperatures stabilized at an average of –7.1 ± 0.3 °C (Fig. 5.4a).

Hourly averages of absolute magnitudes of current velocities monitored at 3.35 m from the ice bottom are shown in Figure 5.4b. The daily maximum current magnitude was minimal between May 10 to 12 (days 130 to 132), corresponding to the predicted neap tide on May 11 (day 131). After May 12 (day 132), current velocities increased steadily until May 18 (day 138).

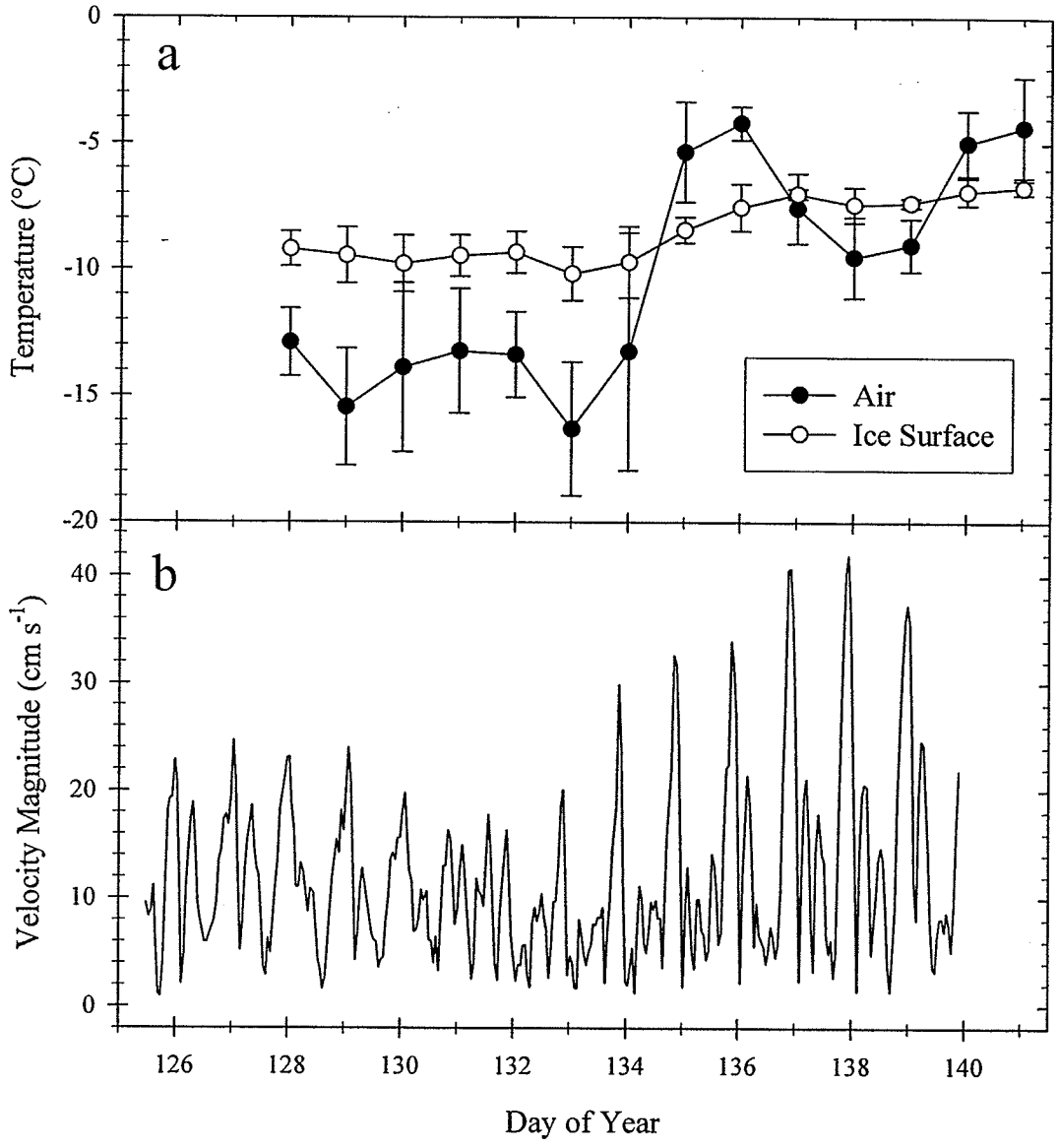

Figure 5.4. Time series of daily averaged (standard deviation error bars) air temperature and ice surface temperature under an averaged 16.8 cm snow cover (a) and hourly current velocities (absolute magnitude) monitored 3.35 m from the ice bottom (b).

5.3.2 Pixel Biomass Distribution

Image distributions of pixel biomass show relatively low variation in their upper and lower quartiles, however, a tail of outliers extended to zero on all images (not shown) due to the assumption of at least one pixel containing zero biomass (Fig. 5.5). The image captured on May 15 (day 135), with a mean chl *a* biomass of 34.6 mg chl *a* m^{-2}, showed the widest range of pixel biomass. Pearson's second coefficient of skewness, *3(mean-median)/standard deviation*, for each image distribution showed that most image distributions were skewed strongly to the left (Fig. 5.5). The degree of skewness decreased at low chl *a* biomasses, particularly at and below the image representing the mean chl *a* biomass of 20.7 mg chl *a* m^{-2}. Therefore, the 4 lowest chl *a* biomass images ($\leq$ 20.7 mg chl *a* m^{-2}) will be referred to as low biomass images whereas high biomass images ($\geq$ 34.6 mg chl *a* m^{-2}) will refer to the remaining 6 images.

The original RDN images show distinct differences between high and low biomass images. Low biomass images clearly reveal the crystal plate structure (Fig. 5.1), whereas crystal plates become less discernable on high biomass images. On the latter, algae occur both between and across the crystal lamellae (Fig. 5.2). There are also images where the lamellae are mostly obscured due to algae which are apparently hanging into the water column (Fig. 5.2b, c). Visual examination of the extracted ice cores during field sampling confirmed that these algae were mostly located below the ice while loosely attached to the bottom ice. It is interesting to note that these algae hanging into the water column appeared to occur parallel to the bottom ice crystal lamellae.

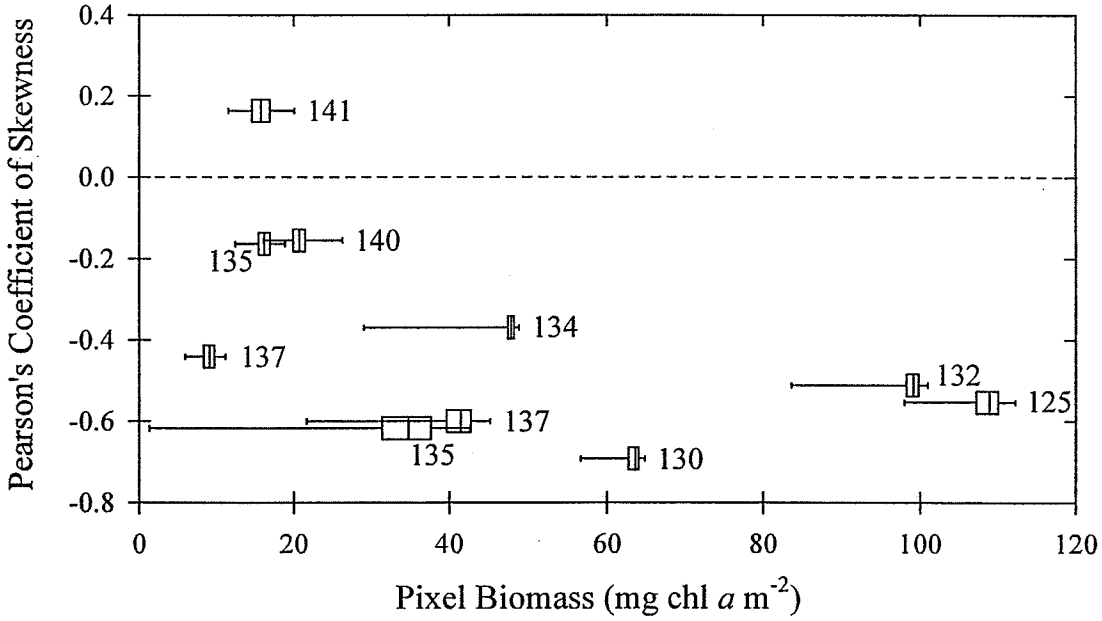

Figure 5.5. Image boxplots (whiskers represent 0.5 and 99.5 percentiles) for pixel biomass distributions. The boxplots are also lined up along the y-axis with corresponding values for the Pearson's coefficient of skewness, $3(\mu\text{-median})/\sigma$, calculated from the distributions. The day of year on which the images were captured is provided next to each boxplot.

The 6 high biomass images, which were collected at random locations within the study area, appeared to reveal a temporal change in algal location. It is noted that these images do not represent a true time series, but rather point samples collected over time. The image from day 125 showed that the pixel biomass was concentrated within the skeletal layer, depicted by the visible lamellae (Fig. 5.2a). On days 130 and 132, algae were hanging from the ice bottom (Fig. 5.2b, c), while on images from days 134 and 135 part of the hanging algae were sloughed off, exposing the crystal lamellae (Fig. 5.2d, e). Finally, the image from day 137 again showed pixel biomass to be concentrated within the ice cover (Fig. 5.2f). Evidence of this temporal pattern was not observed in the 4 low biomass images.

5.3.3 Spatial Structure (Variogram Analysis)

Figure 5.6 shows start lag plots for the 4 low biomass images. On all 4 plots, the modeled variogram ranges deviated from the maximum lag range near the origin followed by an increase in the percent nugget. These observed features in the start lag plots led to the conclusion of a dominant spatial continuity in these images at length scales of 1.7, 2.0, 3.3 and 3.9 mm (Fig. 5.6a-d, respectively). These scales corresponded to the patchiness of algae in the image as observed through patches of higher pixel biomass between crystal lamellae and as circular features on the images (Fig. 5.1). Interestingly, based on the 4 low biomass images, a significant relationship existed between algal pacthiness (h_D) and the corresponding field estimate of chl *a* biomass (B_{Field}) ($h_D = 0.19\ B_{Field} - 0.21$; $R^2 = 0.74$). The high biomass images did not show similar small scale patchiness (Fig. 5.7). For the high biomass images from days 125, 135 and 137, there were increases in the percent nugget near the origin. These nugget increases suggests that there may be very small scale patchiness in pixel biomass in these images, however it was not confirmed by the modeled variogram range.

On 4 of the 6 high biomass images, dominant spatial continuity was observed at scales between 10 and 26 mm (Fig. 5.7a-c, f). These scales corresponded to roughly circular patch sizes of low pixel biomass on the images (Fig. 5.2 a-c, f). There was no dominant spatial continuity observed in the images taken on days 134 and 135 over the start lags we examined (Fig. 5.7d and e, respectively). However, a small deviation in the range curve from the maximum lag range followed by an increase in the percent nugget did occur at a range of 18.1 mm and start lag of 6 pixels on day 134, suggesting a weak spatial continuity at this scale existed in the image (Fig. 5.7d).

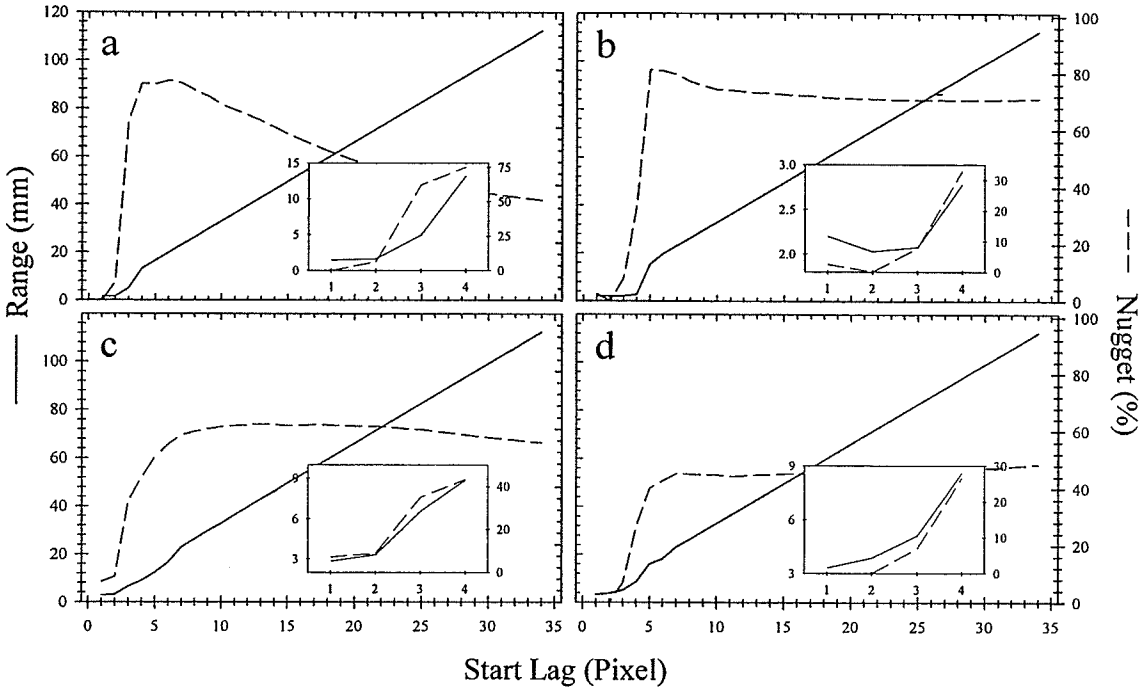

Figure 5.6. Range (left axes) and percent nugget (right axes) as a function of start lag from omnidirectional variograms using 15 total lags for low biomass images taken on days 137 (a), 141 (b), 135 (c) and 140 (d). Insets are a close up of the first start lags up to 4 pixels. Note that y-axes vary between plots. See text in Section 5.2.4 for interpretation of the start lag plot.

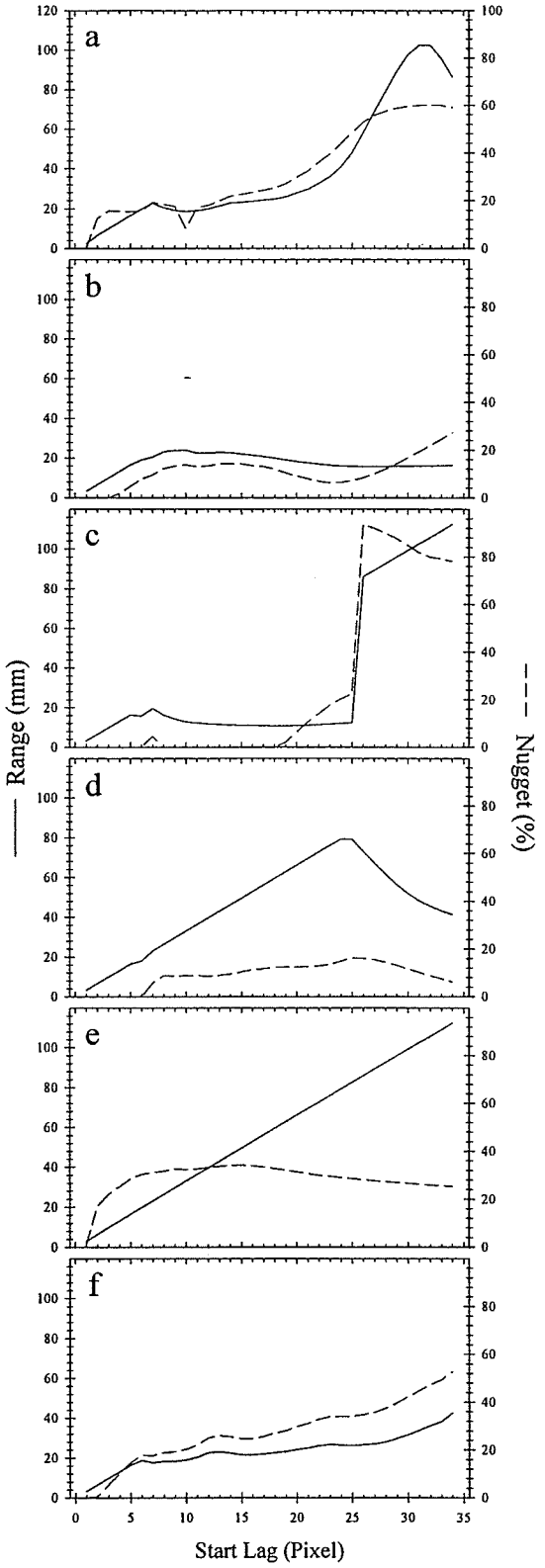

Figure 5.7. Range (left axes) and percent nugget (right axes) as a function of start lag from omnidirectional variograms using 15 total lags for high biomass images taken on days 125 (a), 130 (b), 132 (c), 134 (d), 135 (e) and 137 (f). See text in Section 5.2.4 for interpretation of the start lag plot.

5.3.4 Ice Morphology

Image averages of brine layer spacing measured on 8 of the 10 images ranged between 1.19 and 1.41 mm. The minimum and maximum values from the images were 0.78 and 1.84 mm, respectively. No significant relationships were found between brine layer spacing and time, snow depth or chl *a* biomass on the images examined.

Example image windows highlighting brine drainage features are shown together with a plot of pixel biomass *versus* distance for horizontal (and vertical) lines of 1 pixel width across the middle of each of the identified features (Fig. 5.8). Noted in section 5.2.5, 6 of the 10 images clearly showed brine channels at the ice bottom, identified by a distinct ring of high pixel biomass (i.e., Fig. 5.1a, c-d and Fig. 5.2b, c, f). These channels can be seen as areas of high light transmission (i.e., low algal biomass). The smallest of channels were of similar size. Larger channels were found to be formed by two or more channels joined together, as evidenced by their more elliptical shapes (e.g., Fig. 5.8d, e) and/or small increases in pixel biomass in the middle of the larger channels which line up with the size of the smaller channels on the line plots (e.g., Fig. 5.8b-d). Circular patches of high pixel biomass of the same diameter as smaller brine channels were also observed on some of the low biomass images. Figure 5.8b shows a number of similar size features within the image window that range from a circular ring of pixel biomass representing a brine channel to a circular feature with pixel biomass peaking in the centre (see numbered arrows 2 and 3).

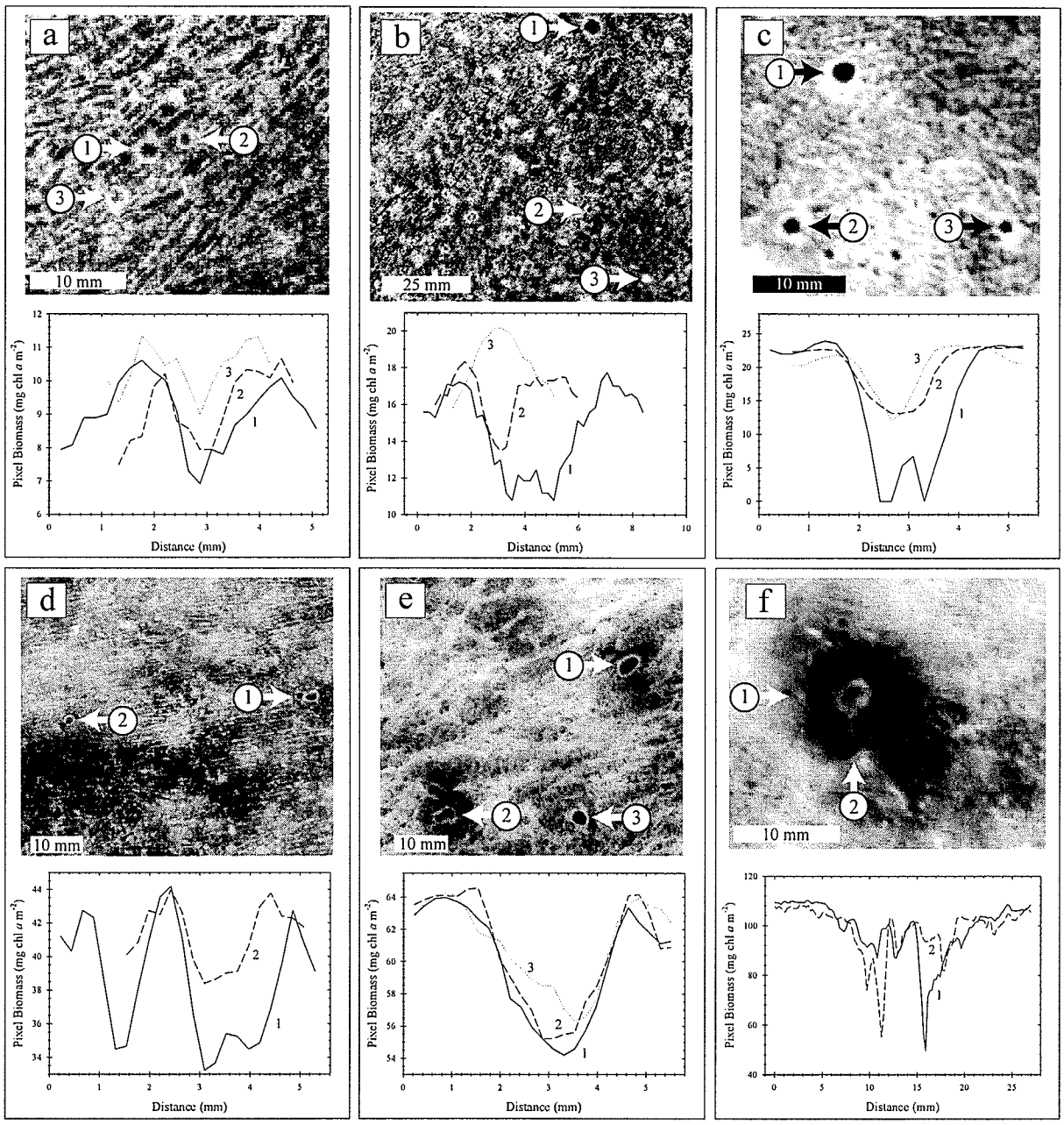

Figure 5.8. Image windows highlighting brine drainage features (numbered arrows) from low biomass images captured on days 137 (a), 135 (b) and 140 (c) and from high biomass images captured on days 137 (d), 130 (e) and 125 (f). Images are calibrated to chl *a* biomass and therefore white denotes higher pixel biomass. Below each image window are corresponding line plots of pixel biomass along horizontal and vertical axes (indicated by arrow orientation) across the center of the identified brine drainage features. Note that scales vary on the line plot axes.

Table 5.1 presents image averaged statistics from the image particle analysis of brine channels. Aspect ratios (major/minor axes from the best fit ellipse for a brine channel) did not deviate substantially from a value of 1, showing that the brine channels were nearly circular. The image averaged channel diameter ± standard deviation, determined from the pixel area, ranged between 1.79 ± 0.48 mm to 2.68 ± 0.96 mm, with brine channel number densities ranging from 5.3 to 10.4 per 100 cm^2 over the 6 images. Table 5.2 shows linear regression parameters and statistics determined using data presented in Table 5.1. Using an α-level of 0.10, significant negative relationships were observed between snow depth with chl *a* biomass and with brine channel diameter. Furthermore, significant positive and negative relationships were observed between snow depth and chl *a* biomass with brine channel number density, respectively (Table 5.2).

Table 5.1. Field site estimates of chl a biomass and snow depth and corresponding brine channel statistics (± standard deviation) derived from the image particle analysis.

			Brine Channel Statistics		
Chl *a* Biomass (B_{field}; mg chl *a* m^{-2})	Snow Depth (H_S; cm)	Image Capture Date	Mean Diameter (∅; mm)	Aspect Ratio (major/minor axis)	Number Density (ρ; 100 cm^{-2})
9.2	19.3	May 17 (137)	1.79 ± 0.48	1.29 ± 0.20	7.22
16.4	20.7	May 15 (135)	1.65 ± 0.67	1.40 ± 0.28	10.35
20.7	12.0	May 20 (140)	1.97 ± 0.52	1.29 ± 0.19	7.84
41.5	5.5	May 17 (137)	2.10 ± 0.49	1.36 ± 0.27	5.33
63.8	4.7	May 10 (130)	1.96 ± 0.85	1.47 ± 0.37	5.96
99.0	4.6	May 12 (132)	2.68 ± 0.96	1.40 ± 0.33	5.65

Table 5.2. Ordinary least squares linear regression (y = ax +b) parameters and statistics calculated from data given in Table 1.

x	y	a	b	R^2	p-value
H_S	B_{field}	–3.79	83.96	0.67	0.05
H_S	∅	–0.036	2.42	0.54	0.09
H_S	ρ	0.216	4.65	0.73	0.03
B_{field}	∅	0.009	1.64	0.78	0.02
B_{field}	ρ	–0.035	8.54	0.42	0.16
∅	ρ	–3.59	14.33	0.46	0.14

Patches of very low pixel biomass were also observed on 5 separate images which corresponded to images representing the highest mean chl *a* biomasses (Fig. 5.2a-d, f). These clearly defined patches ranged in size from approximately 15 mm to 30 mm in diameter and only 1 or 2 were visible per image. A closer examination revealed the characteristic ring of higher pixel biomass around a brine drainage channel within a few of these patches (e.g., Fig. 5.8f). The brine channel is apparent in the middle of the patch with a size of 2.6 mm in diameter.

5.4 Discussion

5.4.1 Bottom Ice Morphological Features

My measurements of brine layer spacing matched with a bottom ice image of a laboratory grown ice sample (see Fig. 3c in Martin, 1979) and with other observations of brine layer spacing associated with slow ice growth rates (Weeks and Ackley, 1982; Nakawo and Sinha, 1984). The vertical gradient between the low air temperature and higher snow-ice interface temperature decreased in magnitude during the experiment and demonstrated opposite gradients toward the end of the period. Therefore, it is safe to conclude that during our study ice growth rates were slow with the potential for bottom ice melt. A slow ice growth rate can explain the wider crystal plates and the fact that no relationship existed between brine layer spacing and variables such as time, snow depth and bottom ice chl *a* biomass.

To our knowledge, the only presentation of brine channel distribution at the ice bottom are the sketches by R. Lake presented in Martin (1979). The range in brine channel number densities observed in our study was higher than that previously documented for

thick ice (Lake and Lewis, 1970; Martin, 1979). Lake and Lewis (1970) observed a channel spacing of 1 per 180 cm^2 and Martin (1979) reported a spacing of 10 cm or 1 to a maximum of 4 per 100 cm^2 at the bottom of thick first-year ice. It is noted that the cross sectional areas of the brine channels referred to in the study of Lake and Lewis (1970) were larger than those estimated from my analysis. However, Martin (1979) included brine channels ranging from 1 to 10 mm in diameter, which encompass the size of channels in our investigation. Both of these previous studies were carried out on extracted ice samples with observations made at temperatures lower than *in situ* conditions. This may have affected the apparent number, size and distribution of the channels.

The discrepancy between my observations and those of Lake and Lewis (1970) and Martin (1979) can be further explained by the relatively short existence of smaller brine channels at the ice bottom. Figure 5.8b shows circular patches the size of small brine channels that had a peak of pixel biomass in their centers. This observation evidences that these were channels sealed off which allowed algae to occur over the channel. Brine channels have been shown to neck (exhibit lateral growth) near the ice bottom where an outflow of cold salty brine is followed by an upward convection of less salty seawater which freezes to the side walls of the brine channel (Niedrauer and Martin, 1979). Eventually, density gradient and hydrostatic pressure forces no longer exist, or these forces cannot overcome opposing forces associated with the size of the channels causing them to become stagnant (Lake and Lewis, 1970; Niedraurer and Martin, 1979; Weeks and Ackley, 1982). Finally, the channels seal off, becoming inclusions in the sea ice which have been observed in numerous studies (e.g., Martin, 1979; Cole and Shapiro, 1998; Cottier et al., 1999; Light et al., 2003).

The temporary existence of these brine channels is supported by observations of channels on the order of 10 to 50 cm in length in thick sea ice (Martin, 1979). We note that the higher brine channel number densities observed in this study were similar to observations for thin (new) ice which range between 3 and 17 per 100 cm^2 (Wakatsuchi and Saito, 1985; Cottier et al., 1999). Furthermore, in melting thick ice, where number densities were a result of sealed channels being reactivated, observations of 50 mm channel spacing (4 to 9 per 100 cm^2) were made (Cole and Shapiro, 1998).

The larger patches (10 to 30 mm) of very low algal biomass were also associated with brine channels. This was supported by both the circular appearance of the patches and by the presence of a ring of high pixel biomass within the center of a number of these patches (e.g., Fig. 5.8f). It is noted that the brine channel diameters measured within these patches were within the size range of larger channels observed on the images (i.e., > 2.5 mm in diameter). The larger diameter of the brine channels would decrease sidewall friction associated with brine convection, allowing for a greater movement of brine into and out of the channel (Weeks and Ackley, 1982). Therefore, I speculate that these large patches are main brine drainage features where algal biomass near the channels is decreased due to strong localized currents and potentially by local ice ablation. The appearance of 1 or 2 of these channels per image is also comparable to the density of the drainage features observed by Lake and Lewis (1970).

Significant relationships between snow depth and brine channel diameter and number density (Table 5.2), suggested that snow cover may also play a role in brine channel density and size at the ice bottom. The low thermal conductivity of snow has a dominant influence on the temperature of sea ice such that, all things being equal, a thick snow

cover will result in a higher snow-ice interface temperature than under a thin snow cover during early spring. This will correspond to higher internal ice temperatures under the thicker snow cover and therefore, an increased ice fraction above the reported 5% brine volume threshold modelled by Golden et al. (1998). This reasoning is used to explain the significant positive relationship between snow depth and brine channel number density, which is in agreement with other studies where elevated ice temperatures result in higher brine channel densities (e.g., Lake and Lewis, 1970; Cole and Shapiro, 1998; Eicken et al., 2000; Light et al., 2003). The weaker relationship between snow depth and brine channel diameter may be related to either the temporal effect of snow on ice temperature or a measurement limitation associated with the amount of algal biomass in the bottom ice. As air temperatures rise above snow-ice temperature in late spring, the internal ice temperature under a thin snow cover will increase more rapidly than under a thicker snow cover. The higher rate of increasing ice temperature could result in stronger density gradients which would lead to stronger desalination events associated with melt and therefore increase the diameter of brine channels through lateral erosion. The explanation of measurement limitation is related to the significant relationship observed between snow depth and chl *a* biomass and between chl *a* biomass and brine channel diameter (Table 5.2). In this case, the larger brine channel diameter is explained by algal growth masking the visibility of smaller brine channels. Further examination of these results is warranted but not possible with my dataset.

5.4.2 Spatial Distribution of Pixel Biomass

Images of low mean chl *a* biomass showed only small scale patchiness of higher pixel biomass values between crystal plates and around brine channels. The significant

relationship between mean chl *a* biomass and algal patchiness, for low biomass images, suggests mechanisms exist which cause algal biomass to preferentially accumulate along crystal lamellae and brine channels. I postulate that these mechanisms can be either physical or biological in nature. The physical mechanism is associated with brine channel necking. In this case, the outward flux of brine can act to melt ice near the channel at the ice bottom which could also loosen the attachment of algal cells to the ice, such that the inward flux of seawater could dislodge the cells and move them up into the channel followed by deposition on the side walls. The biological mechanism follows that algae are at a growth advantage higher up into the bottom ice between the lamellar plates and along the side walls of brine channels and therefore algal biomass may accumulate there through growth and potentially migration. For example, brine tubes, which occur between crystal lamellae, extend 2 to 3 cm into the ice from the ice-water interface (Lake and Lewis, 1970) and brine channels, which occur at the boundaries of individual crystals, extend 10 to 50 cm in cold ice and up to the surface in melting ice (Martin, 1979). The extension of these features into the ice maximizes space and light availability which can be limiting factors on algal growth (Lengendre et al., 1990; Krembs et al., 2001; Smith et al., 1988; Cota and Horne, 1989). Further, brine convection associated with tubes and channels would ensure a regular supply of nutrients, particularly under a growing ice sheet (Reeburgh, 1984). When brine channels seal off, it would be possible for algae to grow, or move, under the sealed tube/channel where light and space are maximized resulting in a circle of algal biomass as was observed (Fig. 5.8b).

On high biomass images, the smaller size structure was not observed in the variogram analysis. This suggests that a potential threshold of mean chl *a* biomass may exist

between 20 and 34 mg chl *a* m^{-2}, above which other factors can become more important in determining the microscale spatial distribution of algal chl *a* biomass. On some of the images the observed nugget increase at small start lags was likely the result of the crystal substructure which was slightly obscured by algae occurring across the lamellae on these images.

Larger scale patchiness of 10 to 26 mm was observed on the high biomass images. The larger size structure corresponded to roughly circular patches of low pixel biomass on the images, which is most readily observed on the image from day 125 (Fig. 5.2a). The circular pattern implies a link to brine drainage features. One explanation for the pattern includes the physical removal of algal biomass near brine holes where salty brine outflow can cause local ice ablation resulting in the removal of algae from the ice. For example, on images where algae were hanging from the ice bottom, pixel biomass was very low over an area surrounding the channels (e.g., Fig. 5.8e). Speculating that localized water currents associated with brine drainage could act to remove algae hanging in the water column led to my assumption that these were active brine drainage channels. It was also evident that brine channels joined together to form larger holes at the ice bottom where a greater convective flow can occur (Weeks and Ackley, 1982). Furthermore, large bare patches observed on most high biomass images appeared to represent main brine drainage channels where, in some images, pixel biomass was near zero.

An additional mechanism to the physical removal of algal biomass includes a potential growth advantage for algae away from the brine channels. Results from dye experiments of Niedrauer and Martin (1979) showed seawater to move as fronts into the skeletal layer peaking in between main brine outflow points. Therefore, the front peaks of seawater

influx into the skeletal layer would maximize local nutrient re-supply, providing a potential growth advantage, particularly for algae higher up in the skeletal layer.

Grazers must also be considered here as having a potential to remove algae from the bottom ice and therefore affect the microscale distribution of algae. Previous studies have shown that copepods, which are numerically abundant in the Resolute Bay region, feed mainly on ice algae during the time period of our study (e.g., Michel et al., 1996; Hattori and Saito, 1997). However, a question remains whether they forage on ice-bound algae or on algae that has been sloughed from the ice due to melting mechanisms. Indirect evidence has been presented that at least a small fraction of the copepod diet must come from ice attached algae (e.g., Michel et al., 1996) and other grazers, such as amphipods, do directly feed on algae attached to the bottom ice (e.g., Werner, 2000). Unfortunately, I cannot quantitatively determine the influence of grazers on the ice bottom. However, the circular pattern in algal patchiness observed in our study provides evidence for a more direct connection to brine channels.

5.4.3 Temporal Pattern in Algal Biomass

It was apparent in my study that over a very short period the ice algae dropped from their location within the ice to hang into the water column while anchored to the ice between the lamellae. Due to the rapid occurrence of algae into the water column, I do not believe these algae represent typical sub ice algal communities as described in Horner et al. (1992) and references therein. As an alternative, the change in biomass location observed in our study was most likely part of a mid bloom sloughing event. Comparison with water currents near the ice bottom (Fig. 5.4b) show that the temporal pattern in algal biomass distribution was in phase with the spring/neap tidal cycle. The appearance of

algae hanging into the water column coincided with neap tide followed by removal of the hanging algae with the spring tide and appearance of algal clumps, which remained somewhat buoyant in the water column floating and reattaching to the ice bottom. Silicic acid and nitrate concentrations have been observed to vary with the tidal cycle (e.g., Gosselin et al., 1985; Cota et al., 1987) and ice algae have been shown to become nutrient limited during neap tides (Cota et al., 1987), followed by at least one observation of a sloughing event in algal biomass (e.g., Cota and Horne, 1989). Therefore, I speculate that the observations in our study represent a sloughing event that may have been associated with nutrient limitation, but ultimately influenced by tidal forcing. Further investigation of the actual cause and importance this temporal change in algal biomass distribution is warranted as we can only speculate with our dataset.

5.5 Summary and Conclusions

In this chapter I have explored the microscale patchiness of ice algal chl *a* biomass and linkages with bottom ice features using an *in situ* photographic technique. My observations of brine channels showed that their number density at the bottom of thick ice was equal to that of thin ice and melting ice observations and therefore, may be greater than previously considered through observations on extracted thick ice samples. The bottom ice crystal lamellae and numerous brine channels at the ice bottom are also linked to the small scale patchiness (~ 1 to 3 mm) of pixel biomass over areas of low chl - *a* biomass supporting the hypothesis that these features provide local maxima of light, space and nutrients and therefore favor algal growth. However, areas of higher algal chl *a* biomass exhibited only larger scale patchiness (~ 10 to 26 mm), which could result from

brine drainage acting to augment sloughing of algae, likely associated with local ice ablation near the brine channels at the ice bottom.

The photographic technique provided unique *in situ* microscale observations of the bottom ice, with the potential to enhance studies of physical-biological coupling operating at the ice bottom. However, the technique does have limitations related to the assumptions made in calibrating images to chl *a* biomass and sensitivity of the camera. In the Chapter 6, I show that normalized difference indices of spectral transmitted irradiance can be used to remotely estimate ice algal biomass. Therefore a spectral radiometer could be used in conjunction with a camera to overcome some of the assumptions in ice algae chl *a* biomass estimation for the bottom ice images. We also note that in order to extend the technique beyond the ice algal growth season, a buoyant dye might be used in place of algal biomass to highlight features of the ice bottom.

Over the last two chapters, I have shown that different scales of physical variability affect the accumulation and loss of algal biomass. Over space these scales range from micrometers through millimeters associated with the bottom ice structure to meters through hundreds of meters associated with the overlying snow cover and thermodynamic state of the ice cover. Whereas over time, scales of physical variability range from days associated with blowing snow events to weeks associated with the neap-spring tidal cycle. It was noted in the conclusions of Chapter 4 that a method has yet to be developed which can remotely estimate algal biomass. In the next chapter, I explore in detail the influence of snow cover and algal biomass on the spectral dependence of transmitted irradiance through snow-covered sea ice in an effort to remotely estimate ice

algal biomass and through association a means to study the effects of changing environmental variables on ice algal biomass.

CHAPTER 6: Influence of snow cover and algae on the spectral dependence of transmitted irradiance through sea ice

6.1 Introduction

In the two preceding chapters, I examined how the high spatio-temporal variability of physical factors in the sea ice environment induces variability on ice algal biomass. This work highlighted the need for both extensive spatial and time-series (i.e., point location) sampling to further develop biophysical relationships from in-situ observations. However, extensive spatial sampling remains limited due in part to limitation in field methods and non-invasive time-series measurements are currently non-existent.

Traditionally, measurements of ice algal biomass have involved destructive and/or time intensive techniques. These techniques include sample collection via: ice cores (Cota and Horne, 1989), subice suction corers (Welch et al., 1988) and diver operated "slurp guns" (Gosselin et al., 1990). Welch and Bergmann (1989) carried out an extensive spatial study using a purpose-built light scraper where measurements of photosynthetically active radiation (PAR) were made at the ice bottom, then at 2.5 cm into the ice. They observed a negative relationship between the attenuation of PAR through the 2.5 cm layer with chlorophyll *a* (chl *a*) concentrations estimated using traditional techniques. However, the light scraper technique was destructive, impeding its use for time-series observations. More recently, an underwater pulse-amplitude-modulated fluorometer (Diving-PAM) was used to estimate chl *a* concentrations at the ice bottom (Rysgaard et al., 2001). The Diving-PAM provided a non-invasive technique that could be used for both spatial and time-series measurements at a horizontal resolution of up to 1 cm.

However, the instrument had to be deployed by divers making the technique fairly time intensive and measurements were restricted to ~1 cm of the bottom sea ice due to reflectance properties of the ice (Rysgaard et al., 2001).

The use of the spectral distribution of light transmitted through the sea ice provides the potential for a quick non-destructive technique to remotely estimate algal biomass throughout the entire sea ice volume. Current spectral sensors and recent advances in automated underwater vehicle (AUV) technology will also allow the application of this technique over large spatial scales never before examined. Maykut and Grenfell (1975) first observed the effect of ice algae on the spectral distribution of light beneath first-year sea ice. Legendre and Gosselin (1991) later provided evidence that a relationship may exist between a spectral transmission ratio (T671:T540 nm) and chl *a* concentration. This spectral ratio was applicable for determining algal biomass from its spectral properties; however snow also has a strong influence at these wavelengths (Perovich, 1990). Thus, this spectral transmission ratio may have been influenced by negative and positive relationships that can exist between snow depth and biomass due to both optical and thermal properties of the snow cover (Gosselin et al., 1986; Welch and Bergmann, 1989; see Chapter 4). Perovich et al. (1993) theoretically demonstrated, with the support of a small dataset, the strong dependence of two spectral ratios, T600:T450 and T700:T600, on algae and snow depth, respectively.

The modeling effort of Perovich et al. (1993) highlighted the need for a more detailed *in situ* data collection of ice algal biomass combined with high resolution spectral transmission measurements through snow-covered sea ice. Such a dataset was collected during the Carcajou'03 field program (see Chapter 3). In this chapter, I take a

comprehensive look at the spectral dependence of transmitted irradiance on snow and ice algal biomass through observational and theoretical data. I employ the use of normalized difference indices (NDI) instead of transmitted irradiance ratios due to their value range normalization of -1 to 1 for easier inter-comparison of results and their more linear dependence on snow depth and ice algal biomass. I conclude with a discussion on the use of NDIs of transmitted irradiance as a method to remotely estimate ice algae biomass and through association a means to study the effects of changing environmental variables on ice algal biomass. I note that the results presented in this chapter have been published in the peer-reviewed literature (Mundy et al., 2007a).

6.2 Analytical Methods

6.2.1 Spectral Correlation Surfaces

Spectral correlation surfaces were constructed to visually examine all possible correlations between the normalized difference index (NDI) with ice algal biomass and NDI with snow depth. NDIs, i.e.,

$$\frac{T(\lambda_1) - T(\lambda_2)}{T(\lambda_1) + T(\lambda_2)} \qquad [6.1]$$

were calculated for all wavelength combinations of λ_1 and λ_2 from transmitted PAR spectra corresponding to specific chl *a* concentration and snow depth measurements. The NDIs for each wavelength pair were then correlated with chl *a* and snow depth, and the resultant Pearson correlation coefficients were placed in two separate matrices with λ_1 and λ_2 as their axes. Each matrix was smoothed using kriging and then plotted in grey-

scale ranging from black (strong negative correlation) to white (strong positive correlation) to create spectral correlation surfaces of biomass and snow depth with NDI, respectively. Spectral correlation surfaces from model output were constructed in a similar fashion, with the exception of not smoothing the data. Correlations were further extracted from each matrix along the offset of $\lambda_2 = \lambda_1 - 4$ to examine the near diagonal of the matrices more closely. These plots provide a visual key to both measured and modeled correlations for use in selection of appropriate NDI wavelength combinations.

6.3 Results and Discussion

6.3.1 Environmental Conditions

Snow depth over the sampling sites averaged 16.2 cm, with a range of 2.6 to 38.6 cm. Snowpacks consisted of 2 to 3 visually distinguishable layers, consistent with previous statistical analyses of snow geophysical properties in this region (Barber et al., 1995; Papakyriakou, 1999). A bottom layer (9 to 22% of snowpack) was characterized by large angular snow grains (4.8 ± 1.4 mm^2), low density (319 ± 36 kg m^{-3}), and high salinity (4.9 ± 2.3) and percent water volume (1.6 ± 1.6%). A wind-packed surface/middle layer (33 to 90% of snowpack) contained medium sized round snow grains (1.28 ± 0.24 mm^2), high density (385 ± 24 kg m^{-3}), low salinity (0.8 ± 0.4) and negligible wetness. Further, a transient layer of fresh or newly drifted dry snow (0 to 56% of the snowpack) consisted of small dendritic to round snow grains (0.88 ± 0.40 mm^2), and low density (296 ± 37 kg m^{-3}) and salinity (0.16 ± 0.3). Snow properties did not noticeably change during the study. Ice thickness ranged from 125 to 175 cm, averaging 157 cm throughout the study

period. The ice sampled was smooth landfast first-year sea ice with a surface 10 to 15 cm frazil layer, a middle layer of columnar crystals and a bottom skeletal layer of 2 to 5 cm.

Snow depth, ice thickness and chl *a* concentrations did not correlate with time (data not presented). However, significant inverse relationships were observed between snow depth and ice thickness and snow depth and bottom ice chl *a* concentrations (Fig. 6.1). These relationships strongly support the controlling effect a snow cover can have on algal biomass and ice thickness in early spring through its radiative and thermal properties, respectively. The small grain sizes of snow act as efficient scatterers of light (Warren, 1982) resulting in light transmission through the snow ice matrix being controlled by the overlying snow cover (Perovich, 1990). Therefore, the negative log-linear relationship between snow depth and ice algal biomass (Fig. 6.1) represents light limitation on algal growth, which has been previously documented (Gosselin et al., 1986; Welch and Bergmann, 1989). The negative linear relationship between ice thickness and snow depth reflects the thermal influence of the overlying snow cover on ice growth. Due to its low density and high basal salinity, snow over first-year sea ice has low thermal conductivity and diffusivity (Papakyriakou, 1999), acting as a thermal insulator between the atmosphere and sea ice. Interestingly, the residuals of the two relationships are significantly correlated with each other ($r = 0.32$, $p < 0.05$). Provided that snow cover does control ice algal biomass and sea ice thickness, I suggest that this correlation between residuals can be explained by the transient nature of the snow cover, which is largely dependent on blowing snow events (see Chapter 4). That is, event driven snow

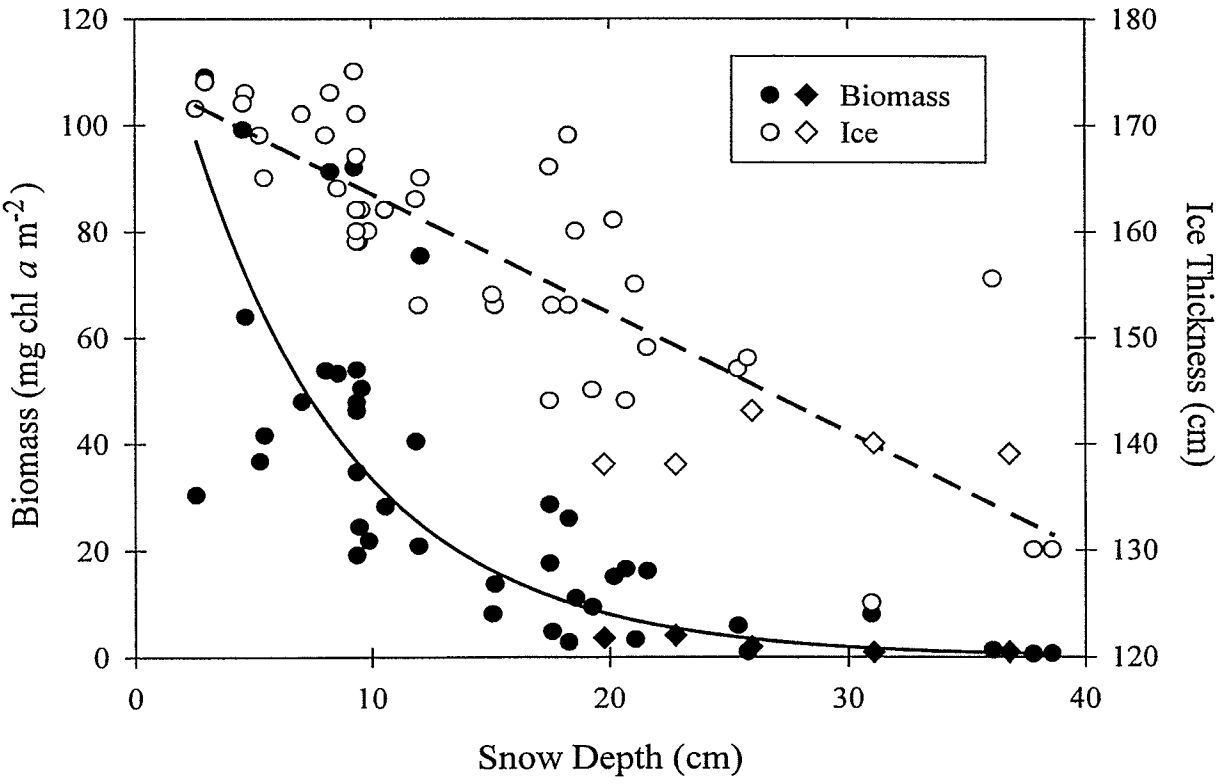

Figure 6.1. Ice algae biomass ([chl *a*]) and ice thickness (H) *versus* Snow depth (h_{snow}). Relationships plotted are [chl *a*] = 141 exp(–0.144h_{snow}) (R^2 = 0.81) and H = –1.13h_{snow} + 175 (R^2 = 0.70). See text for significance of diamond denoted points.

depth changes will result in coincident horizontal shifts of biomass and ice points on Figure 6.1 as the biological and thermal responses to snow depth changes operate on much longer time scales. With the spatial point measurements collected in this study, I can only speculate on these different temporal processes, making the need for a method of time-series measurements of ice algal biomass even more pertinent.

Figure 6.1 also highlights the need to support field data with theoretical data to examine the effects of snow and algal biomass on the spectral transmitted irradiance of PAR, independent of a snow-ice-biomass relationship. The effects of ice thickness on the spectral distribution of transmitted light are assumed negligible compared to that of snow and algae following Perovich et al. (1993).

6.3.2 Light Attenuation Observations and Model Inputs

Over the biomass and snow depth ranges observed during the field observations, snow and ice algae had a similar effect on the magnitude of PAR attenuated in the snow-ice matrix (Fig. 6.2a). However, the spectral effect on PAR transmission differs greatly. The spectral effect of algal biomass on transmitted irradiance is apparent from increasing chl *a* concentrations and decreasing snow depth which cause a shift towards longer wavelengths and a narrowing of the spectral band of maximum PAR (Fig. 6.2a). In Figure 6.2b spectral attenuation curves were estimated using measured spectral irradiances transmitted through the snow and ice (E_Z) and a reference surface irradiance curve (E_0) to calculate the relative attenuation of light ($\ln(E_0/E_Z)$). The spectral attenuation curve for a thick snow cover and negligible algal biomass shows a minimum near 470 nm, increasing on either side in a monotonic fashion similar to other

observations and models (Grenfell and Maykut, 1977; Warren, 1982). Therefore, this curve is assumed to represent relative snow cover attenuation. As algal biomass increases and snow depth decreases, the relative attenuation curves show new peaks and troughs, which increase with increasing biomass, demonstrating the effect of spectral absorption in the algal layer.

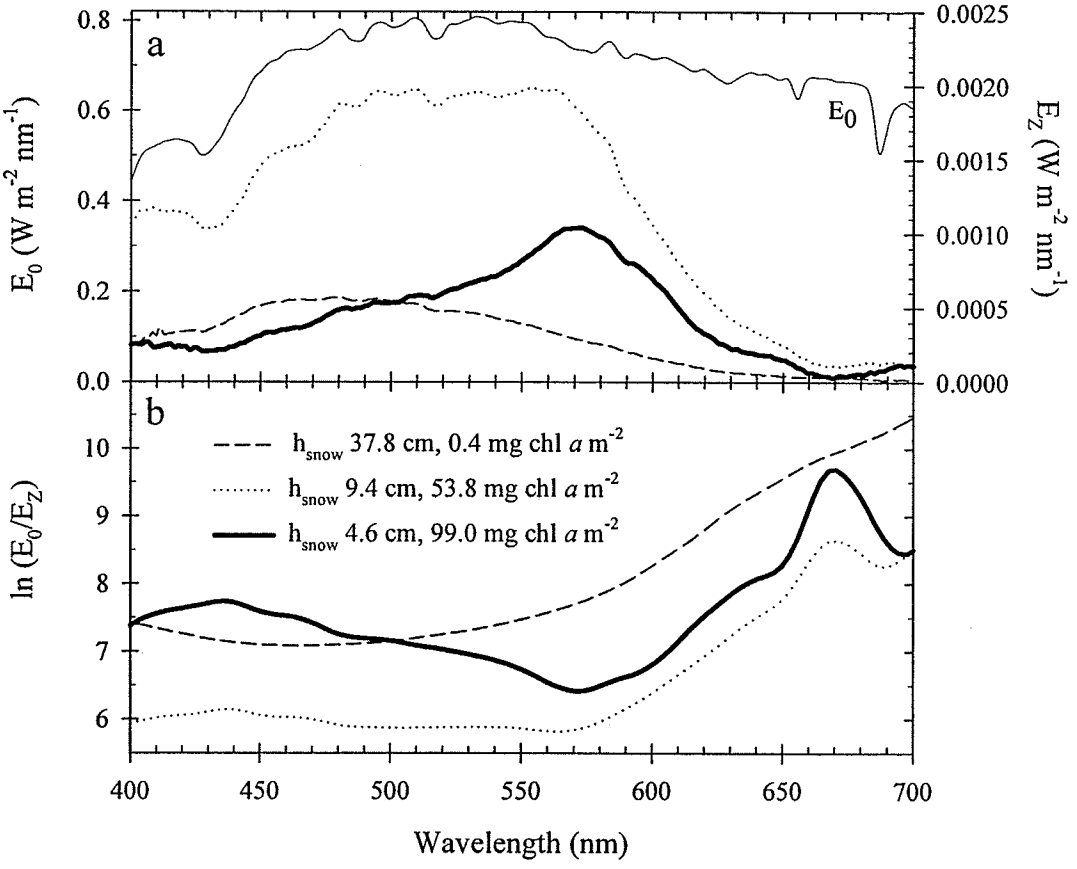

Figure 6.2. Smoothed spectral surface, E_0, and transmitted, E_Z, irradiance (a) and relative attenuation, $\ln(E_0/E_Z)$, (b) curves for varying snow depths (h_{snow}) and chl *a* concentrations.

Matching observed transmitted irradiance spectra to bulk model parameterizations described in Perovich (1990), absorption and scattering properties for snow and ice

corresponded to wet snow and cold blue ice, respectively. Since the physical observations of the snow cover showed that the snow was not "wet" during our field study, I examined the field measurements closer. Five data points are highlighted as diamonds in Figure 6.1. These points represent measurements where snow depth had a range of 20 to 37 cm, ice thickness was nearly constant at 140 cm (± 2 standard deviation) and chl *a* concentrations were less than 3 mg chl *a* m^{-2}. The measurements of surface and transmitted PAR irradiance from these data were used to estimate the PAR diffuse attenuation coefficient (κ_{PAR}) for wind-packed layers of snow using the slope from a linear regression of snow depth (m) against relative PAR attenuation ($\ln(PAR_0 / PAR_Z)$). The resultant κ_{PAR} was equal to 11 m^{-1} (Fig. 6.3; $R^2 = 0.98$). This value fits within the lower range of κ_{PAR} observed in Chapter 4 for similar air temperatures and time of year.

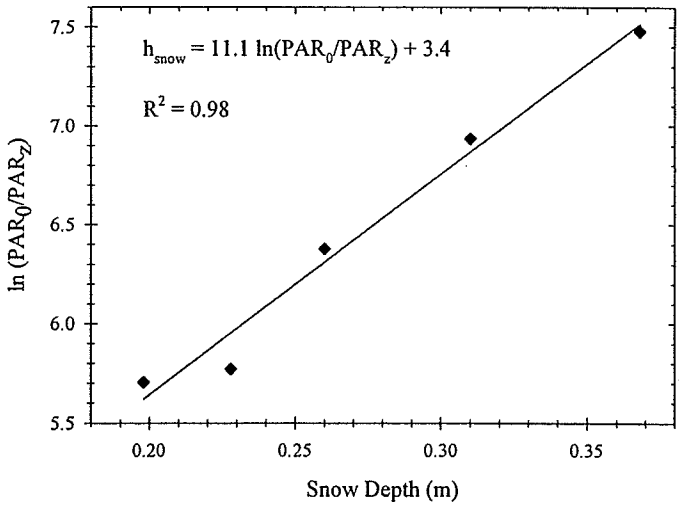

Figure 6.3. Snow depth (h_{snow}) versus the relative attenuation of PAR ($\ln(PAR_0 / PAR_Z)$) through snow-covered sea ice with similar ice thicknesses and negligible biomass concentrations.

The spectral attenuation measurements of Grenfell and Maykut (1977) (i.e., source of the model parameterizations in Perovich (1990)) may have been larger due to smaller

snow grain sizes and particulates in the snow. Particulates are incorporated in the snow and sea ice during ice formation through scavenging by frazil ice (Reimnitz et al., 1990), or from above as a part of ice nuclei scavenged in the atmosphere by falling snow and through direct deposition (Warren and Wiscombe, 1980). Using the WW model, Warren (1982) needed to add 0.1 ppmw of soot using a snow grain radius of 110 μm to match the albedo and encompass the range of the dry snow attenuation coefficient observed in Grenfell and Maykut (1977). Running the WW model with the average drifted snow layer grain radius and density of 638 μm and 385 kg m^{-3}, respectively, 0.24 ppmw soot had to be added to match κ_{PAR} equal to 11 m^{-1} (Fig. 6.4). A strong decrease in spectral dependence of the modeled curve with the added soot is evident in comparison to the wet snow attenuation curve of Perovich (1990), as was also observed by Warren (1982). It is noted that the spectral range of the WW model curve matches this study's observations closer than parameterizations used by Perovich (1990; Fig. 6.4 and Fig. 6.2b). Therefore, I used the WW model output for κ_λ^{snow} in the two-stream radiative transfer model described in Chapter 3. In order to incorporate this attenuation curve into the two-stream model, a scattering coefficient for snow had to be applied. The snow scattering coefficient was determined to be 184 m^{-1} through iterations of the two-stream model to match κ_{PAR} equal to 11 m^{-1} using the cold dry snow parameterization.

The chl *a* specific absorption coefficient for the model was obtained from field data. Given the strong relationship between biomass and snow depth, when snow is low, biomass will be exponentially greater and dominate changes in the spectral distribution of transmitted irradiance. Thus, the deep snow attenuation curve was used as a reference to subtract the effect of the overlying snow and ice matrix from the high biomass curve

using equation (3.9). The result is a chl *a* specific absorption curve, highlighting the contribution of algae to spectral attenuation through the snow-ice matrix (Fig. 6.4). A similar approach was taken by Maykut and Grenfell (1975) and Perovich et al. (1993).

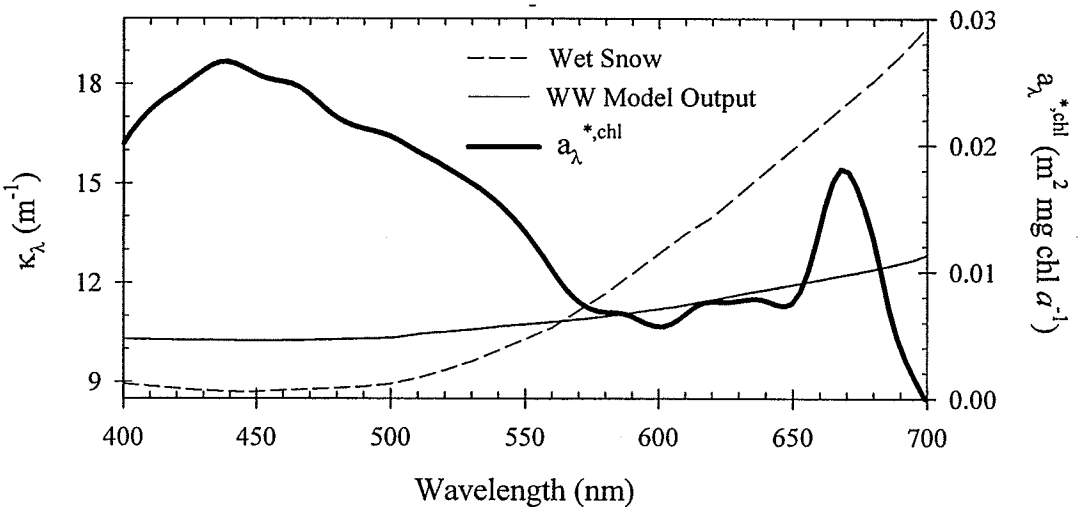

Figure 6.4. Model parameterizations of the chl *a* specific absorption coefficient ($a_\lambda^{*,chl}$) and spectral diffuse attenuation coefficients (κ_λ) of wet snow (Perovich, 1990) and WW model output for a snow grain size, density and soot concentration of 638 μm, 385 kg m^{-3} and 0.24 ppmw, respectively.

The peaks and troughs of the specific absorption curve are similar to other *in situ* measurements of spectral absorption curves for ice algae (Legendre and Gosselin, 1991; Perovich et al., 1993; Arrigo and Sullivan, 1994). These peaks are caused by relative contributions of photosynthetic and accessory pigments. In particular, contributions from chl *a* (440, 620 and 670 nm), chl *c* (460, 585 and 630 nm) and fucoxanthin (500 nm) are evident (Bidigare et al., 1990).

6.3.3 Spectral Correlation Surfaces

The NDI correlation surfaces with biomass (Fig. 6.5a) and snow (Fig. 6.5b) illustrate a strong negative correlation with each other. This inter-correlation of surfaces is influenced by the strong relationship between biomass and snow (Fig. 6.1). The most prevalent feature of the correlation surfaces is observed near the diagonal (Fig. 6.5a, b insets). Abrupt changes in the sign of correlation coefficients along the diagonal occur near the wavelengths of 440, 600, 620, 650, and 670 nm. Strongest correlations with NDI occur at wavelengths less than 570 nm for both algae (maximum $|r| = 0.95$) and snow (maximum $|r| = 0.86$). Moving away from the diagonal on the NDI-algae correlation surface, the strength of correlation coefficients tends to decrease with some exceptions where strong correlations: follow λ_1-values centered at 660 nm and λ_2-values centered at 610 nm until they intersect on the correlation surfaces; occur near λ_1-values centered at 685 nm; and within the range of λ_1-values between 470 and 525 nm and λ_2-values between 440 and 485 nm. The sign changes along the diagonal of the correlation surfaces (Fig. 6.5a, b) are due to inflection points in spectral attenuation and absorption curves (Fig. 6.3), which cause the NDIs to be positively or negatively correlated with biomass or snow depending on which side of the peak the wavelength combination is derived from.

A comparison between the correlation surfaces and spectral attenuation properties of snow and algal biomass show that the inflection points only line up with the algae attenuation curve (Fig. 6.3). This suggests a dependence of the NDIs on algal biomass

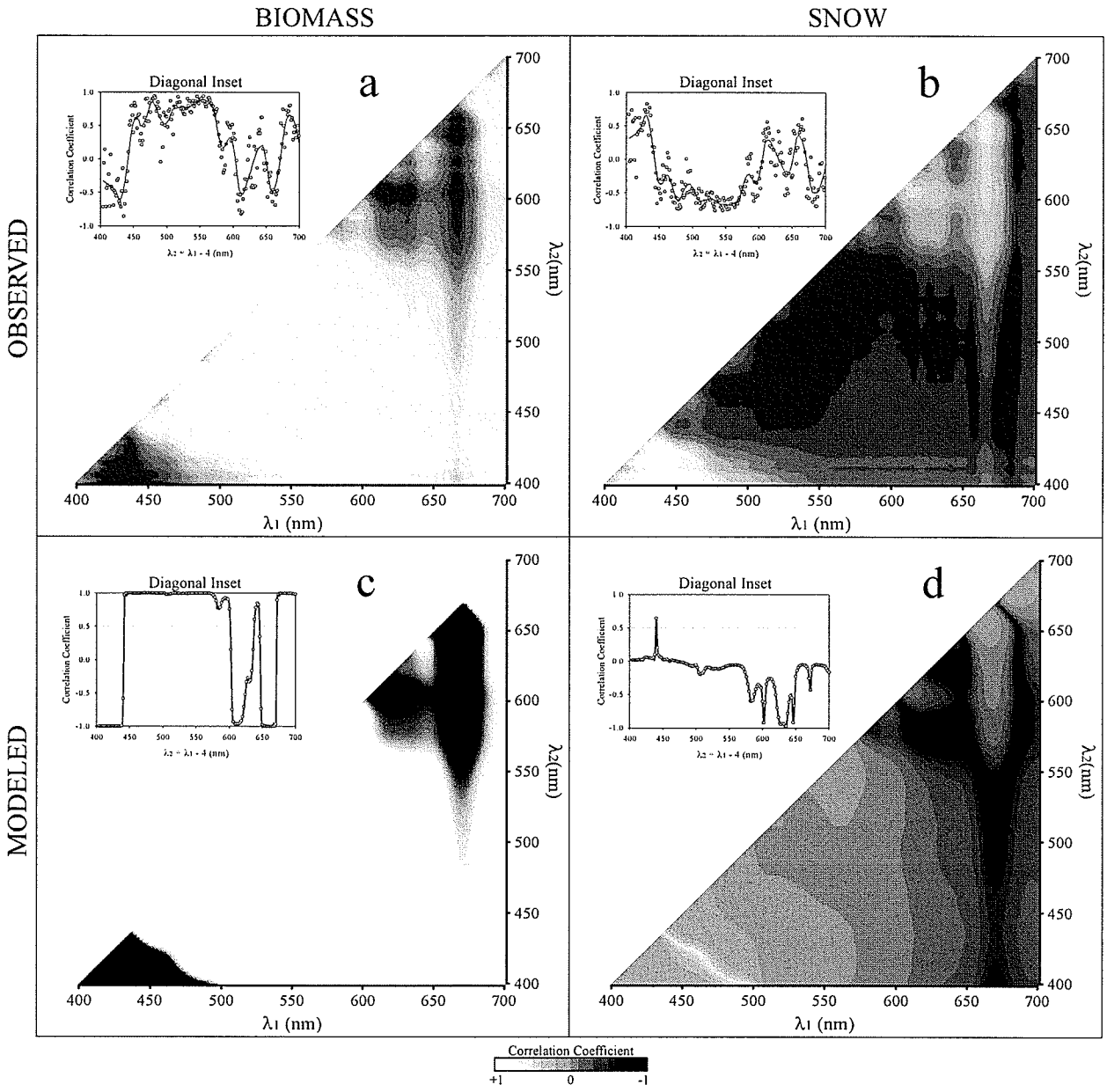

Figure 6.5. Observed and modeled correlation surfaces of normalized difference indices, $[T(\lambda_1) - T(\lambda_2)]/[T(\lambda_1)+T(\lambda_2)]$, with algal biomass (a and c, respectively) and with snow (b and d, respectively). Insets of raw correlation coefficients along the diagonal of $\lambda_2 = \lambda_1 - 4$ are plotted. Observed data were smoothed. See text in section 6.2.1 for further description.

rather than snow near these inflection points. Theoretically, NDI correlations where $\lambda_1 > \lambda_2$ should follow the attenuation curves inversely. For example, if spectral attenuation for a particular material is increasing with increasing wavelength, NDIs should be negatively correlated with the material as more light is being transmitted at shorter wavelengths. Therefore, the dependence of the normalized difference indices on algae is particularly evident for parts of algae absorption peaks that follow the snow attenuation curve (i.e., $[440 < \lambda < 470]$, $[600 < \lambda < 620]$ and $[650 < \lambda < 670]$). Indices within these ranges result in a change of sign in the correlation coefficients for snow in comparison to the snow attenuation curve.

It is apparent that the absorption peaks of photosynthetic and accessory pigments provide a stark contrast to the more monotonic changes of snow spectral attenuation. Equation 3.8 shows that the wavelength dependent attenuation coefficient is defined by both scattering and absorption coefficients. At optical wavelengths, scattering in snow and sea ice is generally assumed independent of wavelength as scattering inclusions are significantly larger than the wavelength (Perovich, 1990). Therefore, it is absorption that contributes to changes in the spectral distribution of transmitted irradiance. The scattering coefficient of snow can be very high ($b_\lambda = 800\ m^{-1}$) relative to its constituent absorption coefficients of ice and water ($a_\lambda < 1\ m^{-1}$ at PAR wavelengths; Perovich, 1990). Thus, as snow depths increase, spectral attenuation tends to change more in magnitude than spectral distribution. In contrast, the algae attenuation coefficient is dominated by absorption, resulting in a much stronger change in the distribution of spectral attenuation. This change could be accentuated at small biomass values by potential acclimative

strategies in light-limited algae (Michel et al., 1988; Stramski et al., 2002). Therefore, algae absorption peaks clearly appear in the transmitted irradiance.

To examine the spectral dependence of transmitted irradiance on algae and snow without the influence of a snow-biomass relationship, the 330 spectra from the optical model output were used. Spectral correlation surfaces from the selected spectra were produced for NDI-biomass (Fig. 6.5c) and NDI-snow (Fig. 6.5d) associations. Comparisons between the modeled and observed data show better agreement between NDI-biomass surfaces. The diagonal for the modeled NDI-biomass surface shows inversions of correlation coefficients at the algae absorption peaks, with the strongest correlations observed below wavelengths of 570 nm and near the 670 nm absorption peak (Fig. 6.5c inset).

In contrast to the observed results, the modeled correlations along the diagonal for the NDI-snow matrix are near zero between 400 and 570 nm, with the exception of 440 nm which corresponds to an inflection point along the spectrum of algae absorption and therefore an increase in the absolute correlation coefficient with snow. The wavelength range 400 to 570 nm corresponds closely to the inflection point of the modeled snow spectral attenuation curve (452 nm) and therefore algae absorption should control changes in the spectral distribution of transmitted irradiance at adjacent wavelengths. It is promising to note that this wavelength range also corresponds to the some of the strongest correlations with algal biomass in the observed data. Further, there is more transmitted irradiance available at these wavelengths due to the spectral attenuation properties of snow, contributing to higher precision of under-ice measurements using a spectral radiometer. At wavelengths greater than 570 nm, snow attenuation follows an

almost linear increase and should therefore have a stronger influence on spectral transmitted irradiance (Perovich et al., 1993). However, increases in the absolute correlation coefficients with snow at longer wavelengths is only slightly evident on Figure 6.5b and d, due to the lower spectral dependence of snow attenuation observed and modeled in this study.

6.3.4 Spectral Indices

To examine the relationships between spectral NDIs and biomass, four wavelength combinations were chosen. I based the choices on two criteria, (1) the strength of their correlation coefficients (Fig. 6.5) and (2) proximity to the strong algae absorption peaks of 440 and 670 nm. Under these criteria, the four best wavelength combinations (λ_1:λ_2) in this study are 415:400, 485:472, 663:655 and 686:676 nm (Fig. 6.6a-d, respectively). All NDIs demonstrate a strong relationship with biomass. In particular, the NDI of 485:472 explains 89% of the total variation in biomass. We note that the NDI wavelength combinations are very close to each other. As noted in the previous section, values closer together will be more dependent on algae absorption peaks and less on the smoother absorption curves of snow or ice. The reason for the specific wavelength choices was also due to the 1st criteria, which could have been influenced by spectral signal noise in the radiometer measurements, a problem associated with low light levels at the ice bottom.

In all scatterplots, variability increases toward higher algal biomasses and at very low biomass (i.e., < 1 mg chl *a* m^{-2}). The variability at high biomasses is attributed to the sampling technique I employed. A common problem with core sampling is the loss of algae due to drainage as the core is extracted from the ice (Welch and Bergmann, 1989).

The ice bottom under a thin snow cover tends to desalinate faster than under a thicker snow cover due to lower thermal insulation from the warming spring atmosphere (see Chapter 4). Therefore, the variability would be enhanced at larger biomasses. It is expected that the use of a spectral NDI to estimate biomass will provide a more stable observation for both spatial and time series measurements of ice algal biomass once it is calibrated to the local area.

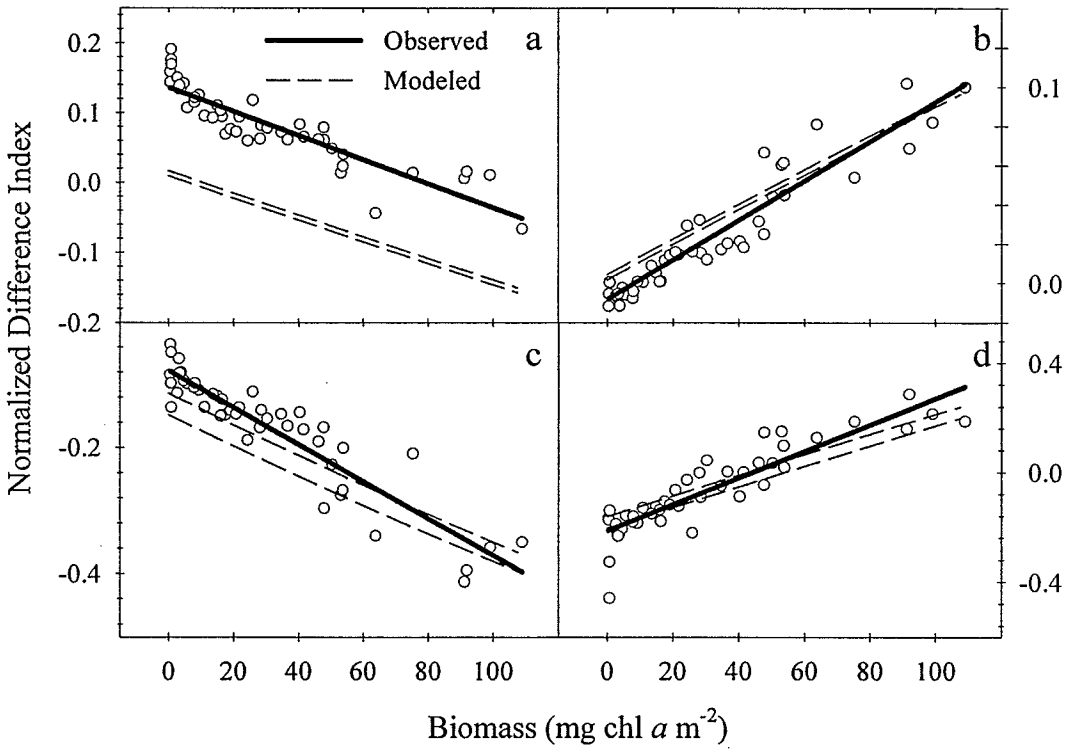

Figure 6.6. Observed (circles) NDIs versus ice algal biomass for wavelength (nm) combinations of 415:400 (a), 485:472 (b), 663:655 (c) and 686:676 (d). Observed relationships (bold line) are: NDI(415:400) = –0.0017[chl *a*] + 0.1364 (R^2 = 0.81); NDI(485:472) = 0.001[chl *a*] + 0.0083 (R^2 = 0.89); NDI(663:655) = –0.0029[chl *a*] – 0.0775 (R^2 = 0.85); and NDI(685:675) = 0.0049[chl *a*] – 0.215 (R^2 = 0.81). The top and bottom dashed lines represent modeled output for 0 and 40 cm snow depths, respectively.

Very low algal biomasses corresponded to very high snow depths in this study. Therefore, snow would have a dominant effect on spectral attenuation of irradiance under

these conditions. Variability in the relationships at these biomasses is smallest for the NDI combination of 485:472 nm, which is also the ratio in closest proximity to the 470 nm inflection point of snow spectral attenuation observed in this study (Fig. 6.2b). Thus, the effect of snow on the spectral distribution of irradiance at these wavelengths would be the smallest, supporting the influence of snow at these low algal biomass values.

A comparison between observed and modeled data is also shown in Figure 6.6. The slope of the model output agrees quite well with the observed data. This demonstrates that the two-stream model used in this study can reproduce reasonable algae spectral attenuation for various conditions. The model plots of 0 cm (upper dashed lines) and 40 cm (lower dashed lines) snowpacks demonstrate the theoretical dependence of the different NDIs on snow through vertical offsets (Fig. 6.6). Substantiating the correlation surface examination, snow has the strongest effect at ratios near the 670 nm peak (Fig. 6.6c and d), however, the effect is not substantial over snow depths typically observed on smooth landfast first-year sea ice in the Arctic. The small effect of snow on all NDI relationships with algal biomass is attributed to the low spectral dependence of snow attenuation due to the presence of particulates in the snow and sea ice.

The linear regressions of NDIs with algal biomass represent curves which summarize numerous transmitted spectra and algal biomass measurements. Therefore, discrepancies between observed and modeled relationships can also be used in a diagnostic application with the two-stream model to examine why they occur. For example, Figure 6.6a shows a large offset between the observed and modeled data. To increase the offset without changing the slope, an increase in the diffuse attenuation coefficient (κ_λ) needs to be

accomplished. In order to encompass the field data, κ_λ of ice at 400 nm had to be increased from 1.29 m^{-1} in the original model to 1.465 m^{-1}, while keeping κ_λ at 415 nm steady. It is speculated that colored dissolved organic matter (CDOM) present in sea ice (Belzile et al., 2000), which absorbs more strongly at shorter wavelengths, could have caused this spectral difference in κ_λ.

6.4 Summary and Conclusions

In this chapter, I have provided a comprehensive look at the spectral dependence of transmitted irradiance on snow and sea ice algal biomass to study radiative processes within the snow/sea ice system. This work has led to the development of a non-invasive technique for algal biomass estimation. Scattering dominates attenuation in the snow, resulting in a minimal influence of snow depth on the spectral shape of transmitted irradiance. In contrast, algae absorption peaks clearly appear in the transmitted irradiance spectra due to a greater role of absorption in the bottom algal layer, which supports the use of a single normalized difference index (NDI) of transmitted irradiance to estimate ice algal biomass. The results show that snow has little effect on transmitted spectral irradiance at wavelengths between 400 and 570 nm. In particular, the NDI wavelength combination of 485:472, which is near the minimum inflection point of the snow spectral attenuation curve at 470 nm, explained 89% of the total variation in algae biomass.

The strong dependence of algal biomass on snow thickness within the sampling region warranted the comparison of observed data with output from a model where biomass, snow and ice can be independently controlled. A two-stream radiative transfer model (Dunkle and Bevans, 1956; Perovich, 1990) was successfully tuned to field data using a

single chl *a* specific absorption coefficient derived from the difference between the transmitted spectra of a high snow, low algal biomass and low snow, high algal biomass site. Deviations between model output and field observations pointed to a difference in spectral diffuse attenuation coefficients for snow. Using the Warren and Wiscombe (1980) radiative transfer model for snow, it was determined that a soot concentration of 0.24 ppmw closely matched the field observations. The inclusion particulates resulted in a decreased spectral dependency of snow attenuation compared to observations by Grenfell and Maykut (1977). These results highlight the fact that using transmitted irradiance to estimate snow thickness will be very difficult if not impossible, unless detailed information of the particulates in the snow cover are known. Furthermore, this highlights work such as Light et al. (1998) to make measurements of particulates in snow and ice to improve the treatment of spectral attenuation over existing model parameterizations. Further adjustments of the model parameterizations to match the observed NDI-biomass relationships also suggested the potential that additional absorbing constituents in the sea ice, such as CDOM, could be derived through the use of spectral transmitted irradiance.

The application of a NDI for biomass estimation in studies involving the use of autonomous underwater vehicles for near-ice measurements provides the potential to improve our understanding of sea ice ecosystem processes at large spatial scales. The method could also be used for true time series observations to support the further development and validation of ecosystem process models. Both of these points show promise of a solution for the lack of spatial and temporal coverage of biological measurements as outlined in the conclusions of Chapter 4. The use of spectral transmitted

irradiance to estimate ice algal biomass has many advantages. The method: is quick and non-invasive; measures algae within the entire ice matrix; would be free of sampling error associated with the physical collection of ice algae; and could be relatively inexpensive if sensors for specific wavelengths (e.g., 472 and 485nm) are used.

However, the method is not without difficulties. The success of this method could be influenced by shifts in the spectral distribution of transmitted irradiance through: variability in spectral attenuation coefficients of snow and ice, acclimative strategies of algae to temperature, nutrient and light limitation (Stramski et al., 2002) and changes in algal community species composition (Moberg et al., 2002). Alternatively, if an improved spectral radiative transfer model is developed for the purpose of estimating ice algal biomass, these influencing factors could theoretically be used to gain information on snow, ice, and algal physiology and community composition. Therefore, more detailed observations of snow, ice and algae optical properties should be collected to improve existing models to assist in this geophysical inversion of biomass from spectral irradiance. In the next chapter, I will apply the improvements made to the parameterizations of the model for the study region to the ice algal model. A subsequent modeling analysis will be undertaken to address several of the process related issues which have been raised in Chapters 4 and 5.

CHAPTER 7: Simulating variability in bottom ice algal biomass

7.1 Introduction

The underlying hypothesis of my dissertation follows that the history and distribution of snow over sea ice control the magnitude of ice algal biomass through both thermophysical and radiative processes. Results presented in Chapter 4 supported this hypothesis indirectly and suggested that over the spring transition period examined in the study, thin snow covers were associated with a thermal effect causing sloughing of algae, whereas under deep snow, algae were still light limited and thermally insulated from the warming atmosphere. However, I was limited in the analysis of my hypothesis due to the destructive and time intensive methods which were available at the time of my study. In Chapters 5 and 6, I was successful in the development of non-destructive methods to estimate ice algal biomass, however I was unable to employ the methods over a successful duration to better examine the hypothesis provided in Chapter 4. Therefore, I change my focus in this chapter from field data to concentrate on the examination of simulated data from an ice algae growth model that was described in Chapter 3. By matching the model to field data and examining sensitivity runs, I will investigate conclusions I drew in Chapters 4 and 5 and in light of these results further investigate the thermophysical state and processes governing my systems diagram (see Figure 1.1).

7.2 Data Input

In order to compare model output to field data, the three different time series of algal biomass separated into low, mid and high snow classes, respectively, were used (see Fig. 4.9). Average snow depths and initial algal biomasses and ice thicknesses were used for each snow class to initialize the models (Table 7.1).

Table 7.1. Model initialization for algal biomass, snow depth and ice thickness per snow class.

Snow Class	Algal Biomass (mg chl *a* m^{-2})	Snow Depth (cm)	Ice Thickness (cm)
Low	40	3.8	156
Mid	40	13.8	150
High	10	28.7	140

7.2.1 Thermodynamic Model

Mentioned in chapter 3, to more realistically model ice growth and ablation in the study area, I used field data from the C-ICE'02 micromet site for LW_D and SW_D as daily input into the thermodynamic model. These data were presented in chapter 4 (see Fig. 4.1). It is noted that the downwelling shortwave data set was intermittent following day 149 due to technical problems (see Table 3.2). Downwelling shortwave irradiance is dependent upon solar zenith angle and attenuation by the atmosphere and clouds. Therefore, the data gaps were filled by copying data from the closest day with a matching daily averaged cloud amount to create an uninterrupted time series of data (Fig. 7.1).

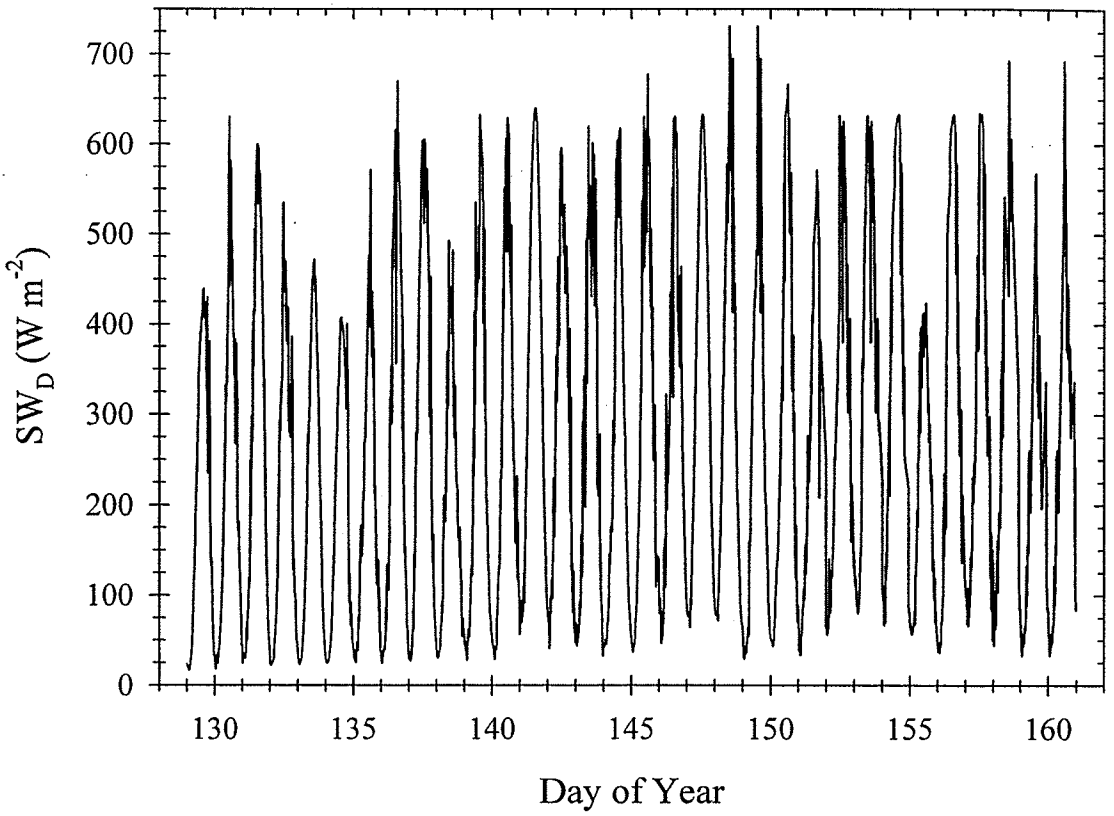

Figure 7.1. Time series (data gaps filled, see text) of 15 minute averaged downwelling shortwave energy used in the model runs.

To test the performance of the one-dimensional thermodynamic model in the study area, the model was initialized with the daily averaged snow-ice temperature profile measured on day 128 (see Fig. 4.2) and snow depth which was measured at the temperature dowel (site B; Fig. 4.7). For the different snow classes, an initial ice temperature profile had to be created. Due to the much lower thermal conductivity of snow, it was assumed that the snow layer limited conductive heat transfer during winter and therefore the daily averaged surface temperature and snow temperature gradient measured at the ice dowel on day 128 was prescribed to the three snow classes. It is noted that this assumption and extrapolation of the temperature gradient to the snow bottom likely resulted in a slight over estimation of snow-ice interface temperature for the high

snow class and under estimation for the low snow class. The ice temperature profile was then linearly interpolated between the extrapolated snow-ice interface temperature and the ice bottom temperature which was set to the model's freezing temperature (–1.8 °C). The initial temperature profiles used in the model runs for each snow class are presented (Fig. 7.2).

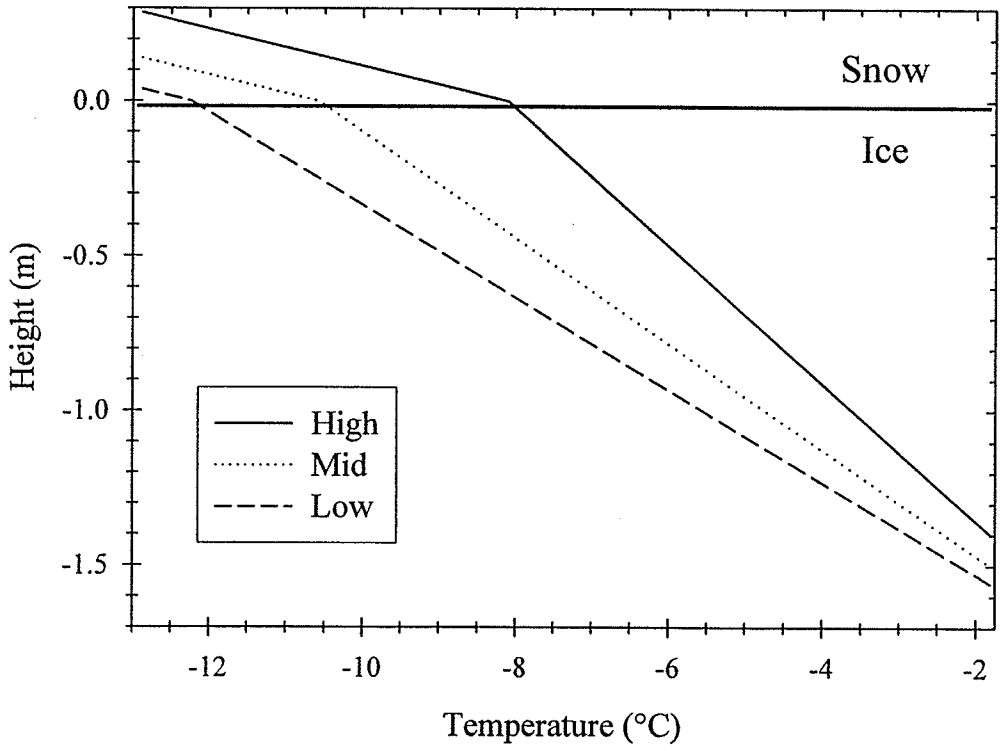

Figure 7.2. Temperature profiles used to initialize the thermodynamic model for the different snow classes.

7.2.2 Radiative Transfer Model

Snow, ice and algal biomass attenuation parameterizations have been presented and discussed in detail within Chapter 6. The only alteration made to the model used in Chapter 6 was a change to the wavelength independent scattering coefficient of snow in order to match the integrated PAR attenuation coefficient, κ_{PAR}, to the time dependent equation presented in Chapter 4 (see Fig. 4.4). The resultant scattering coefficients

ranged from 495 m^{-1} on day 129 to 176 m^{-1} on day 160 to match a κ_{PAR} of 18.0 m^{-1} and 10.8 m^{-1}, respectively.

7.2.3 Ice Algal Growth Model

The ice algae model was originally run with a daily time step as was the thermodynamic model. However, a single time step allowed algal nutrient uptake to greatly exceed nutrient replenishment into the skeletal layer. This caused the algal growth coefficient, μ, to oscillate between zero and just greater than zero with every time step. Therefore, a 15 minute time step, which matched Lavoie et al. (2005), was used to run the radiative transfer model and nutrient fluxes. Running the model in this mode resulted in two outcomes: 1) nutrient fluxes were more gradual and 2) algae were always light limited diurnally. These two effects resulted in a more regular nutrient concentration within the skeletal layer that responded to algal growth requirements. The model was also run with daily mixed layer nutrient concentrations from field data using linear interpolation to fill data gaps. In accordance with Lavoie et al. (2005), initial nutrient concentrations in the skeletal and surface mixed layers were set to 6 and 10 mmol m^{-3}, respectively.

Spectral downwelling PAR was parameterized in the model with consideration of the spectral distribution of surface irradiance under a cloudy and clear sky. A collection of downwelling spectral irradiance measurements for both clear and 100% cloud cover days was obtained. These spectra were set to units of μE m^{-2} s^{-1} nm^{-1} and then normalized to integrated shortwave irradiance (W m^{-2}) by dividing the spectra by coincident measurements of SW_D made at the micromet site. The cloudy ($Cloud_\lambda$) and clear ($Clear_\lambda$)

sky normalized spectra were averaged, respectively (Fig. 7.3). PAR downwelling spectral irradiance ($PAR_{D,\lambda}$) was then parameterized in the model by applying equation (7.1) with SW_D data presented in Figure 7.1 and daily averaged cloud amount (tenths; C_{amt}) which was observed during C-ICE'02 (see Mundy and Barber, 2003):

$$PAR_{D,\lambda} = SW_D[(Cloud_\lambda C_{amt}) + (Clear_\lambda (1 - C_{amt}))] \quad [7.1]$$

Daily averages of integrated $PAR_{D,\lambda}$ matched closely to field measurements (Fig. 7.4). Discrepancies between the parameterized and observed values were due to varying cloud opacities which was not considered, however it is not expected to greatly affect the model outcome over the period examined.

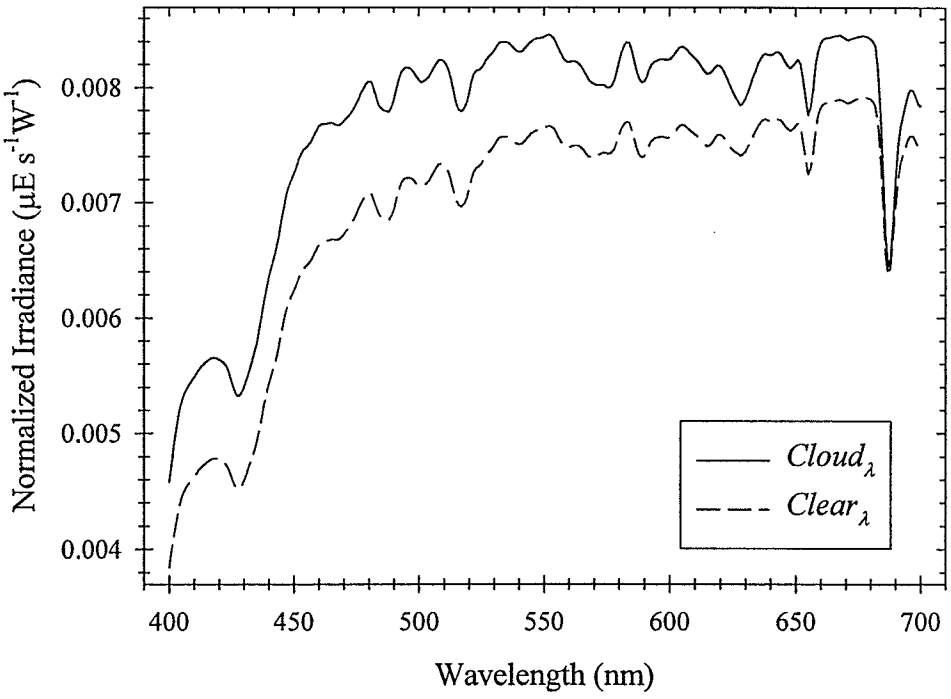

Figure 7.3. Cloudy ($Cloud_\lambda$) and clear ($Clear_\lambda$) sky parameterizations for downwelling spectral irradiance (μE m^{-2} s^{-1}) normalized to SW_D (W m^{-2}).

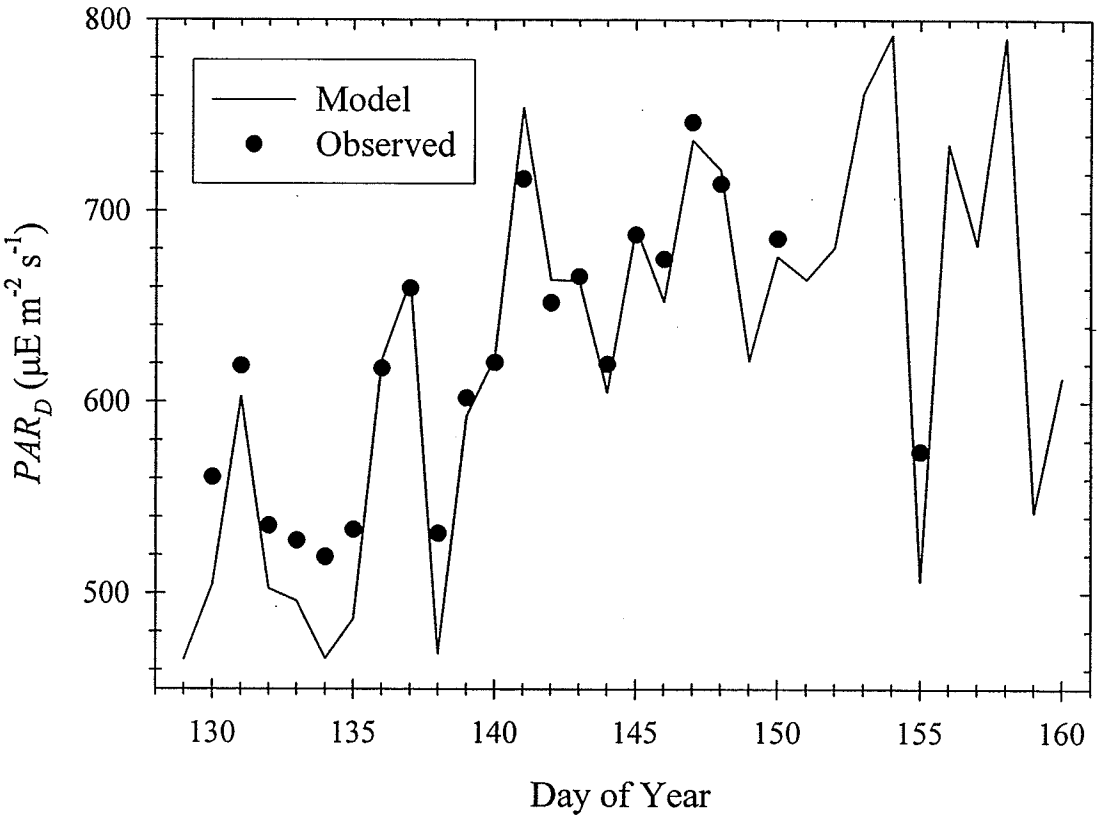

Figure 7.4. A comparison between observed and parameterized model input for daily averaged downwelling PAR.

7.3 Model Performance and Adjustments

7.3.1 Thermodynamic Model

As the thermodynamic model does not consider brine channel enlargement and flushing associated with interior ice melt, negative ice thickness change is not expected to be a good indicator of model performance, particularly for the spring period transition examined in this study. Instead, the temperature profile was used to assess the model's performance.

The first model run resulted in much cooler ice temperatures in comparison to field measurements and ice thickness increased throughout the period which was in contrast to

field observations (Fig. 7.5). It is noted that the model does not employ a detailed ocean mixed layer formulation; rather a steady oceanic heat flux value is set at the start of a model run. In the original model the heat flux was set to 2 W m^{-2}, an average value for the central Arctic Ocean (see Wadhams, 2000 and references therein). The Canadian Arctic Archipelago is thought to have a much stronger oceanic heat flux than the central Arctic (Melling, 2000). Time series observations made near Resolute Bay show maximum first-year ice thicknesses to range interannually from approximately 1.7 to 2.4 m (Flato and Brown, 1996), varying with annual snowfall rates (Brown and Cote, 1992). However, ice thickness observed near Truro Island during C-ICE'02 averaged 1.52 m ± 0.09 SD, suggesting that an even greater heat flux exists near Truro Island. Supporting this argument is the occurrence of a polynya at northern tip of Truro Island which formed at the beginning of spring over the years of 2000, 2001 and 2002 (personal observation). An enhanced oceanic heat flux is the most probable cause for the formation of this polynya as suggested for other documented polynyas in the region (e.g., Queens Channel and Penny Strait polynyas; Stirling and Cleator, 1981). Therefore, the oceanic heat flux was increased to 20 W m^{-2} in the model, where bottom ice temperatures between the model and field data matched (Fig. 7.5).

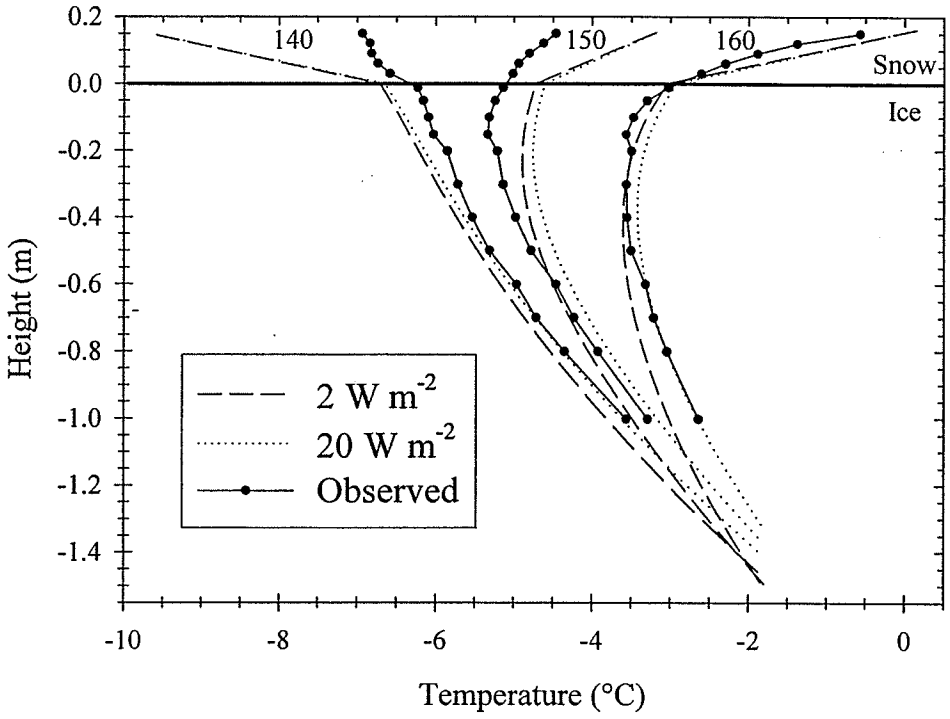

Figure 7.5. A comparison of observed temperature profiles on days 140, 150 and 160, 2002 with model output using an oceanic heat flux of 2 and 20 W m^{-2}, respectively.

The oceanic heat flux to the ice will also be affected through a tidal influence on the molecular/viscous sublayer thickness at the ice-water interface in addition to enhanced vertical mixing of heat in the mixed layer. The thermodynamic model does not consider this oscillatory influence; however its effect on ice algae may be significant as noted by Lavoie et al. (2005). Lavoie et al. (2005) calculated the oceanic heat flux to the ice based on a mixed layer model and mixed layer temperature measurements made in Resolute Passage. Due to the similar vicinity of their study and C-ICE'02, I used the oceanic heat flux presented therein. The calculated heat flux varied from about 2 to 18 W m^{-2} with the fortnightly tidal cycle during the period of the C-ICE'02 study; however, the average over the C-ICE'02 study period was only 10 W m^{-2}. Correspondingly, running the

thermodynamic model with this time series resulted in cooler ice temperatures than observed during C-ICE'02. Therefore, the times series was multiplied by two to obtain an average oceanic heat flux of 20 W m^{-2}. The resultant model output matched the observed data and was therefore used in subsequent model runs.

Figure 7.5 also shows that the surface temperatures did not match well in the model run in comparison to the observed. At the ice surface and in the snow layer, the model simulated a slower warming rate for the first 10 days, then a faster rate, followed by a slower rate until values matched by the end of the study period. This discrepancy between modeled and observed results is thought to be a factor of the treatment of snow in the model and the treatment of sea ice salinity. The model provides a bulk thermal snow layer that does not contain geophysical factors important for calculations of thermal properties of the snow cover such as salinity, density and snow grain size. Therefore, the thermal conductivity and heat capacity of snow is not very realistic. For example, the presence of salinity in a snow cover can increase the thermal conductivity of snow if at the expense of air spaces (Steffen and DeMaria, 1996), but decrease the thermal conductivity when at the expense of snow crystals and is even more pronounced over time with the added effect of phase changes (Papakyriakou, 1999). Furthermore, brine movement within the ice can also greatly affect the ice temperature through convection of heat (Yen et al., 1991). The model's mistreatment of snow thermodynamics is noted here as a caveat in the model, however, no changes were made to the thermodynamic model due to the complexity of the problem and the need to couple a further snow thermophysical model to account for this problem.

7.3.2 Ice Algal Growth Model

Snow depths were found to range between 2 and 45 cm in the study area during C-ICE'02. Therefore, it is noted that snow depths at the edge of the natural range were not considered in the model analysis of Lavoie et al. (2005). That is, their high and low snow sites had approximately 10 and 20 cm snow depths on average, respectively, which fit within the mid snow class examined here. It is noted that nonlinear responses of the model to various factors would result in effects that may not be considered if the model was only tuned to a mid snow depth range. For example, under the low snow class (3.8 cm), the warming rate of the ice cover was simulated to be nearly 5 times larger than under the other two snow classes (Fig. 7.6). Whereas, under the high snow class (28.7 cm), the model simulated ice melt due to the oceanic heat influence which caused the loss term accounting for the algal layer thickness change, L_{IGR}, to be greater than the algal growth rate that was limited by light. These noted differences relating to snow depth classes guide the following discussion regarding adjustments made to the model to match field data.

The original ice algal growth model was run for each of the snow class time series for which ice algal biomass output are presented with comparison to field data (Fig. 7.7). Similar to results presented in Lavoie et al. (2005) for the same time period, the model output did not reproduce the timing of algal biomass decline relative to field data in the mid and low snow classes. In response to the discrepancy, Lavoie et al. (2005) added a new loss term that was proportional to the warming rate of the ice. This addition was justified based on the rationalization that the increase in ice temperature would result in brine channel enlargement and connectivity, leading to an increase in brine drainage and

subsequent sloughing of algae (Lavoie et al., 2005 and references therein). This rationalization was supported by results presented in Chapter 4 where the strongest decrease in algal biomass was observed under the low snow class which also displayed the fastest bottom ice desalination rate. Noted earlier, these changes are not simulated in the thermodynamic model and therefore, a loss term as a function of the daily change in mean ice temperature seems reasonable.

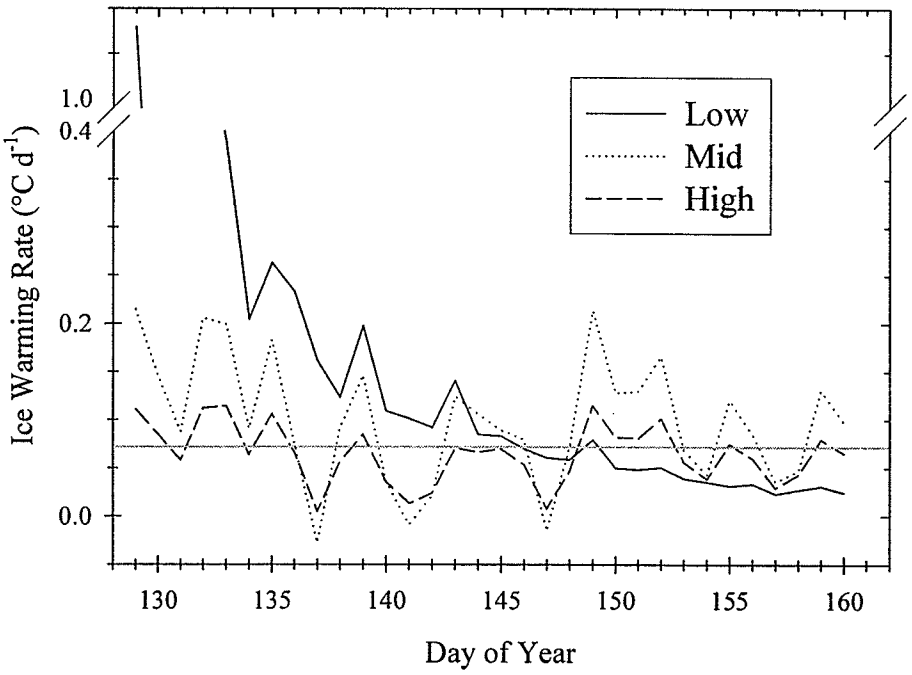

Figure 7.6. Daily simulated ice warming rate for the three snow classes. The grey line denotes the cut-off of 0.07 °C d^{-1}, above which L_{WARM} is effective.

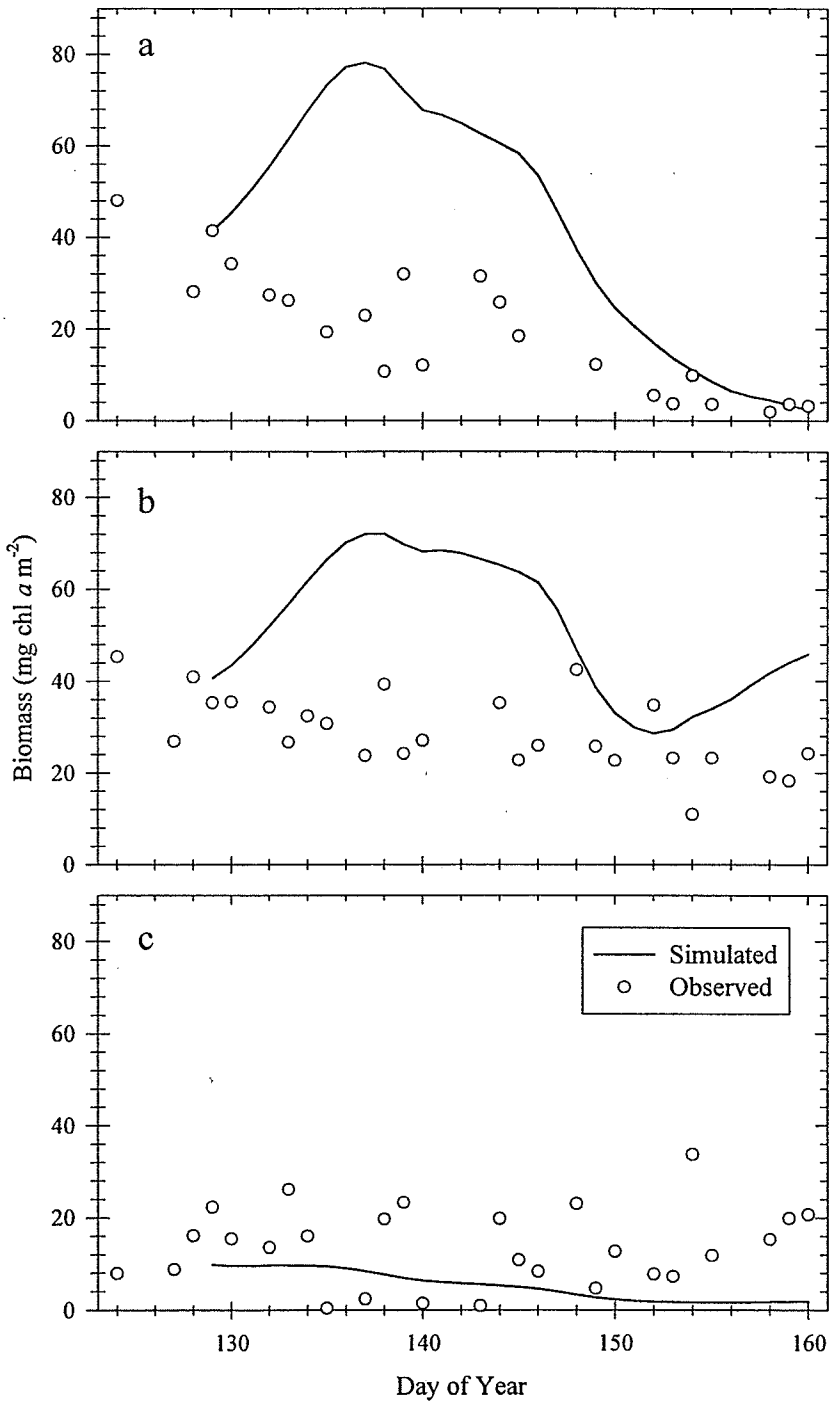

Figure 7.7. Observed and simulated algal biomass using the original ice algal growth model for low (a), mid (b) and high (c) snow classes.

For the high warming rate under the low snow class, using a linear function to parameterize the new loss term from the ice warming rate would result in an unbalanced loss compared to the field measurements of algal biomass. Furthermore, the effect at a very low warming rate should be much smaller. Therefore, a one-sided Gaussian model equation (Cressie, 1993) was used to calculate the new loss term (L_{Warm}):

$$L_{Warm} = 0.25\left[1 - \exp\left(\frac{-dT_I^{\,2}}{0.2^2}\right)\right] \qquad [7.2]$$

where dT_I is the daily ice warming rate (°C d^{-1}). This formulation for L_{Warm} follows an exponential increase at low warming rates then reaches an asymptote of 0.25 at high rates, balancing out the nonlinear influence of snow depth on the ice warming rate. For L_{Warm} to be effective in Lavoie et al. (2005) the ice temperature and warming rate had to be greater than –4 °C and 0.17 °C d^{-1}, respectively. However, in the model used here, L_{Warm} is not defined as brine flushing due to a hydrostatic head created from snow melt as it was in Lavoie et al. (2005). Instead, a strong warming rate is assumed to result in a density influenced desalination of an ice sheet with interior ice melt. A recent study suggests that this bottom ice brine flushing may actually be directly related to peak events in the ocean-ice heat flux (Widell et al., 2006). Therefore, the ice temperature cut-off was not employed. This decision was justified by observations presented in Chapter 4 where mean ice temperatures were below –6 °C at the start of the period yet a steady desalination of the ice cover occurred throughout the study. However, in order to match field data, a warming rate of 0.07 °C d^{-1} was used as a cut-off (see Fig. 7.6), below which L_{Warm} was equal to zero. L_{Warm} was added to equation (3.27) as a new loss term in the

model and produced simulations that matched well with field measurements of algal biomass in the low and mid snow classes (Fig. 7.8).

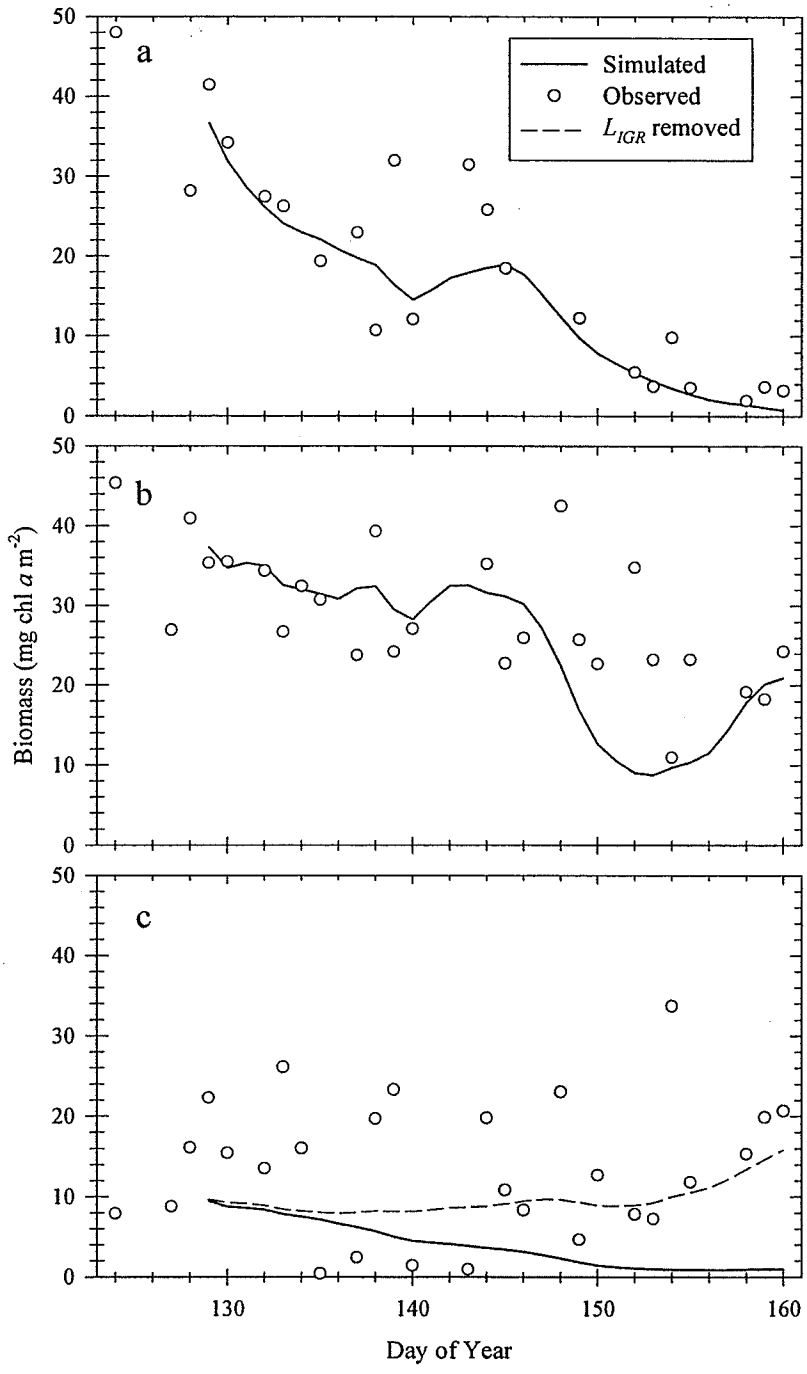

Figure 7.8. Observed and simulated algal biomass using the adjusted ice algal growth model for low (a), mid (b) and high (c) snow classes.

Although the comparison is with highly variable data, simulation of algal biomass in the high snow class did not appear to match the field data, particularly near the end of the period when observations showed a tighter trend of increasing biomass. Even though L_{IGR} was small under the high snow class, it still exceeded the algal growth rate which was strongly limited by light, resulting in a simulated decline of algal biomass (Fig. 7.8). Presented in Chapter 5, it was apparent that in low concentrations, algal biomass was only found along brine channel walls and in brine spaces between ice platelets where in the case of a deep snow cover, light would be maximized. Furthermore, it was suggested that a threshold between 20 and 34 mg chl *a* m^{-2} may exist where the microscale distribution of bottom ice algal biomass changes with respect to the mechanism resulting in the distribution. With low algal concentrations under the high snow class, light is the main simulated limiting factor during the study. Therefore, I speculate that algae concentrate high up in the skeletal layer where light is maximized and access to nutrients is still possible. This difference in the vertical distribution of algal biomass would limit the sloughing of algae with ice bottom melt (i.e., L_{IGR}). Therefore, it seems plausible that L_{IGR} should not apply to the high snow class. To accommodate this, L_{IGR} was assigned as effective only when snow thickness is less than 20 cm and algal biomass is greater than 20 mg chl *a* m^{-2}. The result of this alteration to the model produced a much better match with field data (Fig. 7.8).

7.4 Sensitivity Analysis

In this section, key thermal and optical model parameterizations (see Figure 1.1) for which little information exists are examined in a sensitivity analysis. The thermal parameter tested was the oceanic heat flux whereas the snow attenuation coefficient and

photoacclimation parameter were tested as key factors that influence the light limitation coefficient in the model. In a similar fashion to Lavoie et al. (2005), model output are compared against the simulated output presented in Figure 7.8 which will be referred to as the control run. In addition to the sensitivity runs, a snow drift simulation is carried out to examine the sensitivity of bottom ice algal biomass to changing snow depths over time.

7.4.1 Oceanic Heat Flux

Discussed in section 7.3.1, the oceanic heat flux was increased to match the observed ice temperature profile time series. Furthermore, the temporal progression of oceanic heat flux, calculated in Lavoie et al. (2005) from ocean temperature data, was used to more realistically represent the influence of tides. Therefore, the sensitivity of the model to a changing heat flux was tested. The sensitivity runs included (1) the oceanic heat flux as presented in Lavoie et al. (2005; i.e., study period mean is 10 W m^{-2}), (2) a constant flux of 20 W m^{-2} and (3) a constant flux of 10 W m^{-2} (Fig. 7.9). The effect of changing the magnitude of the oceanic heat flux was dramatic for the low and mid snow classes. However, the effect under the high snow class was minimal. Furthermore, the timing of the heat flux did not have a substantial effect, with the exception of the mid snow class and the constant 20 W m^{-2} sensitivity run.

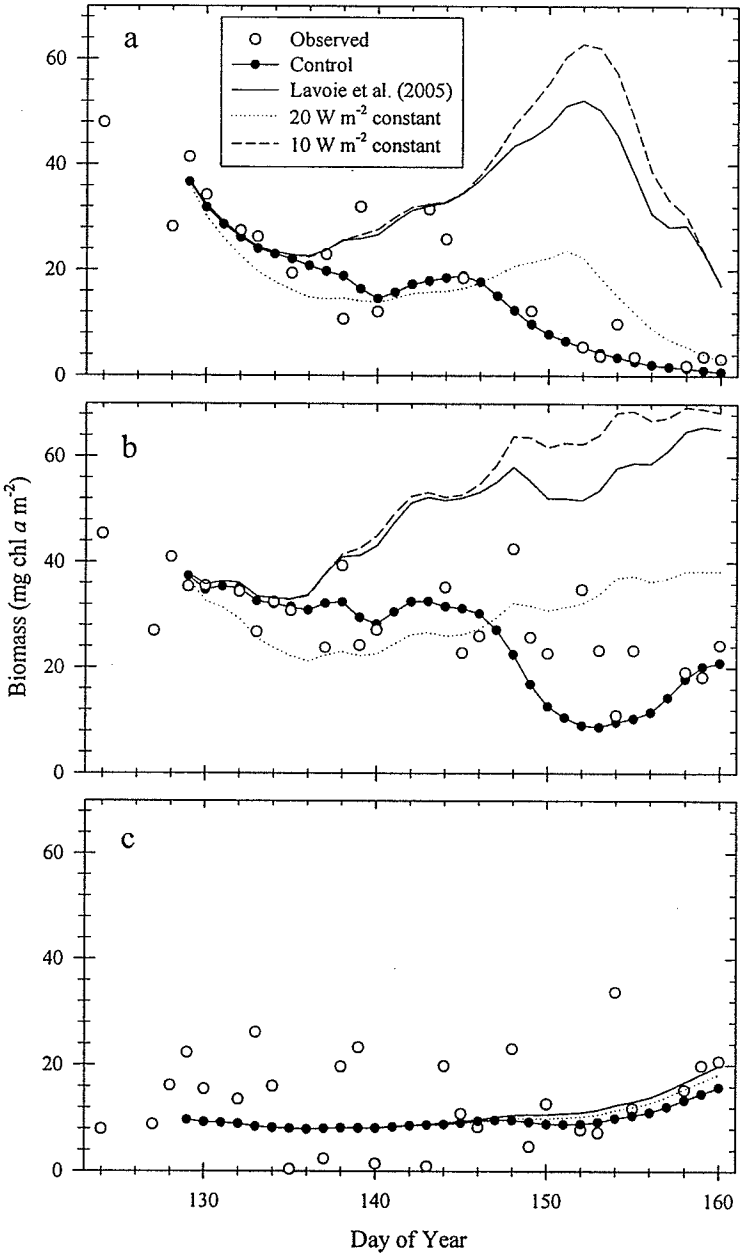

Figure 7.9. Observed and simulated algal biomass for low (a), mid (b) and high (c) snow classes. The control refers to simulated values presented in Figure 7.8, which is compared with simulations using the original oceanic heat flux presented in Lavoie et al. (2005) and a constant heat flux of 20 and 10 W m^{-2}.

By lowering the oceanic heat flux, ice bottom melt and warming rate both decreased resulting in less algal biomass loss and therefore an increase in accumulation. The sensitivity was greatest under the low snow class until IGR_{Ir} became the limiting factor

past day 152 when air temperatures remained near 0 °C and substantial ice melt was simulated. Under the mid snow class, the air temperature increase was buffered by the thicker snow cover and therefore algal biomass increased steadily beyond day 136 when the simulated light limitation became much greater than loss factors. Under the high snow class, light was the main limiting factor and the air temperature influence on ice temperature was greatly reduced by the thick snow cover. It is noted that these responses of the model to changes in the oceanic heat flux support conclusions made in Chapter 4. Further, in accordance with Lavoie et al. (2005), it is clear that the heat flux from the ocean is a key variable to consider when modeling and observing bottom ice algal biomass.

7.4.2 Light Limitation

Snow attenuation coefficients used in the control run were equated to observed values presented in Chapter 4. It was concluded in Chapter 4 that snowpacks varied in age across the study area resulting in varying attenuation coefficients, which accounted for the observed variability. It is also noted that estimations of attenuation from measurements in the snowpack may be subject to disturbance of the light field from the radiometer head (Warren, 1982). Therefore, for the first sensitivity run I tested the model's response to changes in the snow attenuation coefficient parameterization, κ_{PAR}, through a negative offset of 2.5 m^{-1} to the κ_{PAR} time series which fits within the lower range of observed values (see Fig. 4.4). For the second sensitivity run, I tested the response of the model to a constant κ_{PAR} which was set to 11 m^{-1} in accordance to observations presented in Chapter 6. This sensitivity run was accomplished noting that in

previous ice algal modeling work (e.g., Arrigo and Sullivan, 1994; Lavoie et al., 2005; Jin et al., Accepted) κ_{PAR} has been parameterized as a single constant value or as a cold and a melt value. It is noted that both κ_{PAR} parameterizations will increase the amount of transmitted irradiance reaching the algal layer and therefore indirectly affect the computed light limitation coefficient. For the third and fourth sensitivity runs, the parameterization of light limitation was directly examined by adjusting the photoacclimation coefficient, I_k, which is assumed to vary with snow depth. I_k was tested as its original parameterization was based on a limited dataset that was available for the general study area (i.e., in the vicinity of Resolute Bay, Nunavut). New values of I_k for each snow class were obtained by fitting different curves to the dataset plotted in Figure 3.5. The first curve was obtained by exclusion of the Smith et al. (1988) observation at a 3 cm snow depth, considered in this case as a data outlier, and using equation (3.21) to fit the data. The resultant curve had a R^2 of 0.98 and regression coefficients, A_1, A_2 and A_3 of 15.22, 86.34 and 4.447, respectively. The second curve was linearly interpolated between data points with an average value for I_k of 4.42 $\mu E\ m^{-2}\ s^{-1}$ at snow depths $\geq$ 5 cm. Both snow dependent I_k curves are plotted with the control curve and observed data points (Fig. 7.10).

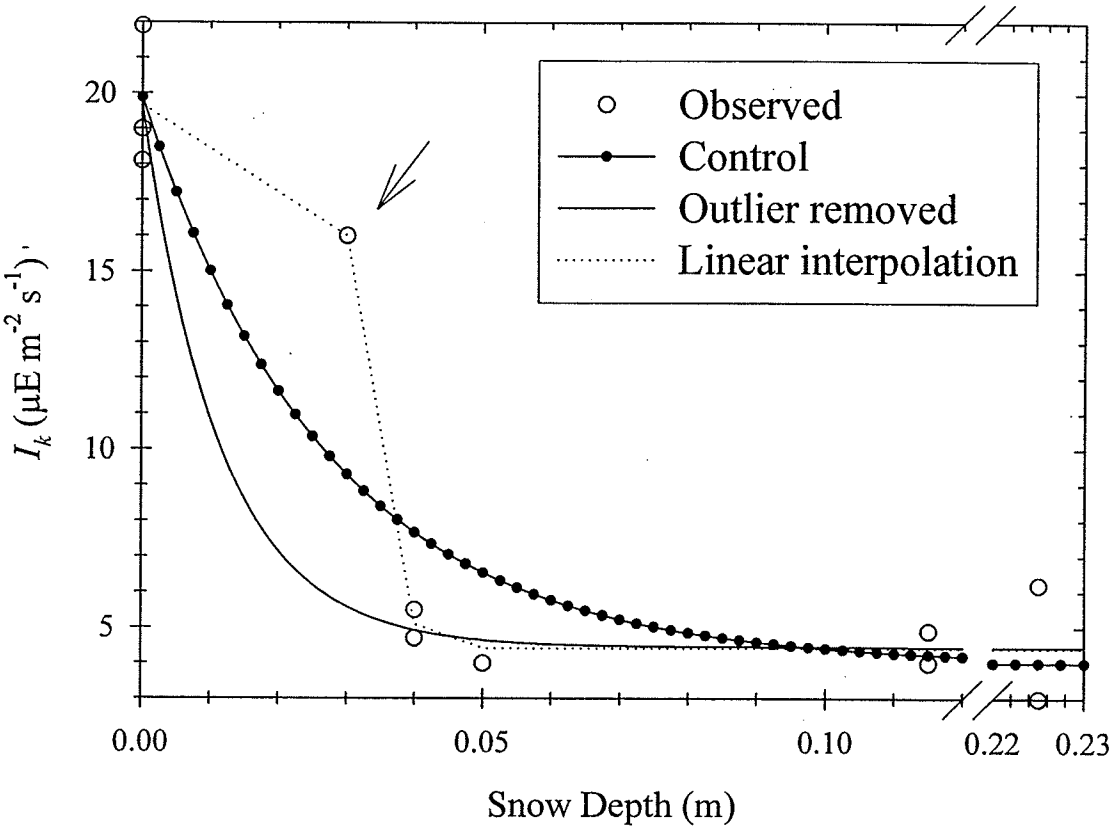

Figure 7.10. Observed data and parameterized curves for bottom ice algae photoacclimation coefficients (I_k) versus snow depth. The arrow signifies an assumed outlier that was excluded from the regression for the "outlier removed" curve.

Figure 7.11 shows the model output from the four light limitation sensitivity runs. All snow classes exhibited a response to the induced changes in the light limitation coefficient as light was always diurnally limiting during the study period (e.g., Fig. 7.1). Under the low and mid snow classes, simulated algal biomass was nearly equal to the control run (i.e., simulated data presented in Fig. 7.8) by the end of the period due to ice warming rate and ice melt losses. However, the high snow class showed a substantial change in simulated algal biomass as light was the main limiting factor on algal growth and losses associated with ice melt and warming rate were minimal.

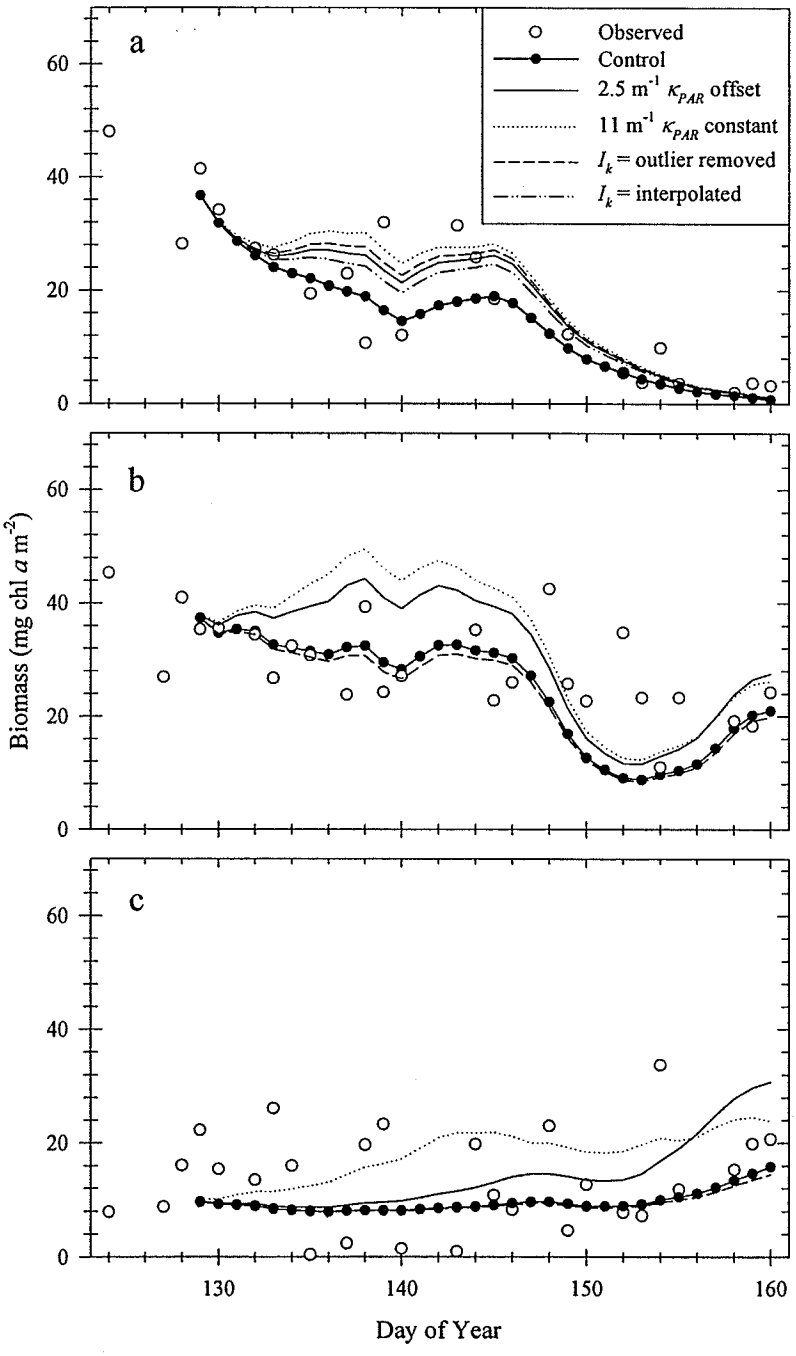

Figure 7.11. Observed and simulated algal biomass for low (a), mid (b) and high (c) snow classes. The control refers to simulated values presented in Figure 7.8, which is compared with 4 separate simulations where the first two involved adjustments to the spectral diffuse attenuation coefficient, κ_{PAR}, and the last two involved adjustments to the photoacclimation coefficient, I_k.

For the κ_{PAR} sensitivity runs, it is interesting to note that the second run resulted in the strongest initial response as κ_{PAR} was larger to start; however, the first run resulted in a higher simulated algal biomass by the end of the period under the high snow class, even though the average κ_{PAR} for the first run was 11.9 m^{-1} (i.e., > the second run's value of 11 m^{-1}). It is concluded that even little changes in the light attenuation coefficient parameterization for snow can cause dramatic changes in the amount of simulated algal growth and accumulation.

The I_k runs did not show as strong of a sensitivity as the κ_{PAR} sensitivity runs. The I_k parameterization reaches an asymptote under deeper snow depths (i.e., lower light levels; Arrigo and Sullivan, 1994) such that a large change in I_k was only made in the low snow for the sensitivity runs. Further, the influence of an increase of the light limitation coefficient, caused by a decrease in I_k, on algal biomass in the low snow class simulation was minor as the simulated effect of biomass losses combined with a small ice growth rate limitation coefficient was dominant. Therefore, the sensitivity of the model to changes in the I_k parameter is small given the time of the study period and the snow depth range observed during C-ICE'02.

7.4.3 Snow Drift Simulation

The hypothesis posed in Chapter 1 was that the history and distribution of snow over sea ice control the magnitude of ice algal biomass through both thermophysical and radiative processes. In this section, I examine this hypothesis through a series of model simulations which mimic a snowdrift moving over a point through time. The snow drift simulation forces a change in snow depth from a deep to shallow snow cover, then back to a deep snow cover after a 5 day period. The deep and shallow snow covers were equal

to the high (28.7 cm) and mid (13.8 cm) snow classes, respectively. Therefore, the high snow class was chosen as the control run. The 5 day perturbation in snow depth was moved 5 days forward for separate simulation runs such that the first day of the perturbation fell on days 129, 134, 139, 144, 149 and 154, respectively. The first day of the perturbation is used to signify the corresponding simulation run.

The snow drift simulation showed that variability in algal biomass among separate simulation runs was high (Fig. 7.12a). However, some of the simulations exhibited particularly strong deviations (e.g., runs 129, 144, 149 and 154). For simulation run 129, decreases in light limitation and ice warming rate occurred at the beginning of the model run (Fig. 7.12b, c, respectively). The decrease in ice warming rate was due to a lower thermal insulation from the cold atmosphere associated with a decrease in snow depth. The combined result was an increase in algal biomass relative to the control run which lasted over the duration of the run. Although a slight increase in the ice warming rate occurred, simulation run 154 also resulted in an increase in algal biomass in response to the increase in the light limitation coefficient (Fig. 7.12a, b, respectively).

Simulation runs 144 and 149 showed an opposite response to runs 129 and 154. Day 149 corresponded to the peak in the spring tide (Fig. 3.4) where the ocean-ice heat flux reached its maximum value (see Fig. 5 in Lavoie et al., 2005). It is noted that in all snowdrift simulation runs, L_{IGR} was effective during the perturbation where snow depth was less than the specified threshold of 20 cm. The model simulated an increase in ice melt during the peak in ocean-ice heat flux, which was accentuated under the thinner snow cover. This resulted in strong increase in L_{IGR} causing algal biomass to decrease substantially. Algal biomass in run 149 was also affected by an increase in the ice

warming rate (Fig. 7.12c) and therefore an increase in L_{WARM} which resulted in a stronger decrease in algal biomass relative to simulation run 144.

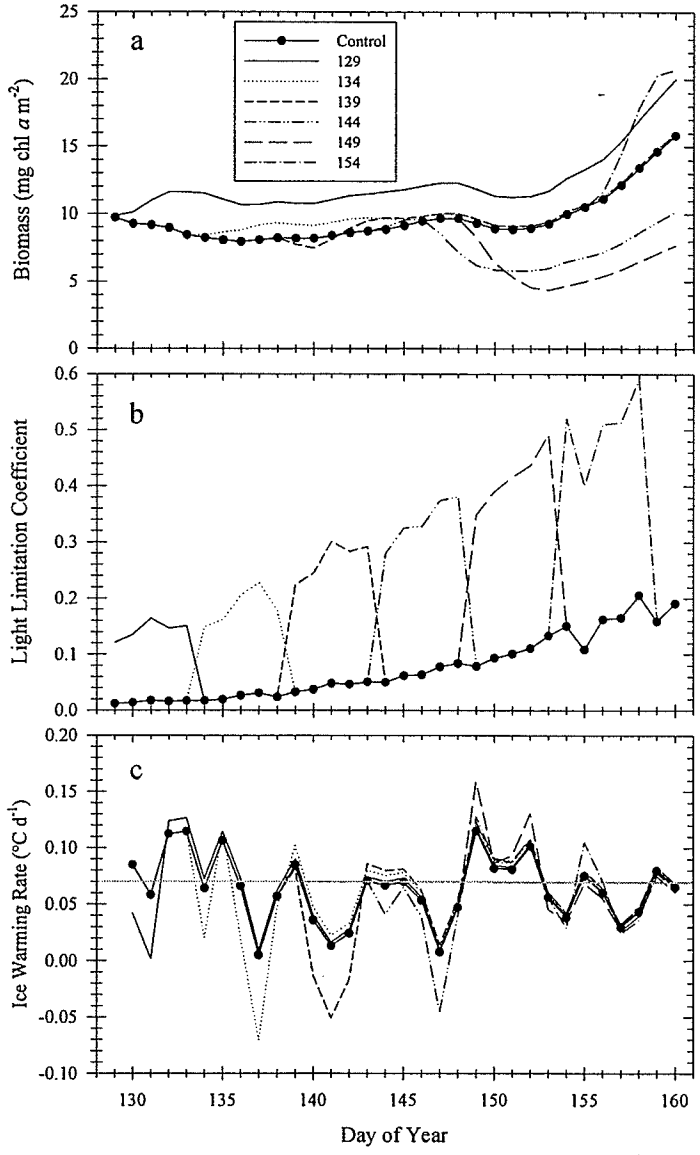

Figure 7.12. Model output of algal biomass (a), the light limitation coefficient (b) and ice warming rate (gray line denotes L_{WARM} cut-off) (c) for a snow drift simulation series of a 5 day snow depth perturbation moved 5 days forward for each separate simulation run such that the first day of the perturbation fell on days 129, 134, 139, 144, 149 and 154, respectively. The snow depth perturbation was a change in snow depth from an initial 28.7 cm to 13.8 cm over a 5 day period, then back to 28.7 cm. The control run is from the high snow class simulation.

7.5 Conclusions and Summary

In this chapter, I investigated the influence of thermal and optical factors on ice algae accumulation and loss through simulations using a one-dimensional bottom ice algal growth model. As concluded in Chapter 4, the model results support a dominant thermal influence on ice algal biomass under thin snow covers during the spring transition period when algae under thick snow covers were mainly light limited. However, the simulations also demonstrated that these thermal and optical factors are not exclusive in their effects on algal accumulation and loss. For example, light was always limiting diurnally and melt associated losses were simulated under all snow cover classes.

Algal biomass simulations exhibited a strong sensitivity to the ice warming rate and ice melt and to variability in the snow attenuation coefficient. In accordance with Lavoie et al. (2005), it was shown that a change in the oceanic heat flux can greatly affect the timing of the algal biomass decline in spring. Therefore, the heat flux from the ocean to the sea ice is a key variable which needs to be considered in future observational studies and in ice algal growth models. Furthermore, an accurate time dependent parameterization of snow attenuation is needed for modeling ice algal growth.

It is concluded from the modeling results that snow depth controls the magnitude of algal biomass through both thermophysical and radiative processes. Results strongly supported my dissertation hypothesis in that the history and distribution of snow over sea ice will be the dominant factor behind spatial variability in algal biomass under smooth landfast first-year sea ice. The conclusions drawn in this chapter highlight the sensitivity of the bottom ice algae ecosystem to climate change through potential shifts in snow depth distribution and ocean temperatures. In the next chapter, I conclude the dissertation

bringing together results and discussion made in the various chapters. A summary of the caveats and limitations of the dissertation is also provided including a discussion on directions for future field observations and modeling that can further the research presented here.

CHAPTER 8: Summary and Conclusions

8.1 Thesis Summary

The changing Arctic sea ice cover has received considerable attention as a major constituent of the polar and global climate system and as a primary indicator for climate change. Due to its vast extent and seasonal variation, snow-covered sea ice influences the earth climate system by increasing the global albedo and dictating the exchange of gas, mass and energy between the ocean and atmosphere. Spatial and temporal variations in ice extent are largely accounted for by first-year (seasonal) sea ice. Furthermore, climate models predict first-year sea ice to be the predominant and, in many cases, the sole sea ice type within this century (ACIA, 2004). These predictions agree with observed trends of the ice cover extent and thickness (e.g., Parkinson et al., 1999; Comiso, 2002; Yu et al., 2004). However, this is not to state that the scientific community understands exactly what will happen in the Arctic marine cryosphere system. On the contrary, there is considerable uncertainty and variability among these model predictions and field observations, which largely circulate around our current understanding of physical processes which affect the snow and ice cover. What is apparent is an increase in relative importance of first-year snow-covered sea ice in the Arctic.

Sea ice also provides a unique polar habitat for algae and other microscopic life forms. In this dissertation, I have focused on ice algae that reside within the bottom few centimeters of first-year landfast ice during spring. The habitat location within the landfast ice environment provides a natural laboratory for the study of physical processes

which affect accumulation and loss of the algae. Through numerous field studies, ice algal growth has been found to be limited by light, nutrients and sea ice structure; and influenced by temperature and salinity. Loss of algae from the ice cover may be related to various physical factors, but perhaps the most dominant process is ice melt (e.g., Lavoie et al., 2005). These physical factors can vary greatly over space and time. For example, transmitted light, ice temperature and ice salinity are largely dependent on the highly variable depth history of the overlying snow cover. This high spatio-temporal variability of physical factors induces variability on ice algal biomass (Gosselin et al., 1986) and has formed the focus of my dissertation.

The principle objective of my dissertation was to determine the importance of various characteristics and scales of physical processes on the accumulation and loss of sea ice algae during the spring season. Given the importance of snow, it was also hypothesized that the history and distribution of snow over sea ice control the magnitude of ice algal biomass through both thermophysical and radiative processes. This objective and hypothesis have been investigated through both observations and modeling.

In Chapter 1, I provided a system level diagram outlining the various physical processes that are important to the accumulation and loss of bottom ice algae during spring. A review of our current understanding of how these processes operate was provided within Chapter 2. The system diagram is used again here as a guide to help present key observations and conclusions made in the dissertation (Fig. 8.1).

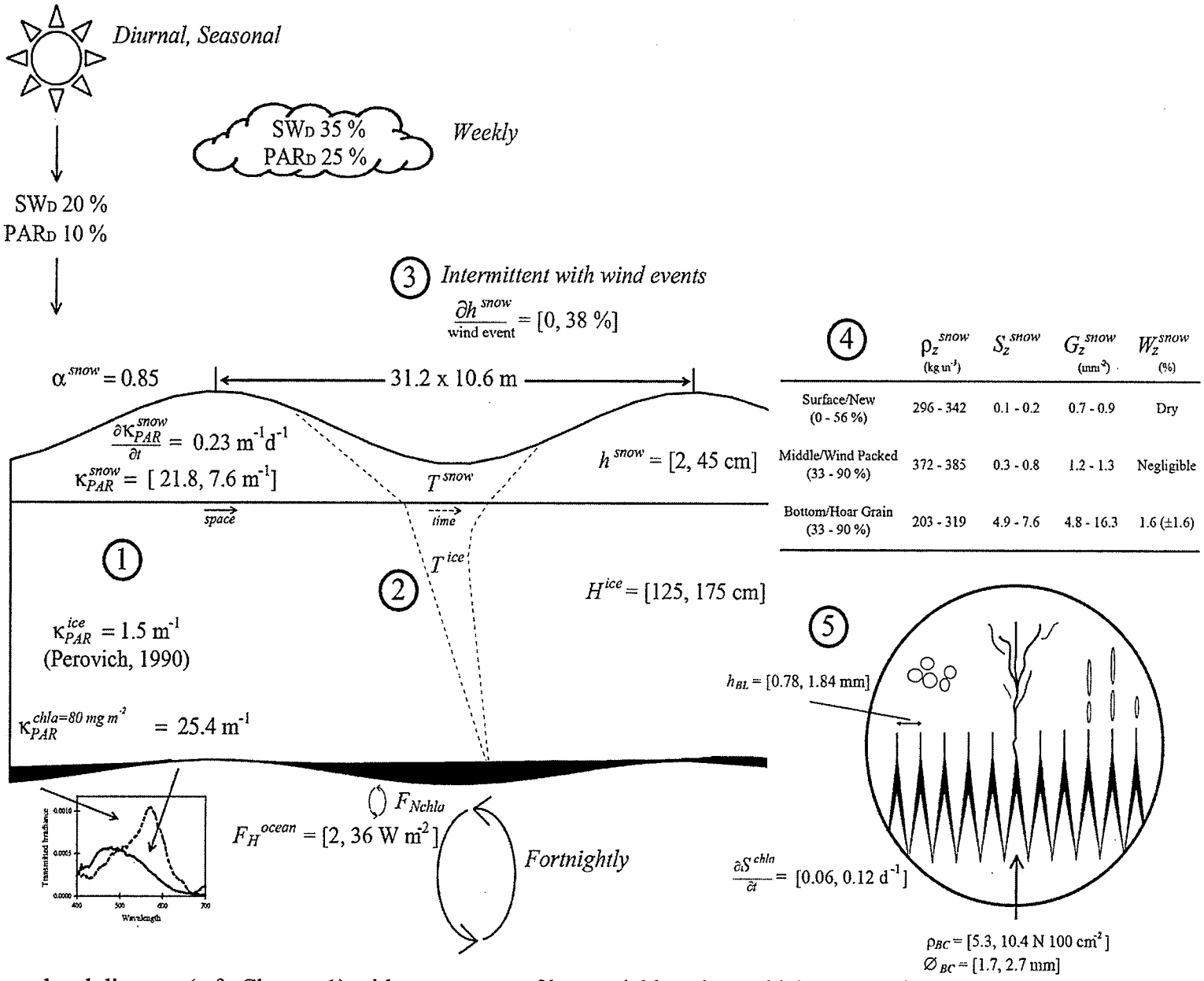

Figure 8.1. System level diagram (c.f., Chapter 1) with a summary of key variable values which account for variability in the system.

The diagram presents key field observations and modeling parameterizations relating to the 5 pertinent processes mentioned in Chapter 1. Large text in italics on the diagram (Fig. 8.1) provides temporal scales of forcing variability. For example, solar insolation varies diurnally and seasonally, weather systems tend to move through the area within a week, changes in snow depth are intermittent with wind events and tides have a fortnightly or two week cycle. Square brackets encase the range of values observed or modeled, whereas values without brackets represent averages and trends.

Observations related to radiative transfer, process #1, include percent of downwelling shortwave (SW_D) and Photosynthetically Available Radiation (PAR_D) attenuated by the atmosphere and clouds, surface albedo (α), PAR attenuation coefficients (κ_{PAR}) for the snow, sea ice and for a 5 cm bottom ice algal layer with 80 mg m^{-2} algal biomass and spectrally transmitted irradiance (graph). Thermodynamics, process #2, is represented by snow-ice temperature profiles observed in early and late spring, and by observed ranges of snow depth and ice thickness over the spring period. The influence of blowing snow, process #3, is shown directly by its influence on snow depth with a wind event and indirectly by the average distribution of snow. Variability in snow geophysical properties, process #4, include vertically distinct snow layers with observed average values from the two field seasons for density (ρ_Z), salinity (S_Z), grain size (G_Z) and wetness (W_Z). Observations in variability in the ice bottom structure, process #5, include desalination rates of the bottom ice ($\partial S/\partial t$), brine layer spacing (h_{BL}), and brine channel density (ρ_{BC}) and diameter ($\varnothing_{BC}$). These observations are summarized in diagrammatic form to show the amount and scales of variability that can be experienced over space and time and how

all of these processes are interconnected. In the following paragraphs, I summarize the conclusions made in Chapters 4 to 7 with reference to Figure 8.1.

In Chapter 4, I examined and discussed surface forcing, including physical, thermodynamic and optical factors, which affects the accumulation and loss of algal biomass in the bottom ice. With an emphasis placed on the snow cover, this observational study examined all processes outlined in Figure 8.1. More specifically, I focused on the following sub-objectives which contribute to my principle objective:

(1) To document variability of thermal, physical and optical properties of snow-covered landfast first-year sea ice pertinent to sea ice algae biomass in spring;

(2) To examine how these physically-based variables affect ice algal biomass.

Variables pertinent to bottom ice algal biomass and associated with surface forcing include the thermophysical state and optical properties of the snow-ice matrix. The physical, thermal and optical properties of snow are an order of magnitude more important than the sea ice and were therefore the focus of this study. Towards the first sub-objective, I found that snow depth varied greatly over space and time. Snow depth distribution accounted for the greatest spatial variability, however, other important factors were found to vary. The attenuation coefficient of snow (κ_{PAR}) varied spatially in age where a lower κ_{PAR} was associated with older snowpacks with larger snow grains and higher salinity. Temporal variability was associated with atmospheric warming and event driven wind redistribution of snow, a process that is intermittent. The second sub-objective for this study was largely examined through a correlation analysis. A competing effect on ice algae was observed. That is, under thin snow covers, lower thermal

insulation from the warming atmosphere led to an increased ice melt rate, as observed through a higher bottom ice desalination rate, which ended up in a sloughing of bottom ice algal biomass. Whereas under deep snow, algae were still light limited and thermally insulated from the warming atmosphere. Intermediate snow covers experienced a balance of these two competing effects on algal biomass accumulation and loss and therefore accounted for maximum observations of algal biomass. In the context of current climate change scenarios, these results suggest that shifts in snow depth could result in decreases of bottom ice algal biomass.

In Chapter 5, I changed my focus from surface forcing to physical factors operating near the ice bottom which affect the distribution of algal biomass. In this chapter, I examined the following sub-objectives:

(1) To describe the spatial elements of algae and ice structure/brine drainage features;

(2) To investigate the linkages between ice structure and brine drainage and the microscale distribution of bottom ice algal biomass.

To examine these objectives, I developed a photographic technique which provided *in situ* observations of ice structure and the microscale variability of algal biomass. Therefore, results presented in this chapter deal with bottom ice structure processes (i.e., process #5 in Figure 8.1). Consistent with published literature, brine layer spacing was relatively stable around 1 mm due to slow ice growth rates during the spring season. However, brine channel size and density were more variable, showing relationships with algal biomass and snow depth. Furthermore, brine channel density at the ice bottom was observed to be greater than previously determined through observations on extracted ice

samples. The numerous brine spaces and channels at the ice bottom were linked to the small scale patchiness (~ 1 to 3 mm) of algal biomass over areas of low biomass supporting the hypothesis that these features provide local maxima of light, space and nutrients and therefore favor algal growth. However, areas of higher algal biomass exhibited only larger scale patchiness (~ 10 to 26 mm), which could result from brine drainage features acting to augment sloughing of algae and was likely associated with local ice ablation near the brine channels at the ice bottom. This speculation agreed with the correlation between algal biomass and the desalination rate observed in Chapter 4. A further link was made between ice algal biomass and the tidal cycle. That is, high ocean currents were associated with sloughing of algal biomass which led to speculation of either a connection with a limited nutrient supply during neap tide and/or enhanced bottom ice melt associated with tidal heat input during the spring tide.

In Chapter 6, I left an exclusive concentration on field observations and began to explore modeling in an effort to develop a non-invasive method to remotely estimate ice algal biomass and through association, a means to study the influence of changing environmental variables on the algae. The development of this method employed the use of transmitted irradiance through the snow and sea ice and therefore, this chapter focused on radiative transfer, process #1 in Figure 8.1. Towards my dissertation principle objective, I had investigated the following sub-objectives:

(1) To provide a comprehensive examination of the spectral dependence of transmitted irradiance on snow cover and algal biomass;

(2) To improve spectral parameterizations of a radiative transfer model using field observations;

(3) To develop a method to remotely estimate ice algal biomass using spectral transmitted irradiance.

The comprehensive examination of spectral transmitted irradiance through the snow and ice led to the conclusions that in contrast to the dominant scattering properties of snow, absorption largely controls the spectral diffuse attenuation coefficient of algae. Results showed that snow had little effect on the distribution of transmitted spectral irradiance at wavelengths between 400 and 550 nm, whereas algae had a strong absorption peak near 440 nm that dominated changes in spectral transmission across this wavelength range. Up to 89% of the total variation in algal biomass was accounted for with a single normalized difference transmitted irradiance ratio at wavebands centered at 472 and 485 nm, respectively. Therefore, the blue wavelength peak in algal spectral absorption provided a means to remotely estimate algal biomass in the ice cover using transmitted irradiance. Given the spectral attenuation properties of snow and ice, it was promising to note that the spectral region of the algal absorption peak was also the region of highest transmitted irradiance. This fact, combined with the sensitivity of current spectral radiometers, will result in more precise field measurements relative to the use of other regions of the optical spectrum.

The improved radiative transfer model employed in Chapter 6 was further coupled with a thermodynamic and ice algae growth model in Chapter 7. The coupled model was

matched to field data and used to address my dissertation principle objective through investigation of the following sub-objectives:

(1) To couple one-dimensional thermodynamic, radiative transfer and ice algae growth models and match to field observations;

(2) To examine the response of the model to a series of sensitivity analyses examining the response of algal biomass to important thermal and optical factors.

In accordance with field observations, the model results supported a dominant thermal influence on ice algal biomass under thin snow covers during the spring transition period when algae under thick snow covers were mainly light limited. The model was found to be very sensitive to the ice warming rate and variability in light attenuation. Therefore, it was concluded that snow depth controls the magnitude of algal biomass through both thermophysical and radiative processes. Results strongly supported the hypothesis that the history and distribution of snow over sea ice will be a dominant factor behind spatial variability in algal biomass under smooth landfast first-year sea ice. Furthermore, the conclusions drawn in Chapter 7 highlight sensitivity of the bottom ice algae ecosystem to Arctic climate change through potential shifts in snow depth distribution and thermophysical changes forced by atmospheric or oceanic changes in temperature.

8.2 Caveats, Limitations and Future Directions

8.2.1 Field Data

From the beginning of this dissertation, it was realized that current methods of field data collection would limit a complete investigation of the principle objective and underlying hypothesis. For example, the conclusions of the dissertation highlight the importance of knowing the snow depth history, complete with better estimates of climate state variables for both physical and thermal properties of the snow. The problem is that this type of sampling is cost prohibitive; it is not feasible to set-up meteorological stations over the entire year at every single location of interest and biological sampling techniques available at the commencement of my PhD program did not allow non-destructive point location estimates of algal biomass. Therefore, I had to explore new sampling techniques and make use of models. This additional investigation further highlighted caveats and limitations of the research.

The photographic technique developed and employed in Chapter 5 provided unique *in situ* microscale observations of the ice bottom, with the potential to enhance studies of physical-biological processes operating near the ice-water interface using a non-invasive method. However, a caveat for the technique was related to assumptions made in normalizing images to algal biomass. Furthermore, a cautionary note is made for the application of this technique to ice that may contain absorbing particulates, such as sediments or algal biomass, higher up in the ice which could influence the precision in bottom ice algal distribution estimates. In Chapter 6, the factor of absorbing materials higher up in the ice was seen to both limit and potentially benefit the use spectral

transmitted irradiance in estimation of material in the snow and ice cover. It was noted that the success of the method for algal biomass estimation could be influenced by shifts in the spectral distribution of transmitted irradiance through: variability in spectral attenuation coefficients of snow and ice, acclimative strategies of algae to temperature, nutrient and light limitation (Stramski et al., 2002) and changes in algal community species composition (Moberg et al., 2002). Alternatively, if improved optical parameterizations would be obtained and applied within a radiative transfer model, these influencing factors could theoretically be used to gain information on snow, ice, and algal physiology and community composition. It also seems possible that the under-ice camera technique could be combined with spectral transmitted irradiance measurements to overcome some of the assumptions in ice algal biomass estimation for the bottom ice images. It seems the next step for this research is to apply these techniques aboard autonomous underwater vehicles for near-ice measurements which will have the potential to greatly improve our understanding of sea ice ecosystem processes at large spatial scales. The methods could also be used for true time series observations to support the further development and validation of ecosystem process models. Both of these points show a future promise to increase our spatial and temporal coverage of physical and biological measurements of snow-covered sea ice.

8.2.2 Modelling

There were many assumptions and cautionary notes made in Chapter 7 with regards to the model analysis. These were mainly made in reference to the thermodynamic model. Of particular note was the treatment of snow and salinity, which includes the lack of interior ice melt and brine drainage processes in the model. Furthermore, the importance

of a coupled ocean mixed-layer model was noted through the use of the oceanic heat flux computations from Lavoie et al. (2005). The relevance of these model caveats was made even more apparent through the model sensitivity analyses, where bottom ice melt was one of the main contributors for simulated algal loss; however field observations suggested that a decrease in algal biomass at the ice bottom was not related to a change in ice thickness. This point is particularly critical for modeling ice algal dynamics during the spring transitional period.

It is noted that snow thermodynamic models which consider geophysical details of the snow cover including metamorphic and blowing snow processes do exist (e.g., Jordan et al., 1999; Lehning et al., 2002). Further, there is at least one example of a successful coupling between a detailed snow model with a sea ice thermodynamic model (Hanesiak, 2001), however, salts were not included in this model, providing a lot of room for improvements. For sea ice, structural processes are not well represented in existing models (e.g., Eicken, 2003). To my knowledge, a fully coupled thermodynamic model that considers snow and ice structure processes does not currently exist. As shown in this dissertation, the development of such a model will be of great benefit not only to the physical sciences, but also to our understanding of biological dynamics in the ice cover.

8.2.3 Closing Comments

It was also made apparent in the dissertation that both field observations and models need to be used for a more complete investigation of the system. A simple, but important relationship between the two is that field observations improve model parameterizations and our understanding and treatment of processes in models, whereas the application of model improvements to sensitivity analyses provides feedback to help direct future field

observations. For example, field observation presented in Chapters 4 and 5 showed a relationship between the process of bottom ice desalination with the decrease in bottom ice algal biomass. This led to the addition of an ice warming rate loss term for algal biomass in the coupled model, in a similar fashion to Lavoie et al. (2005), which was meant to represent the influence of desalination. The representation of desalination with an ice warming rate demonstrates our current inability to account for this process in a model. Furthermore, the sensitivity of the warming rate loss term to the oceanic heat flux clarified the importance of this flux and its representation in the model. Recent research by Widell et al. (2006) has indicated that turbulent heat forcing on the ice bottom may play an important role in the desalination of the ice bottom. Looking back, it could be this process which the model was indirectly accounting for when matching to field observations, and therefore provides a direction for further field research.

The research presented in this dissertation highlights the importance of considering system theory and the various processes that give rise to spatial and temporal scales of variability in the ice algal ecosystem. It further highlights the requirement of interdisciplinary and multidisciplinary research for a better understanding of the Arctic marine cryospheric system. I close in noting that this requirement is of utmost importance in the face of a changing climate for predictions of how the system may change and in turn how these changes will affect the Earth system as a whole.

References

ACIA. 2004. *Impacts of a Warming Arctic: Arctic Climate Impact Assessment.* Cambridge University Press.

Aguilera, J., K. Bischof, U. Karsten, D.Hanelt and C. Wiencke. 2002. Seasonal variation in ecophysical patterns in macroalgae from an Arctic fjord. II. Pigment accumulation and biochemical defence systems against high light stress. *Mar. Biol.*, 140: 1087-1095.

Arrigo, K.R. 2003. Primary production in sea ice. IN *Sea Ice: An Introduction to its Physics, Chemistry, Biology and Geology*, D.N. Thomas and G.S. Dieckmann (Eds). Blackwell Science Ltd., Oxford, UK. pp. 143-183.

Arrigo, K.R., J.N. Kremer and C.W. Sullivan. 1993. A simulated Antarctic fast ice ecosystem. *J. Geophys. Res.*, 98: 6929-6946.

Arrigo, K.R. and C.W. Sullivan. 1992. The influence of salinity and temperature covariation on the photophysiological characteristics of Antarctic sea ice microalgae. *J. Phycol.*, 28: 746-756.

Arrigo, K.R. and C.W. Sullivan. 1994. A high resolutionbio-optical model of microalgal growth: Tests using sea-ice algal community time-series data. *Limnol. Oceanogr.*, 39: 609-631.

Arrigo, K.R, C.W. Sullivan and J.N. Kremer. 1991. A bio-optical model of Antarctic sea ice. *J. Geophys. Res.*, 96: 10,581-10,592.

Arrigo, K.R., D.L. Worthen, M.P. Lizotte, P. Dixon and G. Diekmann. 1997. Primary production in Antarctic sea ice. *Science*, 276: 394-397.

Assur, A. 1958. Composition of sea ice and its tensile strength. Arctic Sea Ice. U.S. National Academy of Sciences-National Research Counsil, Pub. 598, 106-138.

Barber, D.G. and S.V. Nghiem. 1999. On the estimation of snow thickness distributions over sea ice using thermal dependence of microwave backscatter change. *J. Geophys. Res.*, 104: 25,789-25,803.

Barber, D.G., S.P. Reddan and E.F. LeDrew. 1995. Statistical characterization of the geophysical and electrical properties of snow on landfast first-year sea ice. *J. Geophys. Res.,* 100: 2673-2686.

Barlow, R.G., M. Gosselin, L. Legendre, J.-C. Therriault, S. Demers, R.F.C. Mantoura and C.A. Llewellyn. 1988. Photoadaptive strategies in sea-ice microalgae. *Mar. Ecol. Prog. Ser.*, 45: 145-152.

Barry, R.G., M.C. Serreze, J.A. Maslanik, and R.H. Preller. 1993. The Arctic Sea Ice-Climate System: Observations and Modelling. *Rev. Geophys.*, 31: 397-422.

Belzile, C., S.C. Johannessen, M. Gosselin, S. Demers and W.L. Miller. 2000. Ultraviolet attenuation by dissolved and particulate constituents of first-year ice during late spring in an Arctic polynya, *Limnol. Oceanogr., 45*: 1265-1273.

Birkeland, K.W. 1998. Terminology and predominant processes associated with the formation of weak layers of near-surface faceted crystals in the mountain snowpack, *Arct. Alp. Res.*, 30: 193-199.

Boer, G.J., G. Flato and D. Ramsden. 2000. A transient climate change simulation with greenhouse gas and aerosol forcing: projected climate to the twenty-first century. *Clim. Dyn.*, 16: 427-450.

Buckley, R.G. and H.J. Trodahl. 1987. Scattering and absorption of visible light by sea ice. *Nature*, 326: 867-869.

Carmack, E.C. 1990. Large-scale physical oceanography of polar oceans. IN *Polar Oceanography Part A: Physical Science*, W.O. Smith (Ed), Academic Press, New York, pp. 171-211.

Colbeck, S.C. 1982. An overview of seasonal snow metamorphism. *Rev. Geophys. Space Phys.*, 20: 45-61.

Cole D.M., L.H. Shapiro 1998. Observation of brine drainage networks and microstructure of first-year sea ice. *J. Geophys. Res.*, 103: 21,739-21,750

Comiso, J.C. 2002. A rapidly declining perennial sea ice cover in the Arctic. *Geophys Res Lett.*, 29: doi: 1029/2002GL015650.

Comiso, J.C. 2003. Large-scale characteristics and variability of the global sea ice cover. IN *Sea Ice: An Introduction to its Physics, Chemistry, Biology and Geology*, D.N. Thomas and G.S. Dieckmann (Eds). Blackwell Science Ltd., Oxford, UK. pp. 112-142.

Cota, G.F. and E.P.W. Horne. 1989. Physical control of arctic ice algal production. *Mar. Ecol. Prog. Ser.* 52: 111-121.

Cota, G.F., L. Legendre, M. Gosselin and R.G. Ingram. 1991. Ecology of bottom ice algae: I. Environmental controls and variability. *J. Mar. Syst.*, 2: 257-277.

Cota G.F., S.J. Prinsenberg, E.B. Bennett, J.W. Loder, M.R. Lewis, J.L. Anning, N.H. Watson and L.R. Harris. 1987. Nutrient fluxes during extended blooms of arctic ice algae. *J. Geophys. Res.*, 92: 1951-1962.

Cota G.F. and R.E.H. Smith. 1991. Ecology of bottom ice algae: II. Dynamics, distributions and productivity. *J. Mar. Syst.*, 2: 279-295.

Cottier F., H. Eicken and P. Wadhams. 1999. Linkages between salinity and brine channel distribution in young sea ice. *J. Geophys. Res.*, 104: 15,859-15,871.

Cox G.F.N. and W.F. Weeks. 1975. Brine drainage and initial salt entrapment in sodium chloride ice. *CRREL Res. Rep.* 345, Cold. Reg. Res. Eng. Lab., Hanover, New Hampshire.

Cox, G.F. and W.F. Weeks. 1983. Equations for determining the gas and brine volumes in sea ice samples. *J. Glaciol.*, 29: 306-316.

Crawford, G., L. Padman and M. McPhee. 1999. Turbulent mixing in Barrow Strait. *Cont. Shelf Res.*, 19: 205-245.

Cressie N.A.C. 1993. *Statistics for Spatial Data*, Revised Edition. John Wiley & Sons, Inc., New York.

Curry, J.A., J.L. Schramm and E.E. Ebert. 1995. Sea ice-albedo climate feedback mechanism. *J. Clim.*, 8: 240-247.

Cutnell, J.D. and K.W. Johnson. 2005. *Physics*, 7th Edition. John Wiley and Sons, Inc., USA.

Déry, S. J., and L.-B. Tremblay. 2004. Modeling the effects of wind redistribution on the snow mass budget of polar sea ice. *J. Phys. Oceanogr.*, 34: 258-271.

Déry, S.J. and M.K. Yau. 1999. A climatology of adverse winter-type weather events. *J. Geophys. Res.*, 104: 16 657-16 672.

Déry, S. J., and M.K. Yau. 2002. Large-scale mass balance effects of blowing snow and surface sublimation. *J. Geophys. Res.*, 107: 4679, doi: 10.1029/2001JD001251.

Drinkwater, M.R. and G.B. Crocker. 1988. Modeling changes in the dielectric and scattering properties of young snow covered sea ice at GHz frequencies. *J. Glaciol.*, 34: 274-282.

Dunkle, R.V. and J.T. Bevans. 1956. An approximate analysis of the solar reflectance and transmittance of a snow cover, *J. Meterol.*, 13: 212-216.

Ehn, J.K. 2001. *Optical Properties of the Sea Ice and Seawater in Santala Bay: Measurements and Modelling.* Master's Thesis. University of Helsinki. 82 p.

Eicken, H. 2003. From the microscopic, to the macroscopic, to the regional scale: growth, microstructure and properties of sea ice. IN *Sea Ice: An Introduction to its Physics, Chemistry, Biology and Geology*, D.N. Thomas and G.S. Dieckmann (Eds). Blackwell Science Ltd., Oxford, UK. pp. 22-81.

Eicken, H., C. Bock, R. Wittig, H. Miller and H.-O. Poertner. 2000. Nuclear magnetic resonance imaging of sea ice pore fluids: methods and thermal evolution of pore microstructure. *C. Reg. Sci. Tech.*, 31: 207-225.

Eicken H., M.A. Lange and G.S. Dieckmann. 1991. Spatial variability of sea-ice properties in the northwestern Weddell Sea. J. *Geophys. Res.*, 96: 10,603-10,615.

Eicken, H., M. A. Lange, H.-W. Hubberten, and P. Wadhams. 1994. Characteristics and distribution patterns of snow and meteoric ice in the Weddell Sea and their contribution to the mass balance of sea ice. *Ann. Geophys.*, 12: 80-93.

Eide L.I. and S. Martin. 1975. The formation of brine drainage features in young sea ice. *J. Glaciol.*, 14: 137-154.

Eppley, R.W. 1972. Temperature and phytoplankton growth in the sea. *Fish. Bull.*, 70: 1063-1085.

Feltham, D.L., N. Untersteiner, J. S. Wettlaufer and M.G. Worster. 2006. Sea ice is a mushy layer. *Geophys. Res. Lett.*, 33: L14501, doi:10.1029/2006GL026290.

Flato, G. and R.D. Brown. 1996. Sensitivity of landfast Arctic sea ice to changes in snow cover and climate as determined by a one-dimensional thermodynamic model. *J Geophys. Res.*, 101: 25,767-25,777.

Flato, G.M. and CMIP contributors. 2004. Sea-ice climate and sensitivity as simulated by global climate models. *Climate Dyn.*, 23: 229-241.

Fortier M., L. Fortier, C. Michel and L. Legendre. 2002. Climatic and biological forcing of the vertical flux of biogenic particles under seasonal Arctic sea ice. *Mar. Ecol. Prog. Ser.*, 225: 1-16.

Garrison, D.L., A.R. Close and E. Remnitz. 1989. Algae concentrated by frazil ice: evidence from laboratory experiments and field measurements. *Antarctic Sci.*, 1: 313-316.

Garrity, C. 1992. Characterization of snow on floating ice and case studies of brightness temperature changes during the onset of melt. Chapter 16. In: Carsey, F.D. (Ed.) Microwave Remote Sensing of Sea Ice. *Geophys. Monogr. Ser.*, 68: 314-328.

Golden, K.M., S.F. Ackley and V.I. Lytle. 1998. The percolation phase transition in sea ice. *Science*, 282: 2238-2241.

Golden, K.M., A.L. Heaton, H. Eicken and V.I. Lytle. 2006. Void bounds for fluid transport in sea ice. *Mech. Mater.*, 38: 801-817.

Goodison, B.E., J.R. Metcalfe and P.Y.T. Louie. 1998. Summary of country analyses and results, Annex 5.B Canada. In: The WMO Solid Precipitation Measurement Intercomparison Final Report, *Instrum. Obs. Meth. Rep.*, 67: 105-112.

Gosselin, M., L. Legendre, J.C. Therriault, S. Demers and M. Rochet. 1990. Light and nutrient limitation of sea-ice microalgae (Hudson Bay, Canadian Arctic). *J. Phycol.*, 26: 220-232.

Gosselin, M., L. Legendre, S. Demers and R.G. Ingram. 1985. Responses of sea-ice microalgae to climatic and fortnightly tidal energy inputs (Manitounuk Sound, Hudson Bay). *Can. J. Fish. Aquat. Sci.*, 42: 999-1006.

Gosselin, M., L. Legendre, J.-C. Therriault, S. Demers and M. Rochet. 1986. Physical control of the horizontal patchiness of sea-ice microalgae. *Mar. Ecol. Prog Ser.*, 29: 289-298.

Gosselin, M., M. Levasseur, P.A. Wheeler, R.A. Horner and B.C. Booth. 1997. New measurements of phytoplankton and ice algal production in the Arctic ocean. *Deep-Sea Res.*, 44: 1623-1644.

Gradinger, R. 1996. Occurrence of an algal bloom under Arctic pack ice. *Mar. Ecol. Prog. Ser.*, 131: 301-305.

Gradinger, R., M. Spindler and D. Henschel. 1991. Development of Arctic sea-ice organisms under graded snow cover. *Polar Res.*, 10: 295-307.

Grenfell, T.C. 1979. The effects of ice thickness on the exchange of solar radiation over polar oceans. *J. Glaciol.*, 22: 305-320.

Grenfell, T.C. 1983. A theoretical model of the optical properties of sea ice in the visible and near infrared. *J. Geophys. Res.*, 88: 9723-9735.

Grenfell, T.C. 1991. A radiative transfer model for sea ice with vertical structure variations. *J. Geophys. Res.*, 96: 16,991-17,001.

Grenfell, T.C. and G. A. Maykut. 1977. The optical properties of ice and snow in the Arctic basin. *J. Glaciol.*, 18: 445-463.

Grenfell, T.C. and D.K. Perovich. 1984. Spectral albedos of sea ice and incident solar irradiance in the Southern Beaufort Sea. *J. Geophys. Res.*, 89: 3573-3580.

Hanesiak, J.M. 2001. *Development of a One-Dimensional Electro-Thermophysical Model of the Snow Sea-Ice System: Arctic Climate Processes and Microwave Remote Sensing Applications*. PhD Thesis. University of Manitoba. 293 p.

Hanesiak, J.M, D. G., Barber, R. De Abreu and J.J. Yackel. 2001. Local and regional albedo: Observations of Arctic first-year sea ice during melt ponding. *J. Geophys. Res.*, 106: 1005-1016.

Hanesiak, J.M., D.G. Barber and G.M. Flato. 1999. The role of diurnal processes in the seasonal evolution of sea ice and its snow cover. *J. Geophys. Res.*, 104: 13,593-13,604.

Haines, E.M., R.G. Buckley and H.J. Trodahl. 1997. Determination of the depth dependent scattering coefficient in sea ice. *J. Geophys. Res.*, 102: 1141-1151.

Hattori, H. and H. Saito. 1997. Diel changes in vertical distribution and feeding activity of copepods in ice-covered Resolute Passage, Canadian Arctic, in spring 1992. *J. Mar. Syst.*, 11: 205-219.

Holm-Hansen, O., C.J. Lorenzen, R.W. Holmes and J.D. Strickland. 1965. Fluorometric determination of chlorophyll, *J. Cons. Int. Expl. Mer.*, 30: 3-15.

Holt, B. and S.A. Digby. 1985. Processes and imagery of first year sea ice during the melt season. J. Geophys. Res., 90: 5045-5062.

Hop H., M. Poltermann, O.J. Lønne, S. Falk-Petersen, R. Korsnes and W.P. Budgell. 2000. Ice amphipod distribution relative to ice density and under-ice topography in the northern Barents Sea. *Polar Biol.*, 23: 357-367.

Horner, R., S.F. Ackley, G.S. Dieckmann, B. Gulliksen, T. Hoshiai, L. Legendre, I.A. Melnikov, W.S. Reeburgh, M. Spindler and C.W. Sullivan. 1992. Ecology of sea ice biota 1. Habitat, terminology, and methodology. *Polar Biol.*, 12: 417-427.

Horner, R.A., EE. Syvertsen, D.P. Thomas and C. Lange. 1988. Proposed terminology and reporting units for sea ice algal assemblages. *Polar Biol.*, 8: 249-253.

Iacozza, J. and D.G. Barber. 1999. An examination of the distribution of snow on sea ice. *Atmosphere-Ocean*, 37: 21-51.

Iacozza, J. and D.G. Barber. 2001. Ablation patterns of snow cover over smooth first-year sea ice in the Canadian Arctic. *Hydro. Proc.*, 15: 3359-3569.

Isaaks E.H. and R.M. Srivastava. 1989. *An Introduction to Applied Geostatistics*. Oxford University Press, New York.

Jin, M., C.J. Deal, J. Wang, K.-H. Shin, N. Tanaka, T.E. Whitledge, S.H. Lee and R.R. Gradinger. 2006. Controls of the landfast ice-ocean ecosystem offshore Barrow, Alaska. *Ann. Glaciol.*, 44: Accepted.

Junge, K., H. Eicken, J.W. Deming. 2004. Bacterial activity at -2 to -20°C in Arctic wintertime sea ice. *Appl. Environ. Microbiol.*, 70: 550-557, doi: 10.1128/AEM.70.1.550–557.2004.

Krembs, C., R. Gradinger and M. Spindler. 2000. Implications of brine channel geometry and surface area for the interaction of sympagic organisms in Arctic sea ice. *J. Exp. Mar. Biol. Ecol.*, 243: 55-80.

Krembs, C., T. Mock and R. Gradinger. 2001. A mesocosm study of physical-biological interactions in artificial sea ice: effects of brine channel surface evolution and brine movement on algal biomass. *Polar Biol.*, 24: 356-364.

Krembs, C., K. Tuschling and K.v. Juterzenka. 2002. The topography of the ice-water interface – its influence on the colonization of sea ice by algae. *Polar Biol.*, 25: 106-117.

Lake R.A. and E.L. Lewis. 1970. Salt rejection be sea ice during growth. J. Geophys. Res., 75: 583-597.

Langlois, A., C.J. Mundy and D.G. Barber. 2006. On the winter evolution of snow thermophysical properties over land-fast first-year sea ice. *Hydrol. Proc.*, In Press, doi: 10.1002/hyp.6407.

Lavoie, D., K. Denman and C. Michel. 2005. Modeling ice algal growth and decline in a seasonally ice-covered region of the Arctic (Resolute Passage, Canadian Archipelago). *J. Geophys. Res.*, 110: C11009, doi: 10.1029/2005JC002922.

Ledley, T.S., 1991. Snow on sea ice: Competing effects in shaping climate. *J. Geophys. Res.*, 96: 17,195-17,208.

Legendre, L., M. Aota, K. Shirasawa, M.-J. Martineau and M. Ishikawa. 1991. Crystallographic structure of sea ice along a salinity gradient and environmental control of microalgae in the brine cells. *J. Mar. Syst.*, 2: 347-357.

Legendre, L., S.F. Ackley, G.S. Dieckmann, B. Gulliksen, R. Horner, T. Hoshiai, I.A. Melnikov, W.S. Reeburgh, M. Spindler, and C.W. Sullivan. 1992. Ecology of sea ice biota 2. Global significance. *Polar Biol.*, 12: 429-444.

Legendre, L. and M. Gosselin. 1991. In situ spectroradiometric estimation of microalgal biomass in first-year sea ice. *Polar Biol.*, 11: 113-115.

Lehning, A., P. Bartelt, B. Brown, C. Fierz and P. Satyawali. 2002. A physical SNOWPACK model for the Swiss avalanche warning Part II. Snow microstructure. *Cold Reg. Sci. Technol.*, 35: 147-167.

Light, B. 2000. *Structural-optical relationships in first-year sea ice.* PhD. Thesis, University of Washington, 160 p.

Light, B, H. Eiken, G.A. Maykut and T.C. Grenfell. 1998. The effect of induced particulates on the spectral albedo of sea ice. *J. Geophys. Res.*, 103: 27,739-25,752.

Light, B., G. A. Maykut and T. C. Grenfell. 2003. A two-dimensional Monte Carlo model of radiative transfer in sea ice, *J. Geophys. Res.*, 108: 3219, doi:10.1029/2002JC001513.

Lillesand, T.M. and R.W. Kiefer. 2004. *Remote Sensing and Image Interpretation*, 5th Edition, John Wiley & Sons, New York.

Liston, G. E., and M. Sturm. 1998. A snow-transport model for complex terrain. *J. Glaciol.*, 44: 498-516.

Livingstone, C.E., R.G. Onstott, L.D. Arsenault, A.L. Grey and K.P. Singh. 1987. Microwave sea-ice signatures near the onset of melt. *IEEE Trans. Geosci. Remote Sens.*, 25: 174-187.

Lønne O.J. and B. Gulliksen. 1991. Sympagic macro-fauna from multiyear sea-ice near Svalbard. *Polar Biol.*, 11: 471-477

Lytle, V.I. and S.F. Ackley. 1996. Heat flux through sea ice in the Western Weddell Sea: convective and conductive transfer processes. *J. Geophys. Res.*, 101: 8853-8868.

Lytle, V.I., R. Massom, A. Bindoff, A. Worby and I. Allison. 2000. Winter-time heat flux to the underside of East Antarctic pack ice. *J. Geophys. Res.*, 105: 28,759-28,770.

Maranger R., D.F. Bird and S.K. Juniper. 1994. Viral and bacterial dynamics in Arctic sea ice during the spring algal bloom near Resolute, N.W.T., Canada. *Mar. Ecol. Prog. Ser.*, 111: 12-127.

Martin S. 1979. A field study of brine drainage and oil entrainment in first-year sea ice. *J. Glaciol.*, 22: 473-502.

Martin, S., R. Drucker and M. Fort. 1995. A laboratory study of frost flower growth on the surface of young sea ice. *J. Geophys. Res.*, 100: 7027-7036.

Maykut, G., A. 1986. The surface heat and mass balance. IN *The Geophysics of Sea Ice*, N. Untersteiner (Ed). NATO ASI Series B: Physics vol. 146, Plenum Press, New York. pp. 395-464.

Maykut, G.A. and T.C. Grenfell (1975), The spectral distribution of light beneath first-year sea ice in the Arctic Ocean, Limnol. Oceanogr., 20: 554-563.

Maykut, G. A., and M. G. McPhee. 1995. Solar heating of the Arctic mixed layer, *J. Geophys. Res.*, 100: 24,691- 24,703.

McBean, G. 1992. The Earth's climate system. *WMO Bull.*, 41: 393-401.

McPhee, M.G. 1990 Small-scale processes, IN *Polar Oceanography: Part A. Physical Science*, W.O. Smith Jr. (Ed). Elsevier, New York. pp. 287-334.

Melling, H. 2000. Exchanges of freshwater through the shallow straits of the North American Arctic, IN *The Freshwater Budget of the Arctic Ocean*, E.P. Jones, P. Wadhams and E.L. Lewis (Eds). Kluwer Academic Publishers, Norwell, USA. pp. 479-502.

Melling, H. 2002. Sea ice of the northern Canadian Arctic Archipelago. *J. Geophys. Res.*, 107: 3181, doi: 10.1029/2001JC001102.

Melling, H. R.A. Lake, D.R. Topham and D.B. Fissel. 1984. Oceanic thermal structure in the western Canadian Arctic. *Cont. Shelf Res.*, 3: 233-258.

Mellor, M., 1977. Engineering properties of snow. *J. Glaciol.*, 19: 15-66.

Mellor M. 1986. Mechanical behavior of sea ice. IN *The Geophysics of Sea Ice*, N. Untersteiner (Ed). NATO ASI Series B: Physics vol. 146, Plenum Press, New York. pp. 165-281.

Michel, C., L. Legendre, S. Demers and J.-C. Therriault. 1988. Photoadaptation of sea-ice microalgae in springtime: photosynthesis and carboxylating enzymes. *Mar. Ecol. Prog. Ser.*, 50:177-185.

Michel, C., L. Legendre, R.G. Ingram, M. Gosselin and M. Levasseur. 1996. Carbon budget of sea-ice algae in spring: evidence of a significant transfer to zooplankton grazers. *J. Geophys. Res.*, 101: 18,345-18,360.

Moberg, L., B. Karlberg, K. Sørensen and T. Källqvist. 2002. Assessment of phytoplankton class abundance using absorption spectra chemometrics. *Talanta*, 56, 153-160.

Mundy, C.J. 2000. Section 2.4 Snow physical properties. IN *C-ICE 2000 Data Report* Iacozza, J. and D.G. Barber (Eds), University of Manitoba, Canada, CEOS Tech 2000-12-01: 33-39. WWW Page, http://www.umanitoba.ca/faculties/environment/geography/ceos/projects/cice/data_reports/C_ICE%20Data%20Report2000.pdf

Mundy, C.J. and D.G. Barber. 2003. *C-ICE 2002 Field Summary*, University of Manitoba, Canada, CEOS-Tech-03-01 WWW Page, http://www.umanitoba.ca/faculties/environment/geography/ceos/projects/cice/data_reports/c-ice_data_report_2002.pdf

Mundy, C.J., D.G. Barber and C. Michel. 2005. Variability of snow and ice thermal, physical and optical properties pertinent to sea ice algae biomass during spring, *J. Mar. Syst.*, 58, 107-120, doi: 10.1016/j.jmarsys.2005.07.003.

Mundy, C.J., J.K. Ehn, D.G. Barber and C. Michel. 2007a. Influence of snow cover and algae on the spectral dependence of transmitted irradiance through Arctic landfast first-year sea ice. *J. Geophys. Res.*, 112, C03007, doi:10.1029/2006JC003683.

Mundy, C.J., D.G. Barber, C. Michel and R.F. Marsden. 2007b. Linking ice structure and microscale variability of algal biomass in Arctic first-year sea ice using an *in situ* photographic technique. *Polar Biol.*, doi:10.1007/s00300-007-0267-1.

Nakawo, M and N.K. Sinha. 1981. Growth rate and salinity profile of first-year sea ice in the high Arctic. *J. Glaiol.*, 27: 315-330.

Nakawo, M and N.K. Sinha. 1984. A note on brine layer spacing of first-year sea ice. *Atmosphere-Ocean*, 22: 193-206.

Niebauer, H.J. and W.O. Smith, Jr. 1989. A numerical model of mesoscale physical-biological interactions in the Fram Strait marginal ice zone. *J. Geophys. Res.*, 94: 16,151-16,175.

Niedrauer, T.M. and S. Martin. 1979. An experimental study of brine drainage and convection in young sea ice. *J. Geophys. Res.*, 84: 1176-1186.

Oke, T.R., 1987. *Boundary Layer Climates.* Second edition., Routledge, London and New York.

Papakyriakou, T.N. 1999. *An Examination of Relationships among the Energy Balance, Surface Properties and Climate over Snow Covered Sea Ice during the Spring Season.* PhD. Thesis, University of Waterloo, 364 p.

Parkinson, C. L., D. J. Cavalieri, P. Gloersen, H. J. Zwally, and J. C. Comiso. 1999. Variability of the Arctic Sea Ice Cover 1978-1996, *J. Geophys. Res.*, 104: 20,837-20,856.

Parsons, T.R., Y. Maita and C.M. Lali. 1984. A manual of chemical and biological methods for seawater analysis. Pergamon Press, Toronto.

Perovich D.K. 1990. Theoretical estimates of light reflection and transmission by spatially complex and temporally varying sea ice covers. *J. Geophys. Res.*, 95: 9557-9567.

Perovich, D.K., G.F. Cota, G.A. Maykut and T.C. Grenfell. 1993. Bio-optical observations of first-year arctic sea ice. *Geophys. Res Lett.*, 11: 1059-1062.

Perovich, D. K., and B. Elder. 2001. Temporal evolution and spatial variability of the temperature of Arctic sea ice, *Ann. Glaciol.*, 33: 207–211.

Perovich, D.K. and A.J. Gow. 1996. A quantitative description of sea ice inclusions. *J. Geophys. Res.*, 101: 18,327-18,343.

Perovich, D. K., T. C. Grenfell, B. Light, and P. V. Hobbs. 2002. Seasonal evolution of the albedo of multiyear Arctic sea ice, *J. Geophys. Res.*, 107: 8044, doi:10.1029/2000JC000438.

Perovich, D.K, C.S. Roesler and W.S. Pegau. 1998. Variability in Arctic sea ice optical properties, *J. Geophys. Res.*, 103: 1193-1208.

Platt, T., C.L. Gallegos and W.G. Harrison. 1980. Photoinhibition of photosynthesis in natural assemblages of marine phytoplankton. *J. Mar. Res.*, 38: 686-701.

Polyakov, I.V., A. Beszczynska, E.C. Carmack, I.A. Dmitrenko, E. Fahrbach, I.E. Frolov, R. Gerdes, E. Hansen, J. Holfort, V.V. Ivanov, M.A. Johnson, M. Karcher, F. Kauker, J. Morison, K.A. Orvik, U. Schauer, H.L. Simmons, Ø. Skagseth, V.T. Sokolov, M. Steele, L.A. Timokhov, D. Walsh and J.E. Walsh. 2005. One more step toward a warmer Arctic. *Geophys. Res. Lett.*, 32: L17605, doi: 10.1029/2005GL023740.

Pomeroy, J.W., D.M. Gray and P.G. Landine. 1993. The prairie blowing snow model: characteristics, validation, operation, *J. Hydrol.*, 144: 165-192.

Pomeroy, J.W. and L. Li. 2000. Prairie and arctic areal snow cover mass balance using a blowing snow model. *J. Geophys. Res.*, 105: 26,619-26,634.

Reeburgh, W.S. 1984. Fluxes associated with brine motion in growing sea ice. *Polar Biol.*, 3: 29-33.

Reimnitz, E., E.W. Kempema, W.S. Weber, J.R. Clayton and J.R. Payne. 1990. Suspended-matter scavenging by rising frazil ice, IN *Sea Ice Properties and Process*, Ackley, S.F. and W.F. Weeks (Eds), CRREL Monogr. 90-1, pp. 97-100.

Roberts, A., I. Allison and V. I. Lytle. 2001. Sensible- and latent-heat flux estimates over the Mertz Glacier polynya, East Anarctica, from in-flight measurements. *Ann. Glaciol.*, 33: 377-384.

Robinson, D.H., K.R. Arrigo, R. Iturriaga and C.W. Sullivan. 1995. Microalgal light-harvesting in extreme low-light environments in McMurdo Sound, Antarctica. *J. Phycol.*, 31: 508-520.

Rothrock, D.A. and J. Zhang. 2005. Arctic Ocean sea ice volume: What explains its recent depletion? *J. Geophys. Res.*, 110: C01002, doi:10.1029/2004JC002282.

Rysgaard, S., M. Kühl, R.N. Glud and J.W. Hansen. 2001. Biomass, production and horizontal patchiness of sea ice algae in a high-Arctic fjord (Young Sound, NE Greenland). *Mar. Ecol. Prog. Ser.*, 223: 15-26.

Sakshaug, E. 2004. Primary and secondary production in the Arctic seas, IN The Organic Carbon Cycle in the Arctic Ocean, Stein, R. and R. W. Macdonald (Eds). Springer, New York. pp. 57-81.

Sarthou, G., K.R. Timmermans, S. Blain and P. Tréguer. 2005. Growth physiology and fate of diatoms in the ocean: A review. *J. Sea Res.*, 53: 25-42.

Schmidt, R.A. 1982. Vertical profiles of wind speed, snow concentration, and humidity in blowing snow. *Boundary Layer Meteorol.*, 23: 223-246.

Schmidt, R.A. 1986. Transport rate of drifting snow and the mean wind speed profile. *Boundary Layer Meteorol.*, 34: 213-241.

Schmidt, S., and J.D. Dent. 1993. A theoretical prediction of the effects of electrostatic forces on saltating snow particles. *Ann. Glaciol.*, 18: 234-238.

Schwarz, J., R.M.W. Frederking, V.P. Gavrilo, I.G. Petrov, K.-I. Hirayama, M. Mellor, P. Tryde and K.D.Vaudrey. 1981. Standardized testing methods for measuring mechanical properties of sea ice. *Cold Reg. Sci. Technol.*, 4: 245-253.

Schwerdtfeger, P. 1963. The thermal properties of sea ice. *J. Glaciol.*, 4: 789-907.

Sinha, N.K. 1977. Technique for studying structure of sea ice. *J. Glaciol.*, 18: 315-323.

Smith, R.E.H., J. Anning, P. Clement and G. Cota. 1988. Abundance and production of ice algae in Resolute Passage, Canadian Arctic. *Mar. Ecol. Prog. Ser.*, 48: 251-263.

Smith, R.E.H., W.G. Harrison, L.R. Harris and A.W. Herman. 1990. Vertical fine structure of particulate matter and nutrients in sea ice of the high arctic. *Can. J. Fish. Aquat. Sci.*, 47: 1348-1355.

Steffen, K. and T. DeMaria. 1996. Surface energy fluxes over Arctic winter sea ice in Barrow Strait. *J. Appl. Meteor.*, 35: 2067-2079.

Steffen, W., A. Sanderson, P.D. Tyson, J. Jäger, P.A. Matson, B. Moore III, F. Oldfield, K. Richardson, H.-J. Schellnhuber, B.L. Turner II, R.J. Wasson. 2004. *Global Change and the Earth System: A Planet Under Pressure*, Springer-Verlag, Berlin, Germany.

Stirling, I. and H. Cleator (Eds). 1981. *Polynyas in the Canadian Arctic.* Occasional Paper Number 45, Canadian Wildlife Service, Minister of Supply and Services Canada.

Stramski, D., A. Sciandra and H. Claustre. 2002. Effects of temperature, nitrogen, and light limitation on the optical properties of the marine diatom *Thalassiosira pseudonana*. *Limnol. Oceanogr.*, 47: 392-403.

Sturm, M., J. Holmgren and D.K. Perovich. 2001. Spatial variations in the winter heat flux at SHEBA: Estimates from snow-ice interface temperatures. *Ann. Glaciol.*, 33: 213-220.

Sturm, M., J. Holmgren, and D.K. Perovich. 2002. Winter snow cover on the sea ice of the Arctic Ocean at the Surface Heat Budget of the Arctic Ocean (SHEBA): Temporal evolution and spatial variability. *J. Geophys. Res.*, 107: 8047, doi:10.1029/2000JC000400.

Syvertsen, E.E. 1991. Ice algae in the Barents Sea: types of assemblages, origin, fate and role in the ice-edge phytoplankton bloom. *Polar Res.*, 10: 277-287.

Thomas, G.E. and K. Stamnes. 1999. *Radiative Transfer in the Atmosphere and Ocean.* Cambridge University Press, Cambridge, UK.

Thorndike, A.A., D.A. Rothrock, G.A. Maykut, and R. Colony. 1975. The thickness distribution of sea ice. *J. Geophys. Res.*, 80: 4501-4513.

Tsurikov, V.L. 1979. The formation and composition of the gas content of sea ice. *J. Glaciol.*, 22: 67-81.

Tucker, W.B., A.J. Gow and J.A. Richter. 1984. On small-scale variations of salinity in first-year sea ice. *J. Geophys. Res.*, 89: 6505-6514.

Untersteiner, N. 1968. Natural desalination and equilibrium salinity profile of perennial sea ice. *J. Geophys. Res.*, 73: 1251-1257.

Wadhams, P. 2000. *Ice in the Ocean.* Gordon and Breach Science Publishers, Newark, NJ.

Wadhams, P., and N.R. Davis. 2000. Further evidence for ice thinning in the Arctic Ocean. *Geophys. Res. Lett.*, 27: 3973-3975.

Wadhams, P., M.A. Lange and S.F. Ackley. 1987. The ice thickness distribution across the Atlantic sector of the Antarctic Ocean in midwinter. *J. Geophys. Res.*, 92: 14,535-14,552.

Wakatsuchi M. and T. Saito. 1985. On brine drainage channels of young sea ice. Ann. Glaciol., 6: 200-202.

Warren, S.G. 1982. Optical properties of snow. *Rev. Geophys. Space Phys.*, 20: 67-89.

Warren, S.G., I.G. Rigor, N. Untersteiner, V.F. Radionov, N.N. Bryazgin, Y.I. Aleksandrov, and R. Colony. 1999. Snow depth on Arctic sea ice. *J. Clim.*, 12: 1814-1829.

Warren, S.G., and W.J. Wiscombe. 1980. A model for the spectral albedo of snow. II: Snow containing atmospheric aerosols. *J. Atmos. Sci.*, 37: 2735-2745.

Weeks W.F. and S.F. Ackley. 1982. The growth, structure, and properties of sea ice. CRREL Monograph 82-1, *Cold Reg. Res. Eng. Lab.*, Hanover, New Hampshire.

Weeks, W.F. and A.J. Gow. 1978. Preferred crystal orientations along the margins of the Arctic Ocean. *J. Geophys. Res.*, 84: 5105–5121.

Weissenberger J., G. Dieckmann, R. Gradinger and M. Spindler. 1992. Sea ice: A cast technique to examine and analyze brine pockets and channel structure. *Limnol. Oceanogr.*, 37: 179-183

Welch, H.E. and M.A. Bergmann. 1989. Seasonal development of ice algae and its prediction from environmental factors near Resolute, N.W.T., Canada. *Can. J. Fish. Aquat. Sci.*, 46: 1793-1804.

Welch, H.E., M.A. Bergmann, J.K. Jorgenson, and W. Burton. 1988. A subice suction corer for sampling epontic algae. *Can. J. Fish Aquat. Sci.*, 45, 562-568.

Werner I. and F. Lindemann. 1997. Video observations of the underside of arctic sea ice – features and morphology on medium and small scales. *Polar Res.*, 16: 27-36.

Widell, K., I. Fer and P.M. Haugan. 2006. Salt release from warming sea ice. *Geophys. Res. Lett.*, 33: L12501, doi:10.1029/2006GL026262.

Wiscombe, W.J. and S.G. Warren. 1980. A model for the spectral albedo of snow. I: Pure snow. *J. Atmos. Sci.*, 37: 2712-2733.

World Meteorological Organization. 1970. *WMO Sea ice nomenclature*. WMO Rep. 259, T.P. 145, Geneva, 147 pp. + 8 suppl.

Yackel, J., J. Hanesiak, and D.G. Barber. 2000. Melt ponds on sea ice in the Canadian Arctic Archipelago: Part 1 – Variability in morphology and surface radiation. *J. Geophys. Res.*, 105: 22,049-22,060.

Yen, Y.C., K.C. Cheng and S. Fukusako. 1991. Review of intrinsic thermophysical properties of snow, ice, sea ice and frost. IN: *Proceedings 3rd International Symposium on Cold Region Heat Transfer*, University of Alaska, Fairbanks, AK. pp. 187-218.

Yu, Y., G.A. Maykut and D.A. Rothrock. 2004. Changes in the thickness distribution of Arctic sea ice between 1958–1970 and 1993–1997. *J. Geophys. Res.*, 109: 8004, doi:10.1029/2003JC001982.

Zeebe R.E., H. Eicken, D.H. Robinson, D. Wolf-Gladrow and G.S. Dieckmann. 1996. Modeling the heating and melting of sea ice through light absorption by microalgae. *J. Geophys. Res.*, 101: 1163-1181.

Zhou, X. and S. Li. 2002. Phase functions of large snow meltclusters calculated using the geometrical optics method. IN *Proc. IEEE 2002 International Geoscience and Remote Sensing Symposium (IGARSS'02)*. VI: 3576-3578.